Decay Heat Measurements of Fission Fragments ^{86}Br, ^{91}Rb & ^{94}Sr Using Total Absorption Gamma-ray Spectroscopy

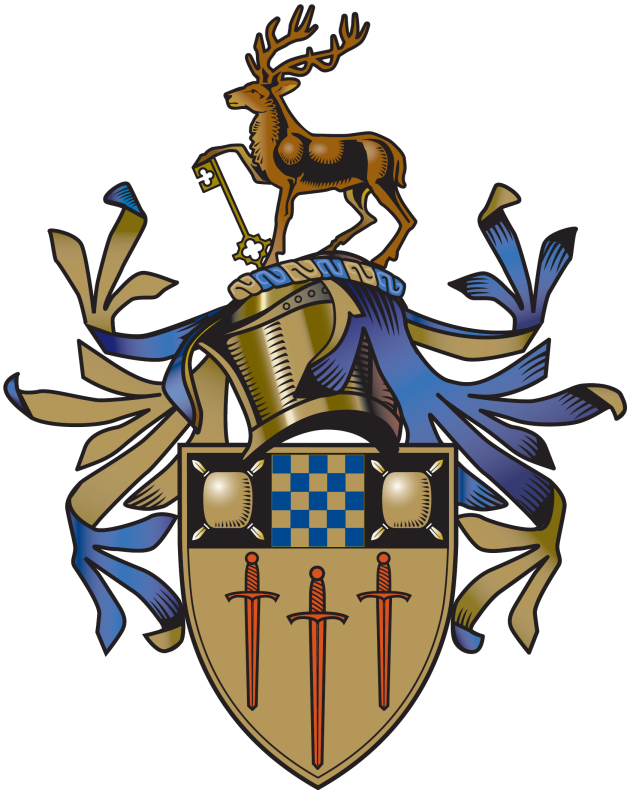

Simon James Rice

Submitted for the degree of Doctor of Philosophy

Centre for Nuclear and Radiation Physics,
Department of Physics,
University of Surrey,
Guildford,
GU2 7XH

10th July 2014

Supervisors:
Professor Patrick H Regan[1]
Doctor Alejandro Algora[2]
Doctor Jose Luis Táin Enriquez [2]

[1]The University of Surrey, Guildford, UK & The National Physical Laboratory, Teddington, UK
[2]Instituto De Física Corpuscular, Valencia, Spain

Abstract

During a nuclear reactor's normal operation, approximately 7-8% of the total heat produced is due to delayed β-decay of the initial fission products, and is known as decay heat. Once a reactor is shut down this decay heat contributes 100% of the heat produced by the fuel. Total absorption γ-ray spectroscopy utilises a near 4π geometry with a high efficiency to collect γ rays produced from a source placed in its centre. This total absorption can be used to determine the β-feeding levels of fission fragments that have large Q_β values. Conventional methods using HPGe detectors to determine β-feeding can be affected by the "*Pandemonium effect*". This occurs due to the low detection efficiency of high-energy γ rays in HPGe detectors. Current decay heat calculations predict lower values than calorimetry measurements and this needs to be addressed. An experiment was carried out in Jyvaskyla to measure the β-feeding levels of key nuclei (^{86}Br,^{91}Rb and ^{94}Sr) for decay heat calculations using a BaF_2 Total Absorption Spectrometer (TAS). This thesis describes the experimental method, the calibration of the TAS and, the analysis procedure to obtain the average mean γ ray and β particle energy for each isotope as well as the β decay strength function. The final results from this work have provided new mean energy values for the β decays of ^{86}Br ($\overline{E_\gamma}$=3822(6)(54) keV $\overline{E_\beta}$=1670(4)(28) keV) and ^{91}Rb ($\overline{E_\gamma}$=2788(5)(29) keV $\overline{E_\beta}$=1330(3)(22) keV) showing that the "*Pandemonium effect*" was present in the previously recorded data and a reduced uncertainty was obtained for the decay of ^{94}Sr ($\overline{E_\gamma}$=1472(9)(15) keV $\overline{E_\beta}$=826(5)(6) keV). The results have given increased validity to previous TAS measurements by Greenwood et al. and subsequently questions work by Rudstam et al. on the measurements of β-particle and γ-ray spectra of many fission fragments.

Copyright

Acknowledgements

The completion of my Ph.D. has been a long and enjoyable journey that I will not forget quickly. Along the way I have been helped and supported by many people both professionally and personally each adding something to the experience.

Firstly I would like to thank Prof. Paddy Regan for his help, energy that got me through, deciphering my "toddler" writing skills, and enabling me to experience may different labs and cultures, taking in over 80,000 miles and 12 different countries in the quest to learn nuclear physics. I would also like to thank the other academic staff at the University of Surrey who have always been available for help and discussion.

This work would not be possible with out the guidance and support of Dr. Alejandro Algora and Dr Jose Luis Táin Enriquez who were always open to listen to ideas and enter into discussions about any part of the analysis whether I was in Valencia or not. Through all of the travelling I managed to spend about half of my PhD in Valencia and would like to thank the IFIC Espectroscopía Gamma group for being very friendly and inviting when I arrived making staying in a foreign country with a different language, very easy. I would like to extend a personal thanks to Ebhelixes Valencia Marin for many a discussion of our analysis technique (and possibly a few times when we both didn't fully understand each other) and also her help with me "trying" to learn Spanish, but speaking it is still beyond me.

As well as my collaboration with Alejandro, Jose and Ebhelixes I would like to thank Zakari Issoufou, Dr. Amanda Porta and Dr. Muriel Fallot from Subatech Nantes for their help and many discussions of the work.

Throughout my PhD I have been surrounded by many fantastic people and I would like to thank all students and post docs of University of Surrey PhD office's for many a fun time out on experiments or even just in the office. From my time in Japan I would like to thank the people I worked with in RIKEN for a fantastic experience learning lots about the lab and equal amounts about karaoke.

I am eternally grateful to Jade Burraston for her love, help and support during my PhD even when we were on different continents. My friends and family have been fantastic support and always a welcome break from too much physics.

I would finally like to thank my Mum and Dad who without them I would not have got this far, and also for letting me lodge for the few weeks I would be back in the country before heading off again.

"*Rivers know this: there is no hurry. We shall get there some day.*"

A.A. Milne, *Winnie-the-Pooh*

Contents

List of Figures

List of Tables

1 Introduction

Discoveries in nuclear physics have helped create a range of technologies including modern day healthcare and power production to name but a few. Along with these creations of new technologies many fields of physics have expanded from these initial discoveries, such as nuclear physics, nuclear astrophysics and particle physics. The field of nuclear physics would not exist without Henri Becquerel's discovery of radioactivity in 1896 [1]. The discovery of radioactivity and work by Ernest Rutherford [2] helped Niels Bohr define the basis of the contemporary atomic model [3] defining the basics of many physical properties including structure of nuclei, α, β and γ decay.

Although the basis of many processes in nuclear physics have been described and are well documented, there are still many important questions that are being explored theoretically and experimentally, such as the search for new super heavy elements, the study of meta-stable excited states or isomers and the search for nuclear magic numbers [4, 5, 6].

1.1 Motivation

A nuclear incident in Japan on 11 March 2011, at the Fukushima Daiichi nuclear power plant, occurred after a 9.0 magnitude earthquake and subsequent tsunami. This incident caused destruction to the power plant, stopping cooling systems. Although power production was promptly halted, the heat produced from decay heat was causing degradation to the containment of the uranium based fuel. Due to a lack of primary cooling, the temperature of the fuel rods and the reactor core increased causing a hydrogen explosion at the plant, damaging the containment [7]. This can be considered an example of the relevance of the decay heat. Greater knowledge of decay heat from the nuclear fuel could have provided better safety plans to be formalised, perhaps reducing the risk of an incident like this occurring with such devastating effects in the future.

1.1.1 Decay Heat

Nuclear fission of uranium produces large numbers of different radionuclide species [8]. Commercial nuclear reactors can produce approximately 1040 different nuclides with the large majority being unstable against radioactive decay [9]. The energy released from these decays within the reactor

fuel is known as decay heat. During operations in thermal fission nuclear reactors, approximately 8% of the total heat produced in the reactor is due to decay heat and this contribution must be factored into the energy production [10]. Decay heat is the sole source of heat from the fuel in the absence of fission and therefore is extremely important in reactor design, irradiated fuel operations and storage.

Decay heat has three components: heavy particles (H_{HP}), light particles (H_{LP}) and photons (H_{EM}). Heavy particles are defined as neutrons, protons, α particles and spontaneous fission fragments, whereas light particles are defined as electrons, positrons, Auger electrons and conversion electrons [11]. These are sometimes referred to collectively as "*Betas*". Photons are defined as γ rays, X-rays, bremsstrahlung and annihilation radiation [11]. Data from evaluated nuclear databases such as JEFF 3.1 (Joint Evaluated Fission and Fusion File) [9] can be used in *Burn-Up* codes [12] to calculate the actinide and fission-product inventories for a specified condition of reactor operation as a function of the cooling period. The decay heat can then be derived by summing the decay energies from the emitted heavy particles, light particles and photons weighted with the activities of the produced fission products (M):

$$H_{HP}(t) = \sum_{i=1}^{M} \lambda_i^T N_i(t) \overline{E_{HP}^i} \tag{1.1}$$

$$H_{LP}(t) = \sum_{i=1}^{M} \lambda_i^T N_i(t) \overline{E_{LP}^i} \tag{1.2}$$

$$H_{EM}(t) = \sum_{i=1}^{M} \lambda_i^T N_i(t) \overline{E_{EM}^i} \tag{1.3}$$

$\bar{E}$, λ^T and N represent the mean average energy released per disintegration, the total decay constant for the nuclide and the number of the nuclides present respectively. The decay heat has also been experimentally measured by calorimetry thus providing an opportunity to test the accuracy of the nuclear datasets [13].

A discrepancy is found between the calorimetry data and the theoretical model developed using the nuclear dataset (see figure 1.1). This discrepancy is thought to be due to incorrect β decay data and more specifically missing β feeding to higher-lying levels in some key nuclei (see [15]). The decay spectroscopy of many fission fragments has been carried out using high-resolution γ-ray spectroscopy, due to the simplicity of this technique [16, 17]. The application of high resolution γ ray

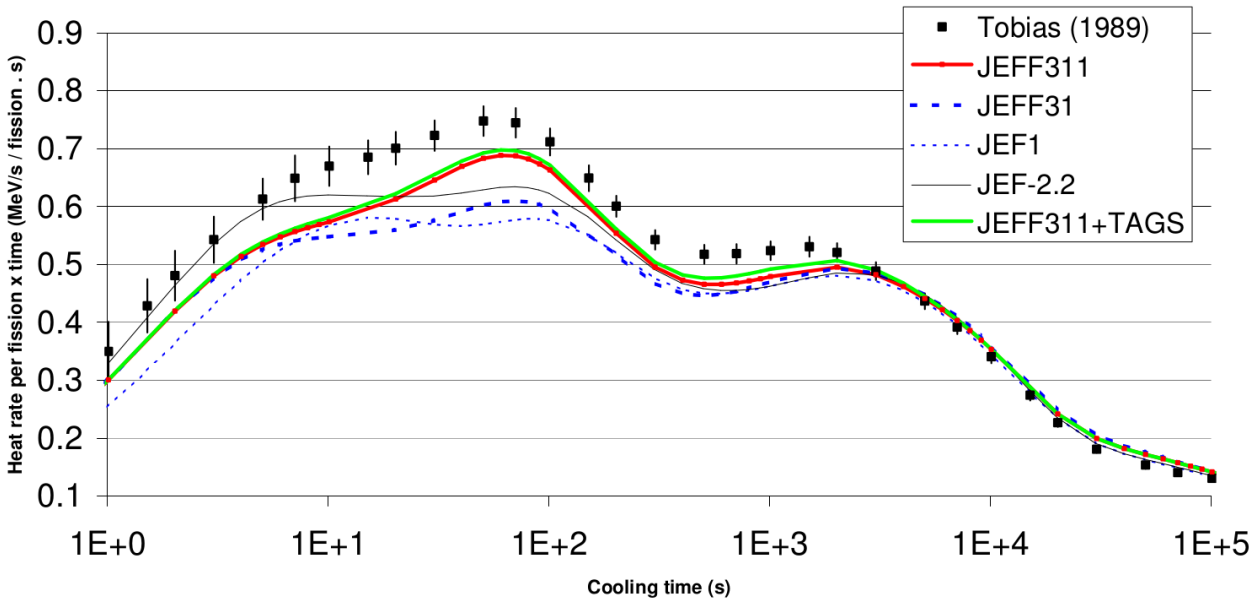

Figure 1.1: Decay heat produced by photons from ^{235}U thermal fission, comparing **Tobias** calorimetry data to **JEFF** database data and the improvements made by recent TAS measurements. Image produced by Mills [14], data taken from [15, 9].

measurements to quantify the individual β decays in some nuclei can suffer from the *pandemonium effect* (see section 2.3) resulting in the incorrect assignment of β feeding to low-lying levels in the daughter nucleus [18]. This results in a systematic error in the deduced mean β-particle and γ ray energies, thereby affecting the decay heat calculations.

1.1.2 The Nuclei of Interest

Work presented for this thesis will show the use of total absorption spectroscopy to measure the β-decay strength functions of the fission fragment nuclei ^{86}Br, ^{91}Rb and ^{94}Sr. The main motivation to measure these isotopes comes from the recommendation from references [11, 19] that contemporary isotope decay data is affected by the *pandemonium effect*, producing false β strength values. As well as an increase in the accuracy of the β strength function, such data will also provide more accurate information on the expected anti-neutrino production in nuclear reactors. The low, but finite, interaction probability of neutrinos provide an unique opportunity to externally monitor a reactor at a distance by studying the neutrino/anti-neutrino spectrum produced [20]. This non-destructive external monitoring can provide covert information about the reactor's operation and can be used to enforce the non-proliferation of nuclear weapons. An outcome of an accurate reactor neutrino/anti-neutrino model of military interest would enable efficient detection and identification of any nuclear reactor close enough to the detector, possibly including ones hidden on nuclear powered submarines. Along with the applicable reasons for remeasuring these isotopes, the data

also provide basic nuclear structure information which can help with the understanding of the evolution of rapid shape change in neutron-rich nuclei with Z ∼ 40 and A ∼ 100 [21, 22].

^{86}Br was long known to be a fission product from reactors but due to poor separation techniques its β decay to ^{86}Kr was not measured until 1962 by Stehney et al. [23]. This study utilised the neutron bombardment of enriched ^{86}Kr followed by chemical separation leading to the discovery of a complex β end point. Further studies by Williams et al. [24] improved the β particle and γ ray data collected, increasing the accuracy of the β end point and proposed an energy level decay scheme. This second work used the chemical separation of the selenium precursor due to difference in the ^{86}Br ($T_{1/2}$ =55.1 s) and ^{86}Se ($T_{1/2}$ =14.3 s) half-lives [25]. Similar measurements [26, 27, 28] have been collated with these original measurements to produce the currently accepted energy level scheme in nuclear decay databases [9, 25].

Decay heat studies by Yoshida [19] and a review by the NEA (Nuclear Energy Agency) [11] have highlighted ^{86}Br, as a priority 1 nuclei to be remeasured by total absorption γ-ray spectroscopy to correct any erroneous data due to the *pandemonium effect*. This NEA priority list contains all isotopes that are thought to either have a big impact on the decay heat (thus low uncertainty is required) or currently have a large recorded (or suspected) uncertainty resulting in its measured uncertainty propagating into the total mean decay heat energy.

The current ^{86}Br→^{86}Kr decay data in ENSDF (Evaluated Nuclear Structure Data File) was last evaluated in 2001 [29] but since, then high precision mass measurements by Rahaman et al. [30] have resulted in a re-evaluated Q_β-value of 7632(4) keV, a correction of 6 keV. A different measurement by Porquet et al. [31] measuring high-spin excitations gives good evidence that the ground state of ^{86}Br is more probable to be a $J^\pi = 1^-$ state rather then the $J^\pi = 2^-$ state reported in the evaluation. The most resent ENSDF evaluation of excited levels of ^{86}Br (not its decay) last evaluated in 2011 [25] revises this ground state giving a tentative $J^\pi = 1^-$ ground state. A subsequent measurement of ^{86}Kr$(n,n')^{86}$Kr has been performed by Fotiades et al. [32] provides multiple levels and joint γ ray transitions not seen in the previously recorded ENSDF data.

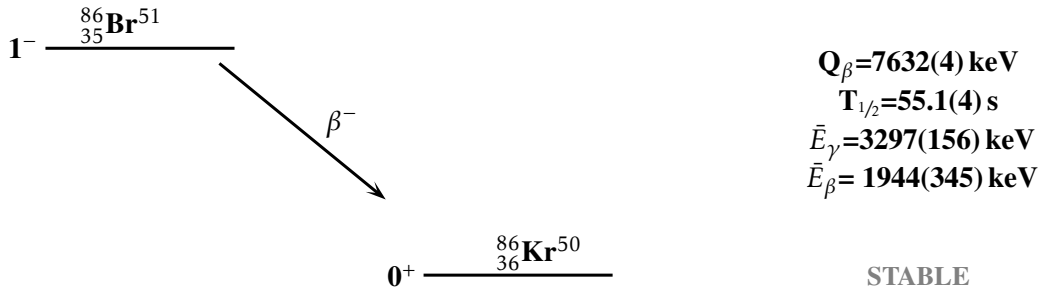

Figure 1.2: Simplistic overview of the previously recorded information for the β decay of ^{86}Br.

^{91}Rb was first identified in 1951 by Kofoed-Hansen et al. [33] from the decay of krypton isotopes and was found to undergo β^- decay. Further studies of the β decay of ^{91}Rb and the level structure of its daughter ^{91}Sr have been performed, [34, 35, 36, 37, 38] giving a very complex β decay structure. The current ^{91}Rb$\rightarrow$^{91}Sr decay data in ENSDF was last evaluated in 2013 [39]. The decay of ^{91}Rb can also occur via β-delayed neutron emission transmuting to ^{90}Sr, but due to the extremely small branch (0.00002%), this decay will be effectively excluded from this work.

Although ^{91}Rb is not a NEA priority 1 isotope to be remeasured for decay heat, like ^{86}Br, the recorded decay of ^{91}Rb has a strong impact on the recorded values for many other mean decay energies of fission fragments. This link is through work by Rudstam at. al [40] who measured the mean decay energies for many short lived fission fragments, via beta and gamma spectra measurements. Rudstam at. al's work expanded the then current known range of mean decay information using a gamma and beta detector set-up that was calibrated with the decay of ^{91}Rb. This calibration used the assumption that the decay of ^{91}Rb contained no significant/obvious *pandemonium effect*. If this assumption is found to be incorrect the recorded values of many other fission fragments may be erroneously recorded.

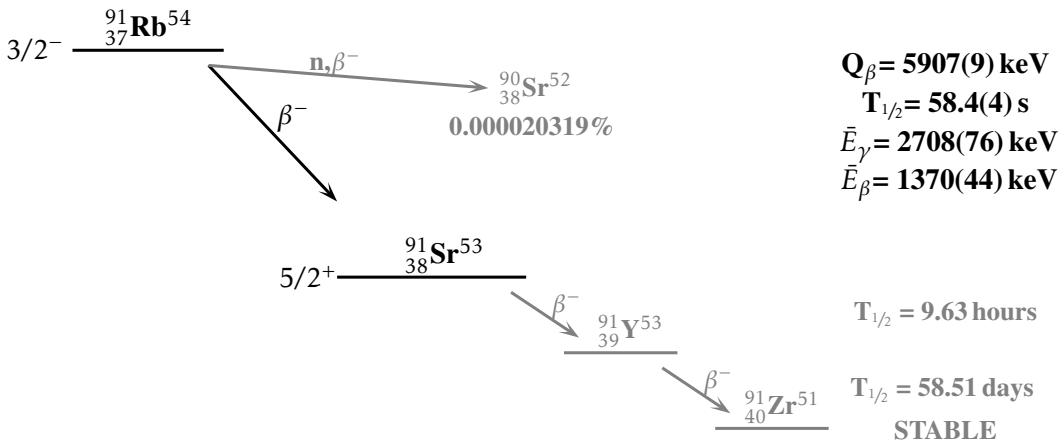

Figure 1.3: Simplistic overview of the previously recorded information for the β decay of ^{91}Rb.

^{94}Sr was first discovered in 1959 by Knight et al. [41] from the irradiation of ^{235}U by neutrons in the Los Alamos water boiler reactor separating out strontium isotopes via chemical separation. Experimental work [42] has provided discrete decay data for ^{94}Sr. The current ^{94}Sr$\rightarrow$^{94}Y decay data in ENSDF was last evaluated in 2006 [43].

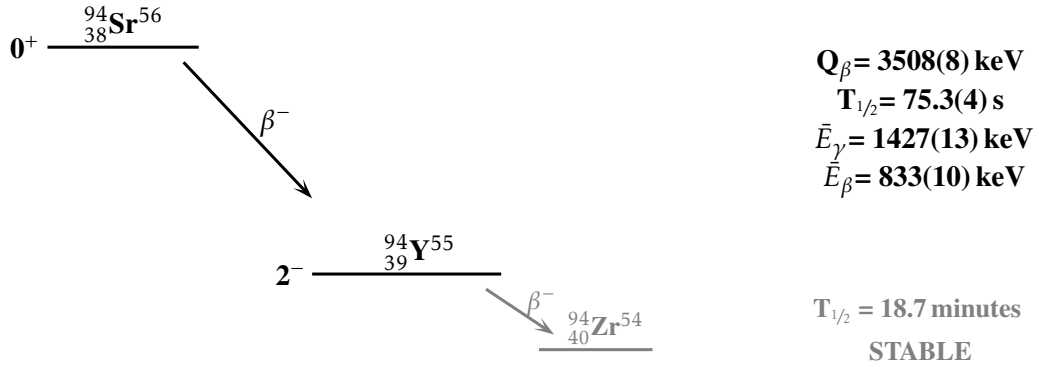

Figure 1.4: Simplistic overview of the previously recorded information for the β decay of ^{94}Sr.

Previous total absorption γ-ray spectroscopy work was performed on ^{91}Rb and ^{94}Sr by Greenwood et al. in 1997 [44] and this is included in the ENSDF database as reference, but is not used in the adopted β decay scheme. Due to the difference in technology and technique used in the analysis of the TAS data, the remeasurement could provide validation of both methods and thus validate a large amount of other data collected by Greenwood et al. A summary of the previously reported

data on ^{86}Br, ^{91}Rb and ^{94}Sr are summarised in Table 1.1 and full, current decay level schemes can be found in Appendix D.

Parent				Daughter				β^- Decay Information			
Isotope	Z	N	J^π	Isotope	Z	N	J^π	Q_β [keV]	$T_{\frac{1}{2}}$ [s]	$\overline{E_\beta}$ [keV]	$\overline{E_\gamma}$ [keV]
^{86}Br	35	51	1^-	^{86}Kr	36	51	0^+	7632(4)	55.1(4)	1943(345)	3297(156)
^{91}Rb	37	54	$3/2^-$	^{91}Sr	38	54	$5/2^+$	5907(9)	58.4(4)	2706(27)	1368(14)
^{94}Sr	38	56	0^+	^{94}Y	39	56	2^-	3508(8)	75.3(2)	833(6)	1427(11)

Table 1.1: Previously reported information on the isotopes to be studied from [25]. The decay on ground state spins / parities (J^π) and information of Q_β value, Half life ($T_{1/2}$), the mean average β-particle ($\overline{E_\beta}$) and γ ray energy ($\overline{E_\gamma}$) produced for the decay taken from [9].

1.2 Thesis Outline

The second chapter of this work describes some of the theoretical background of, or associated with, β decay, the nuclear structure effects which gives rise to decay heat issues and the technique of total absorption spectroscopy. The third chapter introduces the experimental equipment, procedure, calibration methods and preparation of the collected data. The fourth chapter presents information on the alteration and optimization of the Monte Carlo model used in this work. Chapter Five describes the approach taken to solve the inverse problem and an overview of the analysis technique. Chapter Six provide more details of the analysis of ^{86}Br, ^{91}Rb and ^{94}Sr and final results. The final chapter summarises the presented work and gives a future outlook.

2 Theoretical Background

2.1 Nuclear Fission

German scientists Otto Hahn and Fritz Straßmann discovered nuclear fission (1938) while trying to create transuranic elements by bombarding uranium with neutrons [45, 46]. Their discovery was not the heavy elements that they expected, but several unidentified products. The discovery that these unidentified products were lighter than uranium proved that they had "*split the atom*".

The basics of nuclear fission is the separation of heavy atoms into two (or more) smaller constituents. This is energetically possible if the energy released from splitting the atomic nucleus is more than the energy needed to create the products. The energy contained within the mass of a nucleus can be expressed in terms of the mass of protons and associated electrons (m_H= the mass of the neutral hydrogen atom) and the neutrons (m_n) minus the binding energy (BE) holding this system together.

$$M(A,Z) = Zm_H + Nm_n - \frac{BE(A,Z)}{c^2}. \tag{2.1}$$

This binding energy can be thought of as the mass difference between the masses of the constituent parts (neutrons and protons) and the final nuclear mass. High resolution measurements of the masses of nuclei, by for example storage ring [47] or penning trap experiments [48], can provide the information needed to calculate these binding energies to high accuracy. As well as uranium, it was found that some isotopes of other heavy elements around this mass region, such as Pu are fissionable when bombarded by neutrons.

Induced fission of high mass nuclei can occur when the deformation of the nucleus increases the Coulomb repulsion between the charged protons in the nucleus to be greater than the attractive, short range nuclear force holding the nucleus together. This imbalance of forces in the nucleus, move it past the fission barrier to the "scission point" resulting in its division into two (or more) parts, known as fission. In contrast spontaneous fission can also occur if the nucleus "tunnels" from its grounds state through the fission barrier to its "scission point", analogous to alpha decay [49].

Nuclear Power

In 1942 Enrico Fermi supervised the creation of the first man-made fission reactor [50] and only 12 years later in 1954 the first commercial reactor *Obninsk* was operational in Russia [51]. The basic tenets of nuclear reactors are to utilise the energy released from nuclear fission and convert it to heat, which in turn is used for generating electricity, as with conventional fossil fuel powered plants. Using a fuel such as Uranium-235 (^{235}U) provides a self-sustaining reaction because it produces enough neutrons from each reaction to initiate further reactions. Nuclear power generation has the advantage over conventional fossil fuel power stations of having low CO_2 production and a high yield to fuel ratio. One of the main disadvantages of nuclear reactors over fossil-fuel-based power generation is the production of radioactive nuclear waste such as fission fragments and their decay daughters, and the transuranic radionuclides formed following neutron capture on the uranium fuel. Currently 13.5% of the world's electricity is produced via nuclear power and with the increasing demand for power across the globe and the limited fossil fuels, this figure is likely to rise [52].

Fission Yields

The fission fragment products of U, Pu fission range in mass but their total combined number of nucleons (A) can not exceed the initial number [53]. The division of the initial nuclei into two fission products means that the mass distribution of the two fragments might naively be expected to be approximately symmetrical around half of the initial mass. The mass distribution from fission is however not random, and is effected by the stability of the fission fragments. The population of each fission fragments is related to their proximity to shells closures (for protons or neutrons) N, Z = 50 and 82. The result of the shell closures drives the distribution of mass towards peak distributions for ^{238}U fission at A= 95 and 140. In practice, some neutrons (typically 2-3) are also released in the thermal fission process, but this has only a small effect on the mass distribution. The distribution of fission products for various nuclear reactor fuel choices is shown in Figure 2.1. The distribution clearly shows a similarity in the yield of products produced by each of the fuels, showing a common maximum at A= 140 corresponding to the N=82 shell closure.

Virtually all of the primary nuclear fission products are radioactively unstable and will undergo further radioactive decay towards nuclear stability. These decays will continue until a stable isotope is reached. This succession of decays is known as a "decay chain". It is important that all of these decay chains are taken into account when investigating the final products of fission. Nuclear power reactors are designed in general to use one type of fissioning fuel and therefore, utilise different fuel

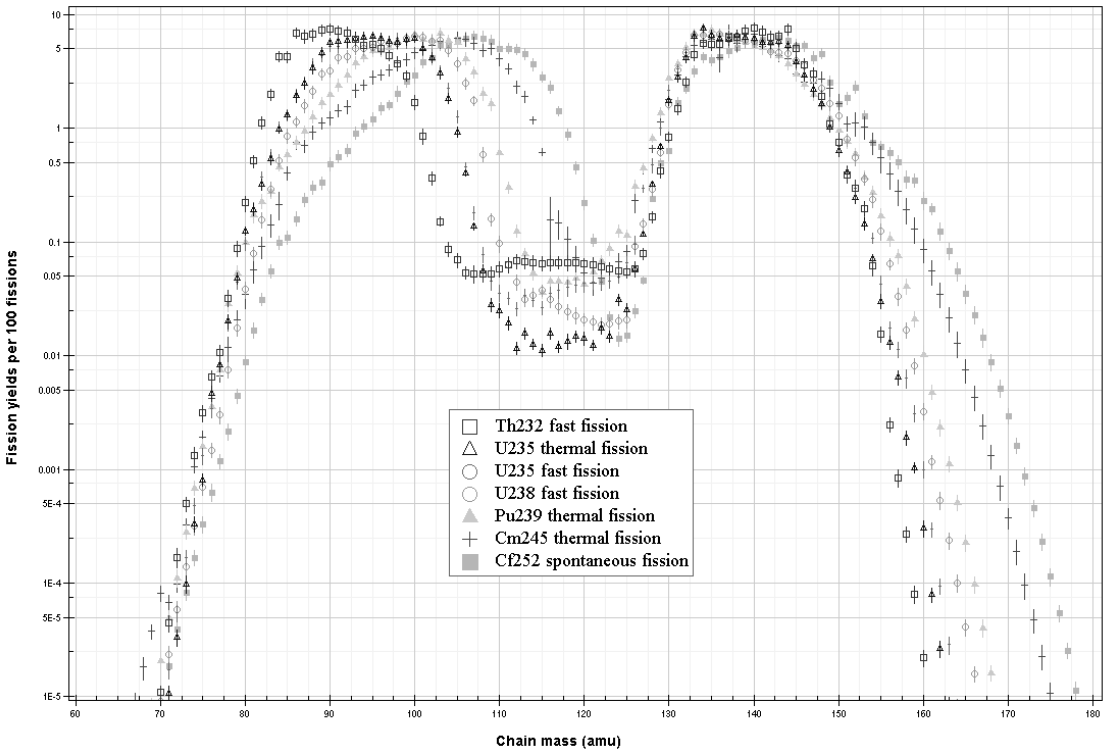

Figure 2.1: Fission yields for neutron induced and spontaneous fission for common nuclear fuels, data taken from [9].

cycles. All reactor designs burn fuel until a certain fraction is used, creating radioactive nuclear waste. Some reactors designs are made to "breed" ^{233}U/^{239}Pu fuel for use in other reactors, or for nuclear weapons material. More efficient reactor designs can use reprocessed fuel, thereby utilising previously discarded waste [49]. Each type of reactor will produce some amount of radioactive waste, because some of the constituents are long-lived, storage is needed until the waste is deemed safe [54].

2.1.1 Nuclear Data

Many theoretical nuclear models are highly dependent on experimental data due to currently undefined phenomena within nuclear physics. Due to the array of different possible properties to measure, large amounts of data need to be recorded. Experimental information about nuclei is needed in many areas such as academic research and industry, including commercial nuclear power stations, healthcare and non-destructive testing. In the example of commercial nuclear reactors, the data is not needed simply to optimise heat production, but also since key information of the reactor fuel content or waste is required. The information of the constituent isotopes in the reactor or waste enables accurate evaluation to be made for safety and power plant design.

Specifically, knowledge of the decay chains and yields from the thermal neutron-induced fission sources enables detailed models to be designed to quantify the most important isotopes within a fission reaction with regards to the generation of decay heat and waste. Whilst academic fundamental nuclear structure research may require cutting edge measurements so that they can decide its validity, other areas require more regulated results. Most nuclear databases are compiled from validated experimental data, with validation parameters being dependent on each database. Each type of database optimises the validation parameters to collate all appropriate data to facilitate its specific design.

There are a number of different nuclear databases; some of these libraries are maintained by a single country e.g. JENDL [55] (Japanese Evaluated Nuclear Data Library) and others are part of larger international collaborations such as JEFF (Joint Evaluated Fission and Fusion File), which is an evaluated library under the auspices of the NEA (Nuclear Energy Agency) data bank. The ENSDF (Evaluated Nuclear Structure Data File) [25] database is one of the repositories for fundamental nuclear structure information and as such contains energy level schemes and decay information about a wide range of radioisotopes. Other databases, such as JEFF, contain this data in a more applicable format for use with large models of a particular system, such as a fission reactor. These libraries contain thermal neutron scattering, neutron reaction, and incident proton energy data for transport calculations, as well as special purpose files with radioactive decay, activation and fission yield data [9]. The variety of the databases reflects the specific needs for different types of data. Each database uses different criteria for the inclusion of theoretical and experimental data. Some of the evaluation processes utilise theoretical models to provide a prediction for missing data points. The TENDL (TALYS-based Evaluated Nuclear Data Library) utilises a "*Total Monte Carlo*" (TMC) method to determine the optimum data points to be included. This TMC utilises a Monte Carlo transport code iterated with a range of inputs from different databases and then compares the results to known benchmark results, enabling the optimum input to be selected.

2.2 Beta Decay

In 1899, Ernest Rutherford differentiated between α and β decay by their penetration though matter. It was later discovered that this β decay particle was an electron [56]. It was not until 1931 that Pauli theorised that β decay was in fact a three bodied process producing an electron and an anti-neutrino [57]. Neutrinos have a very low reaction probability with matter resulting in a low detection probability. The neutrino was therefore not measured until 1956 by Reines and Cowan

[58]. Now it is well documented that β decay is the transformation of a neutron to a proton or a proton to a neutron which can occur by the following schematic paths:

$$ {}^{A}_{Z}X_{N} \longrightarrow {}^{A}_{Z+1}Y_{N-1} + e^{-} + \overline{\nu_e} \qquad (\beta^{-}) \tag{2.2} $$

$$ {}^{A}_{Z}X_{N} \longrightarrow {}^{A}_{Z-1}Y_{N+1} + e^{+} + \nu_e \qquad (\beta^{+}) \tag{2.3} $$

$$ {}^{A}_{Z}X_{N} + e^{-} \longrightarrow {}^{A}_{Z-1}Y_{N+1} + \nu_e + X_{ray} \qquad (EC) \tag{2.4} $$

where e^{-}, e^{+}, ν_e, $\overline{\nu_e}$ are an electron, positron, electron-neutrino and an anti-electron-neutrino respectively. X and Y represent nuclei with atomic number A, proton number Z (or $Z \pm 1$) and neutron number N (or $N \mp 1$) respectively [49]. Positive β decay (β^{+}) and electron capture (EC) are competing processes, for a proton transition to a neutron in a bound nuclear state. In comparison to β^{+}-decay, EC occurs by capturing an orbital electron followed by the emission of a mono-energetic x-ray [59].

Half-Life Radioactive decay is a stochastic process and as such the prediction of the decay of a single atom is impossible. However, because it is a quantum process, the probability of the decay occurring over a time period is finite. The decay rate for a large number of radioactive atoms can be described modelled by an exponential decay and quantised by a decay constant λ, where λ is defined by:

$$ \frac{dN}{dt} = -\lambda N \tag{2.5} $$

for time t, and number of decaying atoms N. The half-life is the time for half of a number of atoms to decay, or simply $t = T_{1/2} = ln(2)/\lambda$. When looking at a decay chain such as the ^{238}U series [60], where the number of atoms is fed from a parent decay but decreased by its own decay, the system becomes more complex. Bateman [61] showed that it is possible to determine the population of each isotope in a decay chain at a time t.

$$ \frac{N_1}{t} = -\lambda_1 N_1(t) \frac{N_i}{t} = \lambda_{i-1} N_{i-1}(t) + \lambda_i N_i(t) \qquad \text{(i=2,...,n)} \tag{2.6} $$

where N_1 is the number of parent atoms with decay constant λ_1 and N_i is the number of daughter i atoms at time t with decay constant λ_i.

Q Value

The Q value of a reaction is the net (binding) energy released. In terms of β decay it is the difference in the total mass of the system before and after the decay. The simplest example of β decay, a neutron (n) decaying into an proton (p), electron (e) and anti-electron-neutrino ($\overline{\nu}_e$) can be described schematically by:

$$n \longrightarrow p + e^- + \overline{\nu}_e. \tag{2.7}$$

Within particle physics, β decay can be described as the weak interaction (via the W^- boson) between an up (u) and down (d) quark, explained in its simplest form by this Feynman diagram [49]:

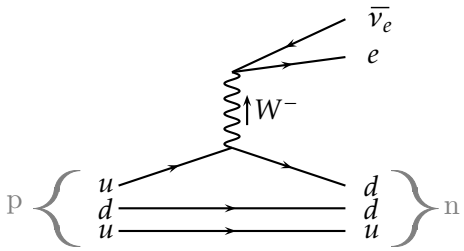

The conservation of total mass-energy means the Q_β value can be calculated for the decay using the masses of the neutron (m_n) proton (m_p), electron (m_e) and anti-electron-neutrino ($m_{\bar{\nu}_e}$) in the equation:

$$\begin{aligned} Q_\beta =& (m_n - m_p - m_e - m_{\overline{\nu}_e})c^2 \\ =& 0.782MeV - m_{\overline{\nu}_e}c^2 \end{aligned} \tag{2.8}$$

Taking the neutron to be at rest and using the assumption that the recoil energy of the proton is negligible, the Q_β-value energy is split between the electron and neutrino. This distribution of energy makes the Q_β-value of β decay difficult to detect just from the β-particle.[1] When the energies from multiple β-particles are collected, it is possible to extract the Q_β-value from the end point energy (the highest energy collected by a β-particle).

[1] Unlike α-decay where the full energy is released into the kinetic energy split between the alpha particle and the recoiling heavy nucleus which can easily be calculated.

The Q-value for each of the decay modes are given by:

$$Q_{\beta^-} = [m(^A X) - m(^A Y)]c^2 \tag{2.9}$$

$$Q_{\beta^+} = [m(^A X) - m(^A Y) - 2m_e]c^2 \tag{2.10}$$

$$Q_{EC} = [m(^A X) - m(^A Y)]c^2 - B_n \tag{2.11}$$

where B_n, $m(X)$ and $m(Y)$ are the binding energy of the captured n$^{\text{th}}$ shell electron, the atomic mass of Y, and the atomic mass of X respectively [49].

Mass Difference

The difference in the mass of a nuclei and the constituent parts (neutrons and protons) is the result of binding energy. Comparing the mass of isotopes with the same atomic number (isobar) results in the comparison of stability (taking the mass of proton to be approximately that of a neutron) where the lowest mass occurs due to an increased binding energy. Plotting mass against proton number for a set of isobars results in a mass chain, where each isotope can decay via β^- or β^+/EC towards stability, although other processes (such as α decay) may be more dominant than these β decays in some cases. Protons and neutrons are fermions and thus obey the Pauli exclusion principle. The result of this is seen by the difference between the even-mass isobars in Figure 2.2 and the odd-mass isobar chain in Figure 2.3 [62]. Due to the pairing of nucleons in the even-mass case, it is energetically possible for ^{86}Rb and ^{94}Nb to decay via β^- or β^+, resulting in two (quasi) stable elements for each mass chain, whereas for the odd mass A=91 chain, a single element (Zr) is the most stable. When energetically possible, double-β decay can occur, where by two β^- (or β^+) particles are released enabling a ΔZ=2. This double-β, could, in theory occur between the (quasi) stable ^{86}Kr and ^{86}Sr bypassing ^{86}Rb [49], but this is as yet unmeasured.

2.2.1 Transition Rules

Beta decay (the weak nuclear interaction) is not only governed by conservation of total mass-energy but also conserves angular momentum (spin, J) and parity (π). The rate of a β decay can be summarised by a set of transition rules. A naive view of β decay might assume that there is one possible decay from a parent to daughter nucleus but most nuclei have multiple transition possibilities each with there own competing transition rates. Mixed with the transition rates are also the probability of more complex decays such as double β decay and β delayed neutron or

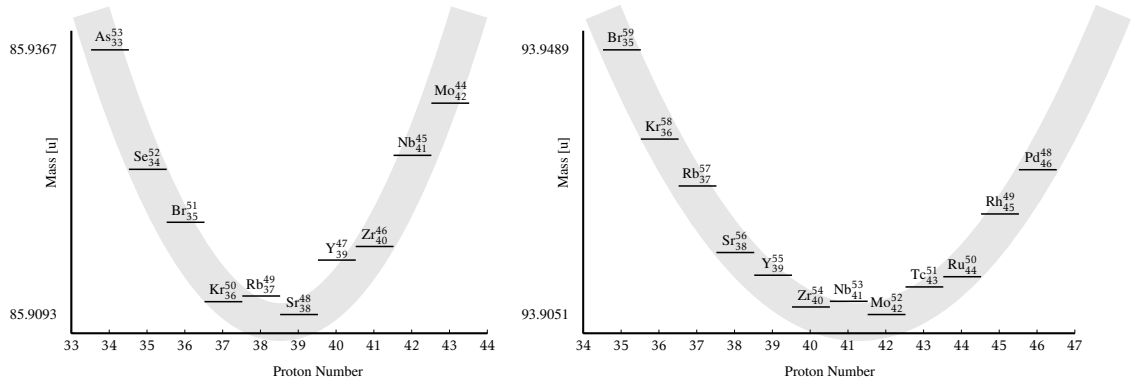

(a) A= 86 **(b)** A= 94

Figure 2.2: Mass parabolas for the even isobaric chains A= 86 and A= 94, highlighting the most energetically bound isotopes of the A= 86 isobar $^{86}Kr_{36}^{50}$ $^{86}Sr_{38}^{48}$ and for the A= 94 $^{94}Zr_{40}^{54}$ and $^{94}Mo_{42}^{52}$. Showing the parabolic curve created by plotting the mass of each isotope against proton number. Isotope mass data taken from Japanese Evaluated Nuclear Data Library (JENDL) [55].

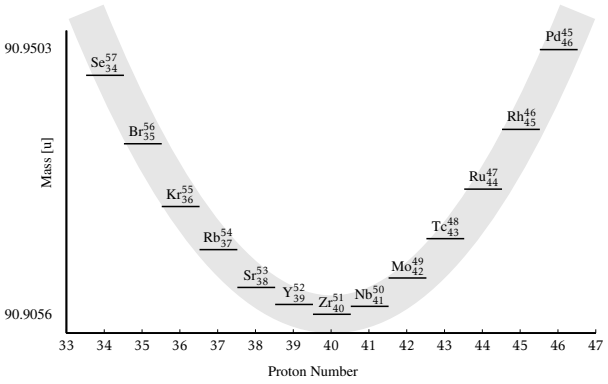

Figure 2.3: Mass parabolas for the odd A= 91 isobaric chain, highlighting the most energetically bound isotopes of the isobar $^{91}Zr_{40}^{51}$. Showing the parabolic curve created by plotting the mass of each isotope against proton number. Isotope mass data taken from Japanese Evaluated Nuclear Data Library (JENDL) [55].

proton emission. For simplicity from this point on an electron will refer to electrons or positrons and neutrino with refer to the anti-neutrino or neutrino respectively, unless specified.

In 1934 E.Fermi proposed a theory of β decay [63, 64] that still stands today. Fermi postulated that the electron and neutrino were created within the nucleus and did not exist before the decay. This implies that the initial nucleus state transforms into its final state plus electron and neutrino. This transition can be calculated from the change in wavefunction of the initial and final states. Starting with Fermi's *Golden Rule* for the transition rates (Γ) of quantum systems [65]:

$$\Gamma = \frac{2\pi}{\hbar}|V_{fi}|^2\rho(E_f) \tag{2.12}$$

where $\rho(E_f)$ is the density of states available to the electron and neutrino and V_{fi} is the matrix element of the integral of V, the operator responsible for β–decay over the initial and final states. When Fermi postulated this theory the mathematical form of V was not known. Today it is possible to substitute in the wavefunctions of the initial ψ_i and final ψ_f state and the electron φ_e and neutrino φ_ν wavefunction [66, 67] :

$$\Gamma = \frac{2\pi}{\hbar}|\langle\psi_f\varphi_e\varphi_\nu|V|\psi_i\rangle|^2\rho(E_f) \tag{2.13}$$

The electron and neutrino created are not bound and can be approximated to have the usual free-particle waveform. With momenta p and q respectively, their wavefunctions can be written as:

$$\varphi_e = \frac{1}{\sqrt{A}}e^{\frac{i\vec{p}\cdot\vec{r}}{\hbar}} \qquad \varphi_{\bar{\nu}} = \frac{1}{\sqrt{A}}e^{\frac{i\vec{q}\cdot\vec{r}}{\hbar}} \tag{2.14}$$

across the spherical volume A at radius r. The plane-wave approximation is considered to be good for the neutrino due to its low interaction probability but the electron is distorted by the Coulomb field and as such, can only be used for electrons at high energy. The allowed transitions can be explained when $pr \ll 1$ (and $qr \ll 1$) as the expansion of the wavefunction of the electron and neutrino reduce across the whole nuclear volume to $\varphi_e = \frac{1}{\sqrt{A}}$ for the electron and $\varphi_{\bar{\nu}} = \frac{1}{\sqrt{A}}$ for the neutrino. In this approximation, the only factor that remains dependent on the electron and neutrino energy is the density of states.

To encompass all possible transitions one can use the nuclear matrix element M_{fi}, removing the dependence on the electron and neutrino. The use of the nuclear matrix element produces the need for a corrective Fermi function $F(Z',p)$ where Z' is the number of protons in daughter and p the linear momentum of the electron. This corrective term includes the effect of the Coulomb field on the oppositely charged β^+ and β^- particles. The transition rate using the nuclear matrix element follows the form [49]:

$$\Gamma = \frac{g^2|M_{fi}|}{2\pi^3\hbar^7c^3}\int_0^{p_{max}} p^2(Q_\beta - T_e)^2F(Z',p)dp \tag{2.15}$$

where g is the decay strength and T_e is the kinetic energy of the electron [53]. The g factor and the $F(Z',p)$ can be obtained using tabulated experimental results where:

$$g \approx 0.9\times10^{-4}MeV\cdot fm^3 \tag{2.16}$$

is obtained from the comparison of super allowed decays and $F(Z',p)$ which can be found in look up tables [68].

It is more common to express β decays in terms of ft values were t is the comparative half-life for that decay and f is the Fermi integral, so that all the nuclear information is included [49]

$$ft = 0.693\frac{2\pi^3\hbar^7}{g^2 m_e^2 c^4 |M_{fi}|^2} \tag{2.17}$$

Formerly, the ft values where used to classify transitions into (unfortunately) named *allowed* transitions and *forbidden* transition where forbidden rather means suppressed compared to an allowed decay. By convention each transition can be defined as allowed, first forbidden, second forbidden, ... etc (see section 2.2.1). Due to the range in comparative half lives, ft values are normally shown as $log_{10}(ft)$.

Gamow-Teller and Fermi Transitions

Beta transitions can be categorised by the angular momentum taken away by the electron and neutrino. The parent nucleus with an initial spin J_i will decay to a state of final spin J_f (the populated spin in the daughter nucleus), the orbital angular momentum L carried away by the leptons and the vector sum S of the intrinsic spins of the electron and neutrino

$$J_i = J_f + L + S. \tag{2.18}$$

As fermions, leptons have half integer spin with the electron and neutrino both having $s = \frac{1}{2}$, resulting in the vector sum $S = 0$ (anti-parallel) or $1\hbar$ (parallel). From the vector sum of the intrinsic spins each β-decay is classed as a Fermi transition (his original assumption) where $S = 0$ (anti-parallel spins) or a Gamow-Teller transition where $S = 1\hbar$ (parallel spins). The measurement of a spin/parity (J^π) 0^+ to 0^+ transition enables a pure Fermi (F) transition to be measured, as this can not be a combination with Gamow-Teller (GT) transitions since the change in spin (ΔJ) is $0\hbar$ and only $0\hbar$ [10]. In many aspects the proton and neutron in the nucleus can be thought of as two projections of the same particle due to their symmetric properties, due to the charge independent strong force. When looking at the magnetic interaction, the nucleons can be thought of as two states of a single particle (spin up = proton and spin down= neutron), this spin is defined as isospin. The total isospin of a system T_3 is the sum of the protons and neutrons isospins $T_3 = (Z-N)/2$. As β decay involves the transition of a proton/neutron to a neutron/proton it is clear that the isospin

of this system will change. Using the definitions for Gamow-Teller and Fermi transitions it is then possible to write the proton and neutron transition probabilities as:

$$B(F) = |<\psi_f^*|\tau|\psi_i>|^2 \quad \text{and} \quad B(GT) = |<\psi_f^*|\sigma\tau|\psi_i>|^2 \tag{2.19}$$

where τ is isospin and, $\sigma\tau$ is the spin–isospin operator. For most mixed F+GT transitions we can now define the ft value as [10]:

$$ft = \frac{K}{g_V^2 B(F) + g_A^2 B(GT)} \tag{2.20}$$

where g_A and g_V are the weak interaction axial vector and vector constants respectively and K is a constant with the form [10]:

$$K = \frac{2ln(2)\pi^3\hbar^7}{m_e^5 c^4} \tag{2.21}$$

Allowed and Forbidden β Transitions

Each type of transition in β decay can be classed as allowed or forbidden depending on the change of spin and parity between the initial and final states of the decay. The conditions for the allowed and the first few forbidden transitions can be found in Table 2.1. As stated above, a forbidden transition is possible, it is simply suppressed compared to an "allowed" decay, with the amount of suppression increasing with the "forbiddeness". This generally results in the least forbidden decay dominating β decay. Nuclei far from the line of stability tend towards larger Q_β-values than nuclei near stability. An increase in Q_β-value will also in general increase the average electron energy emitted, resulting in a larger range of possible forbiddeness.

Type	$\Delta\pi$	ΔJ	Example	Approximate $\log(ft)$
Allowed	no	0,1	$n \longrightarrow p \quad (\frac{1}{2}^+ \longrightarrow \frac{1}{2}^+)$	3.5-7.5
First forbidden	yes	0,1,2	$^{76}\text{Br} \longrightarrow {}^{76}\text{Se} \quad (1^- \longrightarrow 0+)$	6.0-9.0
Second forbidden	no	2,3	$^{137}\text{Cs} \longrightarrow {}^{137}\text{Ba} \quad (\frac{7}{2}^+ \longrightarrow \frac{3}{2}^+)$	10.0-13.0
Third forbidden	yes	3,4	$^{40}\text{K} \longrightarrow {}^{40}\text{Ca} \quad (4^- \longrightarrow 0^+)$	14.0-20.0
Fourth forbidden	no	4,5	$^{115}\text{In} \longrightarrow {}^{115}\text{Sn} \quad (\frac{9}{2}^+ \longrightarrow \frac{1}{2}^+)$	21-...
			etc ...	

Table 2.1: β-decay allowed and forbidden selection rules [49]

The example β decay of ^{208}Tl to ^{208}Pb is shown in Figure 2.4, with multiple transitions from the parent to the daughter. This data collected in the ENSDF database [69] give $\log_{10}(ft)$ vales to each of the feed levels revealing possible transitions types. The spins and parity for this decay are known, showing that most transitions from the $J^\pi = 5^+$ parent ground state occur via first forbidden decay (decays to spin/parity $3^-4^-, 5^-, 6^-$ and 7^- states) and only one transition via an allowed transition to the 4323 keV level $J^\pi = 4^+$ state.

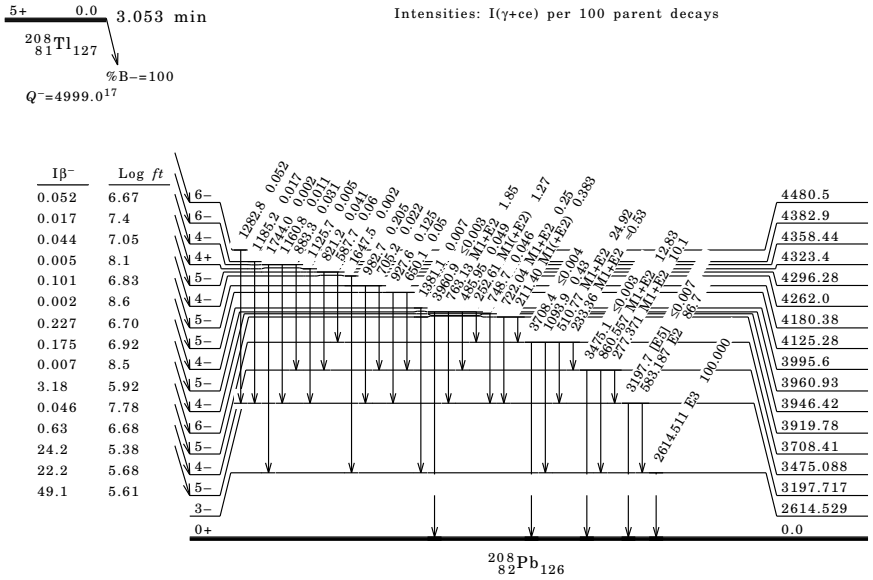

Figure 2.4: Example of the β decay of ^{208}Tl to ^{208}Pb showing transition to different excited stated in the ^{208}Pb(daughter) nucleus. Image taken from ENSDF [69]

2.2.2 Kinetic Energy of β Particles

The energy created in each β transition, from parent to excited state in the daughter is released as (kinetic) energy shared between the recoiling nucleus, β particle and neutrino. Rather than determining the energy of a single β particle from a transition it is simpler to estimate the energy distribution for each transition. The number (N) of β particles with linear momentum (p) for a transition can be approximated as [49]:

$$N(p) \propto p^2(Q - T_e)^2 F(Z', p)|M_{fi}|^2 S(p, q) \tag{2.22}$$

where T_e is the β particles kinetic energy and $S(p, q)$ is the *shape factor* with the additional momentum dependence of the electron and neutrino as a result of any forbidden transitions. This approximation accounts for the Coulomb effect for β^+ transitions within the Fermi function ($F(Z', p)$). Using this equation it is possible to approximate the shape of the kinetic energy distribution for

allowed transitions ($S(p,q)=1$) by randomly sampling momenta (p in units of $m_e c$) from [70, 71]:

$$N(p) = p^{2\sqrt{1-\alpha^2 Z^2}} \times \left(E - \sqrt{1+p^2}\right)^2 \times e^{\pm \pi \alpha Z \sqrt{1+1/p^2}} \times \left|\Gamma\left(\sqrt{1-\alpha^2 Z^2} \pm i\alpha Z \sqrt{1+1/p^2}\right)\right|^2 \tag{2.23}$$

where $E = 1 + E_\beta/m_e c$ and E_β is the maximum available β kinetic energy, Z is the daughter atomic number, α is the fine structure constant ($e/\hbar c$) and Γ is the complex gamma function [70]. This equation can generate the kinetic momenta for β^- with the $\pm$ set to + and set to – for β^+ particles, accounting for the differing effect of the Coulomb Force.

Figure 2.5 shows the expected shape for a fictitious allowed transition of β end point energy 1 MeV for a β^- and β^+-decay for a Z=40 (Zr) daughter nucleus. The shape difference between the distribution is a result of the difference in change of the β particles and the effect of the Coulomb Force on it.

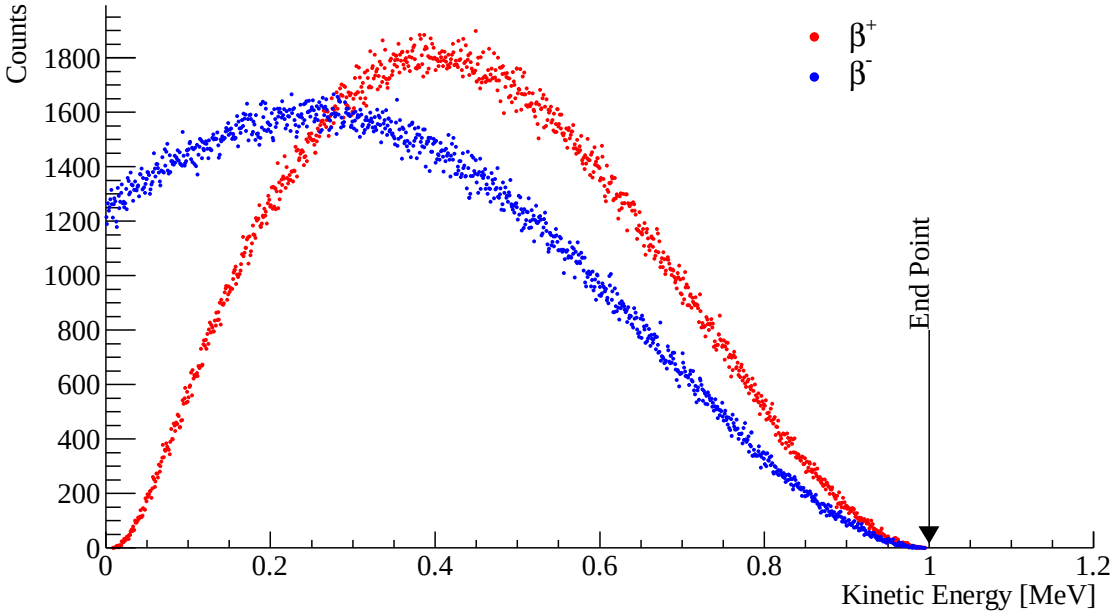

Figure 2.5: Example of kinetic energy distribution for one million allowed 1 MeV transitions for β^- (blue) and β^+ (red) decays (with Z=40).

2.2.3 Beta Strength Functions

For β decays with large Q_β information is some times better shown as the β strength function (S_β) [70, 72]:

$$S_\beta(E_x) = \frac{I_\beta(E_x)}{f(Q_\beta - E_x, Z) \cdot T_{1/2}} \tag{2.24}$$

where $I_\beta(E_x)$ is the direct β–feeding to a state of energy E_x, $T_{1/2}$ is the β–decay half life of the parent nucleus and $f(Q_\beta - E_x)$ is the statistical Fermi function, from the kinetic energy distribution of

the β particle shown above. The β strength function can be rewritten to account for the binning energies for transitions producing [10]:

$$S_\beta(E_x) = \frac{1}{T_{1/2}} \sum_{E_x \in \Delta E} \frac{1}{\Delta E} \frac{I_\beta(E_x)}{f(Q_\beta - E_x)} \tag{2.25}$$

with and average energy binning of ΔE. The integral of the produced β strength function can then be used to obtain the total ft value for a decay by:

$$ft_{\text{total}} = \frac{1}{\sum_{E_x} S_\beta(E_x)\Delta E_x} \tag{2.26}$$

2.2.4 Gamma Decay Selection Rules

It has been shown that β decay can populate excited levels in a nucleus above the ground state. To de-excite these states, the nucleus can release discrete energy photons called γ rays or can pass the energy onto an orbital electron and eject it through a process known as known as *internal conversion*. Analogous with β decay, these decays have a set of selection rules to follow and have different transition rates for each type of decay. A γ ray transition from an initial state, spin J_i^π to a final state, spin J_f^π can be defined to produce a photon with a multipole order L where, by vector addition,

$$|J_i - J_f| \leq L \leq |J_i + J_f| \qquad (\text{ for } L \neq 0\ ). \tag{2.27}$$

This order, L, defines the type of multipole (2^L) so $L = 1$ is equivalent to a dipole, $L = 2$ a quadrupole and so on. Separate from the order a transition can be defined as electric or magnetic nature, resulting in the terminology of XL, with X being electric (E) or magnetic (M) and L being the order. The available parity change ($\Delta\pi$) for electric transitions are defined as $\Delta\pi = (-1)^L$ whereas magnetic transitions have $\Delta\pi = (-1)^{L+1}$. As with the forbiddeness in β decay, increasing the multipole orders decreases the transition probability. When more then one γ ray multipolarity transition is permitted for a given transition, a mixing between transition modes is possible. Mixed transitions are usually dominated by the lowest order multipole [49]. As with Gamow-Teller and Fermi transitions it is possible to measure the electric and magnetic transition strengths by measurements of transition rates. In the de-excitation of β decay it is expected that most decays will occur via (prompt) E1, E2 and/or M1 transitions.

Internal Conversion

As stated above, internal conversion (IC) is a competing process to γ ray emission in the decay of bound nuclear states. The process of internal conversion is not a multiple stage process and thus the characteristic energy E_e of the ejected electron can be defined.

$$E_e = E_\gamma - BE_e \tag{2.28}$$

where E_γ is the energy of decay transition (i.e. the competing γ ray energy) and BE_e is the binding energy of the electron that is emitted, with energy specific to the electron shell. Due to the characteristic energy of conversion electrons, these particle energies can be identified easily in β spectra as well defined peaks on top of the broad β continuum. One IC transition that does not compete with γ decay is the (J^π) $0^+ \rightarrow 0^+$ transition because it is impossible to have a γ ray multipole of L=0, since a photon has an intrinsic spin of $1\hbar$.

2.2.5 Nuclear Level Density

The level density of nuclei increases as excitation energy increases, due to a number of different physical phenomena. The "reference input parameter library for theoretical calculations of nuclear reactions" (RIPL) contains experimental and theoretical data on level densities for many isotopes and combined with the ENSDF database it is possible to extract the number of levels at each nuclear excitation energy [73]. Data from Hartree-Fock-Bogoliubov (HFB) tables (e.g. [74]) can be used to produce theoretical predictions of level density for specific isotopes. This prediction can be optimised using experimental data giving a good fit of the level density against excitation energy [75, 74].

It is possible to use generic mathematical models to fit the level density of a nucleus against excitation energy, producing a smooth distribution over a selected energy range. The mathematical form of each model can vary due to trying to fit different areas of the nuclear chart or trying to be more specific to a set region. Previous analyses of TAS data have utilised the best fit from various nuclear models (e.g. [76]) and this thesis will concentrate on four models described below, enabling the best fit of nuclear level density to the available experimental and theoretical data. Each of these models assumes an even distribution between positive and negative parity states across the range of excitation energy. It should be noted that the density of the daughter nucleus is needed

only up to the relevant Q_β value, since the daughter nucleus can not be populated above this via β^--decay.

The Back-Shifted Fermi Gas (BSFG) model can be fitted to the nuclear level density as a function of excitation energy. This model has been shown to include shell effects and the odd-even effect on the nuclear density [77]. The inclusion of the back shift parameter adds a fictitious / fixed ground state position, Δ, to the level density parameter a, improving the original shifted Fermi gas model, enabling a good fit to experimental data for a large section of the nuclear chart. Work by Dilg et al. [77] has shown it is possible to parametrise this model and fit the level densities for excitation energy and spin distribution ($\rho(E,J)$) to experimental data in the form of:

$$\rho(E,J) = \frac{1}{24\sqrt{2}}\frac{(2J+1)}{\sigma^3\sqrt{a}}\frac{e^{\left(2(a(E-\Delta))^{1/2}-J(J+1)/2\sigma^2\right)}}{(E-\Delta+t)^{5/4}} \tag{2.29}$$

where t is the thermodynamic temperature defined by:

$$E-\Delta = at^2 - t \tag{2.30}$$

and σ is the spin-cut-off parameter taken as:

$$\sigma^2 = I_{eff}t/\hbar \tag{2.31}$$

for this model, with effective moment of inertia I_{eff} taken to be at 0.5 unless specified. Later work by von Egidy et al. [78] has shown that a slight change can be made to this formula enabling the BSFG model to be parametrised as:

$$\rho(E,J) = f(J)\frac{e^{\left(2\sqrt{a(E-\Delta)}\right)}}{12\sqrt{2}\sigma a^{1/4}(E-\Delta)^{5/4}} \tag{2.32}$$

and σ in this model takes the form:

$$\sigma^2 = 0.0888A^{2/3}\sqrt{a(E-\Delta)} \tag{2.33}$$

where A is the mass number and the predicted spin distribution can be defined by:

$$f(J) = e^{-J^2/2\sigma^2} - e^{-(J+1)^2/2\sigma^2} \simeq \frac{2J+1}{2\sigma^2}e^{(J+1/2)^2/2\sigma^2} \tag{2.34}$$

Egidy et al. [78] also found that is was possible to model the nuclear level density via a Constant Temperature (CT) model utilising the nuclear temperature T (assumed to be nearly constant below 10 MeV) and back-shift E_0 giving

$$\rho(E,J) = f(J)\frac{1}{T}e^{(E-E_0)/T} \tag{2.35}$$

Previous work by Gilbert and Cameron [79] showed that it is possible to combine the BSFG and CT models using the CT for the lower energy range then using the BSFG model for the higher energy range, due to previous poor fitting of the BSFG model at low energy. For this mixed model result, σ^2 was taken to be $0.0888E^{1/2}A^{2/3}$ [79].

2.3 The Pandemonium Effect

High resolution γ-ray spectroscopy can be used to measure β decay by collecting the γ ray intensities that both populate and subsequently depopulate the daughter nuclear levels. Individual β feeding levels can be deduced from the balance of γ ray intensities populating and depopulating each level.

Decays with large Q_β values may lead to the population of a large number of levels in the daughter nucleus including some at high excitation energies (Figure 2.6a). The *pandemonium effect* occurs when these β-feeding distributions to the higher excitation states are erroneously derived from the γ-ray spectra [18] (see Figure 2.6b).

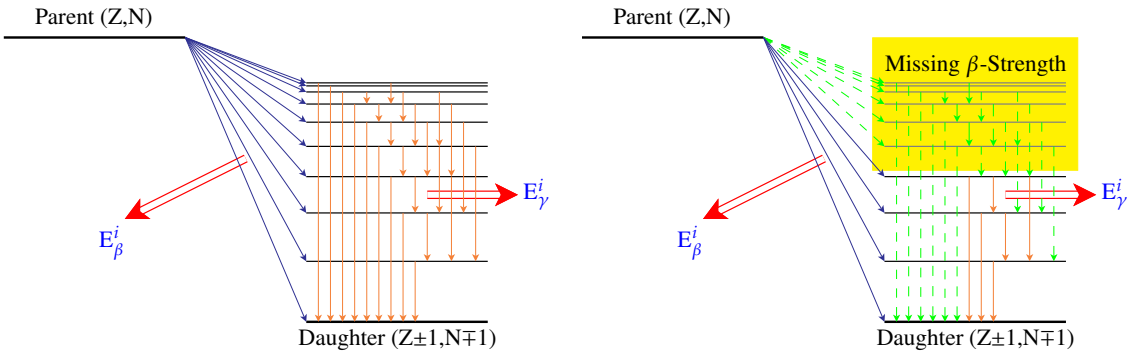

(a) Real β feeding levels

(b) Detected β feeding levels

Figure 2.6: Schematic representation of the *pandemonium effect* in a fictitious β decay. Blue arrows (↘) showing possible β decay transitions and possible collected energy (E^i_β) and orange arrows (↓) showing de-excitation via γ decay or IC. Green dashed arrows (⇢) showing possible missing transition due to the *pandemonium effect* and yellow region showing possible missing β strength.

The reason for the missing detection of levels, shown schematically in Figure 2.6b, is a combination of features in the decay and the detection. A large Q_β window provides a large option of excited states in the daughter to be populated due to the increase of level density with excitation energy.

The increased, discrete number of states means that there are more possible branches for decay producing weaker feeding to/from any specific level. The separation of excitation states in the daughter nucleus are very close at high energy resulting in multiple decay possibilities with very little energy difference between them. Gamma de-excitation of these high-energy states can depopulate by high-energy γ rays or multiple smaller energy transitions resulting in a few, discrete high-energy γ rays and a sea of parallel sum-energy smaller decays. Ideal γ-ray spectroscopy of a large Q_β value decay would collect all the high-energy γ rays and the plethora of lower-energy γ rays from cascades, to create coincidence measurements to determine the final β level feeding characteristics. Such high-resolution measurements utilising HPGe detectors have very strong γ ray energy dependence on their full energy peak efficiency [80]. This can result in the low-energy γ rays being measured but the higher energy γ rays often being missed due to the reduced detection in particular for efficiency for γ rays above 2 MeV [81]. This "missing energy" collection results in an incorrect γ ray cascade evaluation, resulting in lower energy states having feeding assigned to them rather than the correct high-energy feeding level.

A large number of β decay measurements were undertaken using HPGe detectors before this effect was fully understood. As a result some decay schemes were thought to be complete and the β-feeding was assumed to be correct. In fact, the incorrect assignment of β-feeding as a consequence of the *pandemonium effect* can produce significant errors in the nuclear data sets. Experimental evidence of this *pandemonium effect* is clearly shown in work by Algora et al. [82] (Figure 2.7) with the *pandemonium effect* in the Cluster Cube (HPGe array) measurement of the β strength function of ^{150}Ho in comparison with the *pandemonium effect* free GSI-TAS (NaI(Tl) TAS detector) measurement.

2.4 Total Absorption Spectrometry

One way of accounting for this *pandemonium effect* is to use a total absorption γ-ray spectrometer (TAS). The concept behind total absorption γ-ray spectrometry is to identify the full energy of the γ ray cascade rather then individual γ rays, thereby reducing the probability of missing the measurement of individual γ ray transitions (see Figure 2.8b). An ideal TAS would be 100% efficient in the detection of γ ray radiation, cover a full 4π solid angle and have good energy-resolution characteristics. Creating a TAS approaching these characteristics requires large volumes of detector material with a relatively high Z value, for the best detection efficiency for the full

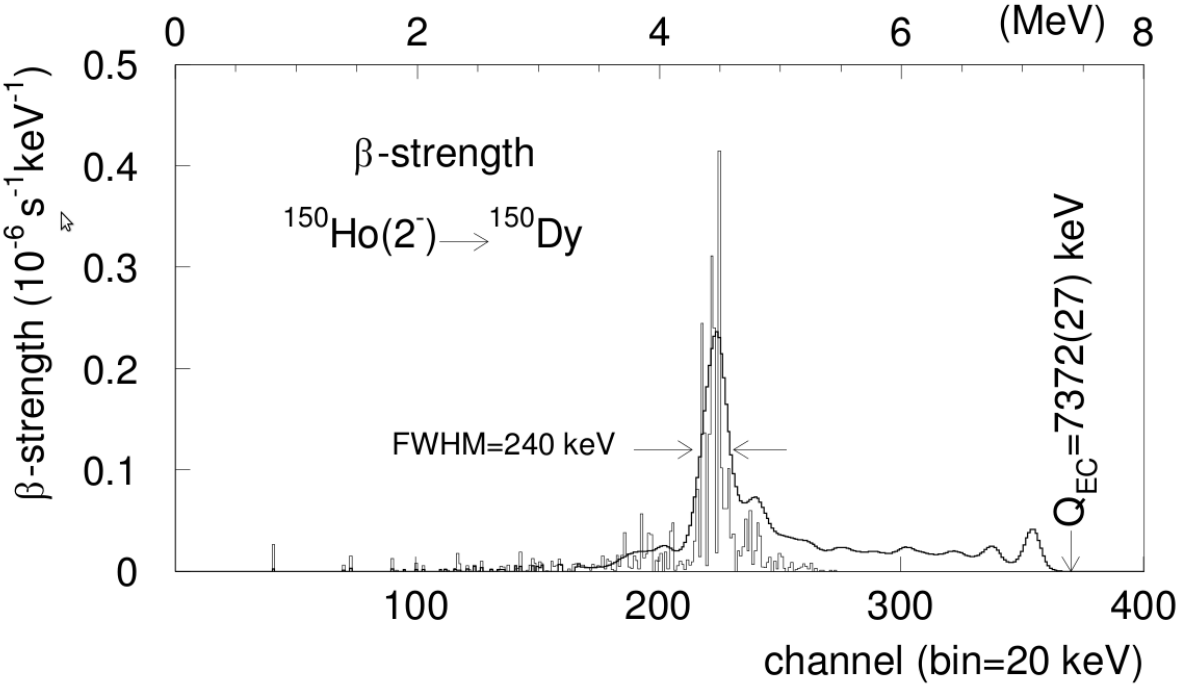

Figure 2.7: Experimental evidence of the *pandemonium effect* shown in a comparison of measurement by a TAS (thick line) and HPGe (thin line) array by Algora et al. [82], image taken from [82].

absorption of γ rays. Obtaining 100% efficiency and a full coverage is not possible with current technology, but a close approximation can be constructed [80].

To satisfy the specifications for a TAS, scintillation detectors are commonly used due to the large volumes that can be created at reasonable cost. Scintillation materials like NaI(Tl) or BaF_2, can be grown to large volumes but have significantly poorer energy resolution characteristics compared with HPGe detectors. Current manufacturing techniques cannot grow HPGe in volumes larger than approximately 0.75 l limiting the absolute detection efficiency of these detectors [80]. The collection of γ rays in the TAS differs from conventional high-resolution γ spectroscopy such as HPGe arrays, in that the TAS detector collects the full γ ray energy cascade from a source, rather than measuring the individual γ ray energies which make up the mutually coincident cascade.

The collection of the full γ ray cascade reduces the *pandemonium effect* collected in the data by increasing the detection of each full decay, providing a solution to the missing β strengths found in some high-resolution γ spectroscopy. The data (d_i) collected by each channel (i) in the TAS can be defined as the sum of responses (R_{ij}), or probability that a decay from level j will be collected

in channel i multiplied by the feeding (f_j) to level j, for all levels:

$$d_i = \sum_{j=1}^{j_{max}} R_{ij}(B) f_j \tag{2.36}$$

The inverse of this equation can be used to obtain the feeding distribution, but only if a solution to this inverse problem can be found (Chapter 5 will cover this in more detail). The use of Monte Carlo simulations can be used to create a theoretical detector response function and in combination with the solution to this inverse problem, a reconstruction of the data is then made possible. Examples of the improvements that can be made to decay heat calculations using total absorption spectrometry can be found in [11, 15] and also figure 1.1.

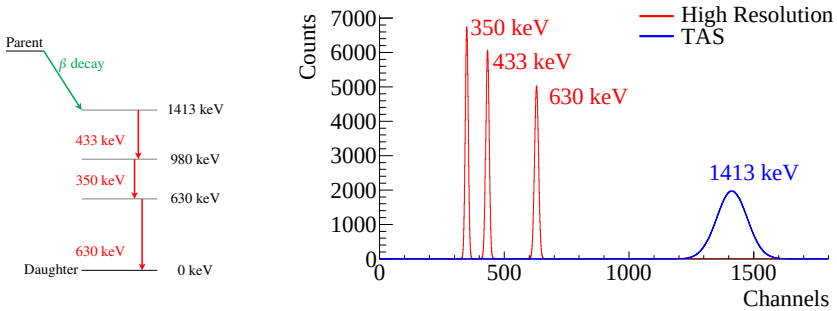

(a) Fictitious β decay (green) with a γ cascade (red).

(b) Conventional high resolution detection spectrum (red) and TAS detection spectrum (blue) collecting the full cascade.

Figure 2.8: A fictitious β decay (a) showing a γ cascade and the energy collection (b), with the conventional high resolution detector collecting the individual γ decays and the TAS spectrum collecting the full γ cascade instead.

Previous Total Absorption Spectrometers

Total absorption γ-ray spectrometers have been used in nuclear physics for many years. One of the first to utilise the full γ cascade to measure β feeding after β decay events was Duke et al. [83] in 1970. Duke's set-up utilised the ISOLDE TAS at CERN ISOLDE [84]. Other groups and facilities have created TAS detectors and most notably the OSIRIS TAS [85] the Russian LNPI TAS [86], the INEL TAS used by Greenwood et al. [87], the LBL TAS used at GSI [88] and Lucrecia installed at CERN ISOLDE [89, 90].

It has been shown that efficiency is key to a TAS and thus the choice of the material used for the detection is very important. The previous TAS mentioned were constructed from large single (like Lucrecia) or two (like ISOLDE/OSIRIS) crystal scintillators of NaI(Tl) to ensure even efficiency

across the full solid angle. Restriction in measurements using TAS may be due to the esoteric data analysis needed or the difficulty of the detector creation. The construction of large pure inorganic scintillator crystals needed for a TAS is a difficult and expensive process and is often limited to the technology available for the chosen material.

2.5 Monte Carlo Simulations

When modelling the movement of or interactions of a few particles it is possible to use classical mechanics. This method soon becomes impractical when looking at a many particle system. A more practical approach is to approximate these many-particle systems using statistical mechanics. This method uses the probability of each event occurring combined with randomly generated numbers to give a statistical output. This process is know as Monte Carlo modelling and was first theorised by Metropolis and Ulam [91] in 1949. The Monte Carlo (MC) method can be applied across a broad range of applications with many degrees of freedom, including computational biology, computer games and fluid dynamics. The generation of perfectly random numbers is an impossible task on current computers; instead pseudo random numbers are used. These pseudo numbers are generated from a starting seed value. It is very important to the outcome of the MC model that this seed is varied to ensure the pseudo random numbers do not repeat. Within nuclear physics MC models were used as early as 1972 to create response functions for total absorption spectrometry [92].

2.5.1 Particle Transport Codes

The complexities of particle transport can be simulated by the use of MC by applying the theoretical understanding on the particle interactions. The basis of most particle transport codes start with a single particle with a defined position, energy and velocity, then a weighting (probability) is assigned to each processes that can occur to that particle at this point. A "random" number is then used to select an option from this range of processes. If the particle is then moving, a second calculation will occur for any processes that can happen along a "*step*" (smallest distance of movement defined). Depending on the process selected further "steps" may be required until a particle satisfies a boundary condition. The generation, excitation or displacement of other particles during this event will continue until they also satisfy a boundary condition. The path of this single particle (event) does not describe much about a physical system. Many iterations of particles with the same starting conditions will however provide a good approximation of the system being modelled. The accuracy of this type of model is highly dependent on the theoretical data included and the number of events that can be simulated. With previous technology, a trade-off

was needed between computational speed and accuracy but with modern computational techniques it is possible to run simulations using large quantities of iterations (events) in a short time scale.

GEANT4

There is a vast array of particle transport MC simulation packages, within the nuclear, high energy and medical physics fields, such as GEANT4, MCNP [93] and FLUKA [94]. GEANT4 (GEometry ANd Tracking 4) is one of the most popular choices due to its versatility within the fields. The high and varied usage of the GEANT4 code provides rigorous testing of most features making it more likely to be selected for future projects [95]. GEANT4 was specifically designed by a group at CERN for particle transport and is the first generation in C++ (object orientational computer language) rebuilt from the original versions of GEANT that started as a `Fortran 77` code in 1974 [96].

The GEANT4 code is written with a minimum of three sections, a *physics list*, *primary generator* and *detector construct* with the possibility to add other sections to this. From the basic make up, the *detector construct* section contains all the physical attributes to the system, including the geometry, material density, composition and other physical properties. The *primary generator* section defines the initial interaction or source of particle of interest, including energy, particle type, direction and position. The third and arguably the most important section is the *physics list* which defines processes that can occur during the simulation process. The inclusion or exclusion of specific properties can have a significant effect on the output of the model thus an optimisation is needed for the inclusion of all necessary packages without including packages that might produce extra sources of error (physical or human error within the code). All processes in GEANT4 are defined as either at rest, along step or post step defined by when the interactions occur, with a step being the smallest unit of movement or interaction for a particle.

3 The Experiment and Calibration

An experiment was performed in 2009 at the University of Jyväskylä (Finland) to measure the β decay strength function of eight separate neutron-rich, fission produced radionuclides (^{86,87,88}Br, ^{91,92,94,95}Rb, and ^{94}Sr) using total absorption spectroscopy. The aim of this experiment was to determine if the *pandemonium effect* is present in their recorded measurements and to improve knowledge of their β feeding distribution. In this chapter the equipment used will be discussed, then the procedure of the experiment and the calibration.

3.1 Valencia-Surrey Total Absorption γ-ray Spectrometer

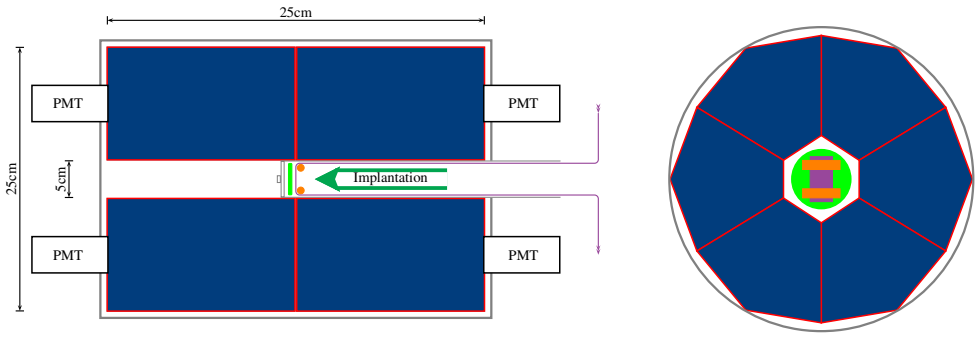

(a) Valencia-Surrey TAS horizontal cut-through

(b) Valencia-Surrey TAS Cylindrical cut-through

Figure 3.1: Schematic of layout within the TAS from two perspectives. Both views show the aluminium (grey) case containing the crystals (blue) with the teflon casing (red) and at the centre the silicon detector (green), the tape (purple) delivery system and the tape rollers (orange). With one roller constructed from PEEK (plastic) rather than aluminium to remove static build-up inside the detector

The Valencia-Surrey TAS was designed by the Valencian group to utilise a split geometry of 12 crystals to make one complete detector shown in Figure 3.1 [97]. Previous TAS designs have avoided a multi-segmented design due to extra complications, a reduction in low energy efficiency due to an increase in the dead (non-sensitive) space between the detector elements, and a more complex data output. A segmented TAS design facilitates a reduced size of individual crystals enabling a

larger array of material possibilities and a reduction in manufacturing costs compared to a single, large crystal. The Valencia-Surrey TAS was designed to utilise 12 barium fluoride (BaF_2) crystals. Detector dimensions of 25 cm length, 25 cm diameter and a 5 cm diameter longitudinal hole gives the TAS an approximate solid angle coverage of 99.5% at its centre. In the construction of this TAS, each crystal of BaF_2 was individually optically insulated with a thin Teflon film to reduce cross talk between crystals and light leakage. All 12 crystals are encased inside an aluminium can with a borosilicate glass windows at the outside end of each crystal, allowing a photomultiplier tube (PMT) to be optically linked to the crystals. The hydrophilic nature of the BaF_2 means it was not possible to open the aluminium casing to the test the thickness of any internal dimensions without the possibility of damaging the detector.

Barium Fluoride

Previous TAS detectors have been made from NaI(Tl), because of its high relative detection efficiency and ability to be grown to large size. However, due to the segmentation, barium fluoride (BaF_2) could be used for the Valencia-Surrey TAS. Barium fluoride has a poorer energy resolution when compared to NaI(Tl), but has much improved temperature stability of scintillation emission. The relatively high atomic number of the barium (Z=56) results in a higher detection probability per volume, enabling the use of smaller volumes for the TAS detector [80]. The neutron capture cross sections of barium and fluoride means that the background produced from incident neutrons on the BaF_2 crystals is lower than for other scintillator materials such as NaI(Tl). However, finite neutron capture cross-section of the BaF_2 (for thermal neutrons $\sigma_{Ba} = 1.1(1)\,b$ $\sigma_F = 0.0096(5)\,b$ [98]) opens up the possibility of also measuring β-delayed neutron emitters, with a reduced detected neutron background, compared to other (NaI(Tl)) TAS detectors [99].

Materials	Scintillation Max Wavelength [nm]	Decay Time [ns]	Specific Gravity	Photons per MeV
NaI(Tl) (20°)	415	230	3.67	38000
BaF_2 (slow)	310	630	4.89	9500
BaF_2 (fast)	220	0.6	4.89	1400

Table 3.1: Comparison of organic scintillator properties, from reference [80].

Barium fluoride is a well known inorganic scintillator and produces two light components, a fast (0.6 ns) and a slow one ($\approx$0.63 μs), see Table 3.1. Utilising these components it is possible to use pulse shape discrimination (PSD) to determine the type of radiation detected in the BaF_2 crystals [80]. The current production method of BaF_2 crystals include contamination from naturally

occurring radioactive ^{226}Ra and ^{228}Ra (from the ^{238}U and ^{232}Th natural decay chains respectively [60]) due to radium and barium being chemical homologues. This contamination gives rise to background α-particle radiation from the radioactive daughters produced following the naturally occurring decay chain of the radium isotopes. This internal contamination can be used with PSD to gain match between separate crystals giving an extra level of stabilisation between the crystals (see Section 3.6).

3.2 Radioactive Ion Source Production

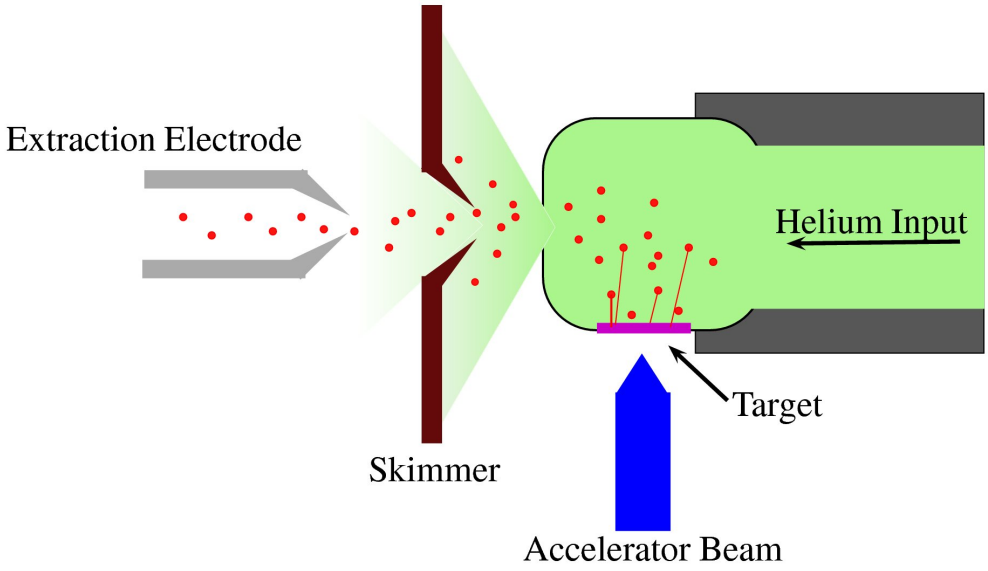

Figure 3.2: Schematic of the basic construction of Ion Guide Isotope Separator On-Line (IGISOL)[100].

The JYFL laboratory at the University of Jyväskylä (Finland [100]) was selected for the production of isotopes for the experiment in 2009 [97]. This laboratory was selected due to the Ion Guide Isotope Separator On-Line (IGISOL) facility attached to its accelerator [101]. This IGISOL facility uses a helium gas flow to carry the reaction products into a mass separator as in Figure 3.2. The experiment in 2009 utilised a 30 MeV proton beam with a beam current of 5 μA to induce fission in a thin natural uranium target, with the fission products passed through a primary mass separator (with poor resolving power) and then into the Penning trap mass separator. The mass separator at the Jyväskylä facility was the JYFLTRAP, a dual Penning trap system which has a very high mass resolution allowing the separation of isobars and even some isomeric states [102]. The combination of this very high mass resolution together with the chemically insensitivity of the IGISOL method allows studies of refractory elements at high mass resolution, making this facility ideal for this type of measurement [103].

3.3 Experimental Set-up

Using the Valencia-Surrey TAS explained above in conjunction with the JYFLTRAP eight nuclei were measured. These nuclei were chosen from the NEA/WPEC-25 priority list [11] and consisted of ^{86,87,88}Br, ^{91,92,94,95}Rb, and ^{94}Sr of which ^{91}Rb, ^{86}Br and ^{94}Sr will be discussed in detail in this Chapter. To utilise these devices to their full potential the isotopes produced from the JYFLTRAP needed to be placed at the centre of the TAS to decay, so that the full decay cascade could be collected. Leaving decaying sources inside the detector for extended periods could possibly contaminate further measurements with any daughter radiation. To enable the removal of any unwanted daughter decays a moving tape system was used.

Each isotopically pure isotope production from the JYFLTRAP was re-accelerated to 30 keV from the dual Penning traps and delivered directly down a beam pipe implanting into a movable micro film tape at the centre of the TAS. Directly behind this tape implantation point a silicon detector was placed onto the endcap of the beam pipe, as shown in Figure 3.1 (and later in Figure 4.4). This silicon detector was used for the detection of β particles emitted from the implanted nuclei and also to check if the beam was implanting on the tape or not. A sophisticated tape movement system was used so that the tape could be moved quickly to a sufficient distance, extracting the decayed nuclei reducing contamination from any further (daughter) decays.

The time between implantation and tape movement was optimised to a few (2-3) half lives of the desired nucleus, whilst taking into account the half-life of daughter products. The design of the tape system was consistent with TAS involving minimal dead material between source and scintillator crystals of the TAS. A more detailed description of the central tape system can be seen in Chapter 4.

3.3.1 Electronics

The signal processing of the output from the TAS PMTs is displayed schematically in Figure 3.3. The TAS PMTs outputs were split, the dynodes though a preamplifiers were used for energy collection and the anodes were used for timing. For the energy collection the dynode signals were passed through amplifiers and an Analogue to Digital converter (ADC) producing the energy collected in each crystal (E01, ..., E12). The dynode signal was also passed through an adder with a pulser signal to create the **Hardware Sum**. This pulser signal was set to 130 Hz with an energy higher than the range expected from the detector, for stabilisation and a time reference. The

Hardware Sum collects energy as if the 12 crystals were a single detector, but is highly dependent on correct gain matching between crystals.

The anode signal was passed through a high speed amplifier (Fast Amp) and the signal was split. One of the signals from this Fast Amp was delayed and then split so that it could be passed thought a Charge to Digital Converter (QDC) set for the fast signal of less than 40 ns (F01, ..., F12) and a QDC set for the slow signal (S01, ..., S12). The second signal from this Fast Amp was passed though a Linear Fan-In (Adder) and then split again to pass one branch to a Constant Fraction Discriminator (CFD) for the production of gates for the two QCDs and give a start to the Time Digital Converter (TDC). The second branch from the Linear Fan-in passes through a Timing Filter Amplifier (TFA) and CFD (producing the logical electronic DAQ Trigger), Gate for the ADC and the common stop signal for the TDC. This common stop signal then creates the time stamp (T01, ..., T12) for each crystal event data. The signal from the silicon detector was collected in parallel, with a silicon trigger combined (OR logic) with the TAS trigger enabling either event to trigger the data collection. As with the **Hardware Sum** (see Section 3.4) a pulser signal was added to the silicon data collection for reference.

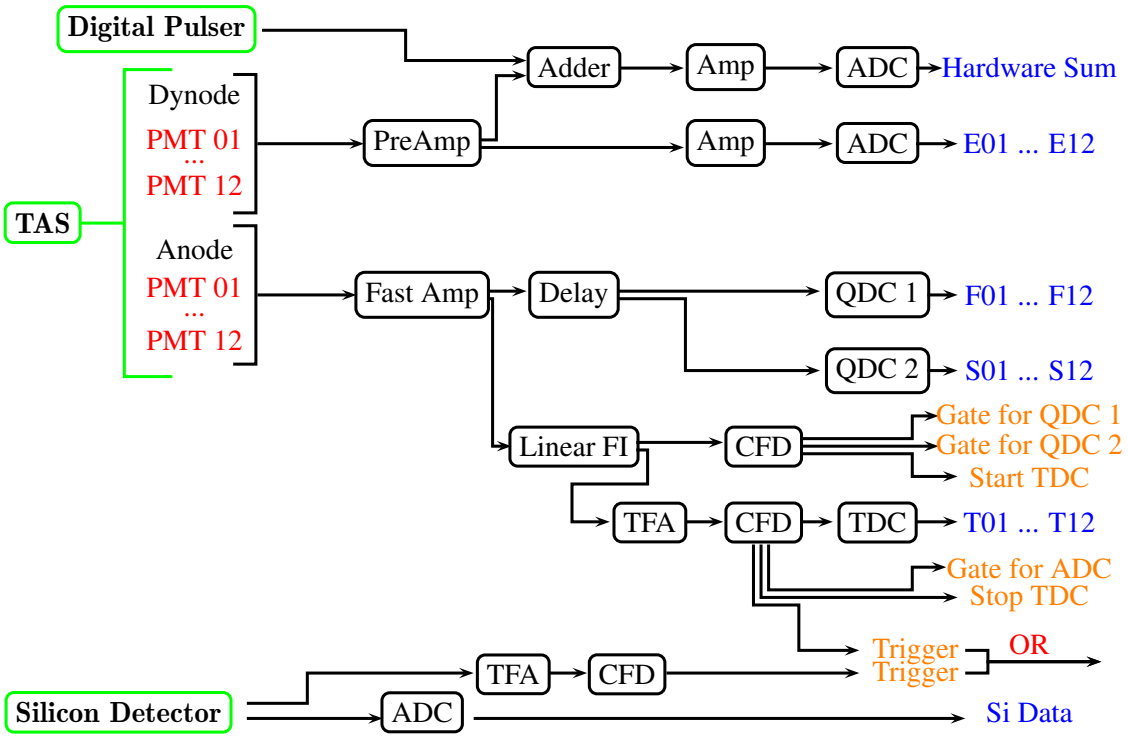

Figure 3.3: Schematic diagram of the electronics readout for the Valencia-Surrey TAS detector system.

3.3.2 Data Acquisition

The optical grease between the borosilicate glass windows and PMTs was suspected to have leaked during travel of the detector and was reapplied in Jyväskylä. After this optical grease change, the detectors were gain matched to each other. During the full experiment the pulser in the **Hardware Sum** was used for reference. A lead blanket and large amount of lead shielding was placed around the TAS as passive shielding. The efficiency required of the TAS makes it very sensitive to background radiation and thus subtraction of this background is needed for each measurement. In order to evaluate the cosmic and other stochastic background sources, a 2 hour background measurement was taken approximately after every 2 hours of isotope measurement.

3.4 Experimental Procedure

3.4.1 Calibration Measurements

Once the detector was in place it could be calibrated. Due to the change in optical grease, an initial calibration was made without the beam pipe and tape system in place ("*NoTube*" set-up). This initial calibration was be used in conjunction with a previous calibration performed by the group in Valencia [104]. Standard sources of ^{22}Na, ^{137}Cs and ^{60}Co were used to calibrate and characterise the detector (validation of the MC model). In addition a ^{24}Na source was produced by the Jyväskylä facility and was also used. Each of the standard calibrants were encased; the ^{24}Na source was implanted into some tape producing an "unsealed" calibrant. For comparison to previous collected data [104], each source was placed in turn on a cardboard stand holding it at the centre of the TAS and data was recorded for approximately 2 hours with background measurements taken before, between and after measurements.

To replicate the position of the final set-up, the tape section and beam pipe was attached ("*WithTube*" set-up) and the sources were separately placed inside the TAS detector between the tape and the silicon detector, accessed via the end cap (^{137}Cs spectra shown in Figure 3.4). Some of the calibrant housings did not allow the same gap between the tape and silicon detector so were placed as close as possible. Data for this "*WithTube*" set-up, was recorded for approximately 2 hours per calibrant whilst recording a background measurement as before. During the calibration measurements the accelerator was not operational thus reducing any unwanted background. Silicon data was collected only for the unsealed ^{24}Na source.

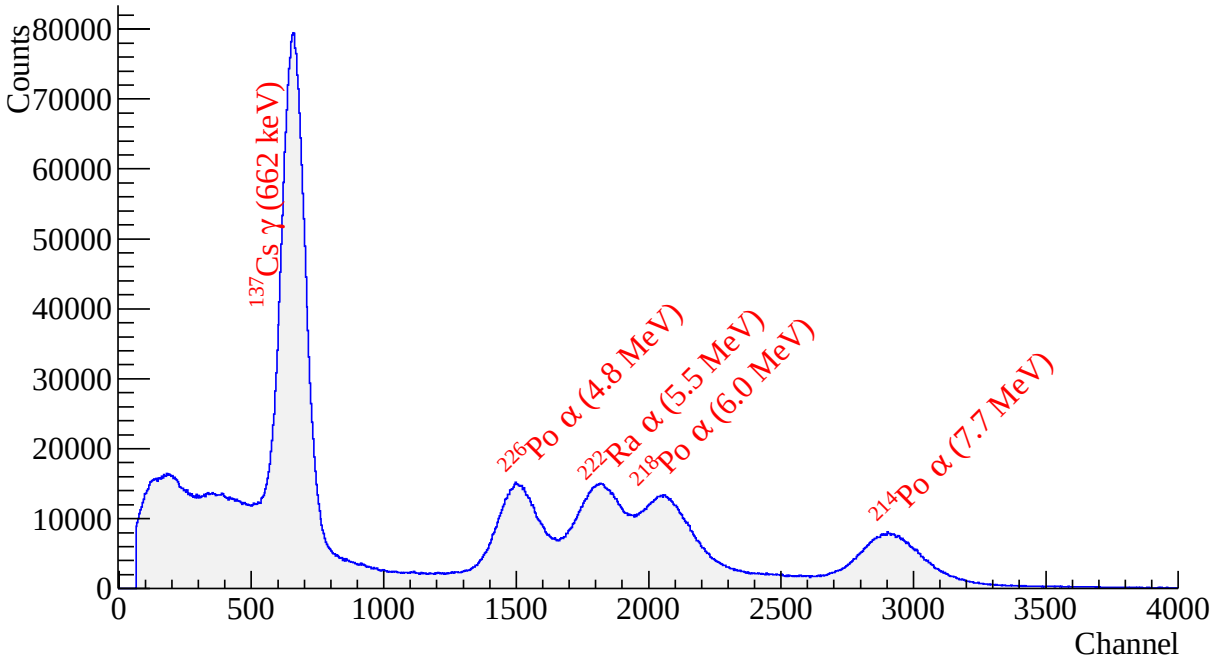

Figure 3.4: TAS **Software Sum** ^{137}Cs spectrum after gain stabilisation, *WithTube* geometry, showing peak identification of the ^{137}Cs 662 keV γ ray full energy peak and the four α internal contamination peaks from the radium decay chain contamination.

3.4.2 Isotope Measurement

Once the calibration data was collected the TAS was set-up for measurement of the sources from the JYFLTRAP. Once tuned for the specified isotope, the isotopically pure source from the JYFLTRAP was re-accelerated producing a low energy beam enabling implantation into the tape at the centre of the TAS. This beam and dual Penning trap system was optimized for each isotope in turn and measurements were taken for approximately 2 hours per run using an optimized tape cycle. Background and measurement runs were then repeated until sufficient statistics were obtained in the online results for each isotope.

During the experiment online analysis (a small percentage of counts sent to monitoring PC, without the loss of collection rate) was checked for sufficient statistics for each run assuming that the full statistic saved *OffLine*, as is common practice. The full statics save as *OffLine* data suffered an unforeseen problem with writing the data resulting statistics writing over previous saved data, resulting in lower statistics collected then expected.

The data collected from the experiment in Jyväskylä was collated from the DAQ into *listmode* files. To make the files more manageable a *ROOT Tree* file [105] was created for each run, containing branches for each of the data streams as shown in Figure 3.3. The complexity of the data collected

by the TAS detector means a solution to the inverse problem set in Equation 2.36 is needed, for the β feeding distributions to be determined. The solution of this inverse problem can be found using the pure total absorption spectrum for the desired isotope. To obtain this pure spectra the collected data needed to be cleaned of any contamination including background.

3.5 Data Preparation

Once the data was sorted into *ROOT Tree* files it was possible to view histograms of the collected data. The initial check of the off-line data showed a poor gain matching between detectors resulting in the miss alignment of the **Hardware Sum** data. An off-line gain matching was possible with the creation of the **Software Sum** and **E-Crystal** (see below). An initial linear energy calibration for each crystal was obtained utilising the well defined 511 keV and 1274 keV full energy peaks from the ^{22}Na calibrant.

3.5.1 Gain Matching

The scintillation response of BaF_2 to incident α-particles and γ rays differs. This difference can be seen clearly when comparing the fast and slow emissions from the crystals and enables pulse shape discrimination [106]. Using the approximate initial calibration on the fast ($F01,...,F12$) and slow ($S01,...,S12$) histograms and plotting them against each other in a two dimensional plot clearly shows the separation of the response to α-particle and γ ray counts in the detectors (see Figure 3.5a). To adjust for gain drifting between the detectors, groups of one million sequential events were plotted on a fast against slow two dimensional plot. Grouping events into millions enabled a continuous gain stabilisation during a run. Applying a two dimensional matrix condition or "banana" gate around the α-particle response region in this two dimensional plot enables the separation of the α-particles and γ ray induced signals.

Plotting these gated α-particle events for each crystal enables a Gaussian fit to be applied to the highest energy α peak, shown in Figure 3.5b, this peak is known to be the α decay of ^{214}Po from the Radon decay chain [60]. The centroid of this ^{214}Po α peak was then used to apply a correction to the energy if this centroid has moved from its reference point. The initial calibration for these spectra was based on the ^{22}Na spectra and as such the ^{214}Po α peak centroid in the one of these crystals was used for this reference point. The comparison of this reference point centroid channel over time (by grouping one million events) enables a continuous stabilisation of each PMT and crystal system for each measurement. It should be noted that the number of scintillation photons produced from an α event differs from the same energy γ ray event. This difference in scintillation

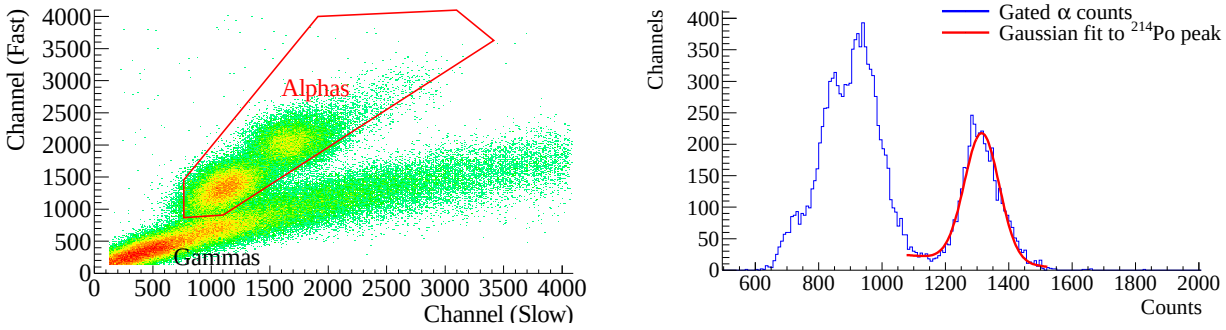

(a) Two dimensional slow channel vs fast channel plot (red) *banana* around α counts, z-axis (out of page) (counts) logarithmically plotted.

(b) Energy spectrum of gated α-particle counts for a cut of one million sequential events, for constant gain matching.

Figure 3.5: Spectrum from a ^{94}Sr run. *a*) The identification of α-particle induced events in the (red) banana cut. *b*) The resultant gated α spectrum with a fit on the high energy ^{214}Po peak.

counts results in a 7 MeV α-particle count not being collected the same channel as a 7 MeV γ ray. This stabilisation of gain drifting removes any problems created from the optical grease or any temperature dependence of individual crystal and PMT systems. An automated algorithm was used to stabilise and gain match the crystals, collected energies for each event as explained above for all of the collected runs. After the stabilisation, this initial calibration was also applied to all the data. Groups of one million events were chosen for this process so that sufficient events where collected for a good fit of the α peak with a symmetric Gaussian peak shapes but only allowing relatively short time periods pass. This resulted in frequent gain matching correction, reducing any final energy drifting in the collected data.

Stabilisation and Summation of Data

The stabilisation algorithm provided a calibration between crystals (E01,...,E12), but these were still only approximately calibrated for energy. To improve the energy calibration the separate crystal data were combined to enable the analysis of the detectors as a single TAS detector. An "**E-Crystal**" spectra was created by summing the final energy data recorded from all 12 crystals and a "**Software Sum**" spectra was created from the sum of the events from all crystals as they occurred (event by event) similar to the **Hardware Sum**. Multiplicity data was also collected for both of these data sets. In the creation of the **Software Sum**, a common low-energy threshold was used on each crystal before the addition to avoid the superposition of noise. This common low threshold was set to the highest energy noisy channel from each of the crystals plus PMT system corresponding to an energy of approximatively 64 keV. As with the **Hardware Sum**, the **Software Sum** collected data as if the 12 crystals are all one detector (see Figure 3.6). The **Software Sum**

is the data of interest for the final analysis but the **E-Crystal** was also used for the calibration check to give a more accurate response for the detector. The **E-Crystal** data is unique to the multi segmented TAS detector and to date the impact of this data has not been explored in detail.

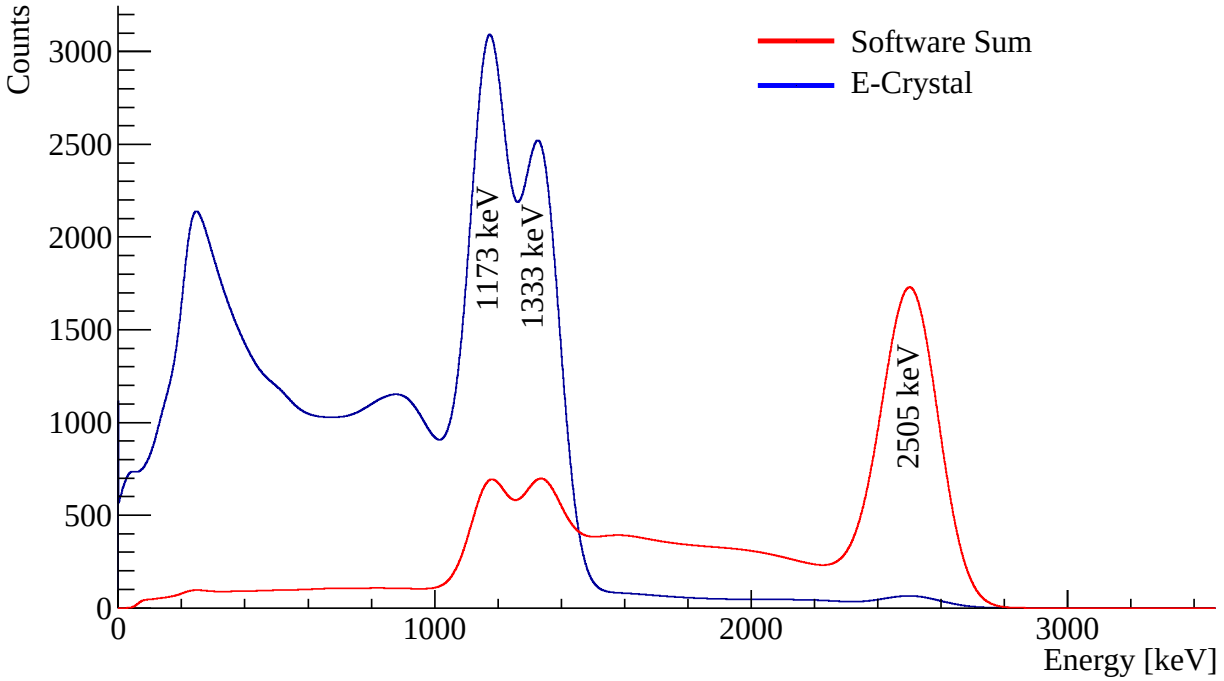

Figure 3.6: Monte Carlo simulation spectra of a ^{60}Co source within the TAS using one million events, showing the full γ rays cascade energy collection in the **Software Sum** (red) and the more conventional looking spectra from the **E-Crystal** (blue).

Background

The calibration data for the detector was collected with the accelerator beam off, resulting in the background measurements being split into the relevant "beam-on" measurements and "beam-off" measurements. Each of the "beam-off" background runs were compared (see Figure 3.7a) for any energy shifts or changes in the background over time. All runs with the same spectrum structure were then combined to create a single, standard "beam-off" background run. Within this background spectrum (Figure 3.7b) it is possible to identify the dominant α peaks from the radium internal contamination of BaF_2. This process was repeated for the "beam-on" background to created a standard "beam-on" background.

3.5.2 Pile-up

Due to the statistical nature of radioactive decay there is a probability that multiple events (from separate cascades) can be detected within the finite detection time window within a single crystal or the whole TAS. This results in the two events "piling-up" and thereby producing a larger energy

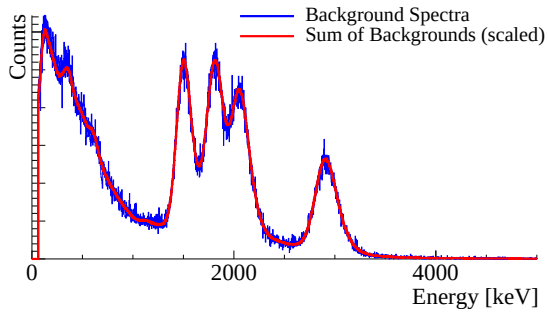

(a) Twelve separate homologous background runs of the "beam-off" **Software Sum** (blue) and for comparison the scaled sum of these measurements (red).

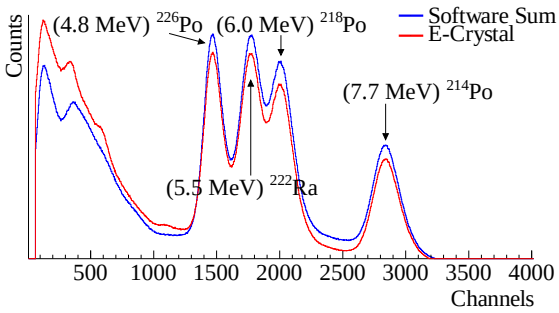

(b) Total "beam-off" background measurement for the **Software Sum** (blue) and **E-Crystal** (red) spectra.

Figure 3.7: Total "beam-off" background measurements. *a*) Showing all combined runs after stabilisation of the spectra. *b*) Identification of the α peaks from the ^{226}Ra decay chain contamination within BaF_2 crystals for the **Software Sum** and **E-Crystal** spectra.

that is recorded for of the separate original events. The high efficiency of the TAS detector increases the possibility of this pile-up occurring. A restriction on the maximum decay rates inside the TAS was used to reduce extensive pile-up, but this could not completely eliminate the problem.

Work by Cano-Ott et al. [107] has shown that it is possible to recreate expected first order pile-up using the true recorded pulse shapes. The addition of two random pulse-shapes from the recorded data spectra using a random time shift between the first pulse to the second results in the creation of first order pile-up as shown in Figure 3.8. This generated pile-up event is representative of a possible pile-up event in the system but does not account for the detection system. In order to include this, a time window of the same length as the ADC needed to be applied and for the **Software Sum**, a low energy common threshold needed to be included. Iterating this process in a Monte Carlo approach to create a full spectrum gives a good representation of the true pile-up spectrum. The low count rate of the experiment results in very low probability of second-order or higher orders of pile-up. Both the **Software Sum** and **E-Crystal** pile-up data was created this way allowing the satisfactory subtraction of pile-up from all spectra.

This newly created pile-up spectra has net counts equal to the number of iterations used in its creation, because of this a normalisation is needed. This pile-up normalisation N can, to a first order approximation, be simplified to,

$$N = \left(A_S\right)e^{-\alpha\tau}\left(1 - e^{-\alpha\tau}\right) \tag{3.1}$$

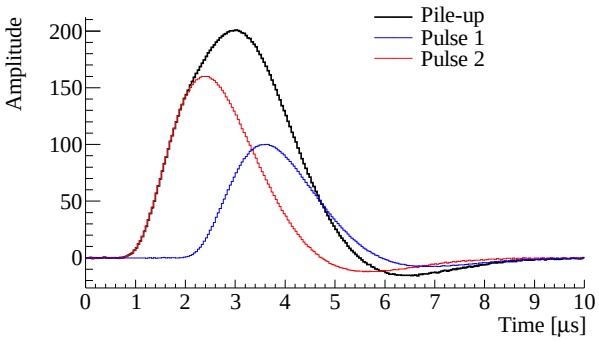

Figure 3.8: An example of the piling up of two true pulse shape (blue & red) within the time window, and the resultant pulse (black) with greater amplitude (energy).

where α is the rate of detection, τ is the ADC time gate and A_S integral counts in the recorded data needing pile-up removal. This method gives a rough approximation, but a further step can be taken to include the pile-up already included in the integral counts (A_S), thus producing,

$$N = \left(A_S + A_P \times N_1\right) e^{-\alpha\tau}\left(1 - e^{-\alpha\tau}\right) \tag{3.2}$$

with N_1 being the normalisation from Equation 3.1 and A_P is the integral counts in the pile-up. An example of the total *Beam-Off* Backgrounds pile-up, its normalisation and removal is displayed in Figure 3.9. The value of τ is set by the ADC to 5 μs and the rate α was obtained from the pulser counts in the **Hardware Sum**. Rates for the calibration data and background measurements are shown in Table 3.2.

3.5.3 Subtractions

All data collected by the TAS will contain some degree of pile-up contamination. This may be negligible but using the method above to calculate and using Equation 3.2 to normalise, it is possible to subtract (mathematically speaking) this contamination. For the background measurements each individual spectra was stripped of its own pile-up before checking and then combined to form the "beam-on" and "beam-off" standard backgrounds. Pile-up was also subtracted from all the calibration data and the measured isotopes data. Both the calibrant data and measured isotope data contained one of the types of background. The amount of this background to be subtracted from each run was calculated systematically using the ratio of counts collected in the pulser region in the relevant **Hardware Sums** data. The recorded pulser counts was found not to be as linear with time as expected so an additional off-set to the background subtraction ratio was included. This value was adjusted visually to enable an acceptable subtraction. The subtraction of the background

Run		Rate [Hz]	Run		Rate [Hz]
Beam-Off Background	Bck_1418	6003	*Beam-On* Background	Bck_1419	6063
	Bck_1614	5855		Bck_1829	6235
	Bck_1904	5877		Bck_1931	6113
	Bck_2137	5921		Bck_0852	6086
	Bck_2239	5916		Bck_1017	6204
	Bck_0935	5973		Bck_1911	6142
	Bck_1123	5993		Bck_0233	6309
	Bck_1255	5986		Bck_0908	6210
	Bck_1346	5989		Bck_2003	6250
	Bck_1736	6018		Bck_2325	6164
	Bck_1948	5851		Bck_0517	6191
				Bck_0928	6125
				Bck_2144	6305
No-Tube Geometry	^{137}Cs	8718	With-Tube Geometry	^{137}Cs	8656
	^{60}Co	15257		^{60}Co	15302
	^{22}Na	8925		^{22}Na	8887
	^{24}Na	10047		^{24}Na	9392

Table 3.2: Experimental rate (in counts per second) during the experiment for background and calibration source runs.

and pile-up from one of the calibration spectra is shown in Figure 3.10. See Appendix B for the other calibration subtractions.

3.6 Calibration

The initial rough calibration and stabilisation was enough to compare the data but for the analysis a more precise calibration was needed. As discussed in Section 3.4 data was collected with each calibrant for two geometries. To maximise the statistics of the calibration, both geometrical results were used. The calibrant **Software Sum** and **E-Crystal** data was stripped of contaminants as described above and then the full energy peaks were fitted using a combination of a Gaussian, step function, slope and a base height to extract the centroid position and sigma (σ) defined by the standard deviation of each full energy photo-peak (a list of these energies can be found in Table D.1 within Appendix D).

The collected data enabled a linear energy calibration and a second order polynomial σ against energy calibration to be created. The limited resolution of the BaF_2 meant that not all of the full energy peaks of the calibrants could be used for the final calibration fits. The poor resolution produced a double (overlapping) peak for ^{60}Co but this could be fitted using a second Gaussian and step function.

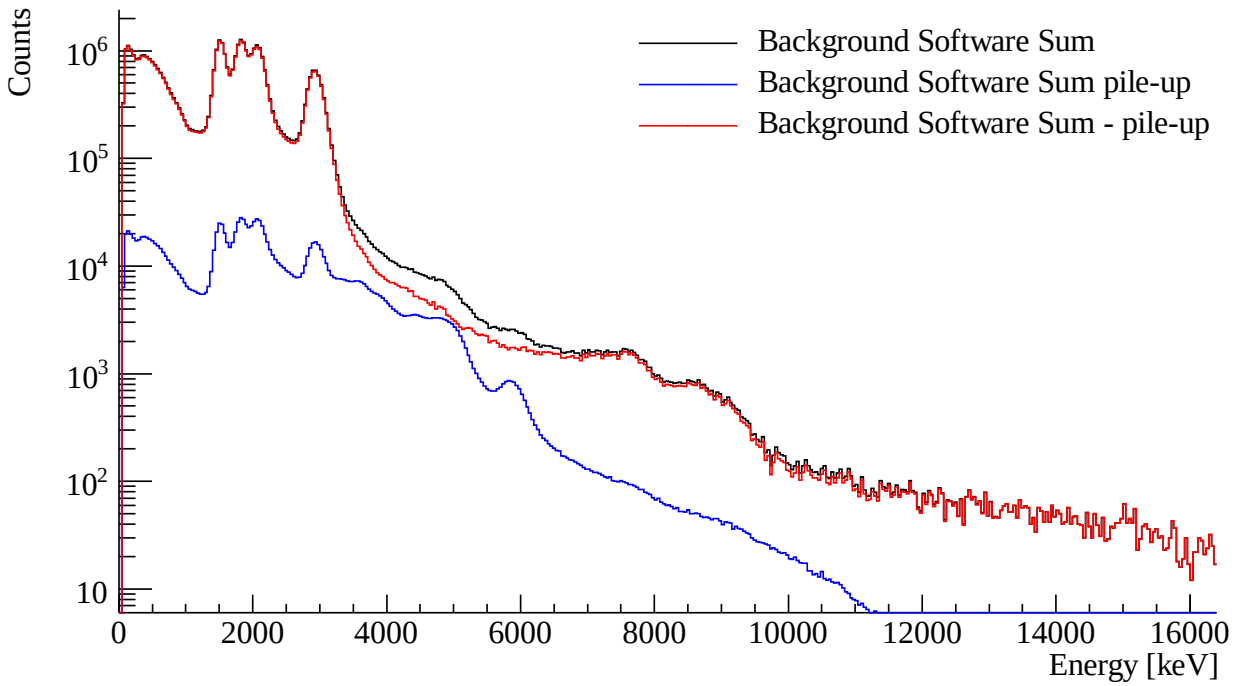

Figure 3.9: Example of the total *Beam-Off* background **Software Sum** with its normalised first order pile-up and the resultant spectrum from its removal.

A comparison of the *NoTube* and *WithTube* results showed little difference apart from reduced efficiency (due to more dead material). To improve statistics both data sets were used for the primary calibration fits. With the use of the Monte Carlo (MC) simulations described in Chapter 4, the calibration was improved. The primary calibration was combined with the MC simulation to produce calibration source spectra without the photo peaks creating a γ-ray background spectrum for each calibrant (geometry specific). The removal of this γ-ray background from the stripped of contamination data as in Figure 3.11 produced more prominent full energy peaks. A final calibration was created by fitting this data as before and are shown in Figures 3.12-3.13. More information on the production of the γ-ray background is described in Chapter 4.

Silicon Calibration

The calibration of the silicon detector is not as straight forward as the calibration of the TAS due to the increased energy spread of the β decay particles. The offline software gating of the silicon detector data in the analysis means that an exact energy calibration is not needed; the only calibration information required is the channel (and relevant energy) of the low energy threshold. This low energy threshold was set to exclude noise when gating on the β events. The decay of ^{92}Rb is known to decay directly to the ground state with a branching ratio of 95% [108] and was included in the measurements, thus the shape of the collected spectra is dominated by this decay.

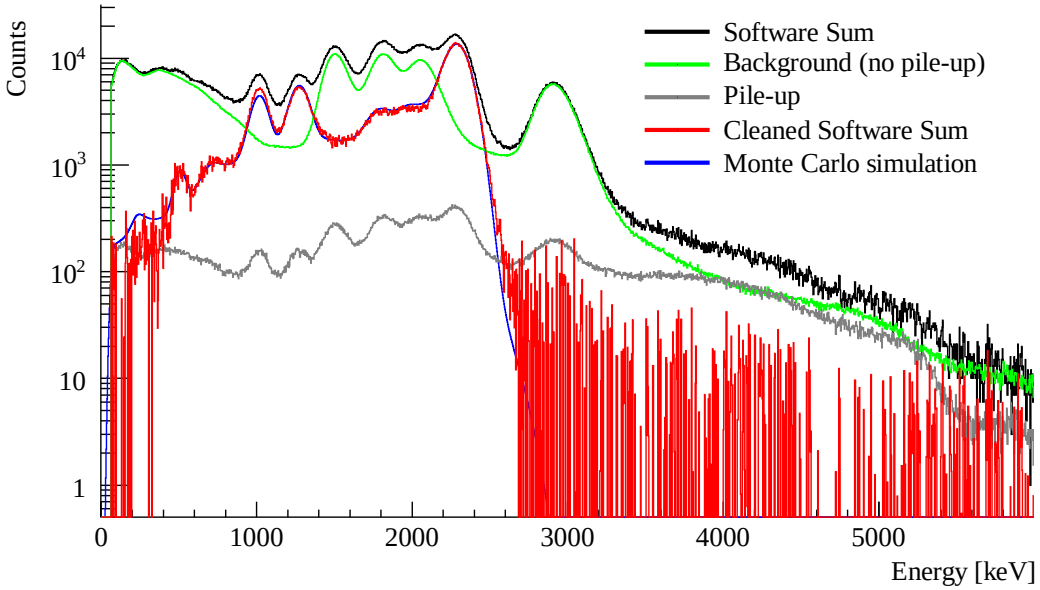

Figure 3.10: Subtraction of background and pile-up from the ^{22}Na **Software Sum** spectrum. Displaying the original data (black), normalised background without pile-up (green), normalised pile-up (grey), final cleaned data (red) and the Monte Carlo generated spectra (blue).

The simulation of this single dominant decay is possible using the Monte Carlo model. An initial calibration of the experimental data can be made using the end point energy. This calibration can then be improved by adjusting the calibration until the experimental spectrum shape is in the same form as the simulated data, where the simulated spectrum from the MC model is "ideally" calibrated. The final result of this calibration reveals that the low energy threshold for the silicon detector is ≈105 keV.

3.6.1 Run Data

The calibration data mainly used sealed sources and thus the efficiency of escaping β-particle from these sources was unknown resulting in the silicon detector outputting no useful data. The run data had silicon detector information and as such a second set of data can be created, by gating on the β events. This data will be referred to as "*β-gated*" rather than the "*singles*" data.

Singles

The data collection for the "*singles*" data was stripped of background (*beam-on*) and pile-up, as with the calibrants. All runs for each isotope were then checked and the homologous runs were combined to maximise the counting statistics. Unlike the pure calibration sources, each desired isotope needed to be checked for any other form of contamination such as daughter and granddaughter decay contamination. The length of the cycle and the relevant half-lives also gave an indication on

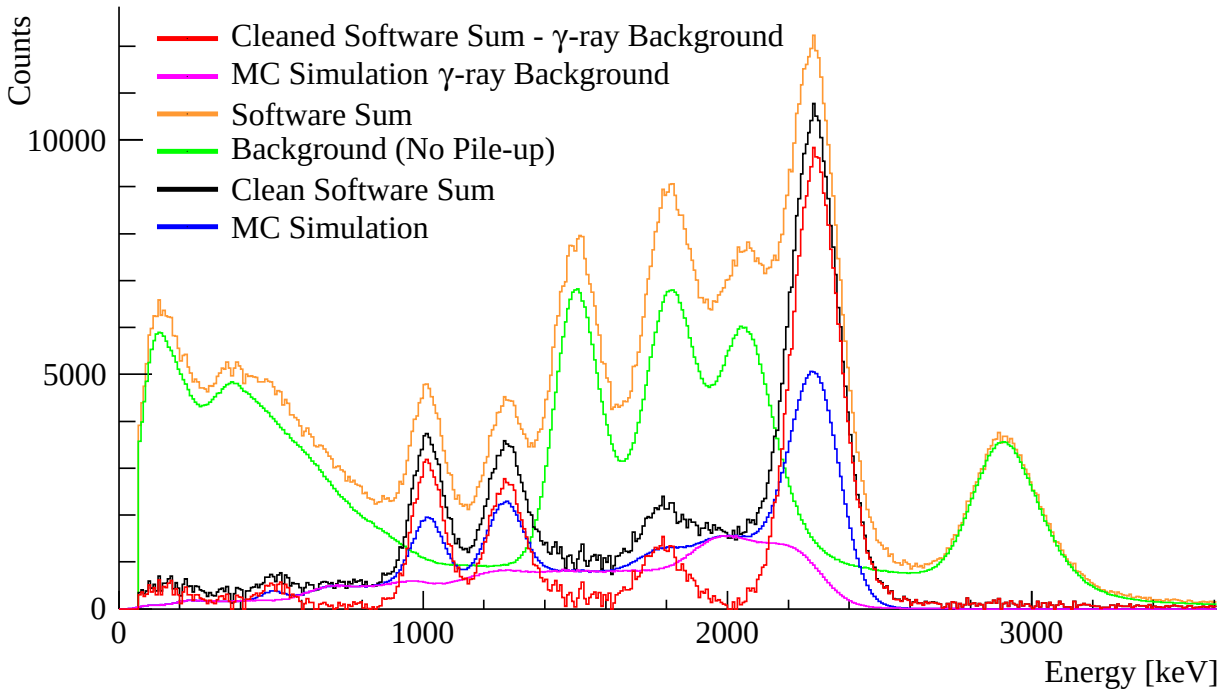

Figure 3.11: Subtraction of γ-ray background generated by Monte Carlo (pink) from the stripped of contamination ^{22}Na **Software Sum** spectrum (black), with the resultant subtracted spectra (red) and full MC (blue). Including the original Spectra (orange) and background (green) collected in *WithTube* geometry set-up.

the amount of possible contamination, but other tests could also be performed to find the correct normalisation required. If daughter or granddaughter decay contamination was present, it would need to be removed in the same way that the constant background was. If this contamination was measured (as one of the other isotopes to be studied) its background and pile-up subtracted spectra could be normalised and subtracted. If any contamination products were not measured but were well known, it is possible to generate the relevant spectra using the MC simulation (explained in Chapter 4) and as before normalise and subtract as with real data. For more information on the subtractions of ^{86}Br, ^{91}Rb or ^{94}Sr see Chapter 6.

Beta Gated

The *β-gated* data was obtained by taking events from the **Software Sum** only when there was a coincident event within the silicon data (above a noise threshold). This new data set was created before any pile-up, background, or contamination was removed, but after the energy calibration and stabilisation. A silicon gated "beam-on" background measurement was created using the same criteria as the *β-gated* run data and was found to contain only a small amount of noise, as expected, due to the low probability of background events being concurrently detected in the silicon and the TAS. Since the background only contains noise, it can be assumed that its removal is not necessary.

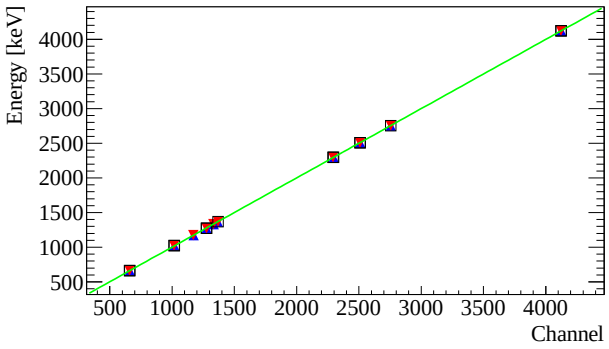

(a) Software Sum energy calibration.

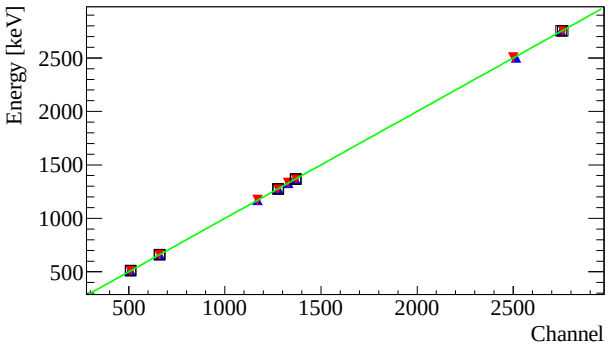

(b) E-Crystal energy calibration.

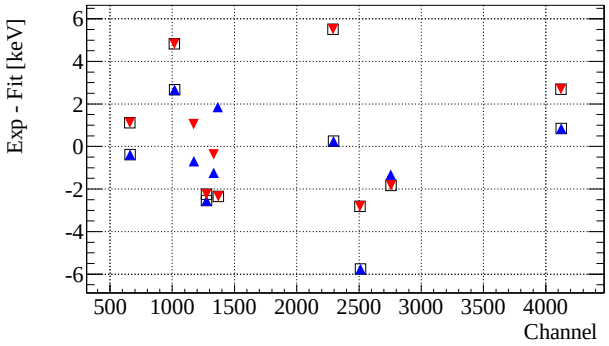

(c) Software Sum energy calibration differences.

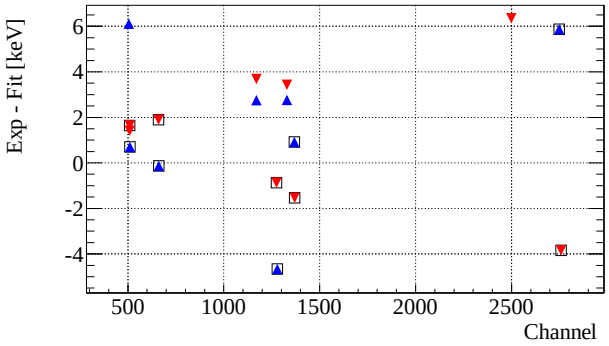

(d) E-Crystal energy calibration differences.

Figure 3.12: Final energy calibration for the **Software Sum** and the **E-Crystal** data, including the difference from the linear fit. With the *WithTube* data in down triangles (▼) and *NoTube* data in up triangles (▲), Black squares (□) highlighting the points included in the calibration and the fit in green.

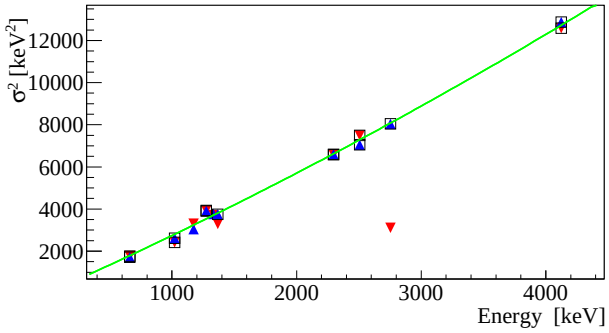

(a) Software Sum σ calibration, with second order fit.

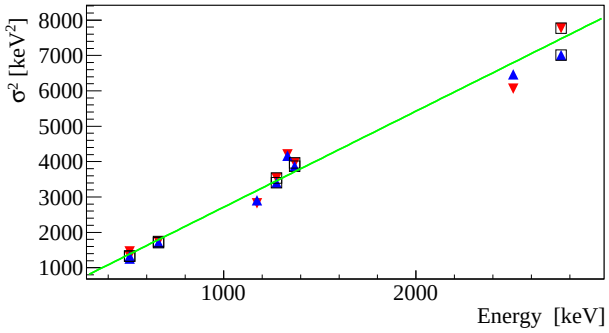

(b) E-Crystal σ calibration, with second order fit.

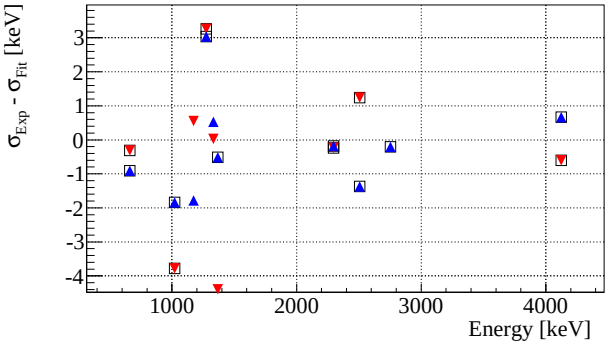

(c) Software Sum σ calibration differences.

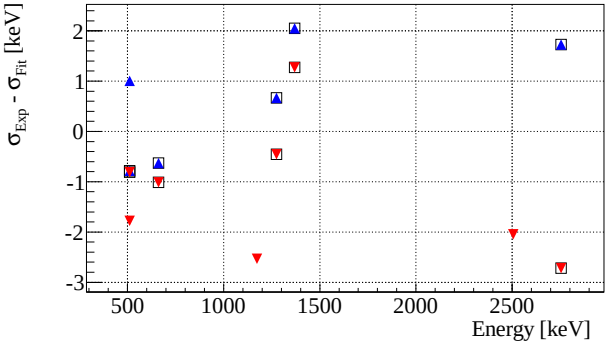

(d) E-Crystal σ calibration differences.

Figure 3.13: Final σ calibration for the **Software Sum** and the **E-Crystal** data, including the difference from the 2nd order polynomial fit. With the *WithTube* data in down triangles (▼) and *NoTube* data in up triangles (▲), Black squares (□) highlighting the points included in the calibration and the fit in green.

A pile-up spectrum was created for each run using the method outlined above with the extra criteria that one of events was in coincidence with a β-particle (silicon detector) event. Due to the lower number of β events, the pile-up code was run using more iterations to produce a smoother spectrum for subtraction. The same normalisation formula was used to subtract the correct amount of generated pile-up from the *β-gated* spectra. As with the *singles* data any contaminants from daughter decays could be subtracted using *beta-gated* experimental data if collected or the MC generated *beta-gated* spectra. As with the clean *singles* data the homologous *β-gated* runs were summed; for more information on the subtractions of ^{86}Br, ^{91}Rb or ^{94}Sr see Chapter 6.

4 Monte Carlo Model

A GEANT4 Monte Carlo (MC) simulation was created for the Valencia-Surrey TAS and tested in 2009 with the simulated geometry of the Valencia-Surrey TAS detector is shown in Figure 4.1 [104]. This MC simulation was designed to output the energy deposited within each crystal for each primary event. Energy values generated were then summed reproducing the electronics in this experiment to create the **Software Sum** and **E-Crystal** data. Data created from this MC simulation excludes the physical processes of scintillation in the crystals, conversion to electrons and their multiplication in the PMTs and the data acquisition systems. The exclusion of these physical processes results in the data being collected in discrete energy bins (Figure 4.2). To mirror the experimental set-up a threshold of ≈64 keV was applied to the MC model **Software Sum** collection. Events with such energies below this threshold where discarded but for normalisation the non-collection was recorded in the 0 energy channel to account for "non-interactions".

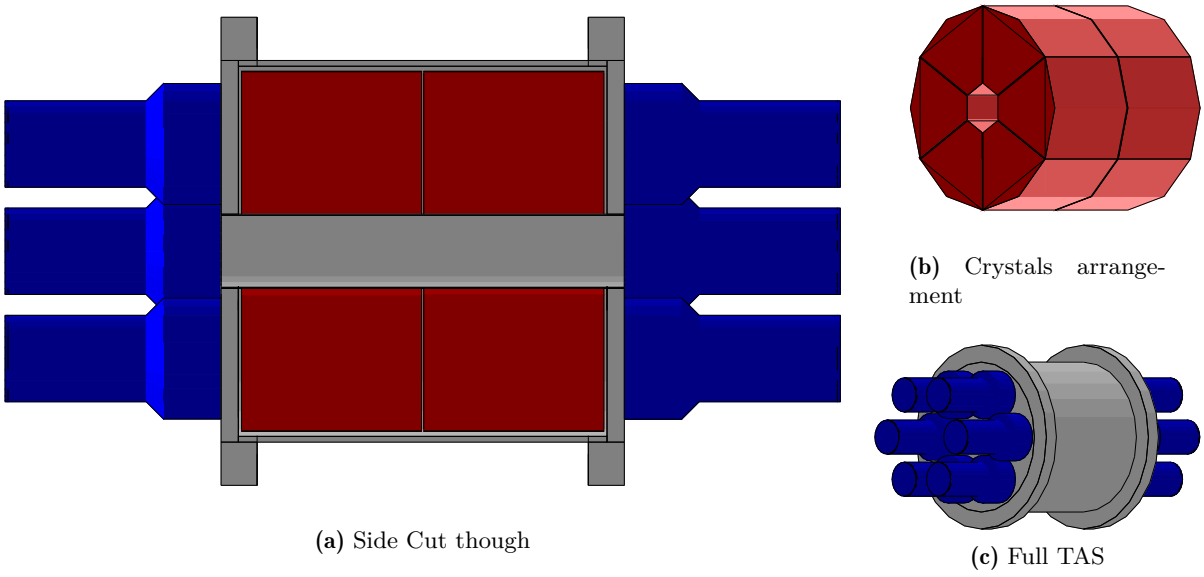

(a) Side Cut though

(b) Crystals arrangement

(c) Full TAS

Figure 4.1: Images from the GEANT4 Monte Carlo simulation showing the simulated geometry of the TAS, without the beam line and tape set-up. Cut though image a) showing half the aluminium can (grey) and four visible BaF_2 crystals (red) and 6 PMTs (blue), where as b) shows the full 12 crystal layout and c) the full TAS.

The near-linear response of the BaF_2 scintillation means the missing physical processes can be approximated by utilising the experimental σ (standard deviation of a full energy photo-peak)

calibration collected. Each energy bin of the MC data was spread using a Gaussian function dependent on the experimental sigma calibration. The broadening of each channel replicates the missing physical processes, producing a more realistic spectra (Figure 4.2). This simple mathematical substitution of the physics processes reduced the computational time needed to run the simulation and the complexity of the code needed.

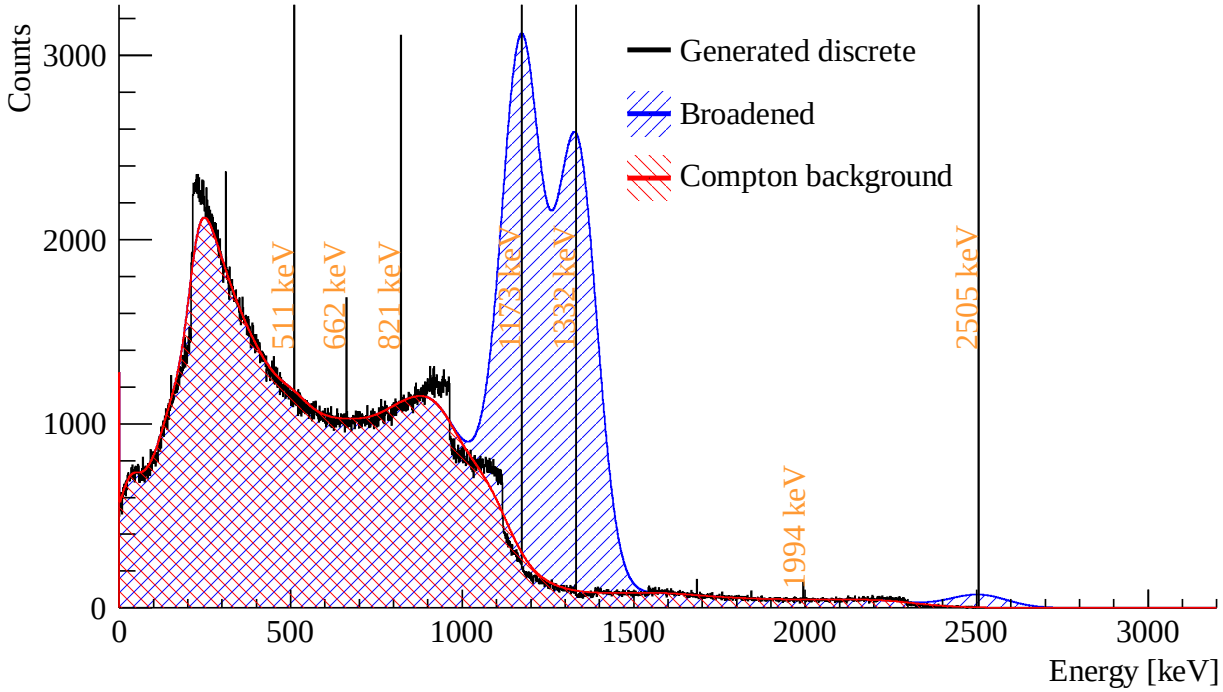

Figure 4.2: A comparison of the Monte Carlo simulation **E-Crystal** data outputs with (blue) and without (black) the broadening applied for ^{60}Co source using the *WithTube* geometry. Also showing the γ-ray background spectra (red) produced by the removal of the γ ray full energy peaks (for use with the calibration see Section 3.6).

The MC simulation model used in [104] simulated the TAS set-up without the tape system or beam line being present (*NoTube* set-up). This enabled a preliminary comparison between the calibrant data collected without the tube in place. The primary particles for this model were generated with an user defined input for the decay structure of the desired decaying nuclei, taking data from the ENSDF database [25]. The inclusion of this user defined decay reduced the reliance on the in-built libraries of GEANT4, reducing the chance of errors. Each calibrant was simulated with runs of one million events to compare the experimental and simulated *NoTube* data (see Figure 4.3). A small discrepancy was found in most fits with the reproduction of the high energy tail of the full energy photo peaks. This is thought to be energy straggling in the electronics that was not accounted for in the simulations, or artefacts of the initial subtraction. The net effect of this difference on the final analysis was negligible.

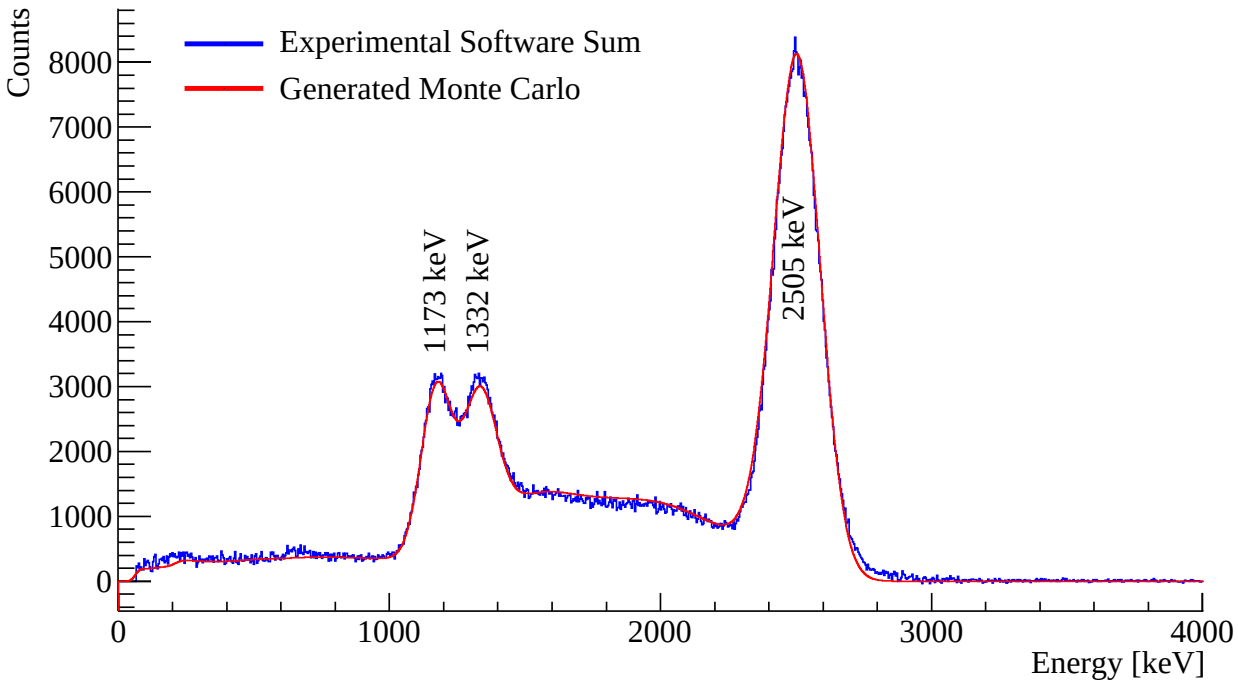

Figure 4.3: A comparison of the clean *no-tube* ^{60}Co calibrant spectrum (blue) to the generated Monte Carlo simulation **Software Sum** data (red) using one million events (after the optimization).

This *NoTube* data was then compared to the previous work to check for any major difference after the reapplication of the optical grease. A small difference was found between the original calibration data and newly collected data. The MC simulation was optimised to the new data by adjusting the dead material (Teflon) around the detector.

The experimental set-up utilised a tape delivery system that was not used previously [104] and as such this new geometry was added to the MC simulation. The replication of this tube and tape delivery system in the simulation needed to be as accurate as possible to reproduce the materials found in the experiment. The complexity of this additional tube section is shown in Figure 4.4. The silicon detector was placed within the end cap of this tube section, and thus was included in the geometry added to the simulation. The active volume of the silicon in the detector was set as a detector medium so that any energy deposited in this region was also collected, to allow the reproduction of β-*gated* spectra.

4.1 Validation of the Monte Carlo Model

The validity of the MC simulation with the new tube and tape section was tested by simulating the calibrant data. Each spectrum was energy broadened using the energy response resolution obtained using the *With-Tube* sigma (σ_{exp}) calibration and then compared to the "cleaned" calibration spectra. These tests show a reasonable fit to the experimental data for both the **E-Crystal** and

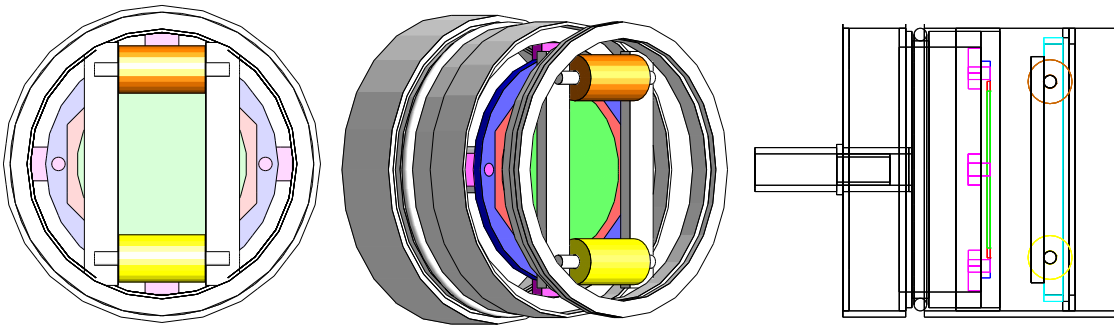

(a) Solid view 0° **(b)** Solid view 45° **(c)** Wire view 90°

Figure 4.4: The Monte Carlo simulation geometry of the endcap and internal tape system showing a wire-view and a solid-view of the central system excluding the beam tube (or tape). Solid view image highlights the printed circuit board (blue), silicon detector (red) with the active area (green) circle and the two tape rollers, the aluminium (yellow) and the peak anti static roller (orange). With the aluminium end-cap (white) surrounding the detector and PCB held by screws and mountspink.

Software Sum spectra of the ^{22,24}Na and ^{137}Cs (see Figure 4.5). The ^{60}Co data showed a reduction in quality of the fit with variations in the matching the sum peak and the rest of the data. A small discrepancy was found for the height of the peak and non peak (Compton continuum etc.) regions between the final simulations and experimental data, shown by the normalisations in Figure 4.5. This discrepancy was thought to be due to differences in the Teflon coverings around the crystals. See Appendix C for more MC and data comparisons.

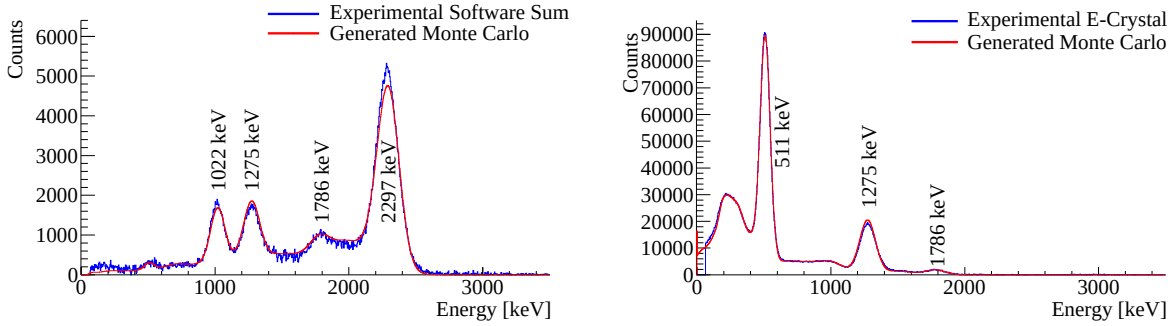

(a) Software Sum **(b) E-Crystal**

Figure 4.5: Cleaned experimental data (blue) with the *Tube* geometry Monte Carlo simulated data (red) for the ^{22}Na calibrant

With the validation complete, it was possible to produce γ-ray background spectra for each of the calibrants in both geometries. These spectra were produced by simulating the sources and then editing the resulting spectra before the energy response broadening was applied, by replacing the reference peak bin counts with the mean count from each side. After this subtraction, the spectra were broadened as before, producing a γ-ray background, (see Figure 4.2). Using the

preliminary energy calibration from Chapter 3, it was possible to match the MC output to the experimental calibration data. This γ-ray background then enabled a further subtraction of the spectra improving the fits needed for the final calibration (see Section 3.6).

4.2 Beta Particle Simulation

Photon simulation within GEANT4 and other transport codes gives a realistic result due to the knowledge on the physical interactions of photons with matter [96]. The transport of electrons in matter is not as well defined due to the larger array of processes possible. This results in a good approximation but not perfect results when dealing with the electrons in a simulation. The three-body process of β decay results in a distribution of (kinetic) energy between the recoiling daughter nucleus and the emitted anti-neutrino (neutrino) and β^- (β^+) particle pair. To simplify the simulation of β transitions all β kinetic energy distributions use the energy spectrum expected for an allowed decay (see Section 2.2.2). The low probability of the β particles entering the TAS and the use of silicon detector as a tag for β events resulted in a negligible effect when using this allowed β-particle spectral shape approximation. With the shape distribution of each decay fixed the binned response could be created for each 40 keV energy bin by changing the distribution shape via the end point energy. For simplicity the binned response for each 40 keV was simulated with a fixed Z=36, rather then adjusting for each daughter. This simplification give negligible effect and is well within the uncertainty due to the limited energy resolution of the TAS detector. The simulation of the precise known decay transitions in the discrete analysis used the specific Z of the daughter nucleus. The differences in the shape of the β^- energy distributions for different end point energies are show in Figure 4.6.

4.2.1 Silicon Detector Simulations

The MC simulation to this point has been with regards to the *singles* data. For a full comparison, the MC *Beta-gated* data needed to be created by using the output of the silicon detector volume. As with the TAS, only the energy deposited into the silicon detector volume was recorded rather than including the full energy collection processes in the semiconductor detector. The silicon detector was only used as a tag for β-particle events and the energy deposited is the only detail needed from the simulation. As with the TAS detector simulations, the same a low energy threshold as the silicon experimental spectra of 105 keV is applied to the simulation data. For normalisation of the *β-gated* response all non interactions also need to be accounted for, thus any event non interaction event (E<105 keV) was counted in the 0 energy column.

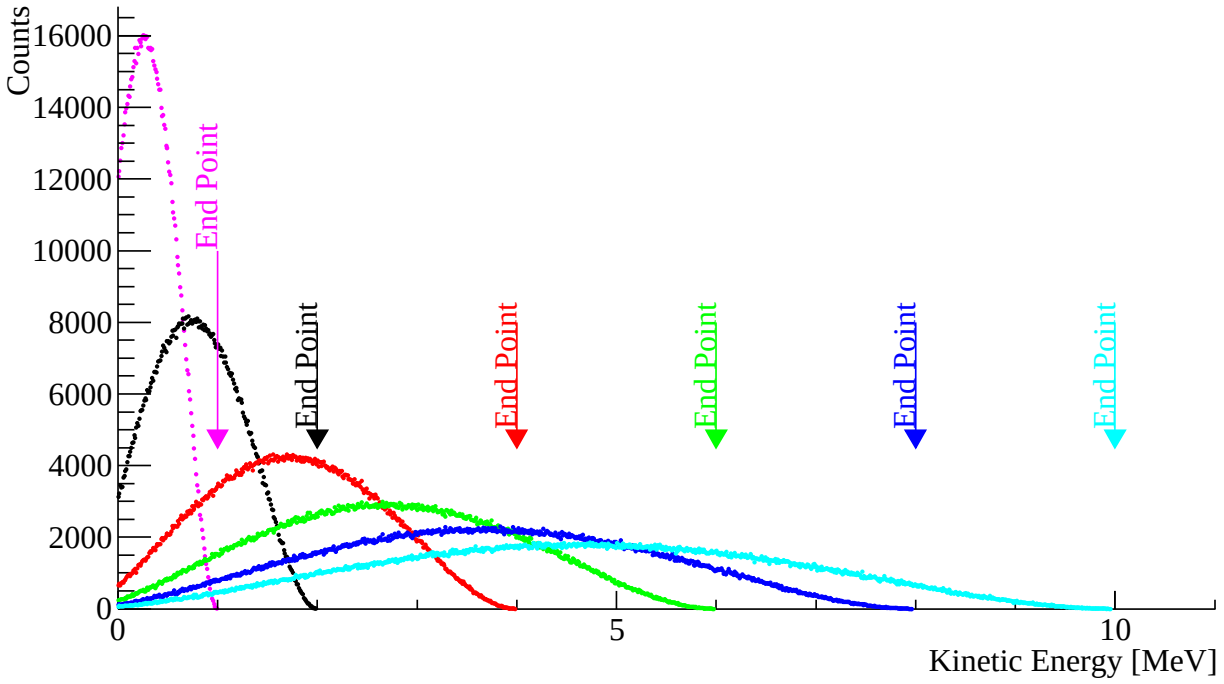

Figure 4.6: Examples of the kinetic energy distributions of one million allowed β decays from a Z=36 nucleus with an endpoint energies of 1,2,4,6,8 and 10 MeV.

4.2.2 Simulation Efficiency

The TAS detector absolute efficiency and approximately the intrinsic efficiency to mono-energetic γ rays, penetrating β-particles and the silicon detectors absolute efficiency to β-particles is shown in Figure 4.7. These efficiencies are as expected for the total TAS detector, with values of 80% $\rightarrow$ 95% for the full range of expected γ rays. The penetration of the β particle into the TAS also shows that the penetration through the aluminium can into the crystals increases with the increase in average kinetic energy of the β particles. For the individual crystals in the TAS, the absolute efficiencies of γ rays range from 9.5 $\rightarrow$ 13% and for β particles is <8%. These values mirror the solid angles of each crystal to the central source position. The silicon detector absolute efficiency plateaus after 2 MeV to 29%.

The readout systems for the detectors were not accounted for within these efficiency calculations but it is reasonable to assume that this still reflects the true Valencia-Surrey TAS γ-ray absolute detector efficiency. The silicon detector efficiency generated should be similar in regards to the readout system but will contain a larger uncertainty due to the difficulty to simulate electrons accurately in comparison to γ rays. The *singles* analysis response to small differences in these efficiencies analysis should be negligible, but for the β-*gated* results the ratio between the silicon and

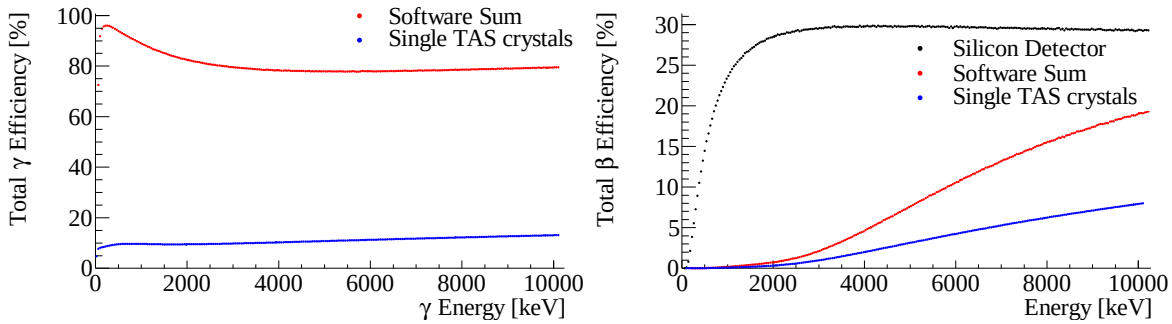

(a) γ **rays.** **(b)** β **particles**

Figure 4.7: Efficiency of the Monte Carlo model detectors (*a*) showing the efficiency to mono-energetic γ rays to the sum of the TAS detector (**Software Sum** in red) and the individual crystals (**E-Crystal** in black), and (*b*) the efficiency to β partials produced from a Z=36 nucleus, on the TAS and Silicon (blue) detector.

TAS efficiency is very important. Using the cleaned spectra from the "open" ^{24}Na source (*With-Tube*) it was possible to compare the normalisation of the *singles* against the β*-gated* spectra, resulting in a silicon β-particle efficiency of approximately 25% (see Figure 4.8). The absolute difference of 4% between the simulated and experimental result could be retested with the recorded experimental data for each isotope (see Chapter 6), enabling a more informed decision on the final value.

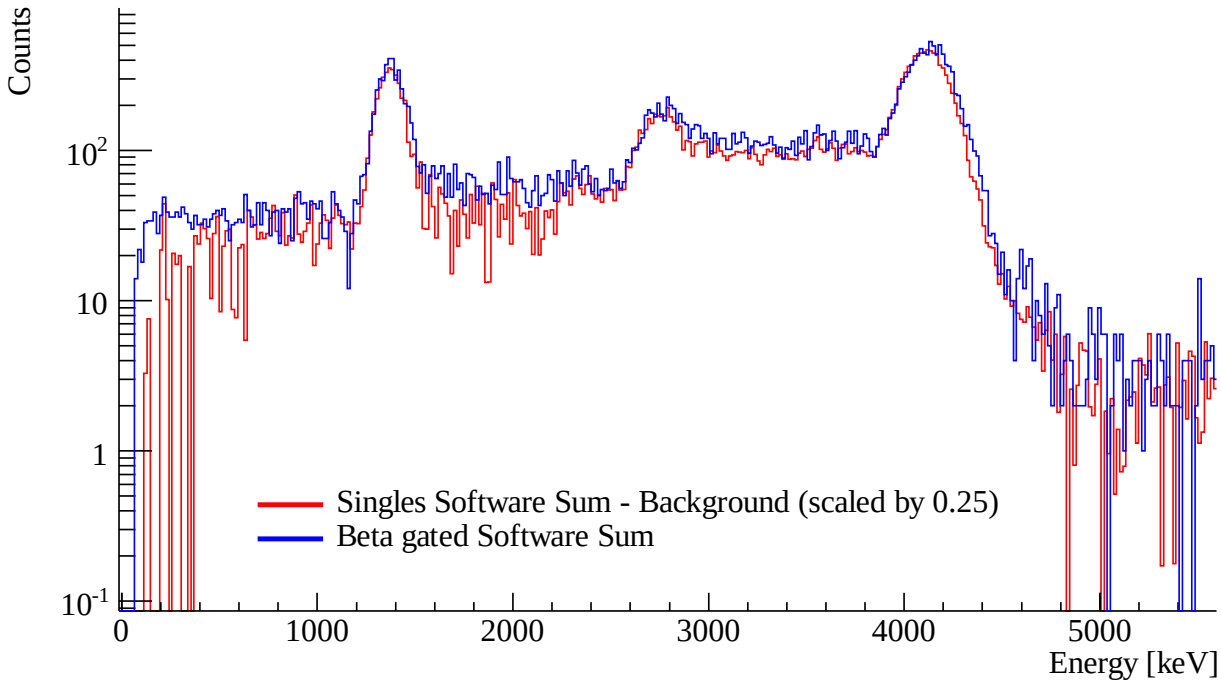

Figure 4.8: Comparison of the background cleaned *singles* (red) and the β*-gated* (blue) **Software Sum** spectra after the *singles* was scaled by 0.25, hinting towards a β-particle efficiency of 25% rather than 29%, as found in the simulations. Both the *singles* and β*-gated* spectra here include pile-up.

4.3 Additional Monte Carlo Checks

4.3.1 Monte Carlo Light Production

To reduce computational time, the GEANT4 simulation described above investigated the collected energy deposited within a crystal, rather than simulation of the physical processes of the light scintillation and collection in the PMT. The scintillation light production in BaF_2 has been documented to follow a Poisson distribution to the energy collected [109]. Using this as a base, the MC simulation was adjusted to apply a Poisson distribution to the energies collected in the crystals at each point before the summation of the crystals energies for the outputs. The newly created light output from the MC simulation produced a broadened spectrum due to the light production only, but this output still does not account for any broadening due to the effects in the PMT or electronics. Due to this extra broadening, a calibration of the light broadening (σ_{light}) was obtained from the measured width of the response to mono-energetic γ rays in the MC simulation. The difference (subtracted in quadrature) between the standard deviations (σ) of MC-light production and the experimental data was calculated. Using this difference a new broadening was applied to this MC-light output to produce a "realistic" output, Figure 4.9.

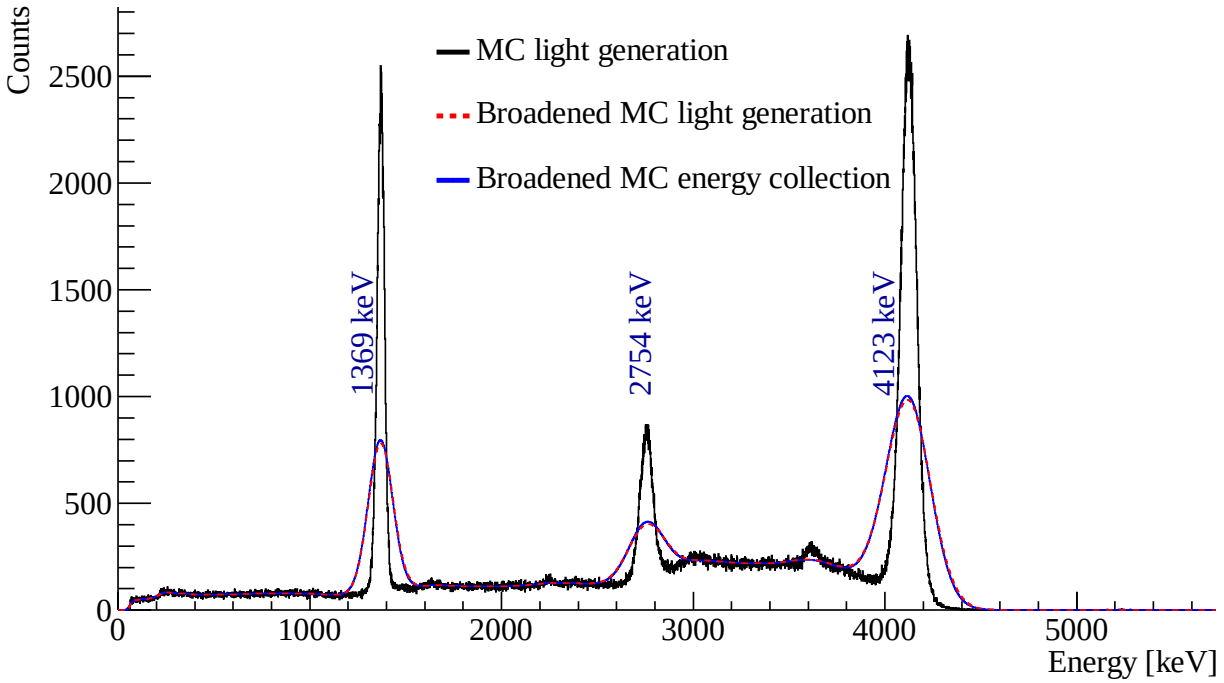

Figure 4.9: Results of Monte Carlo simulation using the light production method before (black) and after broadening (red) and the energy production after broadening (blue) for comparison.

The results from the internal light production with the extra energy broadening, produced similar final spectra to the spectra produced without the internal light production, rather than increasing

the accuracy of the model (see Figure 4.9). This result justifies that the original process of external broadening gives a realistic spectra without the need to include the scintillation responses within the MC simulation. Due to the extra computational time needed to compute the light production within the MC and the need for an increase in the number of events to provide smooth statistics, this process was not used. A second test was performed to use the experimental σ calibration within the MC to assign the energies randomly to a Gaussian function for each energy in each crystal. This was found however to be computationally inefficient.

4.3.2 Source Placement

To reduce unnecessary simulation time, the decaying source in the simulation started at the centre of the TAS detector. This situation removed superfluous simulation of the ions flight down the beam pipe and implantation into the tape. This simplification should have limited effect on the outcome of the results, due to the limited probability of the ions decaying in flight and the number of statistics used in the experiment. The simplification of the source placement means approximations were made to where the source decay actually occurred. The initial version of the MC simulation used a point source at the centre of the TAS emitting in a (isotropic) random direction and included no tape medium for simplicity. This tape was not included as it was assumed that it would have very low impact on the attenuation of β particles and little if no effect of the γ rays due to its low density and volume.

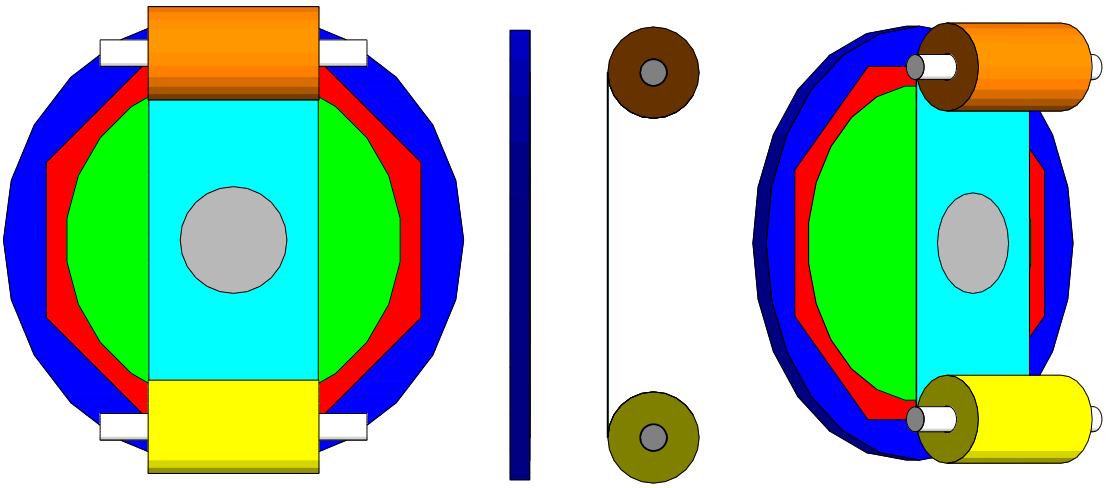

(a) Down Beam ⟨0°⟩ **(b)** Parallel ⟨90°⟩ **(c)** ⟨45°⟩

Figure 4.10: Schematic of the tape position and possible source divergence of a 8 mm disk (red) on the tapes (grey) outer surface. With The beam incoming from right hand side in (c) parallel to beam image.

The Tape

A simple test was performed to ascertain if this assumption was justified, using a 125 μm thick Mylar strip at the centre of the detector aligned to the rollers as with the real tape, similar to the tape shown in Figure 4.12. Simulating multiple mono-energetic γ rays and different energy β particles resulted in negligible differences for the γ ray energy collected but a small difference to low energy β particles was noticed. This difference prompted more research into the composition of the computer tape used which was found to be a magnetic tape consisting of a 10 μm magnetic layer (a suspension of Fe_2O_3 in Mylar) with a 30 μm Mylar backing. A simple SRIM (The Stopping and Range of Ions in Matter) [110] calculation was performed with a 30 keV ^{94}Rb ion impacting on to this tape composition and was found to penetrate only 35±8 nm. This tape composition and geometry was entered into the MC simulation, enabling a more realistic simulation at the centre of the TAS, keeping the source origin on the surface of the "up beam" (relative to the beam direction) side of the tapes.

Spot or Point

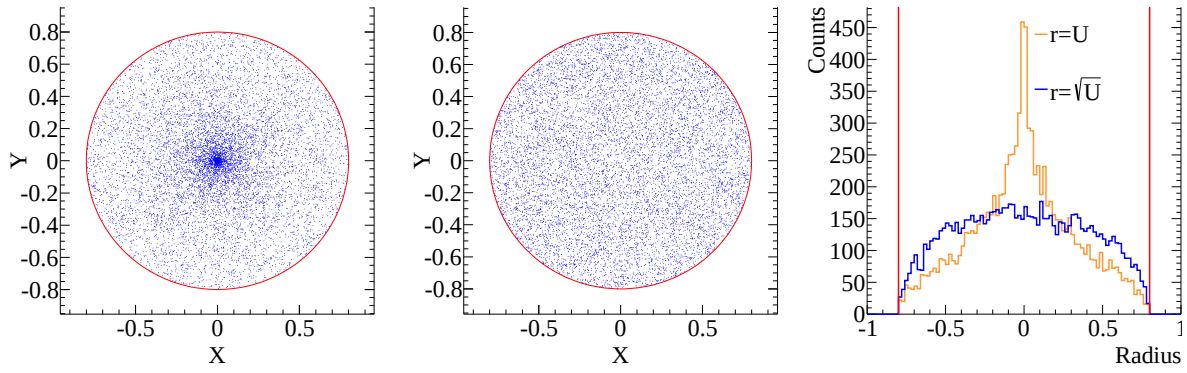

(a) Radius= U **(b) Radius= $\sqrt{U}$** **(c) Linear distribution**

Figure 4.11: The uniform distribution (U) of 10,000 random point in a circle, highlighting the importance of radial dependence of the random placements.

The focus of the beam was assumed to produce a point source on the tape, because of the nature of the beam it was impossible to check the accuracy of the spread of implantation. The Monte Carlo model was adjusted once more to ascertain if a beam divergence of 8 mm (approximate maximum divergence) would give different results. To enable this divergence in the code, random numbers where used to place the decay source within a circle with the diameter of 8 mm. The uniform placement of an object randomly in polar coordinates in a circle is not as simple as might first appear. Using an uniformly distributed radius r parameter between 0 and r_{max} and angle (ϕ) from

0 to 2π creates an excess of points near the centre. A solution can be found by sampling the square root of an uniform distribution for the radius, due to the area of coverage equalling πr^2 for a circle, as shown in Figure 4.11.

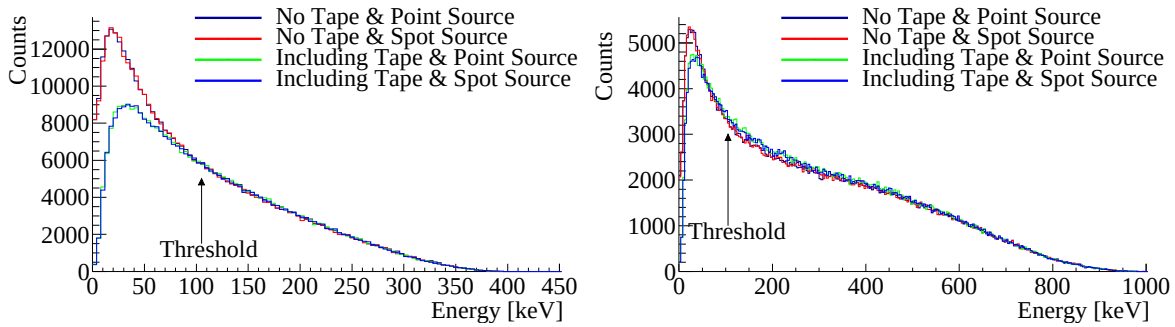

(a) 400 keV Beta **(b) 1000 keV Beta**

Figure 4.12: Silicon detector spectra recorded for MC simulations using geometries including and not including the tape and with spot or point source of β particles with an allowed β decay shaped kinetic energy distribution for set endpoint energies (a)400 keV b)1000 keV. Superimposed on top of this data is the threshold in the experimental silicon detector, showing that these differences make no obvious difference to the MC recorded spectra once the threshold is applied.

These additions to the original MC simulation were tested individually and then combined to enable the full test of the source placement. Figure 4.12 shows the silicon detectors spectra recorded for MC simulations with β particles with an allowed β-decay shaped kinetic energy distribution for set endpoint energies and MC geometries with or without the tape and with a spot or point source. The results from these tests justified that with a 105 keV threshold for the silicon detector neither the a diverging beam or the inclusion of the tape is necessary for the simulations. For completeness the tape was included in the final MC geometry keeping the source at a point on the surface of the tape and at the centre of the detector.

5 The "Inverse Problem"

The collection of the full γ-ray cascades from β decay events by the TAS results in a very complex data set. Unlike high resolution (HPGe) measurements, individual γ-ray de-excitations after β decays were not recorded and therefore information on the separate γ transitions are lost in the data collection. The results of this collection mean that the conventional γ-ray spectroscopy methods such as constructing of an energy level schemes can not be used [49].

5.1 Earlier forms TAS analysis techniques

Earlier TAS analysis such as Greenwoods et al. [44] have used a different process to obtain the beta feeding distribution. These methods, rather then solving the "inverse problem", used an iterative process to determining the beta feeding for a set TAS spectrum. This analysis uses the recorded level schemes to create the detector response using a Monte Carlo simulation. This created data is then compared to the collected TAS data enabling a visual check of possible missing transitions and levels. The level scheme is then adjusted by adding "pseudo" levels. These levels are selected by using the combination of non-assigned γ transitions from previous work to improve the match of the response to the real collected data. This iterative process is heavily dependent on the recorded level scheme and unassigned gamma transitions found and take no information on the density of levels or possibility of erroneous data collected.

5.2 Response matrix

Chapter 2 described how the data in each channel (i) could be characterised as:

$$d_i = \sum_{j=1}^{j_{max}} R_{ij}(B) f_j \tag{5.1}$$

The aim of this work is to extract the feeding distribution (f_j) of a β decay from the data collected d, to obtain the mean average γ ray ($\overline{E_\gamma}$) and β ($\overline{E_\beta}$) energy produced. To ascertain the β feeding distribution from the known collected data, the inverse of this equation is needed, thus the "inverse problem". The solution for this inverse problem has been shown by Jordan et al. [76], using a

method developed by Taín and Cano-Ott et al. [111, 70]. This solution requires the knowledge of the β decay response matrix $R_{ij}(B)$ of the TAS detector. The creation and characterisation of this matrix will be explained in this chapter.

The β decay response matrix consists of a combination of the decay (β emission and nucleus de-excitation) branches and the detector response to these branches. Mathematically this can be thought of as the response from a feeding level in convolution with the response for levels below this level, and thus:

$$R_j = \sum_{k=0}^{j-1} b_{jk} g_{jk} \otimes R_k \tag{5.2}$$

where b_{jk} and g_{jk} are the branching ratio and the γ response from level j to k and R_k is the response to level k. With the use of the MC model, the response of the detector can be recreated if the decay paths are known. However these decay paths need to be ascertained and are built up from the (often many) possible β and γ transition combinations. The probability of each β decay feeding a level and the subsequent γ transitions from these fed level depends on the initial and final states of the physical nuclear system. The nuclear structure of the daughter nucleus is paramount in providing information to which transitions are most probable[49].

Existing Level Scheme Data

The level scheme of the daughter nucleus is needed to determine the β branching ratio and γ-ray transitions for each excitation level. Most level schemes in the ENSDF database have been devised by validating data from high-resolution measurements. Due to this method, the *pandemonium effect* may be present in the recorded data. Any *pandemonium effect* in the ENSDF recorded level schemes should only affect higher excitation energy levels and therefore excluding the higher energy excitation section should avoid the inclusion of erroneous data.

The γ-ray transition (or IC) from one level to another level depends on defined transitions rules (see Chapter 2). To determine the multipolarity of transitions possible from each level, the spins and parities for all included levels are needed. This should, in theory, enable the correct transition strengths to be applied when working out the γ branching. To build the response matrix a base level scheme can be combined with a continuum of levels for the higher excitation region.

To create this base level scheme, data is taken from the ENSDF database. The inclusion of more levels in this base level scheme increase the contained measured data thus increasing the accuracy of the end result. This accuracy can only increase if all lower levels are included (possible errors from

unmeasured levels) and each level included is not affected by the *pandemonium* effect. Above the last level in this base level scheme, an energy threshold is set for the start of a continuum of levels (set at 40 keV per bin for this work). To determine the probability of feeding to each level, directly (β feeding) from the parent or indirectly (via γ transitions) from a higher excitation level, the spins and parity of each level included in the analysis are always required. Due to the requirement for the spins and parity information, one of the deciding factors for the energy threshold is the degrees of freedom, in J^{π}, created in the used known excitation levels in the daughter. The inclusion of levels with undefined or multiple options of J^{π} can be utilised if values can be selected with justification, possibly creating multiple options for the base level scheme of an isotope.

The statistical Model of Level Densities

The branching of transitions in this base level scheme are defined but feeding from above the energy threshold (from continuum of levels) are undefined, as are transitions between levels in the continuum. The population of levels in the continuum can be assigned using a model for the level density. Chapter 2 describes how a level density can be approximated by the back shifted Fermi gas (BSFG) and Constant Temperature CT functions [77, 78, 79]. Fitting each model to available experimental and theoretical data enables their parametrisation (as shown in Figure 5.1).

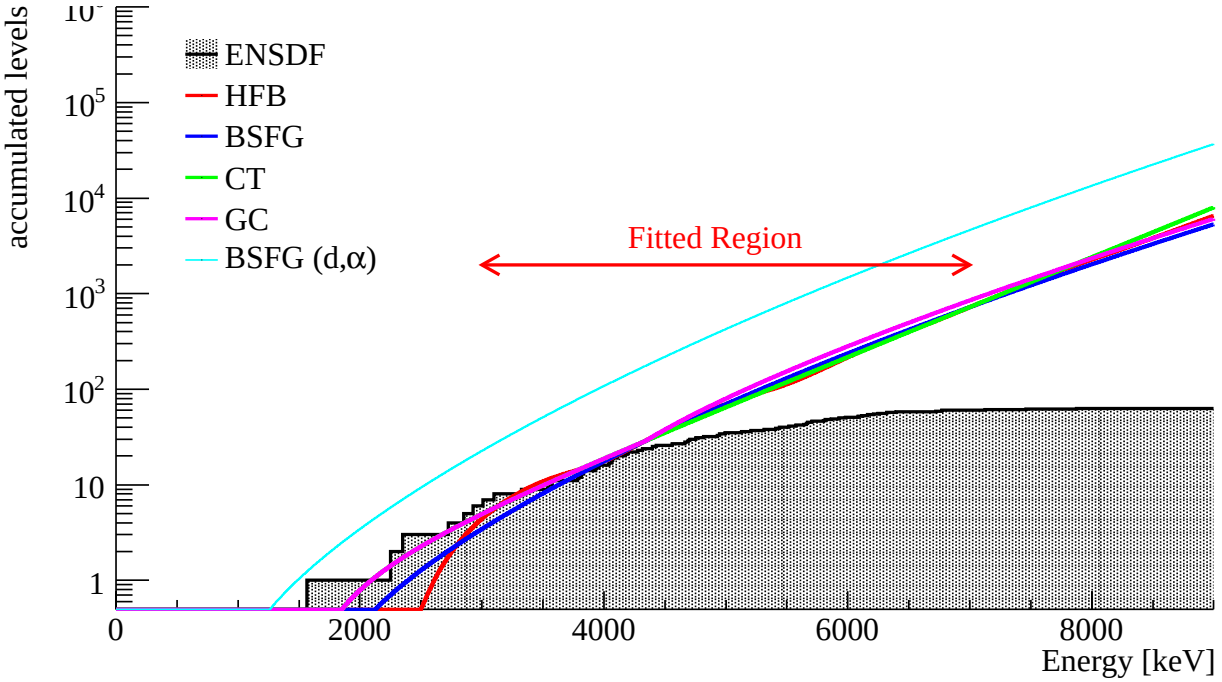

Figure 5.1: Modelled excitation level density of ^{86}Br of experimental data taken from [73, 25] theoretical predictions from the Hartree-Fock-Bogoliubov HFB model. Fitted to this level excitation function are two different Back Shifted Fermi Gas (BSFG) models , the Constant Temperature (CT) model and a Gilbert and Cameron (GC) statistical models. (see Section 2.2.5 for details)

Data from ENSDF database and the RIPL3 library contain details on the number of excitation levels per energy and also information on whether these levels are no longer confined to the current complete level scheme [25, 73]. These additional levels (i.e. those outside the known level scheme) are used for reference only. The low energy level density can be shown by plotting this experimental data for the selected isotope (see Figure 5.1). Note that, due to the presence of possible missing or low detection efficiency levels, the higher energy region is missing.

To counteract effects from levels not included in the level scheme, a prediction of accumulative number of levels for given excitation energy can be obtained from the HFB model using data tables, the atomic number, mass number and correction factors (found in RIPL3) for the desired nuclei [75, 74]. This model can then be optimised to a specific isotope by fine tuning the correction factors so that this model fits the highest accumulative level number and energy of the RIPL data, adjusting for shell effects.

The BSFG model can now be fitted to this experimental and theoretical data resulting in the parametrisation of the ground state position (Δ), level density parameter (a) and taking the effective moment of inertia as 0.5 for the Egidy et al. model [77, 78]. The Constant Temperature (CT) model can then be fitted, parametrising the nuclear temperature, T and back-shift, E_0 [78]. Using these parameters it is possible compare the outputted predictions of the Egidy et al. [78] BSFG and CT models, the Dilg et al. [77] BSFG model, and a model created by Gilbert and Cameron [79] from a combination of the CT and BSFG model shown in Figure 5.1.

A second method of obtaining parameters for the BSFG is possible using a method proposed by Egidy et al. [112] using the deuteron-alpha reaction energy ($Q(d,\alpha) = [M(A,Z) - M(A-2,Z-1) - M(^2H) - M(^4He)]c^2$) of the nuclei of interest and its neighbouring isospin analogue states. An example of these level density models are shown in Figure 5.1 for ^{86}Kr and more information on this nucleus is included in Chapter 6.

The poor resolution of the BaF_2 (in comparison to HPGe) means that a response at the 1 keV resolution level is not necessary and a response based on a 40 keV binning of levels is sufficient to contain all the relevant decay information. Combining the level density models with a continuum of 40 keV bins means that the probability of a β decay feeding an individual bin together with the possible transitions between bins and the base level scheme can be determined. The uses of a binned response has been shown by Duke el al. [83] to remove the complexity of densely spaced levels, enabling them to be simplified to an average probability of decay per bin, similar to the β strength function.

Gamma Strength

A β decay to an excited state in the daughter nucleus will de-excite mainly via γ rays or internal conversion. These γ-ray transitions are most probable to decay via E1, M1 or E2 transitions due to their larger decay strengths in comparison to higher multipolarity transitions. Work by Kopecky and Uhl [113] have characterised the average total γ-ray radiation width $\langle\Gamma_\gamma(E,J,\pi)\rangle$ for a state with initial excitation energy E_i, spin J_i, and parity π_i transitioning via a E_γ energy γ ray to a final state of spin J_f and parity π_f by

$$\langle\Gamma_\gamma(E_i,J_i,\pi_i)\rangle = \frac{1}{2\pi\rho(E_i,J_i,\pi_i)}\sum_{XL}\sum_{J_f\pi_f}\int_0^E T_{XL}(E_\gamma)\rho(E_f,J_f,\pi_f)dE_\gamma \tag{5.3}$$

where ρ is the level density as before, but with a dependence on parity (π). $T_{XL}(E_\gamma)$ is the γ-ray transmission coefficient, E_f is the final state excitation energy ($E_i - E_\gamma$) and XL state the transition type, electric or magnetic (X) and multipolarity (L). The effects of the parity dependence on Γ_γ showed 10% less in the work by Kopecky and Uhl [113], and therefore in this work an even parity distribution will be used. The γ-ray transmission coefficient is directly related to the strength function ($f_{XL}(E_\gamma)$) and thus key aspect differing the transmission widths, taking $T_{XL}(E_\gamma)$ as:

$$T_{XL}(E_\gamma) = 2\pi E_\gamma^{(2L+1)} f_{XL}(E_\gamma) \tag{5.4}$$

In previous work by Jordan et al. [76] and Estevez et al. [114] it has been shown that taking a Lorentzian shape for E2 and M1 transitions and a generalised Lorentzian shape for the E1 transition strengths is a good approximation. With these transition strengths taking the forms [113],

$$f_{E1} = 8.68\times10^{-8}\times\left[\frac{E_\gamma\Gamma(E_\gamma)}{(E_\gamma^2-E^2)^2+E_\gamma^2\Gamma(E_\gamma)^2}+\frac{0.7\Gamma_0 4\pi^2T^2}{E^5}\right]\sigma\Gamma_0, \tag{5.5}$$

$$f_{M1} = 8.68\times10^{-8}\times\left[\frac{\sigma E_\gamma\Gamma_0^2}{(E_\gamma^2-E^2)^2+E_\gamma^2\Gamma_0^2}\right], \tag{5.6}$$

$$f_{E2} = 5.22\times10^{-8}\times\left[\frac{\sigma E_\gamma^{-1}\Gamma_0^2}{(E_\gamma^2-E^2)^2+E_\gamma^2\Gamma_0^2}\right], \tag{5.7}$$

where

$$\Gamma(E_\gamma) = \Gamma_0\frac{E_\gamma^2+4\pi^2T^2}{E^2}, \quad \text{And} \quad T = \sqrt{\frac{S_n-E_\gamma}{a}} \tag{5.8}$$

Here E_γ [MeV] is the γ ray energy, S_n [MeV] is the neutron separation energy and a [1/MeV] is the level density parameter. The giant resonance parameters E [MeV], Γ_0 [MeV] and σ [mb] are taken from experimental data. For this work, the parameters were taken from references [73, 115, 116]. Specific E1 parameters have been taken from reference [117], M1 parameters from reference [113] and the E2 parameters from references [118, 119].

The addition of the γ-ray width function to the level density models mean that it is possible to extrapolate the probability of transitioning from each level in the continuum down to lower levels, resulting in the building of the branching matrix (shown in Figure 5.2). The binning of this continuum means each bin feeds all lower energy bins with a finite probability, resulting in a quantitative measure, for use in the analysis as a branching ratio matrix.

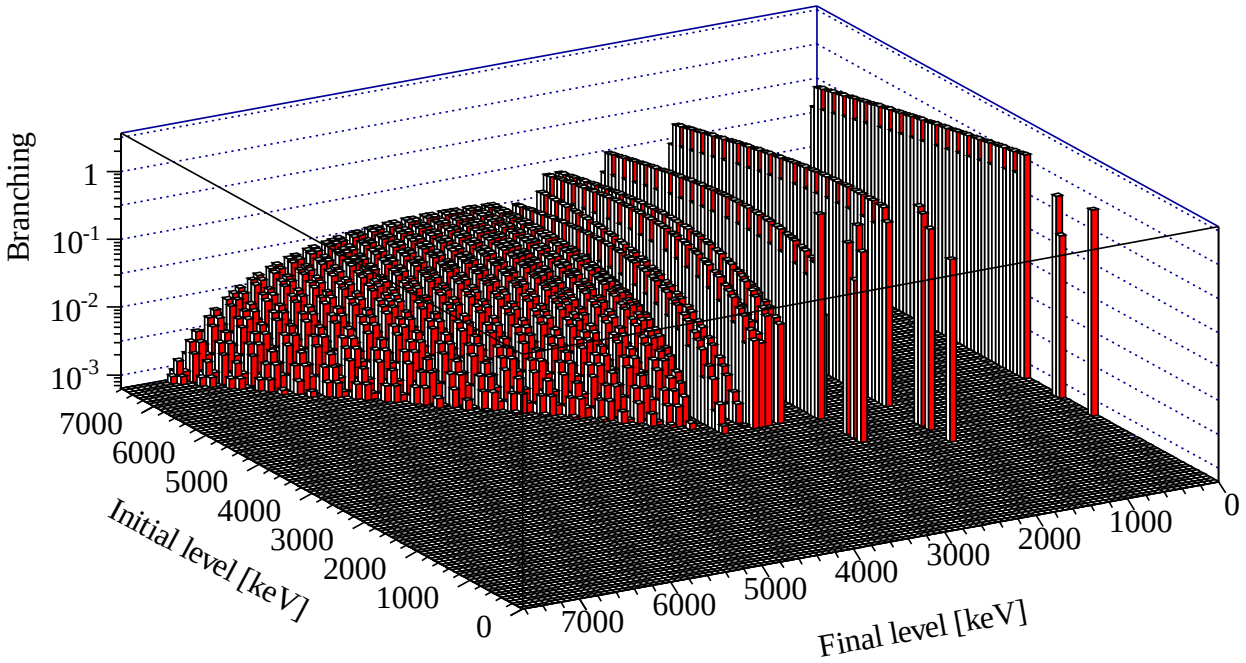

Figure 5.2: Example of the branching ratio matrix created for the β^- decay of ^{86}Br, displaying the feeding ratio from each initial level to each of its final levels. This figure shows the level continuum starting above 3560 keV.

The Response

The γ-ray response between each level can be MC simulated using mono-energetic photons (Figure 5.3a). The 40 keV binning of the continuum results in all the γ-ray responses being multiples of 40 keV, and for the initial analysis the base level scheme can be approximated into the closest 40 keV bin, whereas a more discrete analysis can be created using the precise energy of the transition. The efficiency of the detector to γ rays is included by utilising the 0^{th} energy bin (number

of non-interactions) of the simulated data. These γ-ray responses together with their branching ratios enable the solution to Equation 5.2 to be obtained. This response R_j, is the response from level j, or more accurately the response to the de-excitation of level j.

To generate the response to each β decay event this de-excitation response needs to be combined with the TAS detectors response to the related β particle. As described in Chapter 4 an allowed shaped β energy distribution was used to to determine the initial energy of each β particle (Figure 5.3b). This approximation of the allowed shaped is used for simplicity, but the response in the TAS for different shape β energy distributions should be negligible due to the low ($< 20\%$) efficiency of the TAS (**Software Sum**) to β particles (as seen in Figure 4.7).

The response matrix generated thus far is for the *singles* data. In order to generate the response to the *beta-gated* data, the response of the silicon detector needs to be included. The data from the silicon detector is only used for the detection of β particles and as such the only response required is if the energy deposited in the detector was above the experimental (105 keV) threshold.

The utilisation of the non-interaction 0^{th} energy column data enables the β response to be correctly normalised in the beta gated data response matrix .

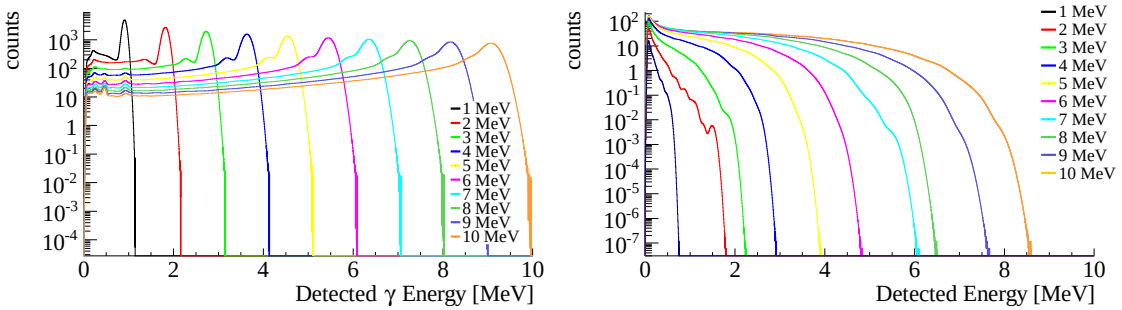

(a) TAS response to mono-energetic γ rays

(b) TAS response to β particles

Figure 5.3: Examples of experimentally broadened TAS Monte Carlo responses to mono-energetic γ rays and single level feeding β-particles (assuming an allowed β energy spectrum), as used in the response matrix.

5.3 The Solution

Work by Taín and Cano-Ott [111] has shown that is it possible to solve the inverse problem via three different approaches: (i) the linear regularisation method; (ii) maximum entropy; and using (iii) expectation-maximisation algorithms. This work stated that the expectation-maximisation algorithm gives the best result and work by Jordan et al. [76] concurs with this result. The expectation-maximisation algorithm "*is a general method for maximum likelihood estimation of*

parameters from incomplete data. The method is in essence iterative and receives the name from the two steps required for its application: (1) compute the conditional expectation of the log-likelihood, (2) perform the maximisation of the expectation." [111]. The algorithm originally taken from [120] is utilised in a Bayesian algorithm in the form of:

$$f_j^{(s+1)} = \frac{1}{\sum_{i=1}^{n} R_{ij}} \sum_{i=1}^{n} \frac{R_{ij} f_j^{(s)} d_i}{\sum_{k=1}^{m} R_{ik} f_k^{(s)}}, \quad j = 1,...,m \tag{5.9}$$

where $f_j^{(s)}$ is the feeding at this iteration and $f_j^{(s+1)}$ is the next iterations feeding response. From the initial parent's spin and parity, an initial feeding distribution can be created as with the γ-ray transitions. Using this as a starting point an iterative process using Equation 5.9 can be used to obtain the β feeding distribution. Reconstructing the detector's response using the response matrix and the generated feeding distribution is then possible, enabling a visual check of this feeding. For a measurement of fit, the χ^2 of this generated response to the original data was obtained using the formalism,

$$\chi^2 = \sum_i \frac{(d_i - Re_i)^2}{{\sigma_{(exp)i}}^2} \tag{5.10}$$

where d_i is the recorded experimental data with experimental error $\sigma_{(exp)i}$ and Re_i the reconstructed response in channel i. The initial analysis of the data can now be analysed using a *binned* analysis with each level placed within a 40 keV bin, enabling only multiples of 40 keV γ-ray transitions. After this initial check is it possible to simulate the precise energy of any transition in the base level scheme enabling there discrete energies to be combined in the *discrete* analysis. This discrete analysis should remove any anomalies in the χ^2 measurement due to poor fitting peaks (i.e. at the wrong energies) in the lower energy section of the response. The analysis up to this point allows feeding to any level. With a finite probability, it is possible to adjust the initial feeding to exclude feeding to specific bins / levels for the base level scheme. The known spin and parity of levels in the base level scheme reveals the type of transitions possible to each state. By allowing only defined direct feeding to specific states it is possible to restrict feeding to allowed β decays or allowed and first forbidden β decays, resulting in a more realistic result.

To avoid statistical oscillations due to the subtraction of different experimental spectra (e.g. background subtraction) the response is built on top of the contamination of each data set enabling a comparison to the un-cleaned calibrated data. A visual comparison can then be made between the clean data and the response by subtracting the relevant contaminants from both spectra.

Recorded Branching Ratio

The ENSDF recorded level scheme contains the ratio of γ-ray transitions relative to each other. It is possible to optimise the final branching ratio matrix so that the final ratio of the γ-ray transition is similar to the recorded ratio. This optimisation can be obtained by renormalising γ-ray feeding from the created continuum of levels in the daughter nucleus. This approach, if possible, should give a more realistic β feeding response due to the inclusion of more previously recorded information.

5.3.1 Strength function

Once the β feeding distribution has been deduced Equation 2.2.3 can be used to determine the β strength function for this decay, enabling a comparison with the current recorded data to be assessed.

5.3.2 Mean energies

The mean average energy from the total decay can be obtain from the unfolded feeding distribution. The average mean γ-ray energy $\overline{E_\gamma}$ is a result of the released excitation energy (E_i) of fed levels in the daughter, thus:

$$\overline{E_\gamma} = \sum_i I_\beta(E_i)E_i \tag{5.11}$$

where $I_\beta(E_i)$ is percentage of β feeding to excitation energy E_i. The distribution of possible energies for each beta decay transitions results in the mean average β-particle being a sum of the feeding percentage to each level multiplied by that transition's mean β-particle energy $\langle E_i \rangle$ or simply [76]:

$$\overline{E_\beta} = \sum_i I_\beta(E_i)\langle E_i \rangle \tag{5.12}$$

where the transition's mean β-particle energy can determined from the average energy of the β continuum for that transition (E_i) $f_\beta(Q_\beta - E_i)$ normalised by the integrated Fermi function $f(Q_\beta - E_i)$. Taking [121]

$$f_\beta(Q_\beta - E_i) = \int_1^{x+1} mc^2(\epsilon - 1)\epsilon\sqrt{\epsilon^2 - 1}(x + 1 - \epsilon)^2 F(Z, \epsilon)d\epsilon \tag{5.13}$$

and

$$f(Q_\beta - E_i) = \int_1^{x+1} \epsilon\sqrt{\epsilon^2 - 1}(x + 1 - \epsilon)^2 F(Z, \epsilon)d\epsilon \tag{5.14}$$

with $x = \frac{Q_\beta - E_i}{m_e c^2}$, $\epsilon = (\frac{E_\beta}{m_e c^2} + 1)$, E_β as the kinetic energy of the β particle and F as the Fermi function as before.

6 Analysis and Derived β-Feeding Strength for ^{86}Br, ^{91}Rb and ^{94}Sr

6.1 Preparation of ^{86}Br

6.1.1 The Measurement of ^{86}Br

The β^-decay of ^{86}Br transitions to the stable ^{86}Kr, therefore daughter contamination is not a problem for this isotope. A total of nineteen runs of ^{86}Br were collected during the experiment, over two collections of approximately 11 hours and 7 hours. The measurement time was planned to obtain good statistics, but due to a problem with the saving of the data (identified after the experiment), reduced statistics were collected. Some of the recorded measurements were highly contaminated or contained errors in their collections and thus were excluded. Preliminary tests and calibrations of the remaining runs enabled homologous runs to be identified and combined (see Table 6.1 statistics). The homologous calibrated *β-gated* TAS and silicon detector spectra are shown in Figure 6.1.

The preliminary aggregate of the ^{86}Br decay *β-gated* spectra shows five clear peaked regions. The TAS collects the full energy cascades, thus these peaks should be representative of β-decay fed levels in the daughter or extremely prominent γ ray transition where there is a possibility for the non-detection of other γ rays in the cascade. Using the previously recorded level scheme (from ENSDF [29] and Fotiades et al. [32]) for reference, the peak labelled *A* is identifiable as the first excited level at 1564 keV. Peak *B* which is broadened from possible multiple peaks is approximately

Data type	Recorded events
Hardware Sum	5.52×10^7
Silicon detector	8.05×10^7
Software Sum	5.22×10^7
(Silicon gated) **Software Sum**	8.01×10^4
E-Crystal	5.22×10^7
(Silicon gated) **E-Crystal**	1.90×10^5

Table 6.1: Overview of the recorded TAS ^{86}Br measurement statistics.

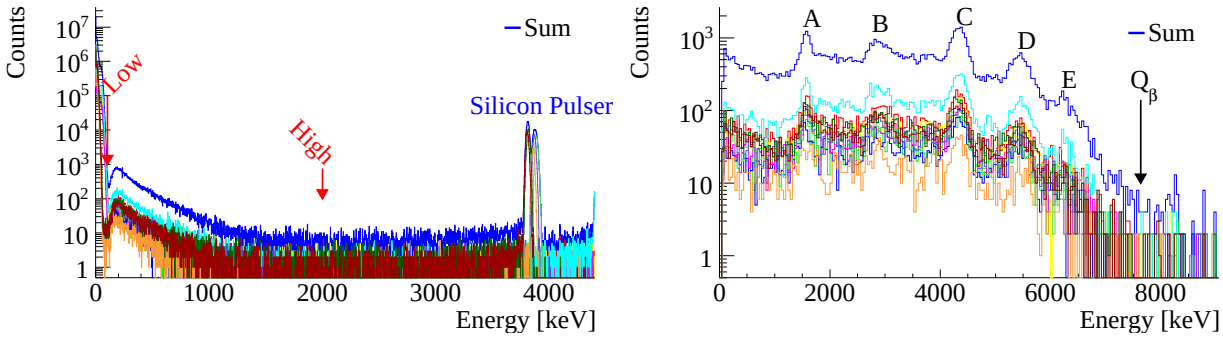

(a) Silicon detector spectra.

(b) TAS *β-gated* **Software Sum** spectra.

Figure 6.1: *a*) Calibrated silicon detector spectra for the ^{86}Br decay runs and the resultant Sum (blue), with the identification of pulser region and the low and high gate thresholds. *b*) Silicon (β particle) gated TAS spectra for the ^{86}Br decay runs and the resultant Sum (blue) and identification of peaked regions of interest.

at 2900 keV encompassing the levels at 2724,2850,2917,2629 and 3098 keV. The peak labelled *C* is at approximately 4300 keV where there is a collection of levels but this is possibly direct feeding to the discrete 4316 keV level, if the spin parity of 3^- is correct. The approximate position of *E* is 6200 keV but due to the lower statistics for the region and the possible uncertainty in the level scheme it is not possible to determine its origins.

6.1.2 The ^{86}Br Contaminant Subtraction

An initial subtraction of the *Beam-On* background was performed on the each of the singles measurements; the sum of each subtraction is shown in Figure 6.2a. These subtractions show similar structure to the *β-gated* spectra as expected. A normalisation of 25 % was applied to the *singles* data in Figure 6.2b, showing good agreement with the normalisation of the *β-gated* spectra. This result is conclusive with the ^{24}Na observation of 25 % for the silicon detector efficiency to β particles (a decrease of 4 % from the simulated efficiency). Due to the lower than expected counting statistics in the *singles* data, the subtractions of background and pile-up results in large statistical oscillations that might not be present with increased counts. These oscillations result in the singles being inadequate for the analysis and therefore only the *β-gated* spectra was used for the ^{86}Br analysis.

Pile-up

Pile-up data was created, normalised and subtracted from the *β-gated* and the *singles* data, as explained above in Chapter 3. A final check was performed for the *singles* data by subtracting pile-up from each measurements (including background measurements) before the background was subtracted, but the resultant spectrum did not improve the oscillation in the final result. Table 6.2

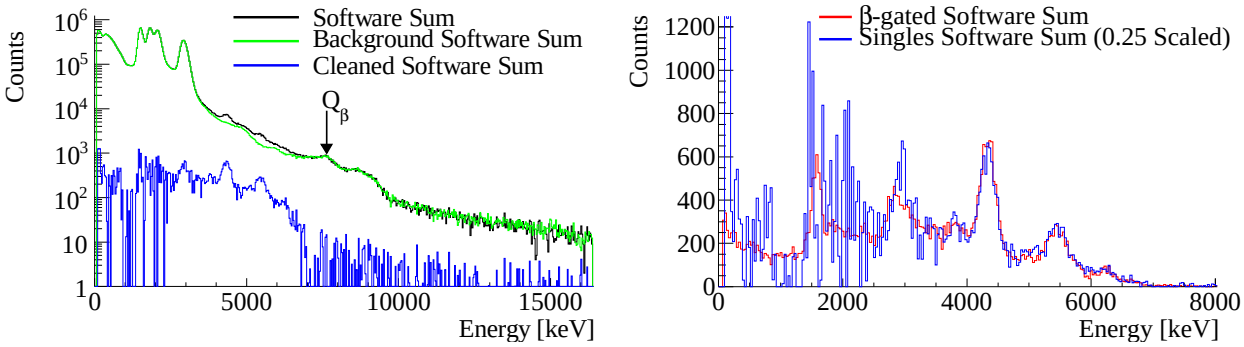

(a) *Singles* subtraction. **(b)** *Singles* & *β-gated* comparison.

Figure 6.2: *a*) Total ^{86}Br decay TAS *singles* **Software Sum** spectrum showing the subtraction of the *Beam-On* TAS background and the resultant spectrum, indicating the Q_β position of the ^{86}Br decay and small statistical oscillations above this. *b*) Comparison of the ^{86}Br decay TAS background subtracted *singles* **Software Sum** data (scaled by 0.25) and the *β-gated* **Software Sum** spectra, showing the improvement in quality of the *β-gated* spectra due to the poor counting statistics available for the singles subtraction. A scaling of *singles* data by 0.25 to estimate the efficiency of the silicon detector for β particles has been applied.

shows the relevant acquisition rates for the *β-gated* data and number of **Software Sum** coincidence with β-particle event for each of the ^{86}Br experimental runs included.

The *β-gated* pile-up was normalised using Equation 3.1 and was checked to make sure an optimal subtraction was performed. A preliminary analysis of this cleaned spectra highlighted that there may be contamination within the recorded data. Since ^{86}Br decays to a stable nucleus the contamination can not be due to any daughter products resulting in either an impure isotope production, background contamination, or some external source of contaminations. Second checks were made of the background runs before and after the measurements for impurities. The second set of measurements had clean (very few counts) *β-gated* background before and after the measurements, but the first set of measurements showed problems with the collection of *β-gated* background measurements before and after the runs, because the silicon detector was not connected. The unavailability of the *β-gated* background, means that the level of any potential contamination is not known. A comparison of the sums of the first and second set of measurements was made (shown in Figure 6.3a) to enable any differences to be ascertained.

The low statistics of each sum of measurements means it is difficult to determine if the first measurement contains any background contamination. It is clear from these spectra (Figure 6.3a)that they are not homologous, even with differing statistics. A second comparison of the collected silicon detector spectra is shown in Figure 6.3b. The silicon detector spectra shows an increased noise within the first measurement that is shifted from the normal electronic noise at the start of the

	Run	number of β-particle event	Rate [Hz]
First	Br86_2320	8.4×10^6	6103
	Br86_0034	4.1×10^6	6158
	Br86_0134	3.9×10^6	6282
	Br86_0239	8.9×10^6	6232
	Br86_0424	3.5×10^6	6246
	Br86_0541	11.4×10^6	6227
Second	Br86_0031	7.4×10^6	6229
	Br86_0132	8.1×10^6	6233
	Br86_0236	2.7×10^6	6150
	Br86_0435	12.4×10^6	6221
	Br86_0536	9.8×10^6	6165
	Background	NA	6195

Table 6.2: Experimental rates (in counts per second) for the^{86}Br measurements and number of β-particle events and the sum *Single Beam-On* background measurement for reference.

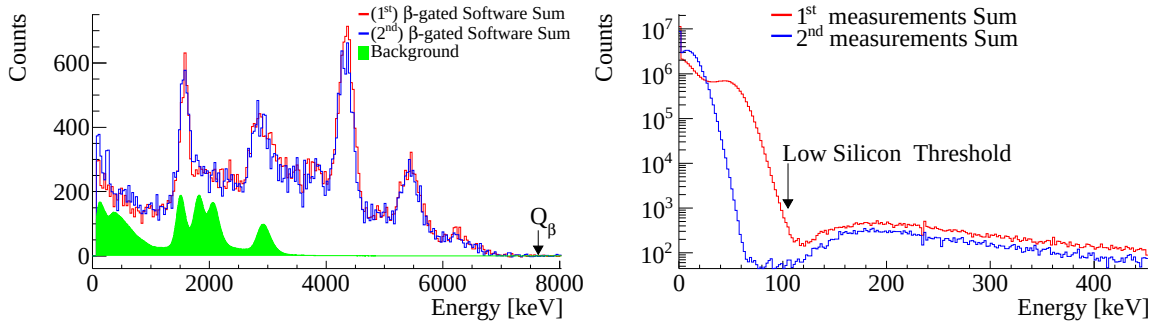

(a) TAS *β-gated* measurements.

(b) Silicon detector measurements.

Figure 6.3: Difference found between the sum of first and second measurements of the ^{86}Br decay. *a)* The TAS *β-gated* measurements (scaled to each other for comparison) and including the *Beam-On* background measurement (scaled) as reference and possible contaminate to the first measurement. *b)*The silicon detector measurements, where the first set of measurements have increased noise.

spectra. An adjustment could be made to the threshold of the silicon detector but due to the tail of this noise, this increase threshold would be hard to determine and would exclude large amounts of data. This noise is thought to be electronic noise (because of the shape) and not due to some other contamination events. Since this noise is electronic in the silicon detector the contamination in the *β-gated* spectra will be any background counts in coincidence with this noise. To remove this contamination the *Beam-on* background (with pile-up removed) was subtracted from the pile-up free *β-gated* spectra using a visual method of subtraction, as there is no information on the amount of background included with in the spectra. A preliminary analysis of the ^{86}Br decay was used as a guide for this visual subtraction of the background. After the final analysis of this isotope a range of subtraction values tested with the same parameters, enabling an optimum value of subtraction to be found, using the analysis χ^2 value as a guide.

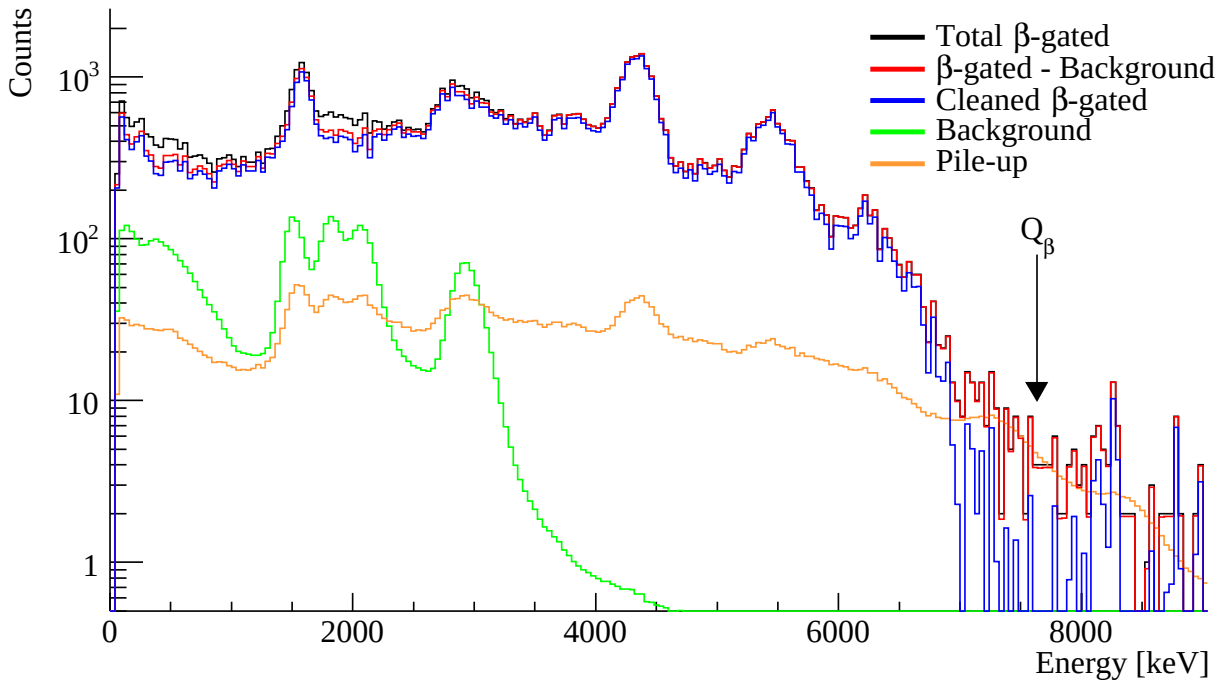

Figure 6.4: Final ^{86}Br TAS *Beta-gated* **Software Sum** Subtraction of pile-up and contaminating background showing the resulting spectra.

This final clean *β-gated* **Software Sum** spectrum of ^{86}Br has a very similar structure to the raw calibrated *β-gated* **Software Sum** spectrum, as the level of subtraction is very small. One noticeable difference is the shape of the spectra at high energy, because of the comparable level of pile-up to raw data. The subtraction still shows some counts above the Q_β value possibly forming a peak shape. This peak occurs at a similar point to the high energy limit of the individual crystal PMT's. Events with energy deposited above this limit may have been collected in the highest energy bin erroneously producing an excess of counts. These counts above the Q_β value could also be artefacts of the subtraction but without more statistics it is not possible to determine their source.

6.1.3 The Nuclear Level Density of ^{86}Kr

Plotting number of experimentally recorded cumulative levels for ^{86}Kr against energy from the ENSDF database gives an approximation of the shape of the level density evolution. The RIPL3 database shows that there are 64 recorded levels with 23 in the completed level scheme. Using this data and an optimised HFB model it was possible plot the level density for ^{86}Kr (^{86}Br daughter), as shown in Figure 6.5. As explained in Chapter 5 the four statistical models (BSFG, CT and CG [77, 78, 122, 79]) will be fitted to this mix of experimental and theoretical data to obtain a fit, resulting in the parametrisation of the ground state position Δ, the level density a (for BSFG), nuclear temperature T, the back-shift E_0 (for CT) and the crossing point E_x of the BSFG and CT

model for the model by Gilbert and Cameron (GC). The result of these fits are shown in Figure 6.5 and the parameters are summarised in Table 6.3.

In contrast to the fitted models the BSFG model calculated by the deuteron-alpha reaction mass method shows a poor fit to the data, leading to it being excluded from further tests and the final analysis. Between the fitted models the BSFG model gives the closest fit to the experimental data at low excitation but for the large excitation energy it is not clear which gives the best fit. Due to the small difference between results, each of the fitted data models will be used for the analysis.

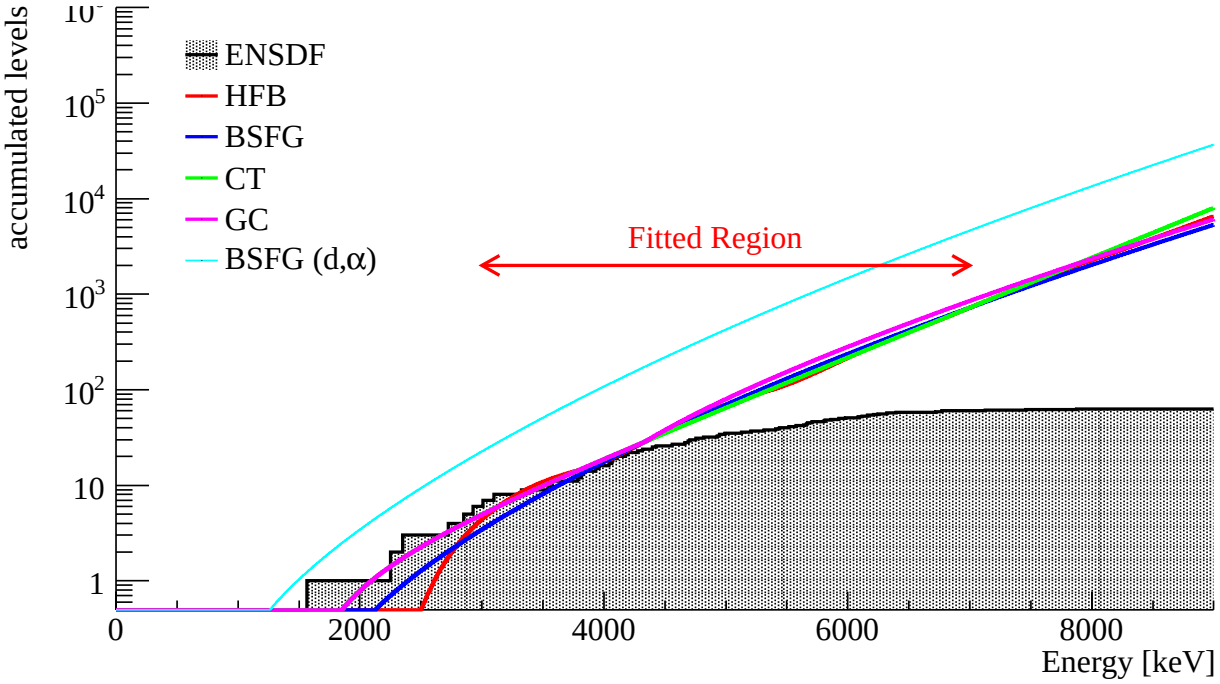

Figure 6.5: Excitation level density of ^{86}Kr showing the collated experimental data from the RIPL3 database [73], the theoretical HFB model and the fitted statistical models BSFG (Dilg et al. and Egidy et al.), CT and GC [77, 78, 79].

a	8.434	[1/MeV]
Δ	1.599	[MeV]
a (Mass)	9.807	[1/MeV]
Δ (Mass)	0.831	[MeV]

T	0.833	[MeV]
E0	1.518	[MeV]
Ex	4.342	[MeV]

Table 6.3: Level density parameters of ^{86}Kr from the fit to experimental and theoretical data.

6.1.4 The Level Scheme of ^{86}Kr & Level Threshold

The evaluated level scheme of ^{86}Kr in the ENSDF database contain many levels resulting in a large number of γ ray transitions, the lower section of the adopted gamma level scheme is shown in Figure 6.6. The low lying level structure of this even-even nucleus shows the expected 0^+ for the ground state. The first few levels are quadrupole vibration resulting in a first 2^+ state and then a

4^+ state, and a first octopole vibration in the low lying 3^-. The ratio of the energy to the 2^+ and then to the 4^+ is 1.5 and not 2 showing that although the neutrons fill a closed shell (N=50) there is still proton outside of a shell closure.

The latest ENSDF evaluation of ^{86}Kr was performed in 2001 [29]. Since this date a new measurement of the level scheme by ^{86}Kr$(n,n')^{86}$Kr has been preformed by Fotiades et al. [32] in 2013, providing a few new levels, and slightly revised excitation energies for some known levels. This difference in energy for some of the levels was far below the resolution of the TAS detector thus giving little or no effect of the final results of this work.

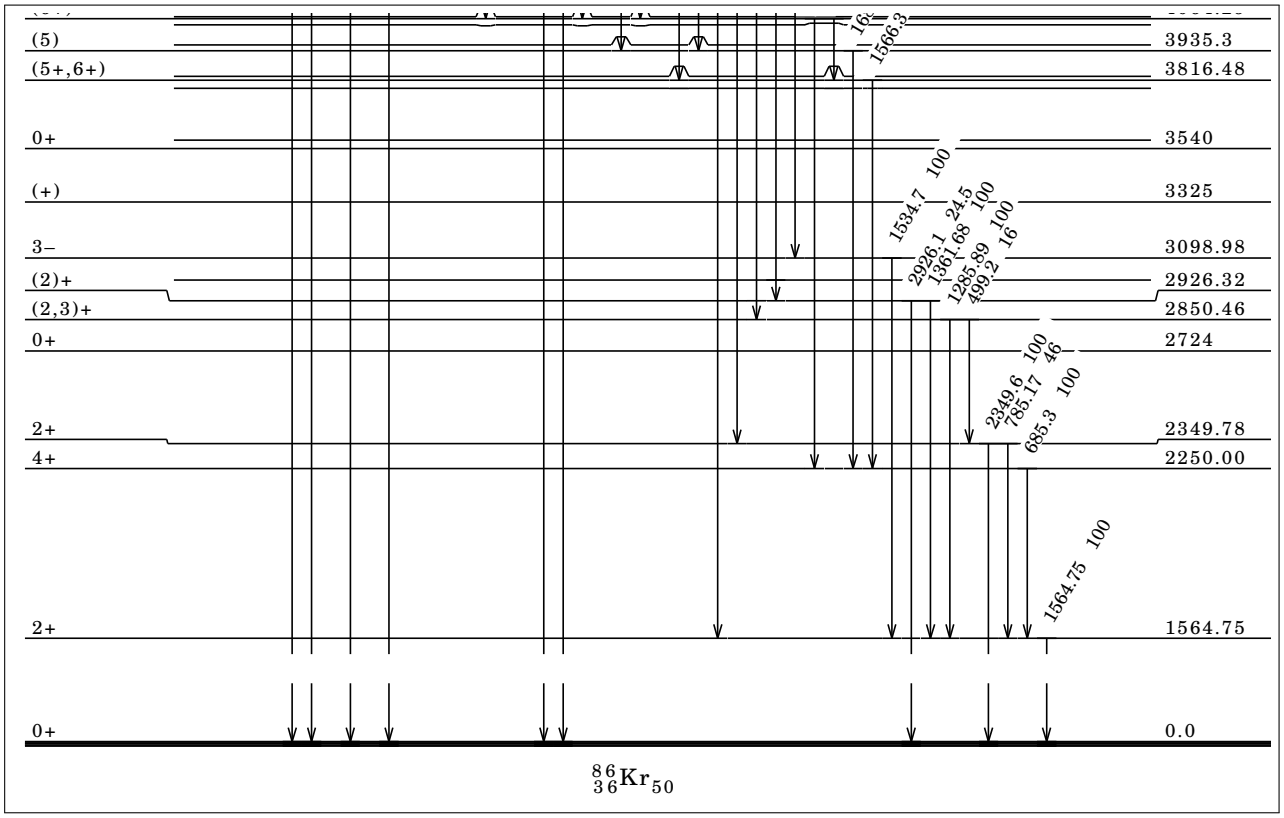

Figure 6.6: Lower section of the adopted gamma level scheme for ^{86}Kr, taken from ENSDF [29].

The excitation energy levels of ^{86}Kr are shown for the low energy region in Table 6.4, where data from ENSDF [29] and work by Fotiades et al. [32] are used to create the option available for the analysis. Data collected for the β decay of ^{86}Br in ENSDF [25] indicated that the 3328 keV level is possibly a spin/parity 4^+ state. Using this information with the γ ray transition multipolarities expected for a transition from this level gives tentative $J^\pi = 2^+$, 3^+ or 4^+ values as possible options to be used in the analysis. Fotiades et al. [32] also compares shell model calculations [123, 124] with the experimental data, resulting in inconclusive results but indicates that the 3010 keV level is most likely a spin/parity 1^+ state rather then the 2^+.

The reported ENSDF ground state (g.s.) of ^{86}Br has $J^{\pi}= 2^{-}$ from systematics with $^{82\text{-}84}$Br however, the more recent (2009) measurement by Porquet et al. [31] suggests a 1^{-} (from the possible low energy $\pi p\frac{3}{2}\nu d\frac{5}{2}$ state) . This change in ground state spin changes the allowed and forbidden transition possibilities. Allowed transitions from ^{86}Br would originally (2^{-} g.s.) feed the 1^{-},2^{-} and 3^{-} stated but the newly recorded 1^{-} ground state would result in allowed feeding the 0^{-},1^{-} and 2^{-}, changing the feeding to the 3099 keV level. When considering the first forbidden feeding the change from a 2^{-} to a 1^{-} ground state results in no first forbidden feeding to the 4^{+} levels, affecting feeding to the 2250 keV level and possibly the 2947 keV and 3328 keV levels (depending on chosen spin).

The test energy thresholds applied on the ^{86}Kr level scheme are shown in Table 6.4, where the first threshold was applied to give a level scheme with no degrees of freedom if recorded spins and parties are trustworthy. The different thresholds were also used giving a range of levels schemes to work with. The close proximity of the 2917 keV and 2926 keV may cause initial problems with the analysis when binning energies in 40 keV steps. Because of this, a threshold was not set in-between the level energies. The highest energy threshold was chosen due to its proximity to a large band gap in the level scheme and levels above this having no parity of spin assignments.

^{86}Kr	Adopted J^{π} for				Threshold
Level [keV]	ENSDF	Fotiades et al. [32]	Analysis	Final choice	cut
0.0 (g.s.)	0^{+}	0^{+}	0^{+}	0^{+}	
1565	2^{+}	2^{+}	2^{+}	2^{+}	
2250	4^{+}	4^{+}	4^{+}	4^{+}	
2350	2^{+}	2^{+}	2^{+}	2^{+}	0
2727	(not detected)	0^{+}	0^{+}	0^{+}	1
2850	$(2,3)^{+}$	$(2,3)^{+}$	2^{+} or 3^{+}	3^{+}	2
2917	(not detected)	$(3,4)^{+}$	3^{+} or 4^{+}	4^{+}	
2926	$(2)^{+}$	$(2)^{+}$	2^{+}	2^{+}	3
3010	(not detected)	$(1,2)^{+}$	1^{+} or 2^{+}	2^{+}	4
3099	3^{-}	3^{-}	3^{-}	3^{-}	5
3328	$(^{+})$	$(^{+})$	2^{+} or 3^{+} or 4^{+}	4^{+}	6
3542	0^{+}	0^{+}	0^{+}	0^{+}	7
3584	(not detected)	(empty)	Not Used		

Table 6.4: Previously recorded low energy excitation level schemes of ^{86}Kr showing recorded and possible spin and parity assignments.

6.2 The ^{86}Br Decay Results

The combination of a low energy level scheme, level density model and detector response matrix means that it is possible to solve the inverse problem using the expectation maximisation method explained in Chapter 5 to obtain the final β-feeding distribution. This β-feeding distribution can then be used with the response matrix to reconstruct the respective TAS spectrum that was used for the analysis. The generated responses can then be used as a test of the accuracy of the analysis against the experimental data visually and via the calculated χ^2 measurement.

6.2.1 The Binned Analysis of ^{86}Br

An initial analysis was performed using only the binned 40 keV responses for γ rays and β particles, where the included known γ ray and β transitions were rounded into energy bins. The resolution of the BaF_2 results in this initial analysis giving realistic results. This preliminary analysis permitted feeding to all levels (free feeding), with only reduced strengths to higher forbidden transitions. Each combination of different level scheme options (given spin and parity) and density models (from the BSFG, CT and GC) was tested using the χ^2 value and visual checks to the experimental data to give an idea of the best result. An example of this (free feeding) binned analysis is shown in Figure 6.7. This analysis used a level scheme cut off threshold of 3560 keV, the BSFG Dilg statistical level density model and the silicon detectors efficiency was set to 25%. The graph in Figure 6.7a shows the generated response for the evaluated feeding with the addition of the experimental contaminants (pile-up and background), in comparison to the unclean experiment data (including pile-up and background).

The free nature of this feeding enables non-physical amounts of feeding to some levels in the daughter (if the spins and parities are correct). Figure 6.7a also shows the result of a fixed feeding response, where in this analysis only allowed and first forbidden feeding transitions are permitted while higher order forbiddeness transitions are restricted. Both the free and fixed feeding in these results are obtained from a spin/parity 1^- ground state for ^{86}Br. The energy binning of the levels results in little difference between the fixed and free response, due it only being possible to permit or restrict feeding to a whole bin containing possibly more than one level. The analysis was also tested with only permitting allowed transitions, but this analysis was found not able to fit to the experimental data, showing that this decay can not occur via allowed transitions only.

The intensity of β feeding to each level in the daughter for both the fixed and free feeding analysis is shown in Figure 6.7b as a percentage of the total feeding. The recorded ENSDF database β-feeding

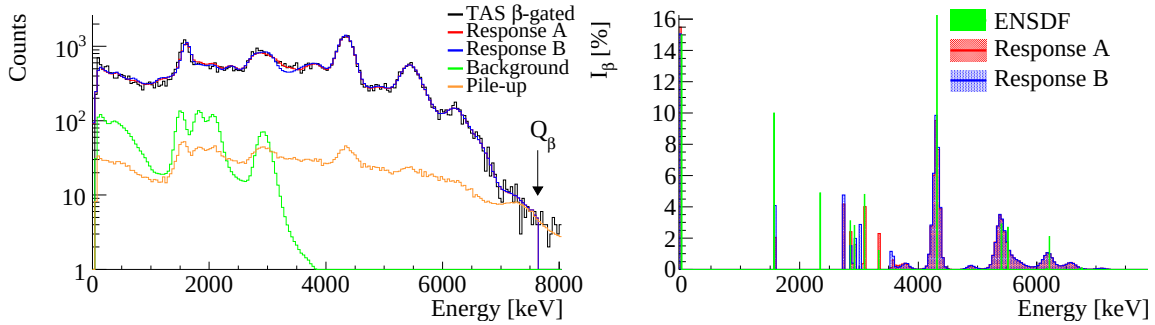

(a) TAS *β-gated* response (black) showing included contaminants (Pile-up and background) and simulated response to that data with free feeding (red) and fixed feeding (blue).

(b) Generated β feeding (%) from the analysis of the free feeding (red), fixed (blue) feeding and the ENSDF record β-feeding distribution (green).

Figure 6.7: Preliminary recreation of the TAS response and β-feeding distribution for the decay ^{86}Br. With response A set to free feeding and response B set to fixed feeding both using a base level scheme threshold of 3560 keV, the silicon detectors efficiency set to 25% and the level density model of the BSFG Dilg statistical model.

distribution data for this decay is also shown. The database data is in discrete bins as it is the feeding only to known levels, whereas the analysis result can feed any level in the continuum of levels. The recently reported levels by Fotiades et al. [32] results in extra level feed by the analysis below the continuum of levels. Both the free and fixed analysis and ENSDF data agree on an $\approx$ 15% feeding to the ground state. The highest energy feeding peak of $\approx$7100 keV in the analysis feeding may be an artefact due to a poor subtraction, but at this point it is not clear.

The produced χ^2 value for each of these analysis are compromised by poor fitting in the lower region of the response, this poor fitting is a result of only using a binned response. The comparison of the different level scheme thresholds also shows that when a lower energy threshold is used the increased freedom in the fitting enabling a better fit to the experimental data but results in a less realistic result due to the increased number of assumptions made.

6.2.2 The Discrete Analysis of ^{86}Br

The binned analysis can only go so far to recreate the spectra as explained in Chapter 5, the inclusion of the MC simulation of the discrete known γ ray transitions and the corresponding discrete β-particle transition into the response matrix enables a more precise analysis to be conducted. The newly created discrete energy response matrix can then be used as before to obtain the β feeding for the decay utilising all permutations of the available options for the analysis while permitted feeding via allowed and first forbidden transitions.

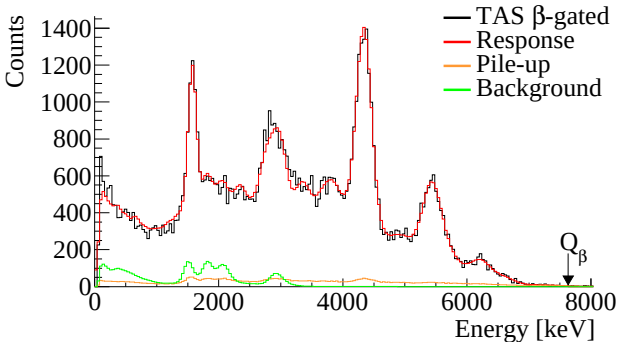

(a) TAS *β-gated* Response (black) showing included contaminants (Pile-up and background) and the discrete simulated response to the data with fixed feeding (red).

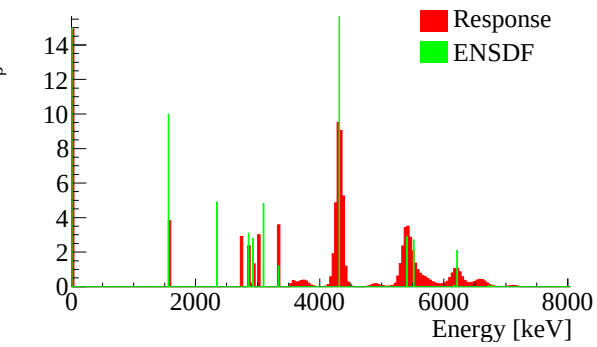

(b) Generated β feeding (%) from the analysis of the fixed (blue) feeding and the comparison to the ENSDF record β-feeding distribution (green).

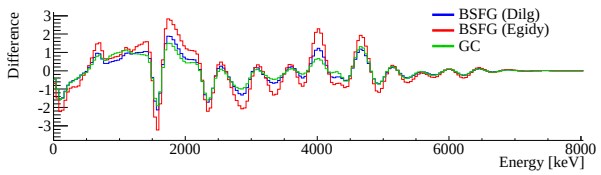

(c) The difference in the discrete simulated response from the CT model (above) for the BSFG's (Dilg & Egidy) and the GC model.

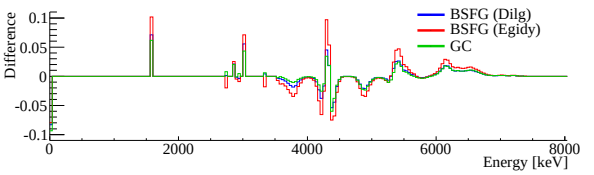

(d) The difference in the discrete β-feeding distribution from the CT model (above) for the BSFG's (Dilg & Egidy) and the GC model.

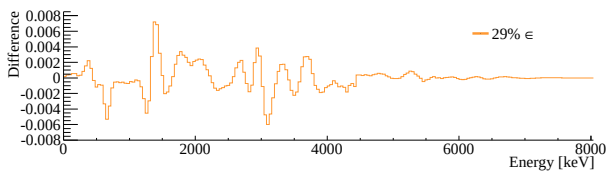

(e) The difference in the discrete simulated response for a silicon detector with efficiency of 29% rather than 25%.

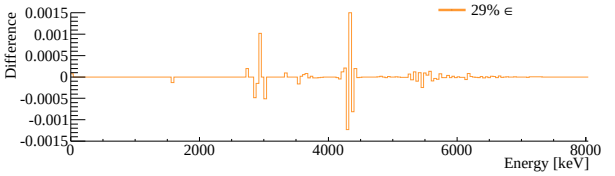

(f) The difference in discrete β-feeding distribution for a silicon detector with efficiency of 29% rather than 25%.

Figure 6.8: The response and β-feeding distribution for the discrete analysis (a,b), the difference of different statistical models (c,d) and silicon detector efficiencies (e,f).

An optimum combination of level scheme cut threshold and statistical model was determined. This best fitting generated response and feeding is shown in Figures 6.8a+(b) (see Appendix:A for the precise inputs). This discrete analysis provides a better fit to the lower energy section of the spectra but still shows some discrepancy with the fit to the peak at approximately 2800 keV.

The changing the statistical density model for this decay had little effect, possibly due to the short energy range that they are fitted over. The differences from this CT response and feeding to the other models is shown in Figures 6.8c+(d), where the difference between response and the feeding is small differing by a maximum of ±3 counts and ±0.1% .

The comparison of the subtracted data proposes a 25% efficiency for the silicon detector rather than the 29% produced from the MC simulation. In addition to the Monte Carlo results other measured isotopes from this experiment concur with this 29%. The analysis was repeated with

identical setting but changing the silicon detector efficiency to 29%. The difference of the results is shown in Figures 6.8e+(f) resulting in a negligible difference (±0.008 counts and ±0.0015%) to the end result.

The uncertainty in the recorded ground state of ^{86}Br between different ENSDF evaluations promoted the comparison of an analysis with the parent ground state J^{π} set to 1^- or 2^- separately. Figure 6.9 shows the effect of the change of the parent's ground state for permitted allowed and first-forbidden transitions. In this instance the contamination (pile-up and background) have been removed from the generated response and experimental data. As stated above the level permitted to feed from the different ground states are different resulting in the $J^{\pi} = 2^-$ ground state feeding the 2250 keV (4^+) level, affecting the quality of the fit. The ground state feeding for the 2^- parent state also increase to 18.8%, possible due to less favourable transitions in the lower levels. There are a few other differences between the spectra, but a parent ground state of 1^- gives better agreement to the data, supporting the new evaluation made in the ^{86}Br ENSDF excited levels data.

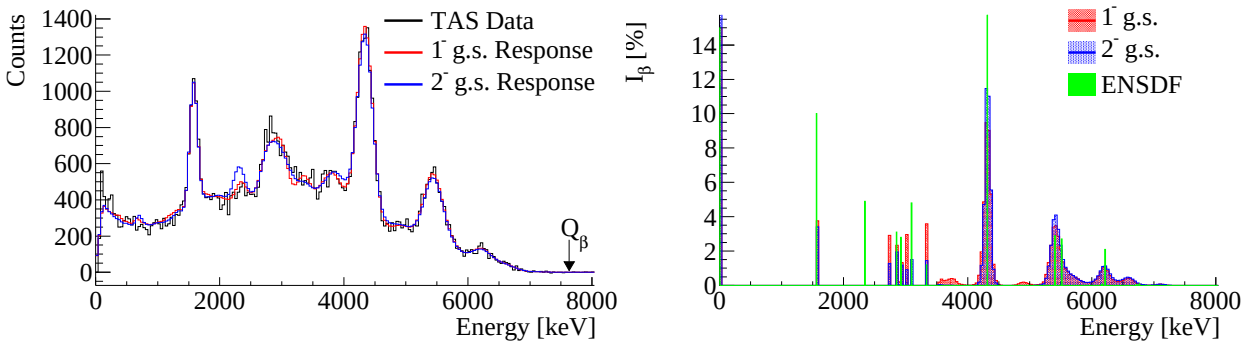

(a) TAS spectrum and response.

(b) β feeding distribution.

Figure 6.9: *a*) The cleaned β-*gated* response and the simulated response with the 2^- g.s. (blue) and 1^- g.s. (red). *b*) The β-feeding distribution for the analysis with 2^- g.s. (blue) and 1^- g.s. (red) and the recorded ENSDF data.

The Final Discrete Analysis of ^{86}Br

After testing the different permutations of possible level schemes, level threshold cuts and level density functions an optimum result was selected, with the best visual and χ^2 performance. A copy of the inputs used are summarised in Table 6.5, and a full breakdown for reference can be found in Appendix:A. The threshold of 3560 keV was chosen as the highest level possible to create a fit, while resolving a good reproduction of that collected data. The optimum Level scheme spins and parities, giving the best visual reproduction and χ^2 performance is shown in Table 6.4.

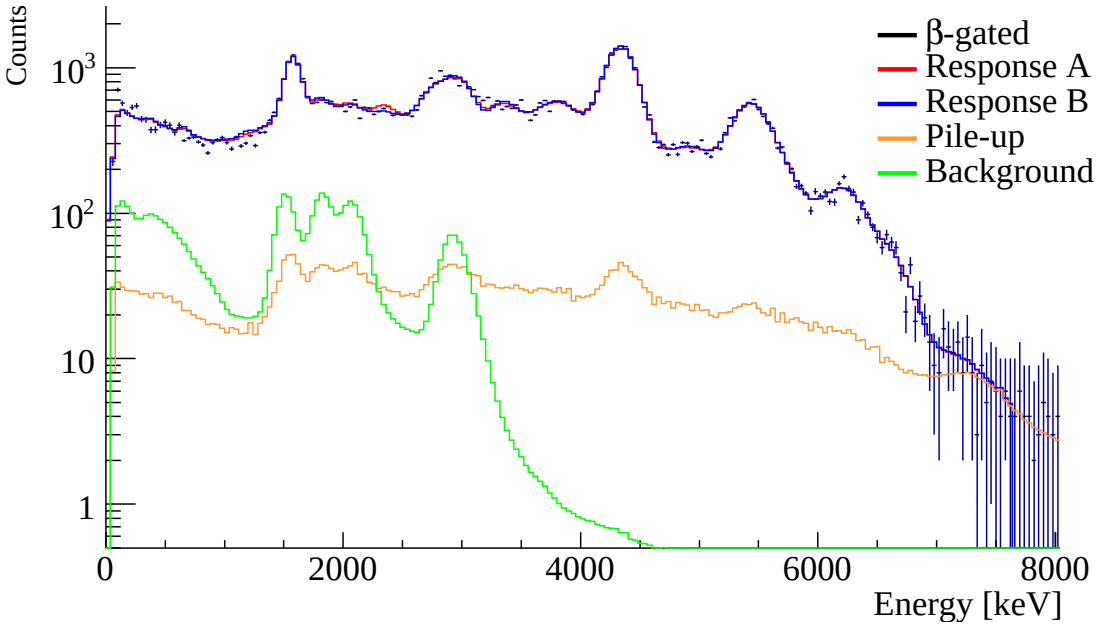

(a) Final Analysis generated responses (plus contaminants) in comparison to the raw *β-gated* spectrum, also showing relevant contaminants (background and pile-up).

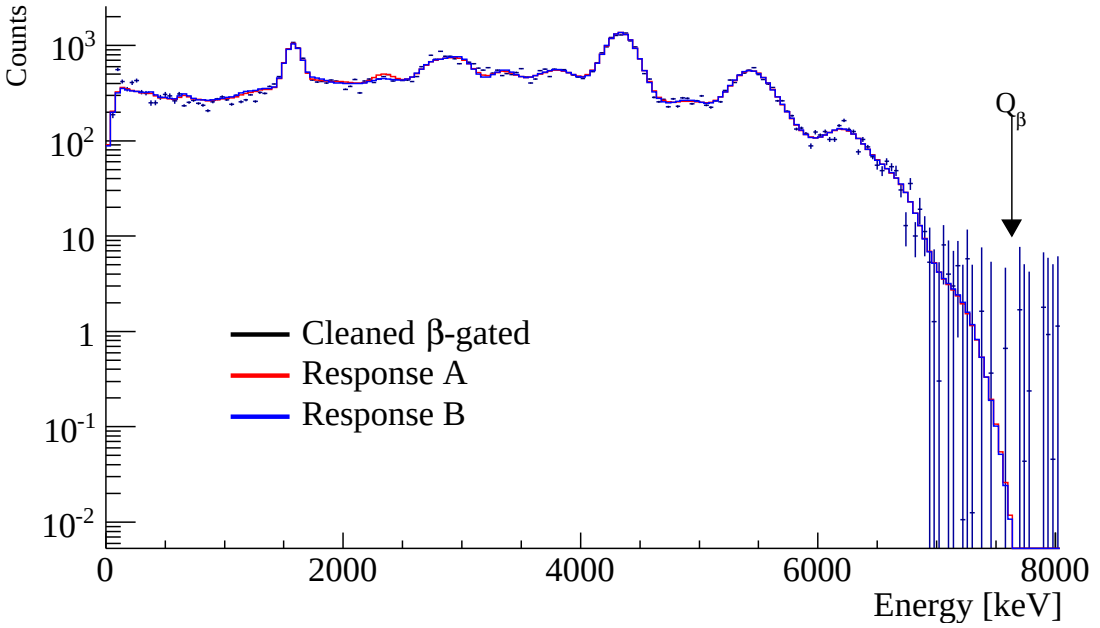

(b) Final analysis generated responses in comparison to the clean *β-gated* spectrum.

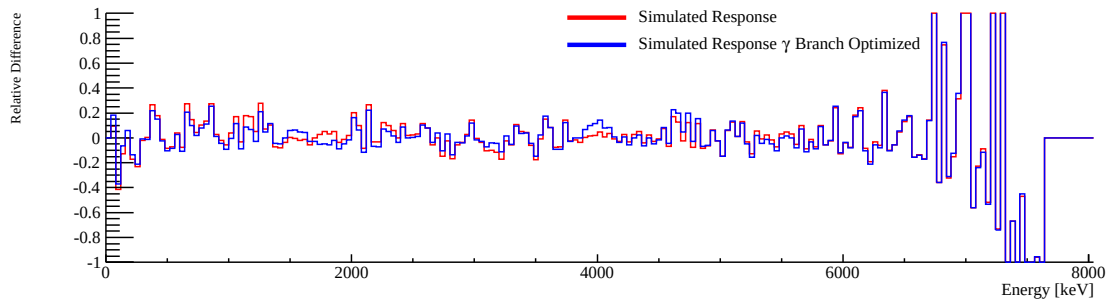

(c) Relative difference from the clean *β-gated* spectrum for each analysis.

Figure 6.10: Final comparison of the generated response for the decay of ^{86}Br against the collected TAS *β-gated* spectrum. With response (A) being the original result with no change to the γ ray branching and (B) being the optimised γ ray branching result.

Highest level	3542
start of continuum	3560
Parent g.s. J^π	1^-
Daughter g.s. J^π	0^+

Levels included	10
statistical model used	Constant Temperature
Feeding	Allowed and First Forbidden
	0^-, 1^-, 2^- and 0^+, 1^+, 2^+, 3^+

Table 6.5: Optimum inputs for the analysis of the β decay of ^{86}Br

Even though high resolution measurements can suffer from the *pandemonium effect*, the γ ray branching ratio can be correct because the experimental method applied. Using this information it is possible to compare the recorded γ ray branching to the generated results in the response matrix. Adjusting the intensity of the γ ray branching inside this response matrix is possible for the known level part (base level scheme) by adjusting the intensities of feeding these levels from each level in the continuum. Table 6.6 includes the branching ratios of the recorded ENSDF data, the original results and an optimised (γ branching ratio to ENSDF) result response. The proximity of the levels and the lack of reported intensities in Fotiades et al. [32] results in the intensity spread between levels. The branching of the highest included level (3542 keV) could not be reduced further due to limited control over the feeding of the levels above the continuum.

Levels	relative γ ray Intensity[%]					
[keV]	ENSDF	original		Optimised		
1564.75	37.08	43.96		37.11		
2250.05	8.16	2.16	14.72	2.23	8.23	
2349.95		12.56		6.00		
2726.75	4.96	4.87	10.64	2.94	5.33	
2850.35		5.77		2.39		
2917.05	7.30	2.17	6.55	2.45	7.25	
2926.32		4.38		4.80		
3010.25	6.33	5.81	6.40	5.60	6.20	
3099.45		0.59		0.60		
3328.25	1.2	5.15		3.60		
3541.65	N/A	0.69		0.92		

Table 6.6: The γ ray branching ratio of the low energy levels in ^{86}Kr for recorded ENSDF data. The original generated response and the optimised response. Both responses include levels not detected in the recorded ENSDF file thus an averaged over multiple level of similar energy was used for comparison.

The effect of this final modification on the reproduction of the experimental data (with statistical errors) is shown in Figure 6.10. This new response is very close to the original result possibly showing a slight deterioration on the reproduction of the data. The resulting difference from the recorded data for each of the responses is also shown, revealing the poor fitting of the higher energy section of the analysis, possibly due to the low statistics in this region.

The produced β feeding distributions for these analysis are shown in Figure 6.11 where Figure 6.11a has been rotated to clearly display the levels fed in the via the β decay. Comparing feeding distribution, in cumulative plots (Figure 6.11b) enables differences between the recorded ENSDF data and the generated feeding distribution in this analysis to be seen clearly. Between the responses, the adjustment of the γ ray transition branching has reduced some high level feeding and placed more at lower levels. The ground state feeding from the original analysis matches the ENSDF feeding of 15% whereas the modified result reduces this to 12.5%. At low energy in the discrete region analysis feeding to the first level is lower for both analyses and each do not feed the 4^+ (2250 keV) or the 2^+ (2350 keV) as with the ENSDF data, possibly hinting to *pandemonium* in these levels. The comparison also highlights that neither of the analyses feed to the 3099 keV level as in the recorded ENSDF data. A full list of feeding distribution to each channel can be found in Appendix:A for a comparison of each level.

As with the binned analysis because of the low counting statistics the higher energy (>6400 keV) feeding for both analyses may not be correct the but the current data infers β feeding to these levels, although this could be residual pile-up. The restriction of the branching ratios at the lower energy (optimised analysis) results in pushing more feeding to these lower levels. This affect may be changed if the individual γ ray branching can be ascertained (from high resolution measurements) rather than the grouping of multiple levels.

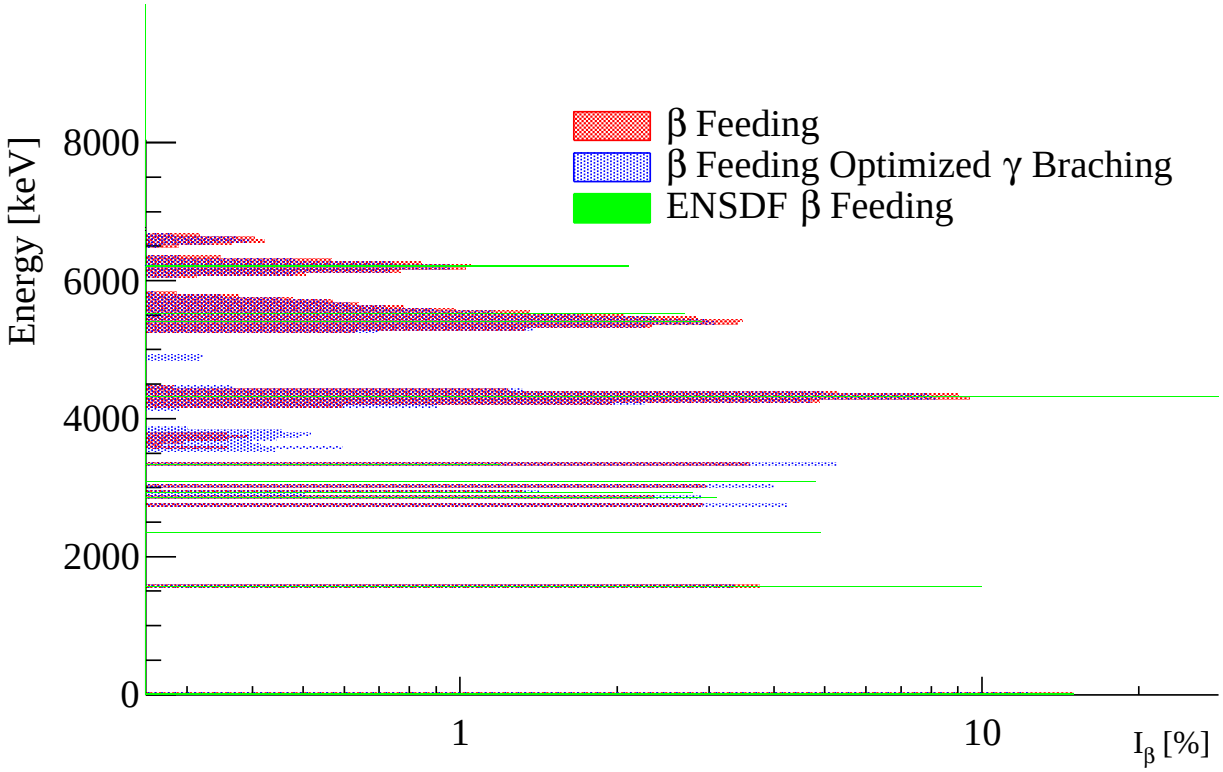

(a) Final generated β feeding distribution (rotated for clearer display which levels are feed).

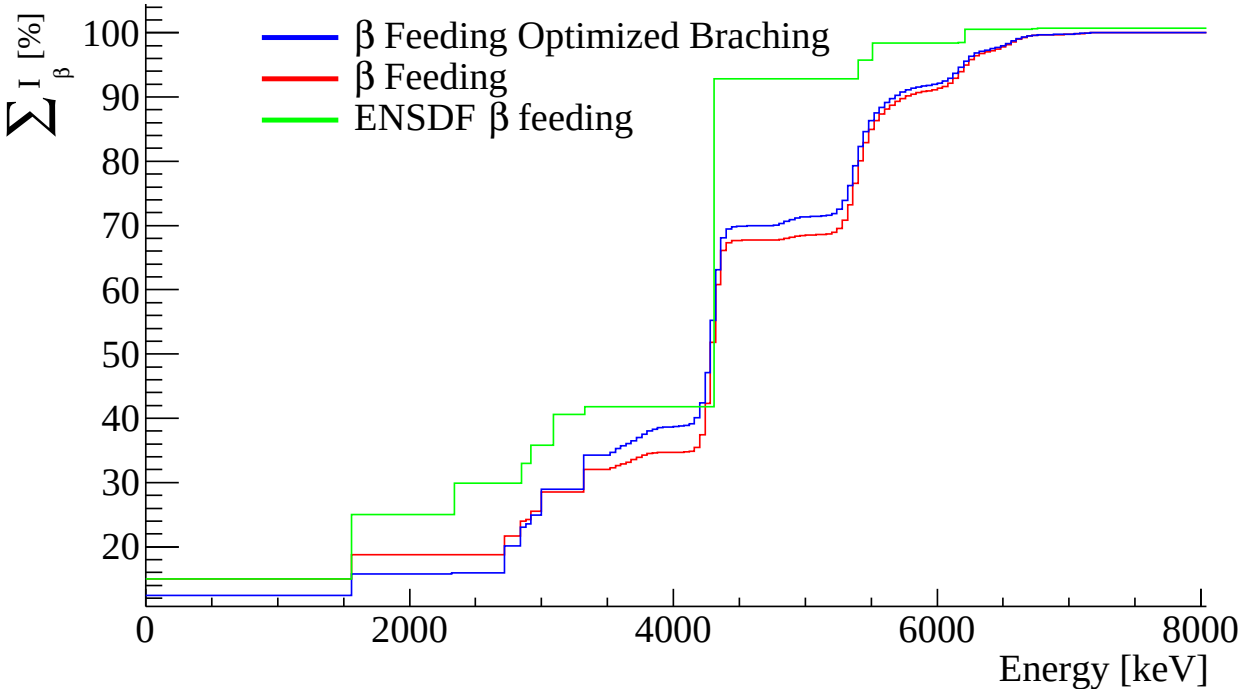

(b) Cumulative sum of the final generated β feeding distribution.

Figure 6.11: Final comparison of the generated β feeding distributions for the decay of ^{86}Br. With response (A) being the original result with no change to the γ ray branching and (B) being the optimised γ ray branching result.

6.2.3 Implications of the ^{86}Br Analysis

The analysis has shown that the inclusion of the level by Fotiades et al. [32] improves the generated response ratifying the existence of these new levels, although due to the low resolution, the precise position of these levels can not be verified. The resultant replication of the data shows a reasonable fit and with increased statistics, more justifiable arguments could be made about the level scheme used.

The β Strength Function of the ^{86}Br Decay

From the recorded feeding distribution it is also possible to generate the strength function (S_β) as described in Section 5.3.1. Figure 6.12 shows the calculated β strength function for the ^{86}Br decay, for both the original and γ ray branch optimised results, and for comparison, the generated strength function using the ENSDF feeding distribution data. These show similar results between the analyses as expected, from the similar feeding. The ENSDF data matches the TAS data for the ground state and for a few low energy states (<3.5 MeV) apart from the 2349 keV level. Above this no strength is recorded until the 5.4 MeV and 5.5 MeV levels where the levels match the TAS data. The comparison of the TAS analysis to the ENSDF data imply that there may be *pandemonium* in the original measurement.

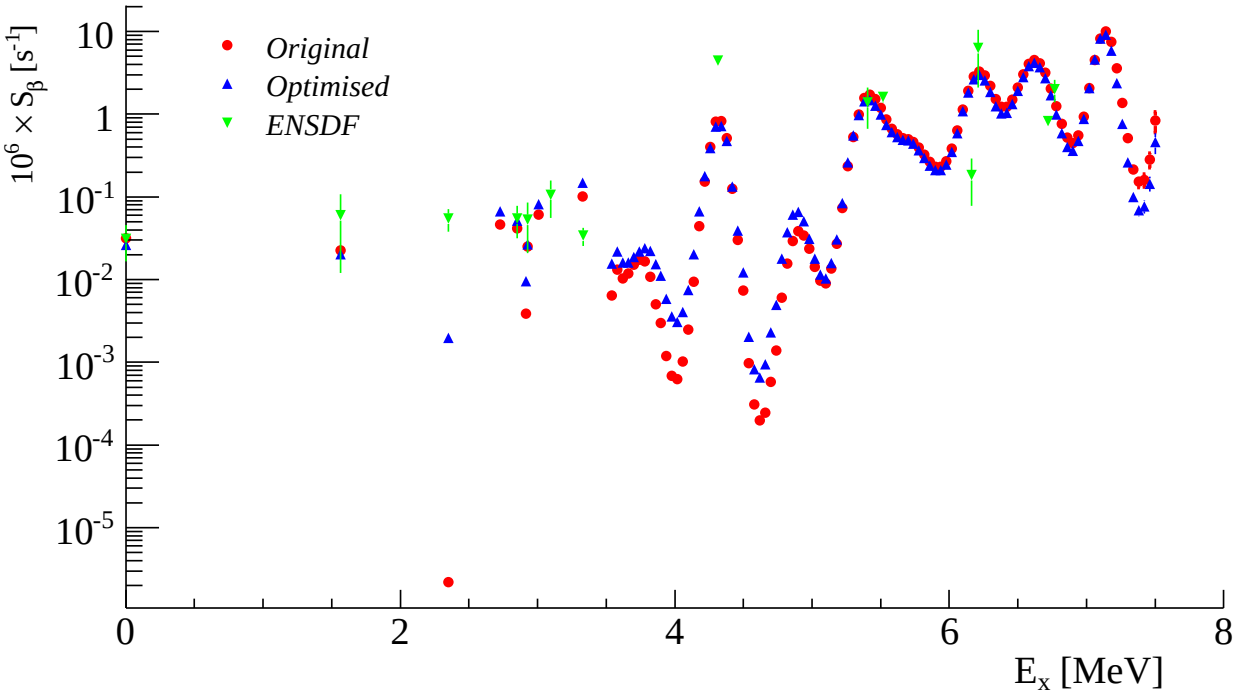

Figure 6.12: The calculated β strength function for the decay of ^{86}Br for the two final analyses and the previously recorded ENSDF data.

	$\overline{E_\gamma}$ [keV]	$\overline{E_\beta}$ [keV]
Original result	3819.2(39)	1671.8(32)
Branching optimised result	3824.6(39)	1668.1(28)
Final results	3821.9(55)^{a}(540)^{b}	1670.0(42)^{a}(278)^{b}
ENSDF/B-VII.1	3297(156)	1944(345)
JEFF 3.1.1	3297(156)	1943(345)
JENDL/FPD-2011	3300(160)	1900(400)

Table 6.7: Mean average energy for β-particles and γ rays (all collected photons) from the decay of ^{86}Br. *a*) statistical uncertainty, *b*) uncertainty due to assumptions of the analysis.

The Mean Decay Energy of ^{86}Br

The results from the analyses enables the mean average energies of the β-particles and γ rays (all collected photons) to be calculated and are shown in Table 6.7.For comparison the average mean energy from several nuclear databases are shown with varying degrees of precision. The average mean γ ray energy from the analysis shows an increase of ≈500 keV whereas the average mean β-particles energy shows a decrease of ≈300 keV, backing up the possible *pandemonium effect* in the previously recorded data. The final generated result is a combination of the original and optimised results due to the uncertainty used in each analysis where the correct γ ray branching ratio is taken into account and the closer fit (lower χ^2 value) to the experimental data.

For each of the analyses a statistical uncertainty was calculated from the uncertainty in the feeding distribution. This used the assumption that the energy is free of uncertainty and the uncertainty of the integrated Fermi function is negligible in comparison to that of the feeding distribution. The final result was a combination of the original and optimised branching ratio model as both give realistic final reproductions of the collected data. This combination resulted in their statistical uncertainties being added in quadrature to encompass the combined statistical uncertainties. This statistical uncertainty alone does not account for the large assumptions (of spin, parity, level distribution) made in each analysis.

The different available level schemes and level density models each provided differing fits to the data. It was found that fixing the parents ground state to $J^\pi=1^-$, the silicon detectors efficiency to 25%, the level scheme up to the 3542 keV level, the constant temperature model and only permitting first forbidden and allowed decays, each result (for all options of spin parity) gave realistic reproductions to the data. These different reproductions of the data do not fit as well as the final results but are still a realistic possibility and as such the variance to the final result was chosen as a good approximation for the uncertainty from the assumptions.

6.3 Preparation of ^{91}Rb

6.3.1 The Measurement of ^{91}Rb

The tape cycle for the measurement of ^{91}Rb was set to 174.8 seconds of implantation with a rate of 1000 ions per second followed by the tape movement. Figure 6.13 shows the accumulation of each ion per second for a tape cycle, with the build-up of ^{91}Rb ions nearly reaching secular equilibrium assuming an implantation rate of 1000 ions per second. The ratio of activity over each tape cycle is 99.9 % ^{91}Rb decays followed by 0.1 % of the daughter ^{91}Sr decays and less then 0.0002 % of the granddaughter decays. Although the constant implantation of 1,000 ions per second is an approximation, it can be assumed from these results that the measurement has negligible daughter and even less daughter contamination, removing the need for their subtractions in this instance.

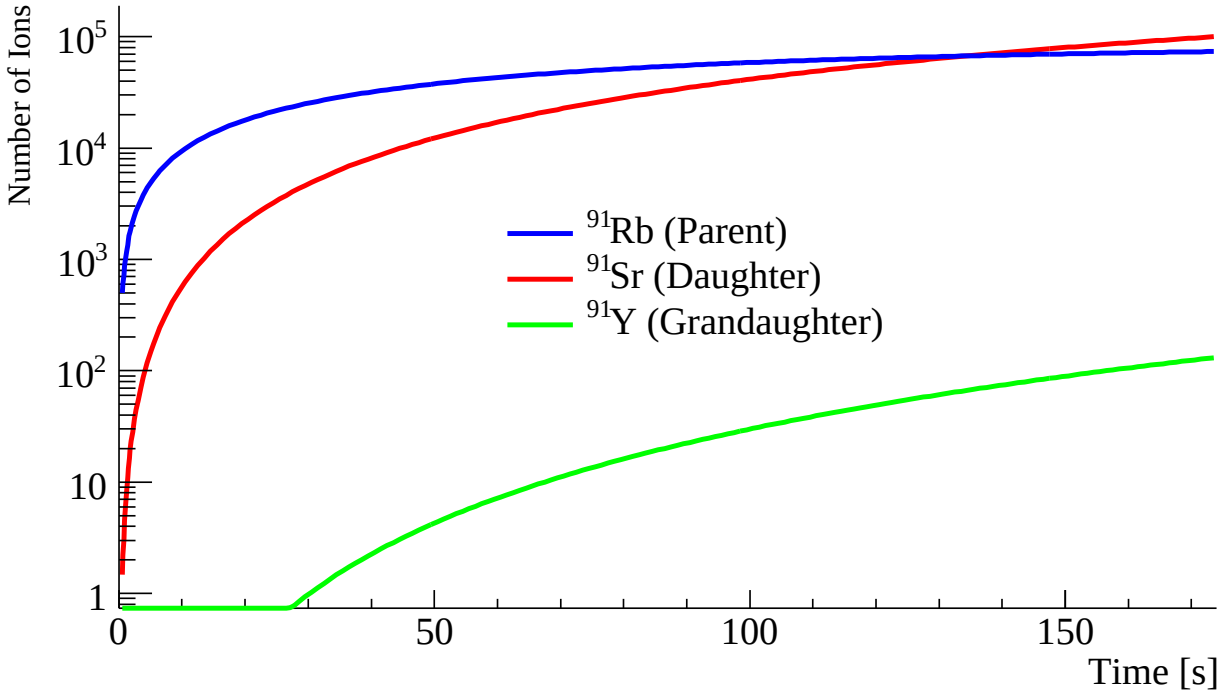

Figure 6.13: Approximation of the number of ions on the tape at time t for the ^{91}Rb measurement, per tape cycle. Calculated using a solution to the Bateman equations [61].

A total of four runs of ^{91}Rb were collected during the experiment over a time period of 7 hours but due to saving problems explained above reduced statistics where obtained. After preliminary tests and calibration each run was found to be homologous and all runs were combined to improve counting statistics. The calibrated β-*gated* TAS and silicon spectra are shown in Figures 6.14 and a summary of the collected statistics are shown in Table 6.8.

Data type	Recorded events
Hardware Sum	1.50×10^{6}
Silicon detector	2.69×10^{7}
Software Sum	1.45×10^{7}
(Silicon gated) **Software Sum**	9.19×10^{4}
E-Crystal	1.64×10^{7}
(Silicon gated) **E-Crystal**	1.77×10^{5}

Table 6.8: Summary of the TAS recorded ^{91}Rb measurement statistics.

The calibrated *β-gated* spectra reveals some features of the ^{91}Rb decay. Peak *A* peaks at ≈90 keV due to the 93.6 keV level, which is possibly prominent due to its 84.3 ns isomeric state, in addition to direct feeding and escapes of higher energy γ rays in a cascade. Peak *B*, peaking at ≈360 keV comes from an escape or non-collection of the 93.6 keV level in the de-excitation of the 439 keV level. At *C* there is a possible double peak in the area ≈1030 keV resultant of the 994 keV and 1042 keV levels. The Peak at *D* ≈1970 keV is more clearly defined but can not be seen directly in the recorded level scheme. As with Peak B this could be due to the escape or missed collection of the 94 keV level from the decays of the 2065 keV and 2077 keV levels. At ≈2620 keV is Peak *E*, most probably from the direct population and decay of the 2657 keV level, with an energy shift possible due to the miss-detection of the 94 keV level in some events. The finite resolution of the BaF_2 results in a less accurate determination of the next few Peaks. *F* ≈3670 keV results from levels at 3693 keV and 3576 keV. The *G* Peak at ≈4060 keV arises from levels 4043 keV and 4073 keV. The highest energy Peak at *H* (3560 keV) may be a peak, but due to the low statistics this is not clear in the current data. This Peak may be due to feeding the 5249 keV level or possibly a level at 5365 keV which is proposed in the level scheme but not confirmed.

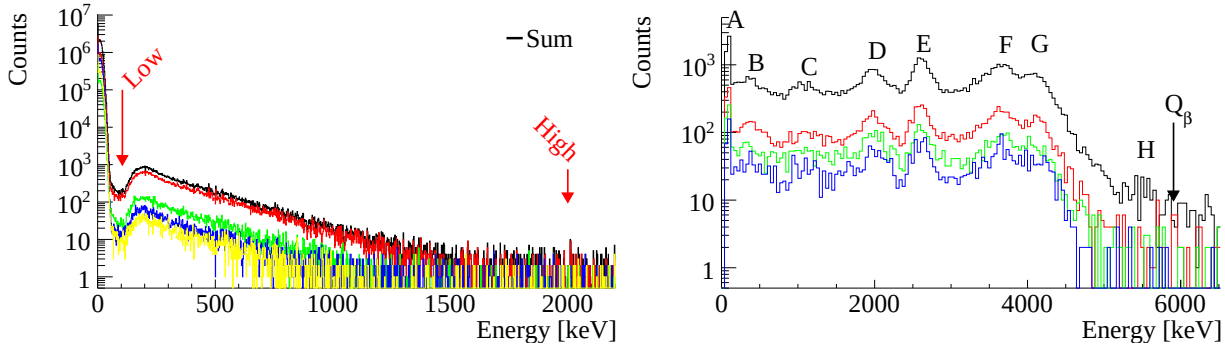

(a) Silicon detector spectra.

(b) TAS *β-gated* **Software Sum** spectra.

Figure 6.14: *a*) Calibrated Silicon detector spectra for the ^{91}Rb decay runs and the resultant Sum (blue), with the identification of pulser region and the low and hight gate threshold. *b*) Silicon (β particle) gated TAS spectra for the ^{91}Rb decay runs and the resultant Sum (blue) and identification of peaked regions of interest.

6.3.2 The ^{91}Rb Contaminant Subtraction

An initial subtraction of *Beam-On* background was preformed on the each measurement of the *Singles* data, using the technique explained in Chapter 3. Due to a small miss-match between the spectra combined with the lower than expected statistics an optimal subtraction of background was not found for the *Singles* data, and a comparison of the "best" subtracted *Singles* data is shown in comparison to the β-*gated* data (a summation of all four measurements) in Figure 6.15a. The large fraction of background from the ^{226}Ra α-particle results in an over subtraction of the ^{91}Rb in each measurement, reducing this subtraction gives an increased background due to α counts. Due to the unverified efficiency of the silicon detector a scaled comparison of the β-*gated* spectrum against this background free *singles* spectrum reveals a 25% scaling factor, agreeing with the result from ^{86}Br. The poor final statistics of the *Singles* data result in it not being used for the analysis of this isotope.

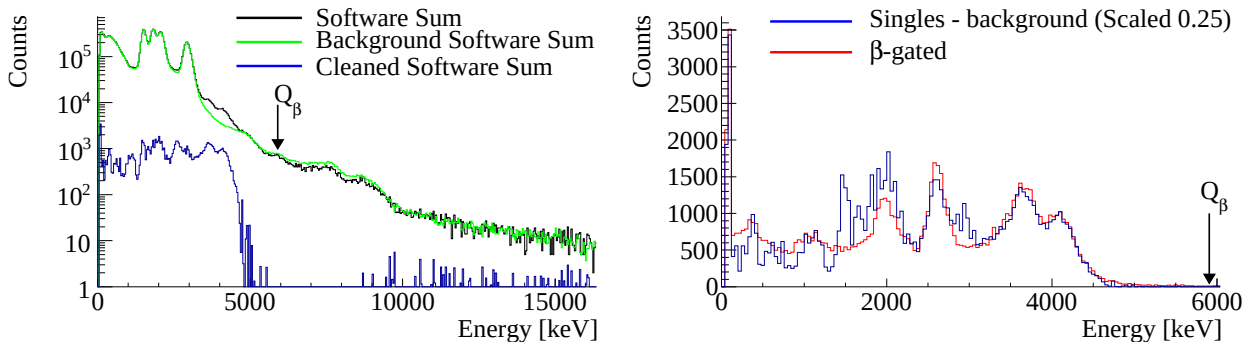

(a) *Singles* subtraction. **(b)** *Singles* & β-*gated* comparison.

Figure 6.15: The total statistics of the ^{91}Rb TAS *Singles* **Software Sum** spectra showing (a) the subtraction of the *Beam-On* TAS background and the resultant spectra. On the right (b) the preliminary comparison to the ^{91}Rb TAS background subtracted **Software Sum** *Singles* data (scaled by 0.25) and the β-*gated* **Software Sum** spectra.

Pile-up of ^{91}Rb

Pile-up data was created normalised and subtracted from the β-*gated* data, as explained in Chapter 3. Table 6.9 shows the relevant rates for each of the β-*gated* runs used and the number of β-*gated* events. The results of this pile-up subtraction and ^{91}Rb spectrum to be analysed is shown in Figure 6.16. This subtraction shows that the possible peak (H) at ≈3560 keV was most probable a result of pile-up, but more statistics would be need to verify this either way.

Run	Number of β-particle events	Rate [Hz]
Rb91_1030	67,615	6417
Rb91_1126	13,786	6410
Rb91_1521	6,639	6124
Rb91_0047	3,895	6654
Background	NA	6195

Table 6.9: Experimental rates (in counts per second) for the^{91}Rb measurements and number of β-particle events and the sum *Single Beam-On* background measurement for reference.

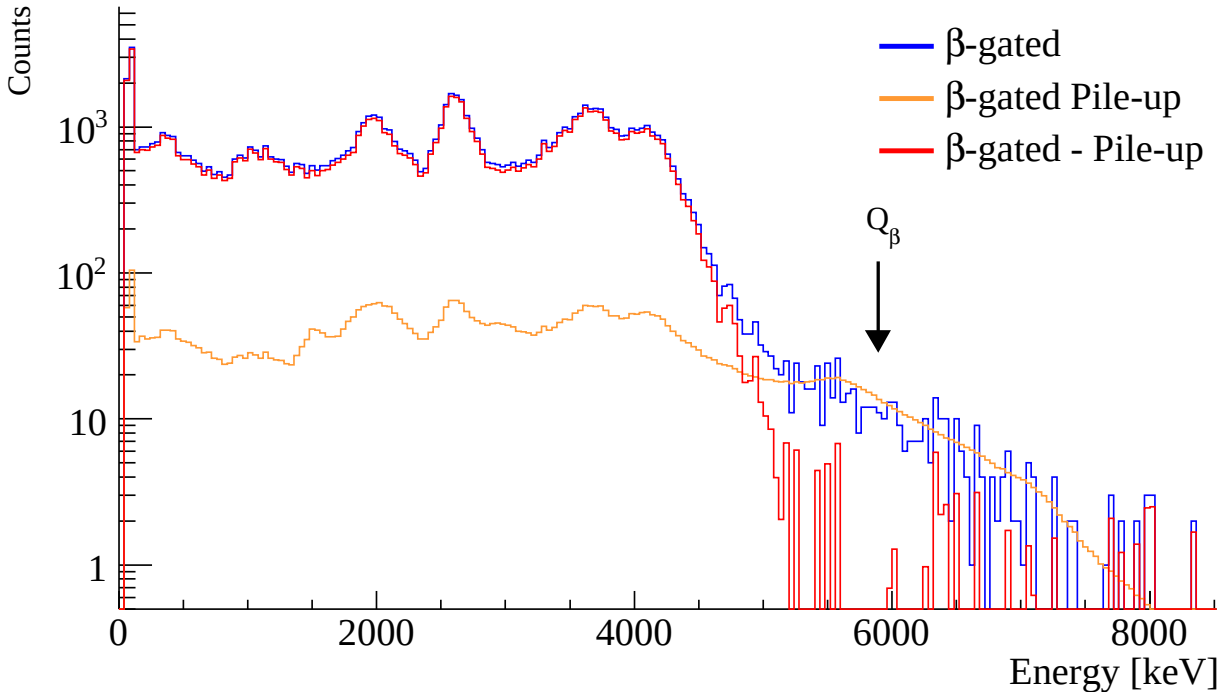

Figure 6.16: Final ^{91}Rb TAS *β-gated* **Software Sum** Subtraction of pile-up and contaminating background showing the resulting spectra.

6.3.3 The Level Density of ^{91}Sr

The level density of ^{91}Sr is shown in Figure 6.17. Data in the RIPL3 [73] database gave 47 levels with the first 45 within the recorded level scheme. Using this 45$^{\text{th}}$ energy level as an energy density reference point for the HFB optimization a continuous level density was created with the experimental data enabling the parametrisation of both the BSFG, the CT and the GC models. Each of the statistical models fitted to the data, shows a reasonable fit to the data, possibly with the GC and CT model giving a slightly improved fit. The calculation of the BSFG model using the deuteron-alpha reaction mass method has (as with the ^{86}Br) provided a poor fit. The parameters generated from these fits are shown in Table 6.10.

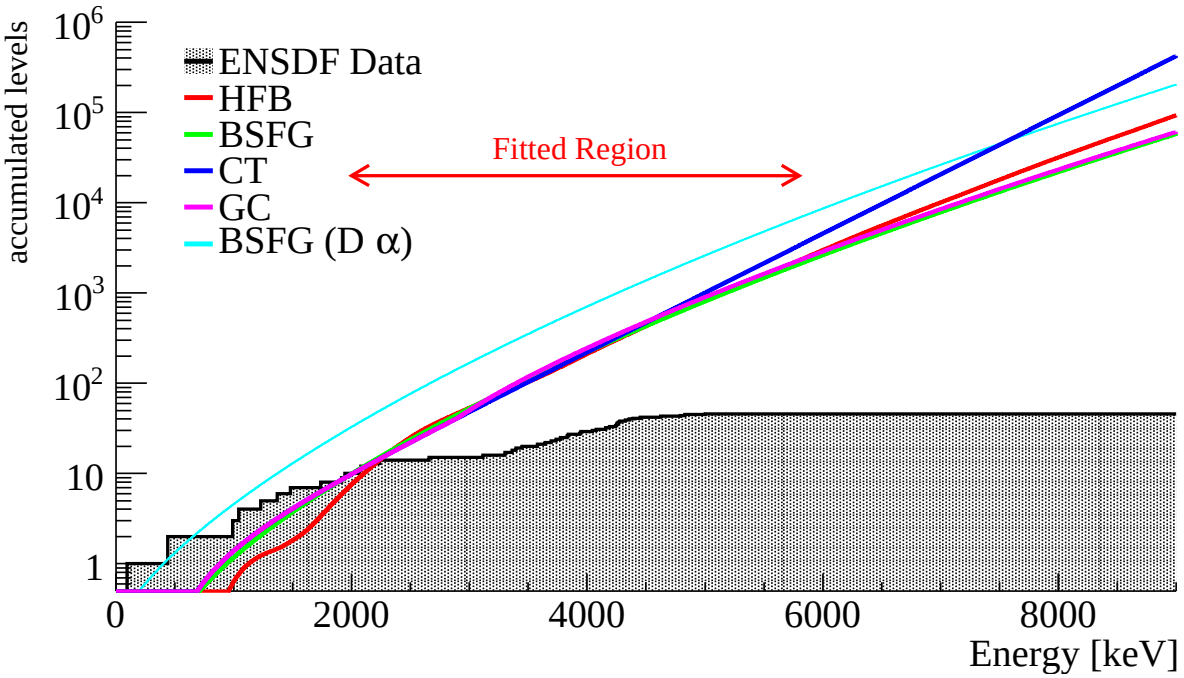

Figure 6.17: Excitation level density of ^{91}Sr showing the collated experimental data from the RIPL3 database [73], the theoretical HFB model and the fitted statistical models of BSFG (Dilg et al. and Egidy et al.) ,CT and GC [77, 78, 79].

a	9.754	[1/MeV]
Δ	0.264	[MeV]
a (Mass)	10.675	[1/MeV]
Δ (Mass)	-0.200	[MeV]

T	0.662	[MeV]
E0	0.425	[MeV]
Ex	1.946	[MeV]

Table 6.10: Statistical level density parameters for the BSFG, CT and GC model to ^{91}Sr level density.

6.3.4 The Level Scheme of ^{91}Sr & Level Threshold

The recorded level scheme of ^{91}Rb contains many levels [39]. The lower region and γ ray transitions of this adopted level scheme is displayed in Figure 6.18. This low-energy section of the level scheme contains low-excitation levels with no evaluated spin or parity, there is also a large band gap between levels 2159 keV and 2657 keV. This gap in the level scheme is a possible region of missing levels. To avoid the inclusion of missing levels an upper level scheme threshold was set to the 2159 keV level. A summary of these adopted lower excitation levels below this gap is shown in Table 6.11.

The missing spins and parities of levels recorded in ENSDF, needed to be estimated. The γ ray transitions between different levels were used in combination with the expectation that most transitions would occur via the most probable E1, E2 or M1 γ ray transition, resulting in a range of options available for the missing spins and parities. A number of these level are recorded to decay via an E2/M1 transitions to the 94 keV, $J^\pi = 3/2^+$, level resulting in the initial decaying level

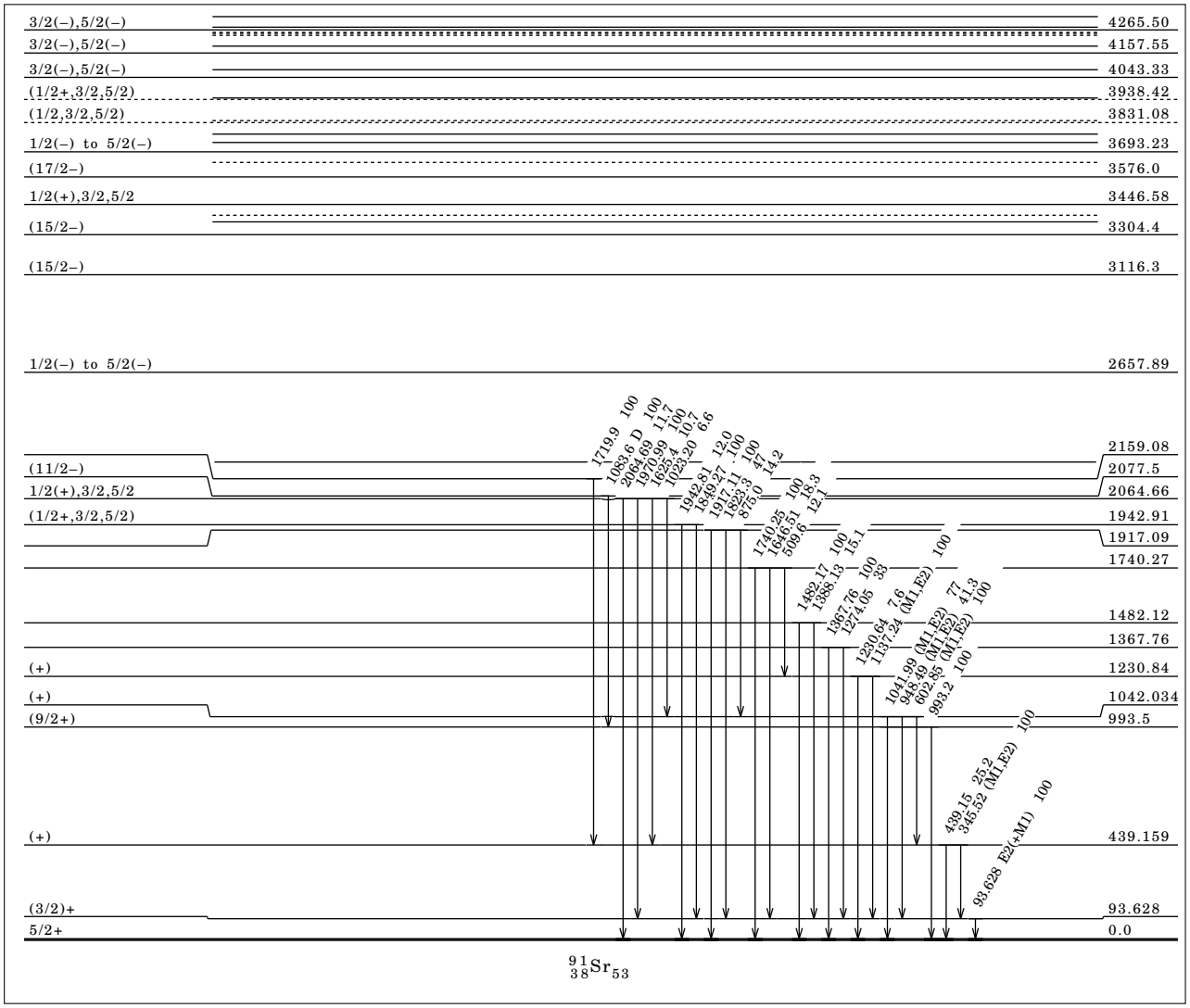

Figure 6.18: Lower Section of the adopted gamma level scheme for ^{91}Sr, taken from ENSDF [39], for the full level scheme see Appendix D.

being likely $J^\pi = 1/2^+,3/2^+$ or $5/2^+$. The β-decay feeding distribution recorded in ENSDF was also utilised when postulating options for J^π for the excited state. This resulted in the 1368 keV level having options of both parity, due it not having any recorded feeding. The large degrees of freedom now available via these options results in a range of level schemes. These created level schemes were then also cut at different energy level thresholds. These thresholds were used to reduce the degrees of freedom included, although the reduction of included level diminishes the validity of the end result.

The parent ^{91}Rb ground state is a $J^\pi = 3/2^-$ resulting in allowed feeding to $1/2^-$, $3/2^-$ and $5/2^-$ levels, which would only (might) feed the 1368 keV level (with selected J^π values) in this low excitation level scheme. The lack of allowed transitions means that it is plausible that the decay will transition

^{91}Sr	Adopted J^{π} for			Threshold
Level [keV]	ENSDF	Options in this analysis	Final choice	
0.0 (g.s.)	$5/2^+$	$5/2^+$	$5/2^+$	
94	$(3/2)^+$	$3/2^+$	$3/2^+$	
439	$(?^+)$	$1/2^+$ or $3/2^+$	$3/2^+$	
994	$(9/2^+)$	$9/2^+$	$9/2^+$	0
1042	$(?^+)$	$1/2^+$ or $3/2^+$ or ,$5/2^+$	$3/2^+$	
1231	$(?^+)$	$1/2^+$ or $3/2^+$ or $5/2^+$	$1/2^+$	1
1368	?	$1/2^{\pm}$ or $3/2^{\pm}$ or $5/2^{\pm}$ or $7/2^{\pm}$	$7/2^-$	2
1482	?	$1/2^+$ or $3/2^+$ or $5/2^+$	$5/2^+$	3
1740	?	$1/2^+$ or $3/2^+$ or $5/2^+$	$3/2^+$	
1917	?	$1/2^+$ or $3/2^+$ or $5/2^+$	$1/2^+$	
1943	$(1/2^+,3/2^+,5/2^+)$	$1/2^+$ or $3/2^+$ or $5/2^+$	$3/2^+$	
2065	$(1/2^+,3/2^+,5/2^+)$	$1/2^+$ or $3/2^+$ or $5/2^+$	$5/2^+$	
2078	$11/2^-$	$11/2^-$	$11/2^-$	4
2159	?	$1/2^+$ or $3/2^+$ or $5/2^+$	$5/2^+$	
2237	?	$1/2^+$ or $3/2^+$ or $5/2^+$	$5/2^+$	
2658	$(1/2^+,3/2^+,5/2^+)$	$1/2^+$ or $3/2^+$ or $5/2^+$	$3/2^+$	5
3116	$15/2^-$	(Not Used)	(Not Used)	
3304	$15/2^-$	(Not Used)	(Not Used)	

Table 6.11: The low energy excitation level schemes and options available for the analysis of ^{91}Sr.

via first forbidden decay thus to $1/2^+$, $3/2^+$, $5/2^+$ and $7/2^+$ states in the daughter resulting in a large number of these lower levels being feed.

6.4 The ^{91}Rb Decay Results

6.4.1 The Binned Analysis of ^{91}Rb

The preliminary binned (40 keV) analysis test of the ^{91}Rb decay enabled the quick testing of different level schemes and permitted feeding rules. Figure 6.19 shows the response and generated β-feeding distribution. This generated response uses the final level scheme with a level scheme threshold of 2680 keV and the CT statistical model for the different permitted feeding. This comparison of the free feeding, allowed feeding and allowed plus first forbidden feeding, shows that the free feeding and the permitted allowed plus first forbidden feeding gives a reasonable fit to the experimental data, apart from for the 2,600 keV peak. The permitted allowed only feeding result shows a poor fit over the base level scheme. All three of the responses fail to provide a good fit for the first excited level at 94 keV. The poor reproduction of the 93 keV level peak could be due to multiple aspects. Firstly this may possibly be due to an energy binning problem where the 94 keV is just above the edge of the 80 keV energy bin and this 40-80 keV bin is not a full bin, as the data has to be above 64 keV threshold. This result may skews any counts spreading to the <80 keV bin and miss shapes the possible Gaussian peak expected by the analysis. A second effect could be due to the short lived isomeric state (89.4 ns) of this 93 keV level resulting in a small probability of its γ ray detection being outside of the collection 5 μs time window when the slow signal collection of the β particle in the silicon is taken into account.

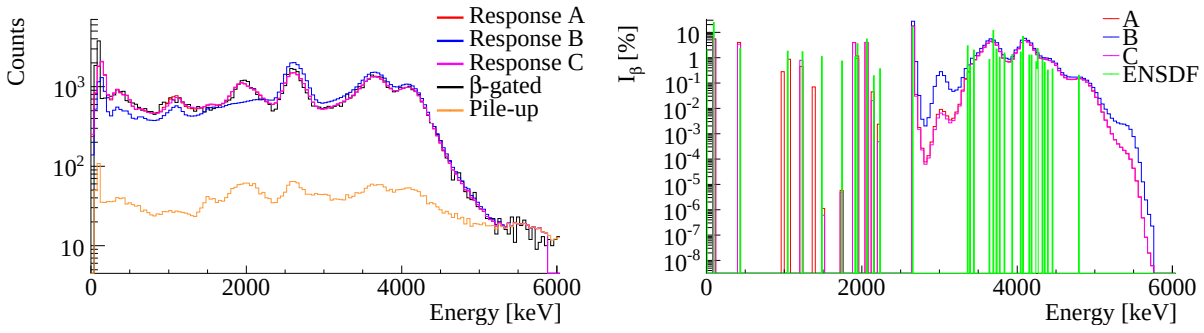

(a) TAS spectrum and response.

(b) β feeding distribution.

Figure 6.19: Preliminary recreation of the TAS response and β-feeding distribution for the decay ^{91}Rb. With a base level scheme threshold of 2680 keV, the silicon detectors efficiency set to 25% and the level density model of the CT statistical model. Where A is the response to free feeding, B the response to allowed feeding and C the response to allowed and first-forbidden feeding.

Figure 6.19 shows the recorded ENSDF β-feeding distribution and the β-feeding distribution for a previous TAS measurement of this decay by Greenwood et al. [125]. The β feeding distribution for the ESNDF data matches that of the Greenwood et al. data for the low energy region but then

diverge at higher energy. The creation of pseudo-levels in the Greenwood data results in feeding to levels that are not seen in high resolution measurements. The difference between the feeding of Greenwood et al. and the ESNDF data is due to Greenwood et al. feeding multiple (pseudo) level and feeding to levels above that fed by the ENSDF data. The ground state feeding at the lower energy end (<2680 keV) of the β-feeding distribution for the free feeding analysis gives a similar result to the ENSDF data but also adds a small amount of feeding to the 994 keV level and 1368 keV level, both of which are not fed in the ESNDF or Greenwood data. The allowed only analysis β feeding distribution only populates levels in the level continuum, as no feeding is permitted to the known levels. The higher energy (>2680 keV) continuum region of the β feeding distributions of the each of the analyses shows more feeding to each level than ENSDF or Greenwood et al., whilst matching the feeding for the 2658 keV level. Since of no feeding is permitted to the lower levels, the allowed only β feeding distribution forces more feeding on each bin of the continuum.

6.4.2 The Discrete Analysis of ^{91}Rb

The discrete analysis of the ^{91}Rb provides an improved fit to the response. Each level scheme created using possible options and thresholds was tested, using the χ^2 fit and then a visual check to determine the best fit to the data. Due to an uncertainty in the recorded parents negative parity ground state, a positive parent ground state option was tested in the analysis, resulting in a rather poor results. It was found that the lower level scheme thresholds (0,1,2,3) resulted in problems reproducing the peak at 2600 keV. Figures 6.20a+b show the response and feeding for the discrete analysis using same parameters as the binned analysis. This discrete response shows a good fit to most of the experimental data, with problems matching the data at the lowest energy peak (94 keV level) and a slight problem of increased counts at ≈1500 keV and also too many counts between the two peaks at 2350 keV. To resolve this problem the lower energy section (>240 keV) was excluded from the fit of the response resulting in an improvement in the recreation of the reaming data. This adjustment means that the validity of the final result will be impaired due to this missing section of the data.

The collected feeding distributions from original and low energy exclusion analysis are shown in Figure 6.20b. Where the two analyses hold the same shape with the low energy exclusion enables some feeding to be put at low levels above the original analysis, resulting in lower feeding for all of the other levels. The analysis shows similar feeding to the recorded ENSDF results, differing slightly on the feeding to the 1482 keV level.

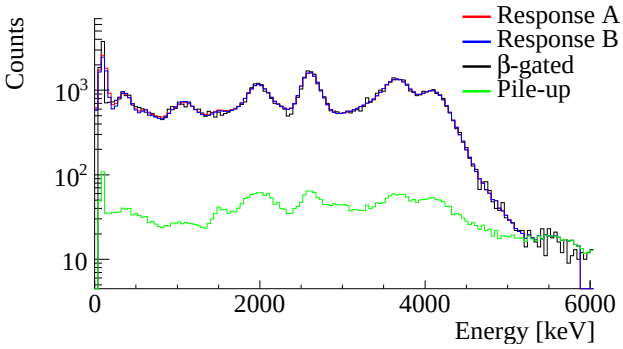

(a) Response against clean β-*gated* TAS spectra.

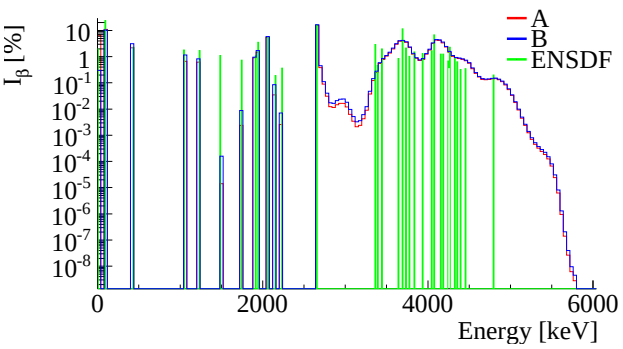

(b) β feeding distribution.

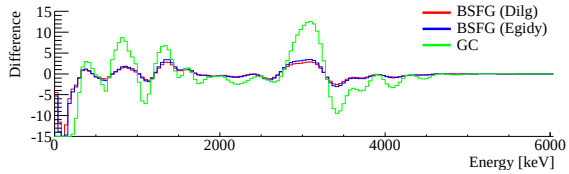

(c) The difference in the discrete simulated response from the CT model (above) for the BSFG's (Dilg & Egidy) and the GC model.

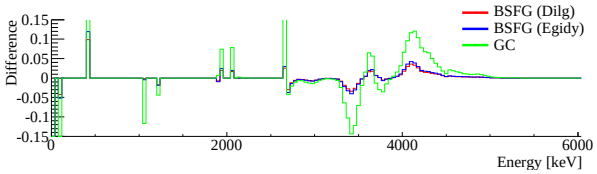

(d) The difference in the discrete β feeding distribution from the CT model (above) for the BSFG's (Dilg & Egidy) and the GC model.

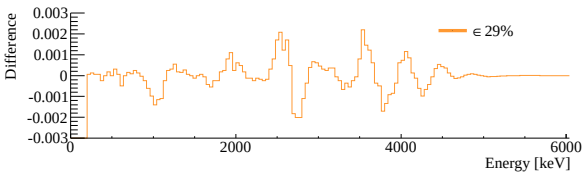

(e) The difference in the discrete simulated response for a silicon detector with efficiency of 29% rather than 25%.

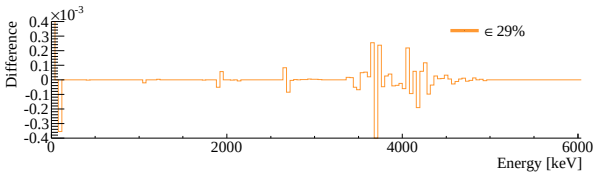

(f) The difference in discrete β-feeding distribution for a silicon detector with efficiency of 29% rather than 25%.

Figure 6.20: The response and β-feeding distribution for the discrete analysis for the full spectra range (A) and the reduced energy range (B). Below the difference of different statistical models (to the CT generated response) and differences for changes in the silicon detector efficiencies.

A comparison of the differences from this optimum (CT model) response using the other statistical models is shown in Figure 6.20c, revealing large differences between response. This is also mirrored in the collected feeding distribution (Figure 6.20d). As with the analysis of ^{86}Br, a test of the silicon detector efficiency shows very marginal difference (see Figures 6.20e+(f)) .

The Final Discrete Analysis of ^{91}Rb

Highest level	2658 keV
start of continuum	2680 keV
Parent g.s. J^π	$3/2^-$
Daughter g.s. J^π	$5/2^+$

Levels included	15
statistical model used	Constant Temperature
Feeding	Allowed and First Forbidden
	$1/2^-$, $3/2^-$, $5/2^-$ and $1/2^+$, $3/2^+$, $5/2^+$, $7/2^+$

Table 6.12: Optimum inputs for the analysis of the β decay of ^{91}Rb

A summary of the inputs used for the final analysis of ^{91}Rb is shown in Table 6.12. As with the analysis of the ^{86}Br decay the final spin and parities of the final chosen level scheme were selected from the optimum reproduction of the recorded data. The large degrees of freedom in spin within this level scheme results in a large uncertainty in the final chosen level scheme. The inclusion of the $7/2^-$ state at 1368keV results in this state not being fed via beta decay due to only permitting allowed and first forbidden decays. However this level can be populated via gamma transitions. The strong feeding to the $3/2^+$ 2658 keV could be an effect of its proximity to the continuum of levels.

The previously recorded decay provides information of low excitation γ ray branching ratios from the decay of ^{91}Rb. This data is shown in Table 6.13 with the current branching within the response matrix and the branching from an (γ ray branching ratio) optimised response matrix. As before, this optimisation is obtained by adjusting the feeding to the level from the continuum of levels.

Level	relative γ ray Intensity [%]		
[keV]	ENSDF	Original Result	Optimized Result
93.63	43.75	67.61	43.62
439.16	6.04	17.34	6.19
993.50	0.00	0.23	0.00
1042.03	3.57	8.70	3.91
1230.84	2.41	4.97	2.86
1367.76	0.58	0.35	0.92
1482.12	0.96	3.15	1.04
1740.27	1.06	2.48	1.69
1917.09	0.71	2.65	1.20
1942.91	2.14	3.23	2.60
2064.66	0.45	8.08	6.65
2077.50	0.00	0.00	0.00
2159.08	0.18	1.29	0.20
2236.95	0.53	1.10	0.71
2657.89	9.69	15.64	15.59

Table 6.13: Gamma branching ratio of the low energy levels in ^{91}Sr for recorded ENSDF data, the original generated response and the optimised response. Both responses include levels not detected in the recorded ENSDF file thus an averaged over multiple level of similar energy was used for comparison.

The response generated from this modified response matrix is shown along side the original result in Figure 6.21 showing the fit to the collected experimental data and their relative difference from this. The separate analysis results in a very similar responses, showing a good fit to the response below 4500 keV (to the low energy threshold of 240 keV).

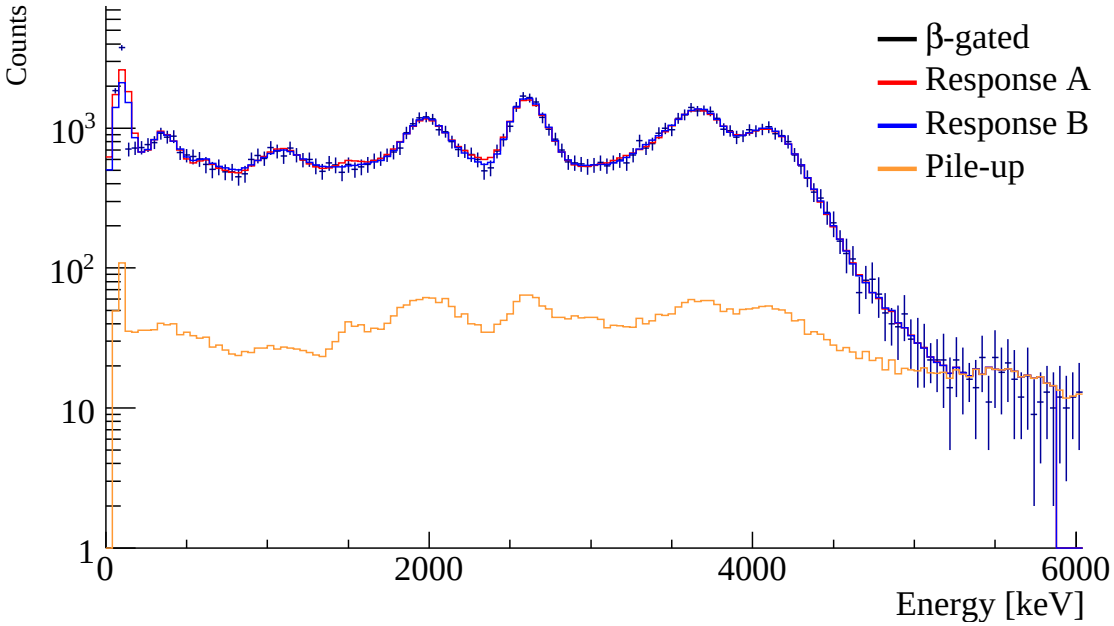

(a) Final Analysis generated responses (plus contaminants) in comparison to the raw *β-gated* spectrum, also showing relevant contaminants (background and pile-up).

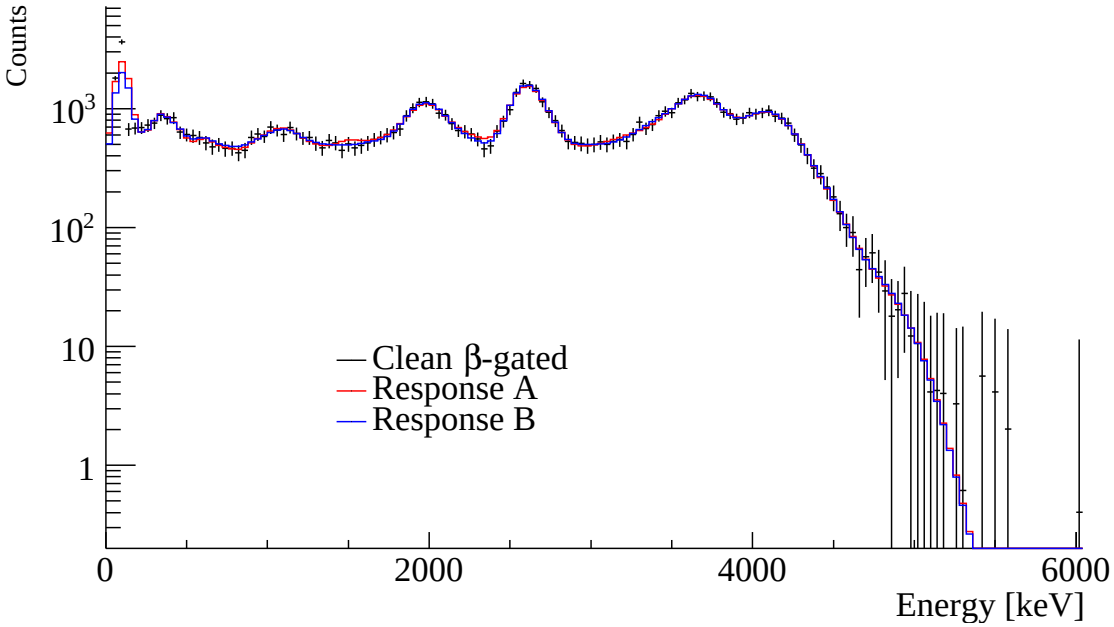

(b) Final analysis generated responses in comparison to the clean *β-gated* spectrum.

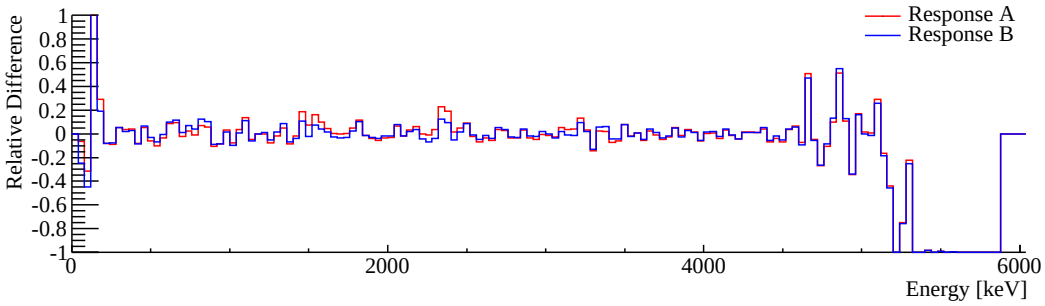

(c) Relative difference from the clean *β-gated* spectrum for each analysis.

Figure 6.21: Final comparison of the generated response for the decay of ^{91}Rb against the collected TAS *β-gated* spectrum. With response (A) being the original result with no change to the γ ray branching and (B) being the optimised γ ray branching result.

The generated β feeding distribution for the analysis is shown in Figure 6.22 (a tabulated full version can be found in Appendix A). For comparison, the previously collected ENSDF data and TAS analysis data by Greenwood et al. [44] is also shown. This comparison reveals that the optimised branching ratio analysis gives results closer to that of Greenwood et al., although both analyses give less feeding above ≈5000 keV than Greenwood et al. The two analyses have similar feeding distributions but differ at the start of the continuum (2680 keV) up to 3530 keV. The recorded ENSDF direct ground state feeding is 2% whereas the original analyses gave a larger feeding of 6.6%, very close to the value provided by Greenwood et al. of 6.2%. The optimisation of the branching ratio reduced this value to 5.3%.

Figure 6.22b shows the accumulation of the feeding as the energy increases, enabling a different comparison of feeding distributions. This comparison shows that the original analysis and the optimised γ ray branching result are very similar, with the original analysis providing more feeding to the lower (<2680 keV) levels than the discrete level section. The modified result reduces the feeing to the discrete level section, providing more to the level continuum. The previous recorded TAS analysis by Greenwood et al. [44] gave very similar results to this analysis. The previously recorded ENSDF data show more feeding to lower levels, but due to the exclusion of these level in the analysis this difference may be smaller. The shape of the feeding of each of the analysis follows the feeding of the ENSDF data.

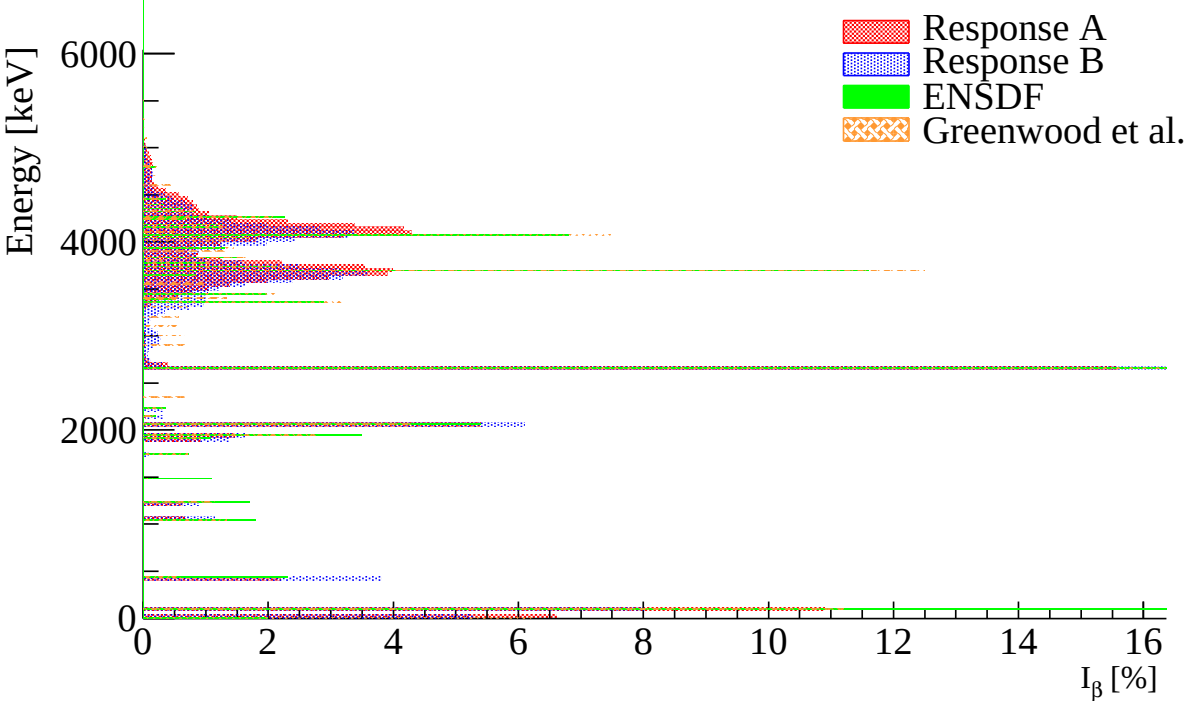

(a) Final generated β feeding distribution (rotated for clearer display which levels are feed).

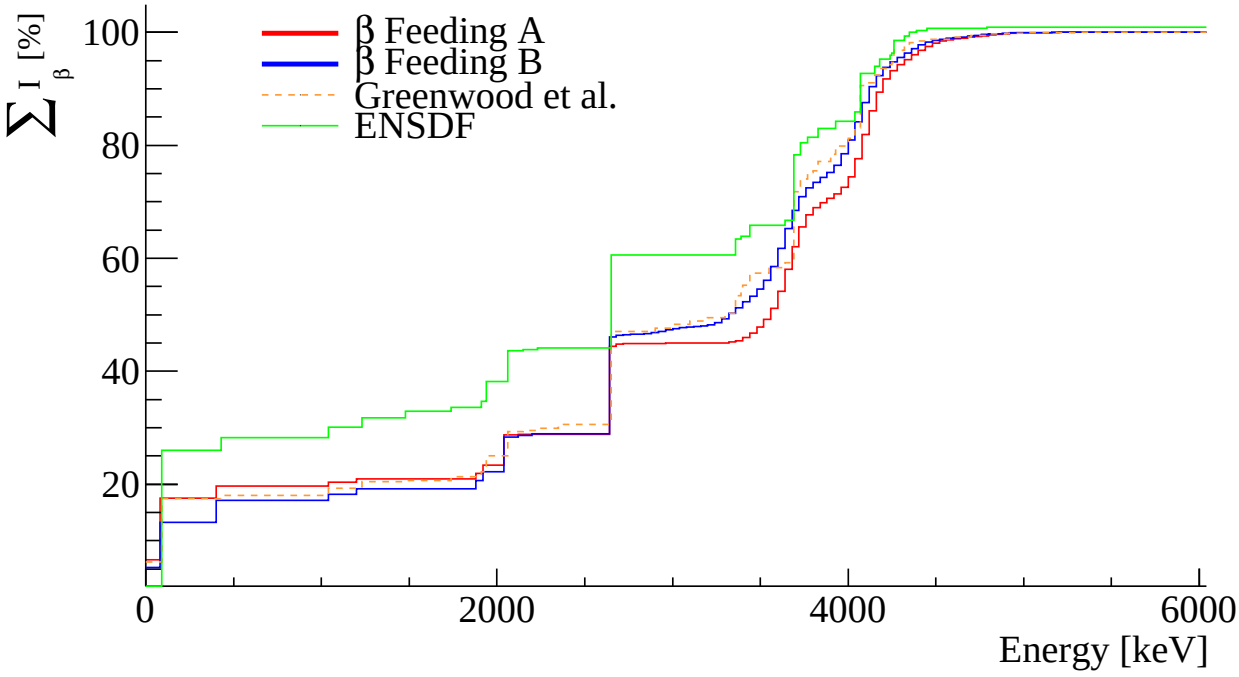

(b) Cumulative sum of the final generated β feeding distribution.

Figure 6.22: Final comparison of the generated β feeding distributions for the decay of ^{91}Rb. With response (A) being the original result with no change to the γ ray branching and (B) being the optimised γ ray branching result.

6.4.3 Implications of the ^{91}Rb Analysis

The analysis of the decay of ^{91}Rb, has shown results similar to the recorded data from Greenwood et al. while excluding the analysis of the first excited 93 keV state in the daughter. The effect of this unknown region could produce similar accumulated feeding distribution to that recorded in ENSDF. The exclusion of the low energy part of the spectra reduces the validity of the result.

The ^{91}Rb Decay β Strength Function

The strength function from the unfolded feeding distributions of the analysis are shown in Figure 6.23, where the difference between the analysis's are negligible. The strength function of the previously recorded ENSDF data and the results obtain by Greenwood et al. are also included in Figure 6.23. the comparison of these results show a lower strength from the analysis in the lower (<2.5 MeV) energy region. The region surrounding ≈3 MeV shows a reduction in the strength in the analysis and non-recorded for the ENSDF data, whereas the work by Greenwood et al. gives some strength in this region. Both analyses reduce the strength at ≈4.8 MeV, the point of the last recorded strength from the ESNDF data, whereas the Greenwood et al. data assigned more strength to these final levels.

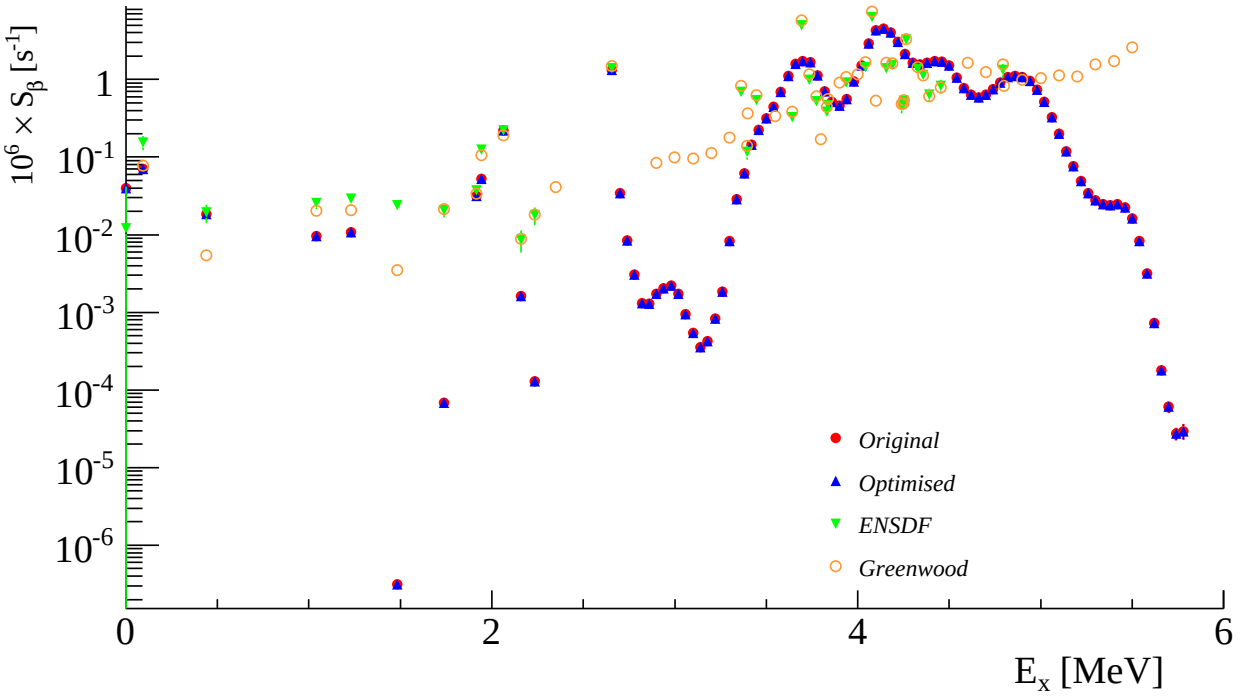

Figure 6.23: The calculated β strength function for the decay of ^{91}Rb for the two final analyses and the previously recorded ENSDF data.

	$\overline{E_\gamma}$ [keV]	$\overline{E_\beta}$ [keV]
Original result	2798.0(32)	1325.2(23)
Branching optimised result	2775.5(34)	1334.3(22)
Final results	2786.8(47)[a](294)[b]	1329.7(32)[a](215)[b]
Greenwood et al.	2885.2[c]	1282.0[c]
ENDF/B-VI.8	2340(140)	1561(25)
JEFF-3.1.1	2706(27)	1368(13)
JENDL/FPD-2011	2340(50)	1610(190)

Table 6.14: Mean average energy for β-particles and γ rays (all collected photons) from the decay of ^{91}Rb. *a*) Statistical uncertainty, *b*) uncertainty due to assumptions of the analysis and *c*) no uncertainty provided.

The Mean Decay Energy of ^{91}Rb

Using Equations 5.11 and 5.12 from Chapter 5 is it possible to extract the mean average γ ray and β particle energy. The results from this analysis compared to previously recorded results are tabulated in Table 6.14. where the value given for the Greenwood et al. measurement was calculated as with the analysis using the recorded feeding distribution and the assumption of a 20 keV binning.

As with the ^{86}Br decay result the statistical error produced from the uncertainty in the feeding distribution, where the final value is produced as before in quadrature from the two combined final values. The final results included a large degrees of freedom in the chosen spins and parities, to account for these assumptions, an analysis with a reduced degree of freedom was chosen to approximate the uncertainty. The analyses with the lower threshold (trusted level) of 1230 keV produced a very good reproduction of the data and fitted this reduced degrees of freedom criteria. Keeping the restriction of the silicon efficiencies at 25%, feeding via allowed and first forbidden decays and using the constant temperature model (as the final results) a range of values for the mean decay energy were generated from the possible spins and parities, the variance of these results from the final value was used as the uncertainty due to the possible assumptions.

The generated results from the analysis are shown to give very similar values, resulting in their combination for the final result to enable a combination of best fit to the data and the inclusion of a closer γ ray branching ratio. This final mean γ ray energy is ≈ 400 keV above the value given in the current ESNDF and JENDL, whereas the value given by JEFF is $\approx$80 keV below the results from the current work. The difference between these data sets could be due to the inclusion of the Greenwood et al. work, which provides mean average γ ray values $\approx$100 keV above the values generated by the analyses. The mean average β-particle energy shows a similar trend to the mean

average γ ray energy. However the analyses values are ≈ 250 keV below the values given by ENSDF and JENDL and only ≈ 30 keV below that of the JEFF values. This trend is continued with the Greenwood et al. values giving the lowest mean average energy at ≈ 50 keV below the analysis result. It should be noted that without the inclusion of the lower energy section (94 keV peak) due to its poor generation by the response reduces the validity of this final result.

Previous work by Rudstam et al. [40] used the ^{91}Rb decay as the normalisation for a NaI(Tl) spectrometer used in the measurements of γ and β spectra of multiple short lived fission fragments. The normalisation of this detector used a mean γ energy per disintegration (mean average energy) of 2335(33) keV similar to the ENSDF data, which this work has shown to contain *pandemonium effect*.

6.5 Preparation of ^{94}Sr

6.5.1 The Measurement of ^{94}Sr

To measure the decay of ^{94}Sr, a high purity beam of ^{94}Rb was created by the JYFLTRAP and then collected allowing this to decay to its daughter ^{94}Sr. The production of this ^{94}Sr was optimised for each tape cycle by using a "collection" period where the ^{94}Rb was deposited on the tape at the centre of the TAS. The beam implantation was then paused enabling a "decay" period, before the tape was moved away for the end of that cycle. This process was possible due to the difference in the half-lives of the ^{94}Rb parent ($T_{\frac{1}{2}}$ =2.7 s) and the ^{94}Sr daughter ($T_{\frac{1}{2}}$ =75.3). The tape cycle for the measurement of ^{94}Sr was set to 108 seconds with the beam implanting ("collection") and then a second ("decay") measurement period of 84.0 seconds without the beam implanting ions to the tape was used, after which the tape was moved. Figure 6.24 shows the number of each type of ion during one tape cycle, highlighting the build up of ^{94}Sr. From the relative half-lives, implantation and decay time the ratio of each isotope's activity was obtained using a solution to the Bateman equations [61] using the assumption that the number of ^{94}Rb decays via β delayed neutron emission were lower then the uncertainty in the implantation rate. The resulting constituents of the collection were 58 % of ^{94}Rb decays, 40 % of ^{94}Sr decays and 2 % of ^{94}Y decays.

As with the other collected isotopes an error occurred with the saving of the offline data resulting in lower final collected statistics then expected. This reduction of statistics is more apparent in these measurements as a subtraction of the parent decay is required before any of the data can be analysed. Two runs of ^{94}Sr were collected, but one run had problems with the tape system resulting in its exclusion from the analysis. A summary of the statistics used for the analysis of the

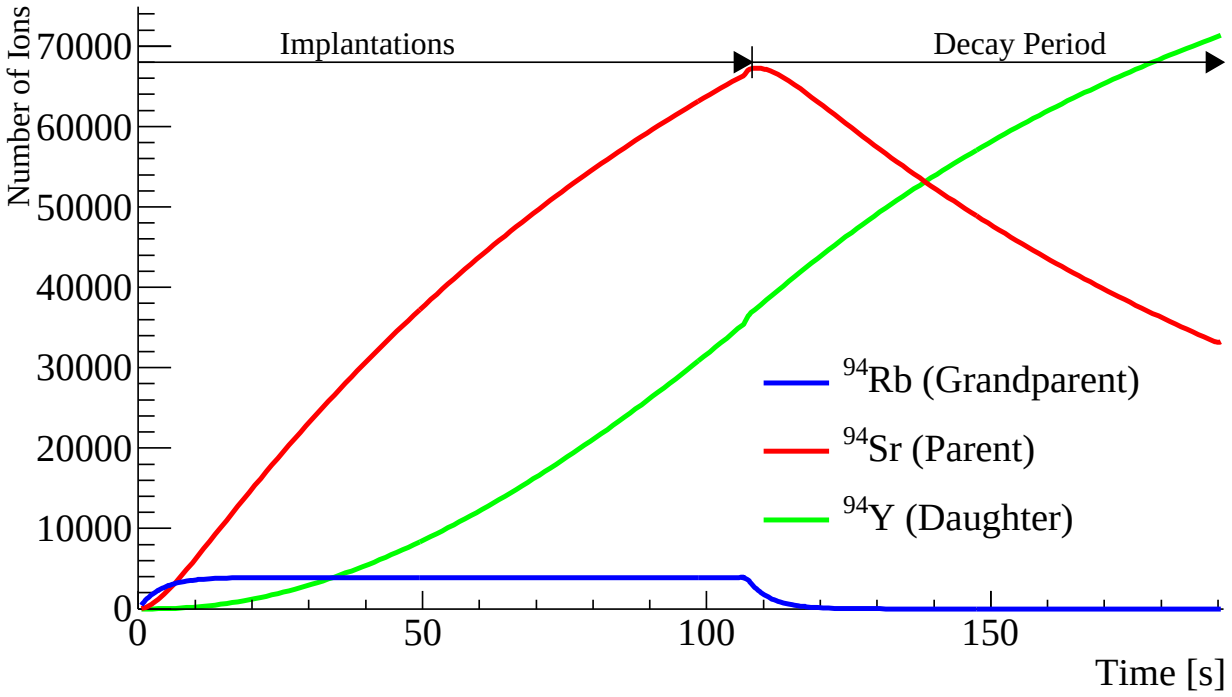

Figure 6.24: Approximation of the number of ions on the tape at time t for the ^{94}Sr measurement, per tape cycle. Calculated using a solution to the Bateman equations [61].

Data Type	Recorded Events
Hardware Sum counts	7.3×10^{6}
Silicon detector	9.2×10^{6}
Software Sum	7.0×10^{6}
(Silicon gated) **Software Sum**	3.1×10^{5}
E-Crystal	9.5×10^{6}
(Silicon gated) **E-Crystal**	7.8×10^{5}

Table 6.15: Overview of the recorded TAS ^{94}Sr measurement statistics.

^{94}Sr decay is shown in Table 6.15 and the calibrated silicon spectra and silicon (beta) gated TAS spectra are shown in Figure 6.25.

The inclusion of the parent's decay for the collection results in large amounts of contamination in the ^{94}Sr measurement. The recorded β-*gated* spectra (Figure 6.25) shows three identifiable peak regions which all lie below the Q_β-value of ^{94}Sr (3508 keV). The peak A (≈880 keV) is most probably due to a combination of the highly feed 918 keV level in ^{94}Zr from the daughter decay of ^{94}Y and the 830 keV level from the parent's ^{94}Rb decay. The peak B (≈1440 keV) is the dominant peak from the ^{94}Sr decay to the 1427 keV level with some additional intensity from the 1437 keV level. The final peak feature that stands out is C (≈2,440 keV) and can be identified at the 2414 keV level from the parent ^{94}Rb decay. For reference the Q_β values for the ^{94}Sr, the daughter ^{94}Y (4,918 keV)

and parent ^{94}Rb (10,287 keV) and ^{94}Rb the neutron separation energy (S_n) of 6746 keV have been labelled on Figure 6.25.

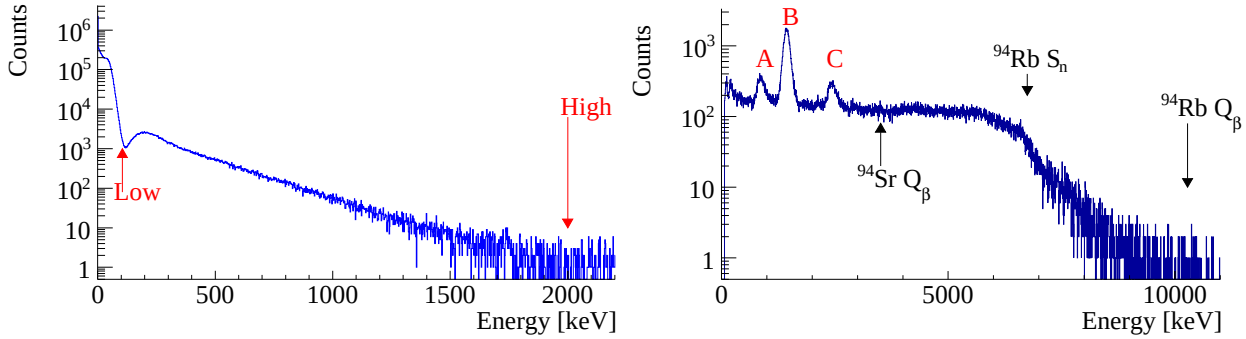

(a) Silicon detector spectra. **(b)** TAS *β-gated* **Software Sum** spectra.

Figure 6.25: *a*) Calibrated silicon detector spectra for the ^{94}Sr decay runs and the resultant sum (blue), with the identification of pulser region and the low and hight gate thresholds. *b*) Silicon (β particle) gated TAS spectra for the ^{94}Sr decay runs and the resultant sum (blue) and identification of peaked regions of interest, the relevant Q_β values and the neutron separation (S_n) energy of the parent ^{94}Rb.

6.5.2 The ^{94}Sr Contaminant Subtraction

Pile-up and background subtractions for this isotope were performed as with previous measurements (See Table 6.16 for rates and net counts of the *β-gated* data). In addition to this subtraction daughter and parent decays needed to be removed. The parent contamination could be removed by using the combined runs of ^{94}Rb measurements, cleaned of pile-up and background. It should be noted that the ^{94}Rb measurements will contain a small percentage of the desired ^{94}Sr decays, but due to a tape cycle of only 8.02 seconds and no decay time, this number of ^{94}Sr decays is expected to be significantly lower then the number of ^{94}Rb decays. The decay of ^{94}Y was not experimentally recorded in these measurements but data collected in ENSDF enabled a Monte Carlo simulation to generate the ^{94}Y decay **Software Sum** spectrum. The final *β-gated* subtraction of ^{94}Sr is shown in Figure 6.26 showing each of the components. Any contamination from the ^{93}Sr decay (the β delayed neutron daughter of ^{94}Rb) will be included in the ^{94}Rb measurement and thus will be subtracted with the ^{94}Rb.

The normalisation of each subtrahend can be calculated via multiple methods. Provided that the assumptions of the implantation rate calculation are correct the ratio of ^{94}Rb decay to ^{94}Sr was determined for the ^{94}Rb decay measurements and the ^{94}Sr decay measurements, thus enabling a normalisation of the ^{94}Rb subtrahend. This ratio (Bateman equation) approach only accounts for total number of decays and not for difference in non-interactions within the TAS or silicon detector

Run	Beta event	Rate
Sr94_1703	306,567	7510
Rb94_1804	39,491	6600
Rb94_1859	87,858	6609
Background	NA	6195

Table 6.16: Experimental rates for the ^{94}Sr measurement and the ^{94}Rb containment measurements also showing the number of β-particle events and the sum *Single Beam-On* background measurement for reference.

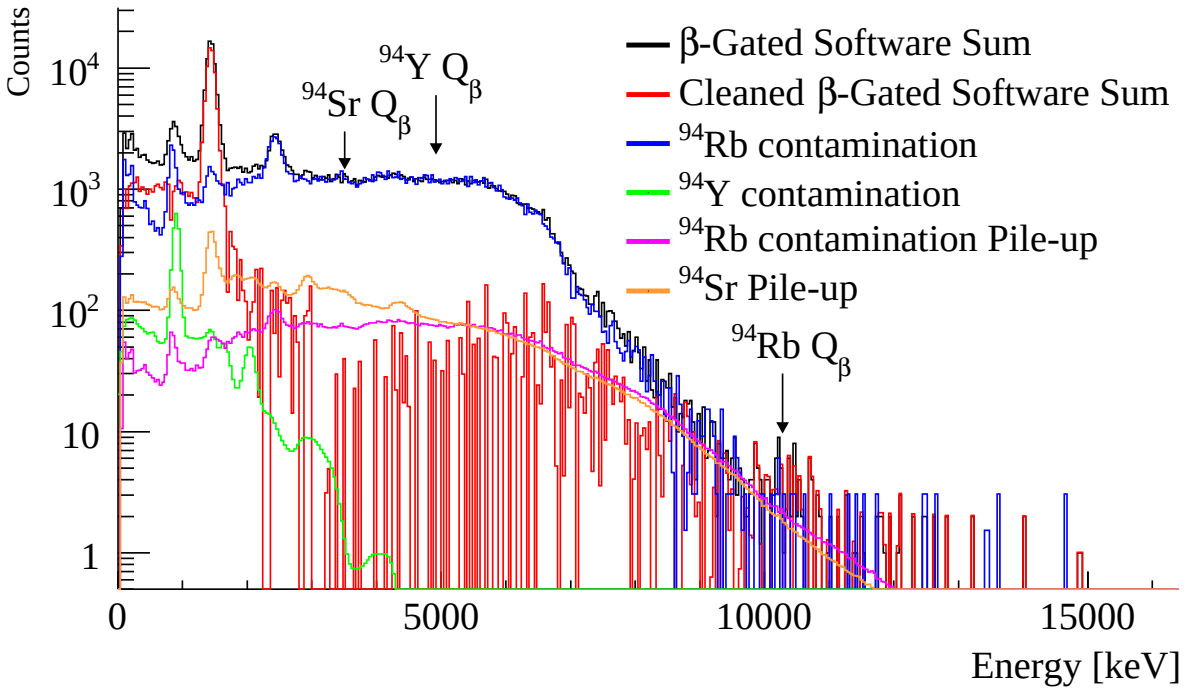

Figure 6.26: ^{94}Sr TAS *β-gated* **Software Sum** Subtraction of pile-up and contaminating background and other contaminants. Also showing the pile-up for the ^{94}Rb containment and the resultant cleaned ^{94}Sr spectra. Normalisation of background via the hardware sum pulser counts,^{94}Rb containment, via the Q_β normalisation and the ^{94}Y containment via the number of decay obtained by the tape method.

due to energy differences. A second approach to the normalisation of each of the contaminates was to use the difference in Q_β-value, as the Q_β-value for the ^{94}Sr is 3508 keV, ^{94}Y is 4918 keV whereas the ^{94}Rb is 10287 keV [25]. This difference enables a normalisation to be found by adjusting the subtraction until the the integral of final counts above the daughter (^{94}Y) Q_β-value is ≈0 (using the 10287 keV as an upper threshold to avoid the inclusion of random events). Both methods of normalisation use large assumptions, but the final results for each normalisation of ^{94}Rb give similar values. The normalisation of the ^{94}Y decay can only be achieved via this first method as close proximity of the Q_β-values and the lack of high energy feeding in the ^{94}Y decay provides no measurable decays between the different Q_β values. The resultant normalisation for the ^{94}Y decay results in very little change. The visual approach was also checked using the subtraction

of peak B (≈880 keV) as reference point. This visual normalisation demonstrated a more realistic approximation of the contamination of the ^{94}Y decay and was used for the final subtractions, a comparison of these final visual subtraction can be seen in Figure 6.28 for the subtraction of ^{94}Rb.

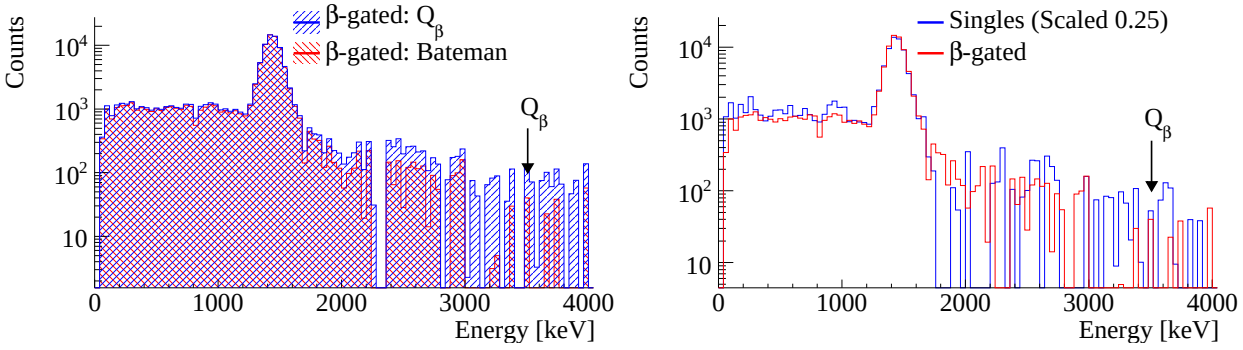

(a) *β-gated* normalisation. **(b)** *β-gated* and *Singles* comparison.

Figure 6.27: *a*) A comparison of the cleaned TAS ^{94}Sr *β-gated* **Software Sum** data using the Q_β-value normalisations for ^{94}Rb containment (plus slight adjustment by eye) and Normalisation of the ^{94}Rb via the Bateman equations method. *b*) A comparison of the cleaned ^{94}Sr **Software Sum** *Singles* data (scaled by 0.25) and the cleaned *β-gated* **Software Sum** spectra, showing the improvement in the *β-gated* spectra due to the poor statistics available for the *Singles* subtraction. Scaling of 0.25 to estimate the efficiency of the silicon detector.

The subtraction of the *Singles* data is shown in Figure 6.28, where background, and pile-up was removed from each measurement before a the same criteria was applied to the parent and daughter contamination. To avoid subtraction errors the normalisation for each spectra was calculated before any subtraction enabling a single background subtraction of the final spectrum. The final normalisation of this background lead to a net deficit of background counts resulting in its addition to the final clean ^{94}Sr *Singles* spectra. The poor statistics of each subtracted item reveals a very poor "clean" *Singles* spectrum. A comparison of this final *Singles* subtraction (scaled by 0.25) is shown alongside the the result from the *β-gated* subtraction in Figure 6.27b, agreeing with other measurements that the efficiency of the silicon detector is 25%.

Both final subtractions show a dominant β decay feeding a level at approximately 1440 keV. The spectra also show that there might be a possible level populated at 900 keV, but due to the low statistics used in the subtractions it is not possible to unambiguously identify this level at this point in the analysis.

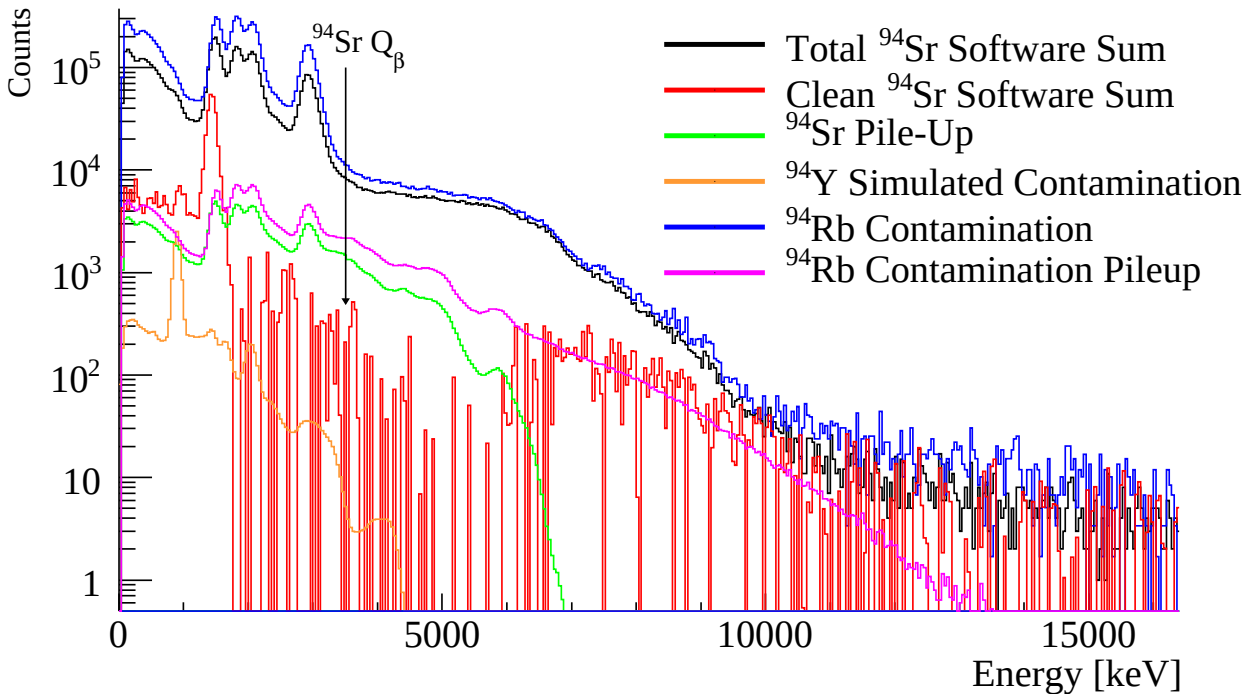

Figure 6.28: Total ^{94}Sr TAS *Singles* **Software Sum** spectra showing the subtraction of the contaminents (^{94}Rb and ^{94}Sr) and the subtraction of relevant pile-up spectra. The result of the *Beam-On* TAS background subtraction is shown in the resultant cleaned spectra, but due to the subtraction of the ^{94}Rb spectra negative *Beam-On* TAS background was subtracted.

6.5.3 The Level Density of ^{94}Y

The odd-odd structure of ^{94}Y needs less energy to excite the free neutron and proton sitting outside of a nucleon spin up-down pair (proton-proton or neutron-neutron) as no energy is needed to split a pair of nucleons to enable its excitation. This lower energy needed can be seen by the number of levels below approximately 2 MeV for odd-odd in comparison to even-even or odd-even nuclei.

The recorded information for ^{94}Y in RIPL3 [73] contains 26 levels with 11 contained within the completed ENSDF recorded level scheme. Using the 11$^{\text{th}}$, recorded level as a reference position for the HFB model, the experimental and theoretical level density could be determined shown in Figure 6.29. The level density was then fitted by the BSFG CT and CG statistical models, parametrised as in Table 6.17. The fit of the BSFG and CT to this density shape is very similar in the low energy range whereas they diverge at higher excitation, but this is above the Q_β value of 3508 keV and thus should not affect the analysis. The BSFG model parametrised via the deuteron-alpha reaction mass method results in a poor fit to the data as shown in Figure 6.29, and thus was excluded from use in the analysis.

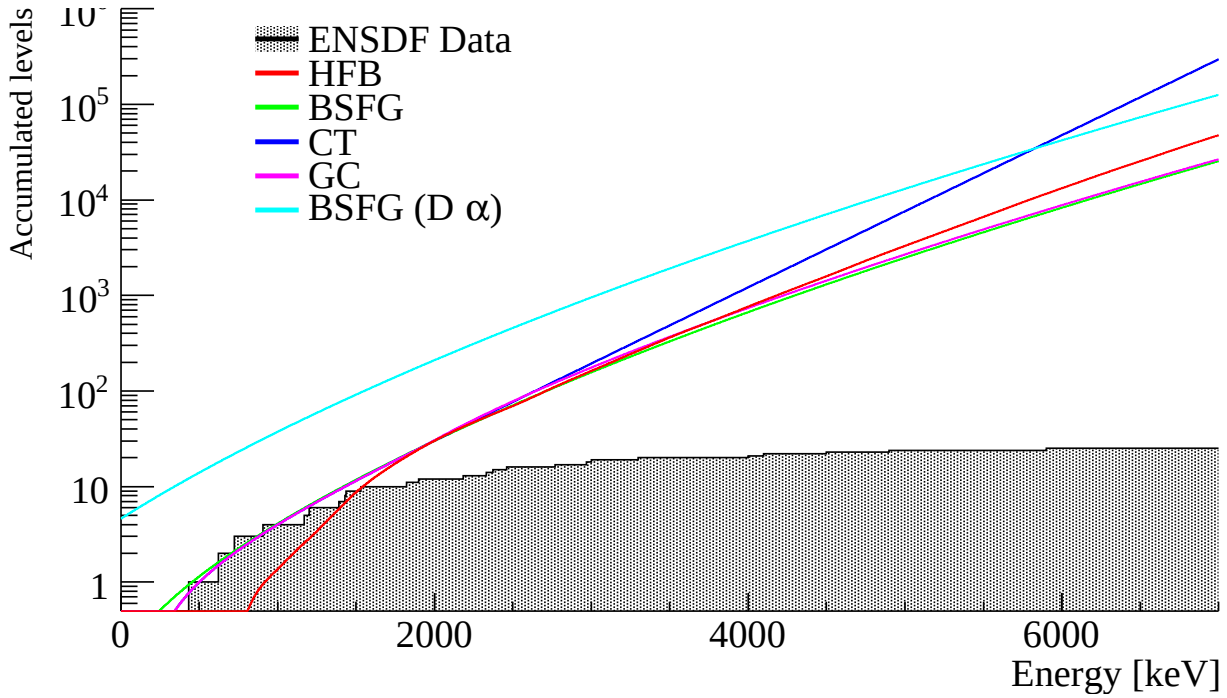

Figure 6.29: Excitation level density of ^{94}Y showing the collated experimental data from the RIPL3 database [73], the theoretical HFB model and the fitted statistical models BSFG (Dilg et al. and Egidy et al.), CT and GC [77, 78, 79].

a	10.723	[1/MeV]
Δ	-0.156	[MeV]
a (Mass)	11.434	[1/MeV]
Δ (Mass)	-1.121	[MeV]

T	.546	[MeV]
E0	0.124	[MeV]
Ex	1.960	[MeV]

Table 6.17: Level density parameters of ^{94}Y.

6.5.4 The Level Scheme of ^{94}Y & Level Threshold

The adopted level scheme of ^{94}Y is not as complex as the previously analysed isotopes and is shown in full in Figure 6.30. This level scheme (assuming that all proposed levels are correct) has 4 levels without a fixed J^π, and two possible options are given for each unknown level resulting in the possible level scheme scenarios shown in Table 6.18. The ground state J^π of parent ^{94}Sr is 0^+, resulting in allowed feeding to 0^+ and 1^+ and first forbidden feeding to 0^-, 1^- and 2^- levels. When combining these feeding rules with the generated level schemes, the levels fed by allowed transitions are constants, whereas the 907 keV level can be fed via first forbidden only when it is $J^\pi = 2^-$. The proximity of the two levels at 1430 keV could provide problems when considering feeding.

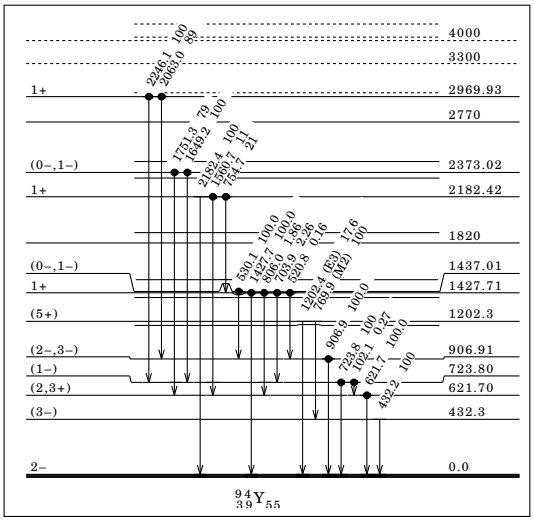

Figure 6.30: ENSDF adopted level schemes for ^{94}Y from [43]

^{94}Y	Adopted J$^{\pi}$ for			
Level [keV]	ENSDF	Analysis	Final 1	Final 2
0.0 (g.s.)	2^-	2^-	2^-	2^-
432	(3^-)	3^-	3^-	3^-
622	$(3^+,2^+)$	3^+ or 2^+	3^+	3^+
724	(1^-)	1^-	1^-	1^-
907	$(3^-,2^-)$	3^- or 2^-	2^-	3^-
1202	(5^+)	5^+	5^+	5^+
1428	1^+	1^+	1^+	1^+
1437	$(0^-,1^-)$	0^- or 1^-	0^-	0^-
2182	1^+	1^+	1^+	1^+
2373	$(0^-,1^-)$	0^- or 1^-	0^-	0^-
2970	1^+	1^+	1^+	1^+

Table 6.18: The available levels for analysis and final level schemes for ^{94}Y

6.6 The ^{94}Sr Decay Results

6.6.1 The Binned Analysis of ^{94}Sr

A preliminary binned analysis was performed to ascertain the effects of permitting feeding to different levels in the daughter nucleus shown in Figure 6.31. The response generated from each of the different permitted feedings (free, allowed and allowed plus first forbidden) give very similar results with only a marginal difference between their responses. It should be noted at the 1427 keV and 1437 keV levels are within the same energy bin thus all feeding options permit feeding to this bin, because of the allowed transition to the 1427 keV level. The overall fit of these response is not

so good due to the the large feeding to the 1427 keV and or 1437 keV levels within one bin of the response and give a peak at approximately 500 keV which is not seen in the experimental data.

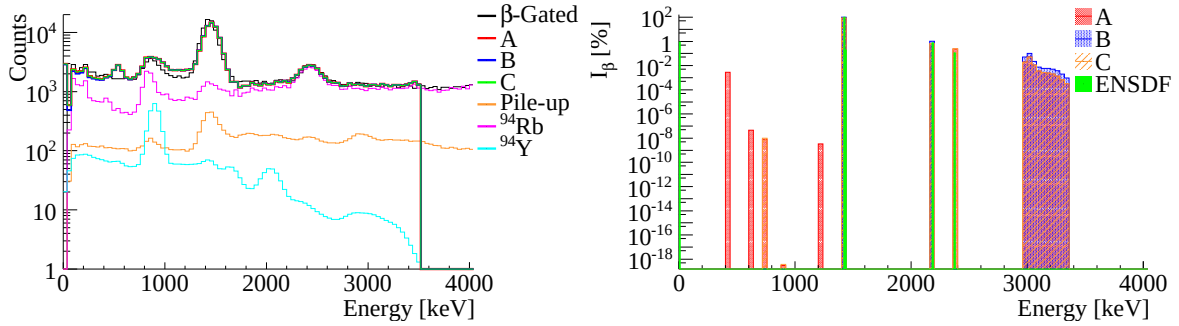

(a) Binned response to the TAS *β-gated* spectra

(b) Binned *β*-feeding distribution

Figure 6.31: Preliminary recreation of the TAS response and *β*-feeding distribution for the decay ^{94}Sr. For any, allowed only and allowed plus first forbidden only permitted feeding, all with a base level scheme threshold of 3000 keV, the silicon detectors efficiency set to 25% and the statistical level density model of the BSFG Dilg.

The *β*-feeding distribution recorded in ENSDF for the decay of ^{94}Sr only feeds to four levels with 0.9% feeding to the ground state, most feeding (98.1%) to the 1428 keV level and then the remain feeding ($\approx$ 1%) spread between 1437 keV, 2182 keV and 2373 keV levels [43]. Each analysis shows that the majority of feeding is to the join 1428 keV and 1437 keV (40 keV) energy bin where the permitted allowed feeding is responsible for 98.8% and the free and allowed plus first forbidden feeding reduce this to 86%. Comparing ground state feeding reveals that the free and allowed plus first forbidden give 12.9% rather then the recorded 0.9%, possibly due to poor response fitting with the binned energy. The spin of the ground state requites a first forbidden transitions thus the allowed only feeding does not feed the ground state. The free feeding also feeds multiple other levels, all with intensity below 1%, but this does not make a big impact on the final response. Each of these analyses also add feeding to the continuum of levels, that is not recorded in the ENSDF decay scheme, but this is possibly due to poor matching of the hight energy part of the TAS spectra.

6.6.2 The Discrete Analysis of ^{94}Sr

The simulation of the precise (known) *β*-particle and γ ray transitions of the ^{94}Sr decay enables the discrete analysis to be performed. Each of the possible level schemes, level thresholds and statistical models were used in each permutation to find the optimum. The outcome of this testing is shown in Figure 6.32 where Figures 6.32a+b shows the response and feeding for the discrete analysis using the final level scheme 1, while permitting feeding to the allowed and first forbidden levels only. This response is a lot closer fit to the experimental data than the binned data, especially

for the 500 keV region. The β-feeding distribution for the discrete analysis shows a similar shape to the recorded ENSDF data with a small ($<10^{-4}$%) amount of feeding to some extra levels, but with the majority of feeding to the 1428 keV level. The split of the 1428 keV and 1437 keV level means the separate feeding can be assessed, the ENSDF recorded result put 98.1% to 1428 keV whereas this analysis gives 80.8% and a larger 14.8% to the 1437 keV rather then the ENSDF value of 0.2%. This increase in feeding to the second level is most likely due to the proximity of the level and the failure of the analysis to separate out each energy event because of the poor resolution of TAS. The ground state feeding of the this discrete analysis is 0.3% which is a reduction from the 0.9% within the ENSDF data.

The comparison of the results from the different statistical models is shown in Figures 6.32c+d, showing little difference between the response and feeding distributions, most probably due to the very narrow energy window for these models. As with the other isotopes the effect of the silicon detector efficiency is included in Figure 6.32, showing slightly more deviation from the first response and feeding then the different statistical models but overall very little difference between the results.

An additional analysis was tested using the same level schemes but excluding the continuum of levels, thus only feeding to the known levels. The outcome of this test shows a bigger difference from the original response, but this difference is still within ±5 counts of the current best response fit per bin (shown in Figures 6.32e+f). The main difference between the feeding distribution occurs within the higher energy region containing fewer experimental counts where it is not clear if there should be feeding to these higher levels. This uncertainty results in a few final results depending on if this continuum is added.

A range of level schemes were tested for this decay utilising all possible permutations of the available level spins and parities. The net result of these permutations is two different feeding distributions due to the feeding to the 907 keV level being either first forbidden transition (2^-) or third forbidden transition (3^-). Whilst comparing different level schemes for this decay it became clear that the difference or the end analysis results were small for the permitted of not permitted feeding of the 907 keV level. A comparison has been made using level scheme 1 (See Table 6.18) and the other level schemes with 2^- for the 907 keV level in Figures 6.33a+b for all statical models. This comparison shows little difference between the final results. A second comparison was also made to the outputted results of level scheme 2 (See Table 6.18) for all level schemes with 3^- for the 907 keV level, shown in Figures 6.33c+d. This second comparison shows a larger difference but is

still very low, showing that the dependence on the different level J^{π} (using available options) for this analysis is small.

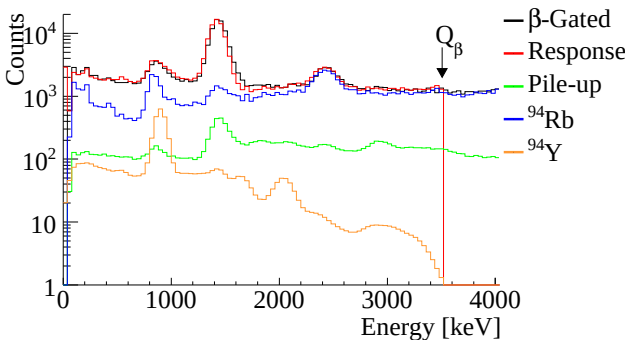

(a) Response against clean β-*gated* TAS spectra.

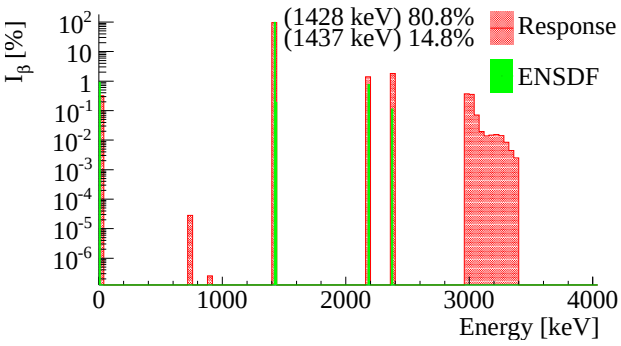

(b) β feeding distribution.

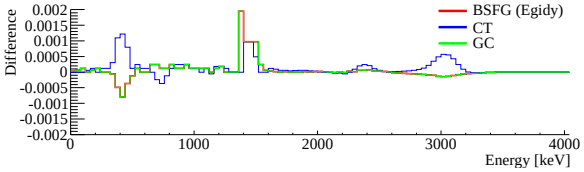

(c) The difference in the simulated response from the BSFG (Dilg et al.) model (above) for the BSFG (Egidy et al.), CT and the GC model.

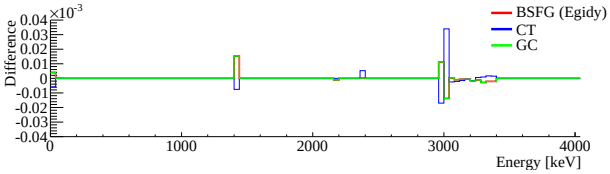

(d) The difference in the discrete generated β-feeding distribution from the BSFG (Dilg et al.) model (above) for the BSFG (Egidy et al.), CT and the GC model.

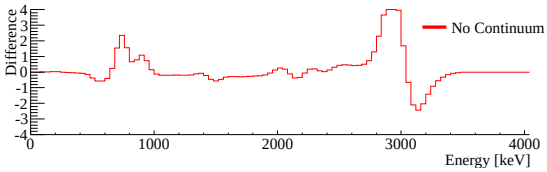

(e) The difference in the discrete simulated response for a silicon detector with efficiency of 29% rather than 25%.

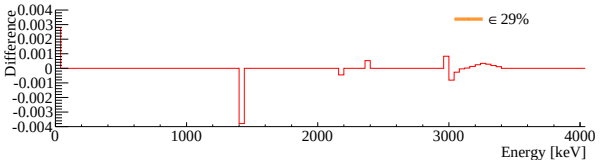

(f) The difference in discrete β-feeding distribution for a silicon detector with efficiency of 29% rather than 25%.

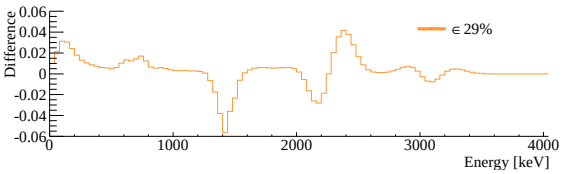

(g) The difference in the discrete simulated response with no level continuum used.

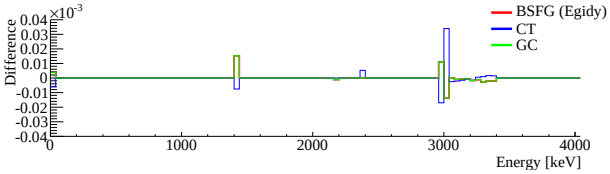

(h) The difference in the discrete generated β-feeding distribution with no level continuum used.

Figure 6.32: The response and β-feeding distribution for the discrete analysis. Below the difference of different statistical models (to the BSFG (Dilg et al.) generated response), differences for changes in the silicon detector efficiencies and the difference with an analysis without the use of a continuum of levels.

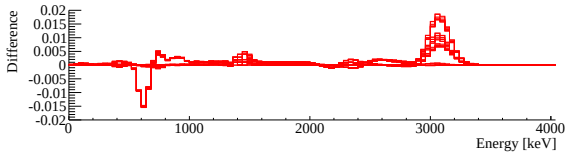

(a) The difference in the simulated response for each analysis with a $J^\pi = 2^-$ 907 keV level.

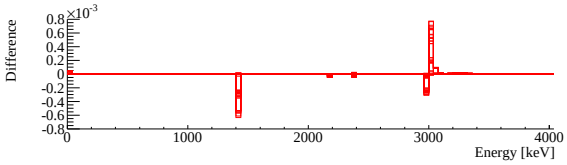

(b) The difference in the generated β feeding distribution for each analysis with a $J^\pi = 2^-$ 907 keV level.

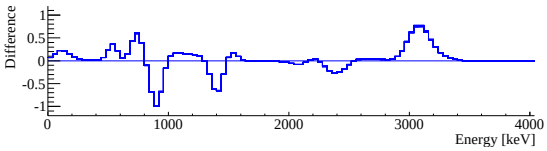

(c) The difference in the simulated response for each analysis with a $J^\pi = 3^-$ 907 keV level.

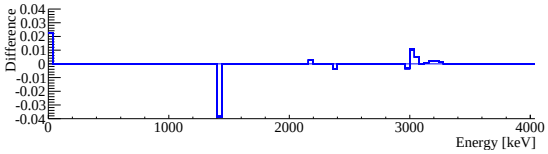

(d) The difference in the generated β feeding distribution for each analysis with a $J^\pi = 3^-$ 907 keV level.

Figure 6.33: The difference between the ^{94}Sr analyses results for each level scheme option where permitted feeding varies for the 907 keV level depending on excitation spin.

6.6.3 ^{94}Sr Final discrete analysis

Highest level	2970	Levels included	10
start of continuum	3000	statistical model used	Back-Shifted Fermi Gas (Dilg)
Parent g.s. J^π	0^+	Feeding	Allowed and First Forbidden
Daughter g.s. J^π	2^-		0^+, 1^+ and 0^-, 1^-, 2^-

Table 6.19: Optimum inputs for the analysis of the β decay of ^{94}Sr

The close proximity of the 1428 keV and 1437 keV results in sharing of feeding between the levels, the recorded ENSDF highlights that the feeding may be very strong to the lower and very weak to the higher of the two levels. Any information to support this ratio was lost in the resolution of the TAS measurement. To counteract the sharing of this feeding an analysis was performed for both level schemes while withholding feeding to this 1437 keV level, forcing feeding to just the one level, the results of which are shown in Figures 6.34 and 6.35. The resultant feeding for the two levels and the ground state are compared in Table 6.20.

Previous TAS measurements by Greenwood et al. [44] have measured the feeding distribution of the β-decay of ^{94}Sr. These results have been added to Figure 6.35 for comparison. The feeding distribution recorded by Greenwood et al. used pseudo level placed within the known (recorded) level scheme to satisfy the reproduction of the data. Due to the addition of levels, a comparison is difficult to evaluate the different distributions. The cumulative feeding sum shown in Figure 6.35b and shows a clearer comparison, revealing that the feeding unfolded by Greenwood et al. is much higher at at the lower energy range then either the recorded ENSDF data or the analysis data. The unfolded results by Greenwood et al. also only use level up to 2969 keV, similar to the results excluding the continuum.

The ground state feeding of the original results (Level scheme 1 and 2) are matched by the results of the analysis when no continuum is used, where the ground state feeding is shown to be 0.32% and 0.34% for each level scheme, which is just below the ENSDF value of 0.9% and far below the Greenwood et al. 1.8±3.6%. The prohibiting of feeding to the 1437 keV level results in a reduction of this ground state feeding to 0.01%. This reduction of ground state feeding could be linked to the increased feeding in the 1428 keV level.

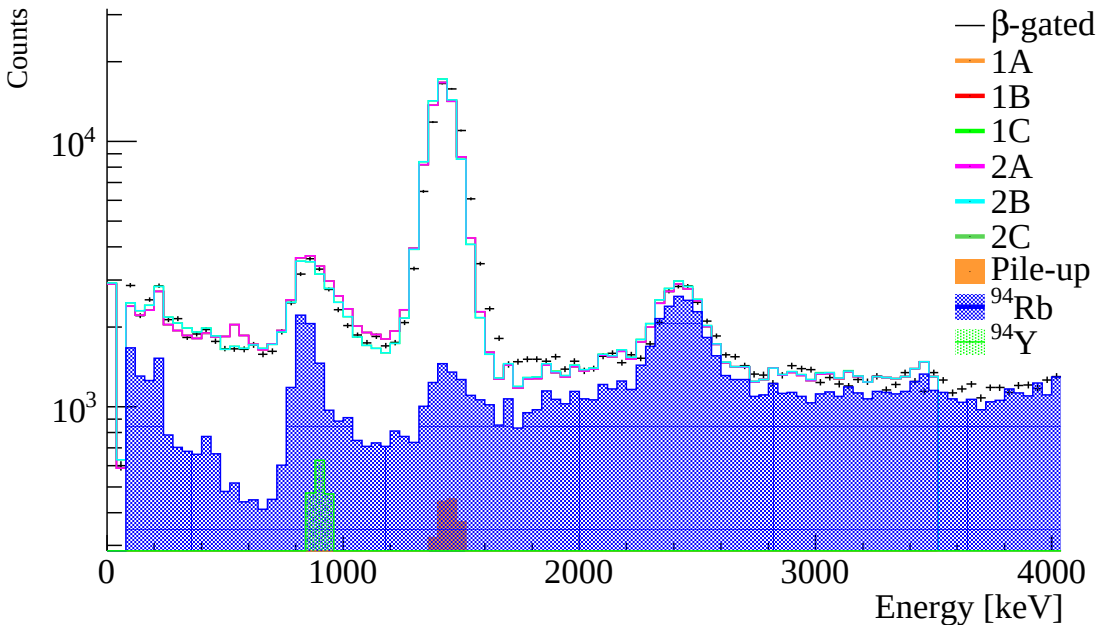

(a) Final Analysis generated responses (plus contaminants) in comparison to the raw *β-gated* spectrum, also showing relevant contaminants (background and pile-up).

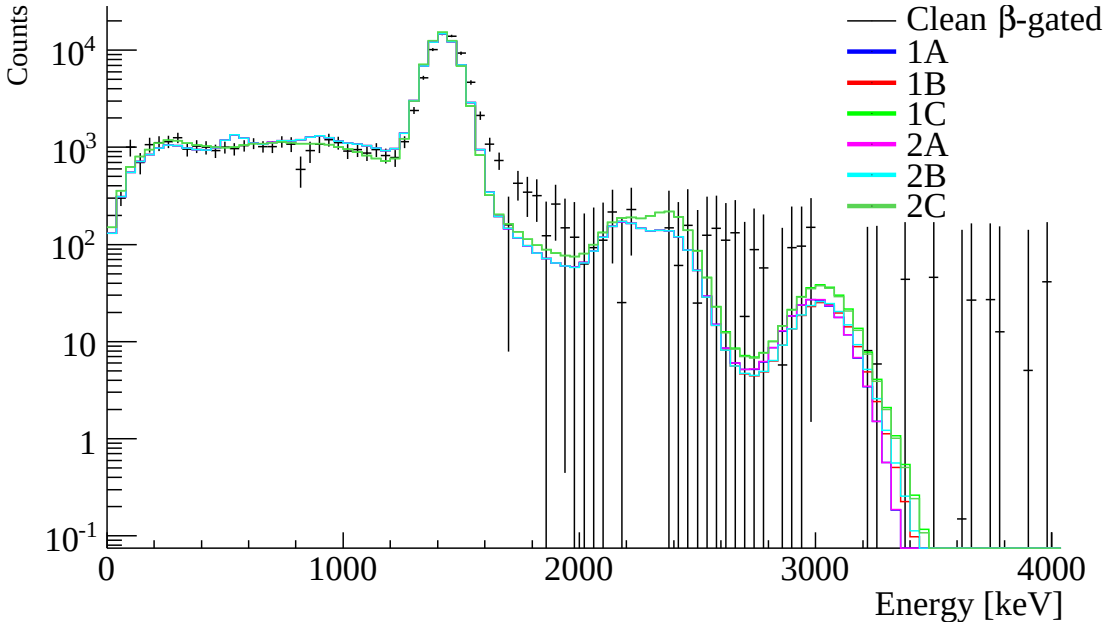

(b) Final analysis generated responses in comparison to the clean *β-gated* spectrum.

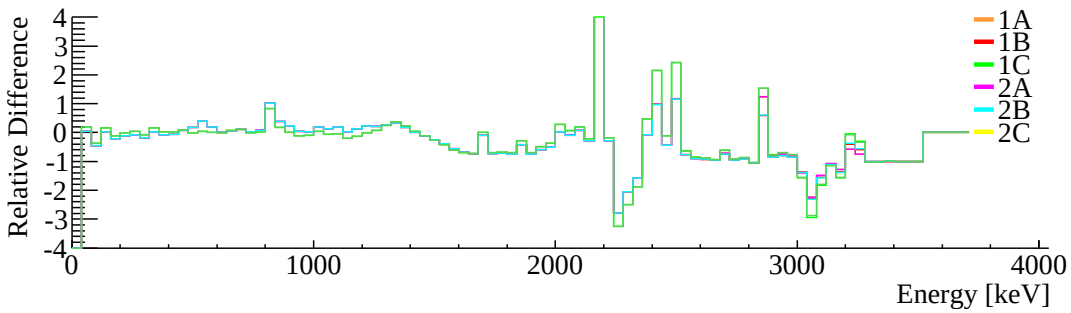

(c) Relative difference from the clean *β-gated* spectrum for each analysis.

Figure 6.34: Final comparison of the generated response for the decay of ^{94}Sr against the collected TAS *β-gated* spectrum. Where LX indicates level (L) scheme 1 and 2 level scheme 2 shown in Table 6.18 and analysis type (X) where A is the analysis without any level continuum, B is the standard analysis and C is the same as option B but without permitting feeding to the 1437 keV level.

Level	β-feeding distribution Intensity [%]							
[keV]	ENSDF	Greenwood	1A	1B	1C	2A	2B	2C
0.00	0.90	1.80	0.32	0.32	0.01	0.35	0.34	0.01
906.91	0.00	0.00	0.00	0.00	0.11	0.00	0.00	0.12
1427.71	98.10	94.80	80.87	80.78	94.24	80.84	80.73	94.31
1437.01	0.19	0.18	14.82	14.82	0.00	14.82	14.82	0.00

Table 6.20: Summary of β-feeding distributions for different analysis of ^{94}Sr. Where LX indicates level (L) scheme 1 and 2 level scheme 2 shown in Table 6.18 and analysis type (X) where A is the analysis without any level continuum, B is the standard analysis and C is the same as option B but without permitting feeding to the 1437 keV level.

The ENSDF recorded γ ray branching ratio for the ^{94}Sr decay is shown in Table 6.21, along side the generated branching from the analyses. Each of these analyses either has low or no feeding to the continuum so unlike the ^{86}Br and ^{91}Rb analysis it is not possible to modify the obtained branching ratio matrix to mirror the recorded levels. Comparing the different analysis options shows that the feeding of the 1437 keV level affects the branching on γ rays in comparison to the recorded branching. Both the analyses with non-permitted feeding to the 1437 keV level are the most comparable to the ENSDF data.

Level	relative γ ray Intensity [%]						
[keV]	ENSDF	1A	1B	1C	2A	2B	2C
432.30	0.00	0.00	0.00	0.00	0.00	0.00	0.00
621.70	1.88	1.95	1.97	2.86	1.95	1.97	2.87
723.80	2.31	2.64	2.58	3.91	2.64	2.61	3.94
906.91	0.37	12.69	12.69	0.71	12.70	12.64	0.60
1202.30	0.00	0.00	0.00	0.00	0.00	0.00	0.00
1427.71	94.34	67.14	67.41	87.95	67.13	67.41	87.96
1437.01	0.18	12.27	12.37	0.07	12.27	12.39	0.07
2182.42	0.73	1.14	1.17	1.26	1.14	1.17	1.27
2373.02	0.11	1.48	1.51	2.66	1.48	1.50	2.67
2969.93	0.08	0.68	0.31	0.58	0.68	0.31	0.62

Table 6.21: Gamma branching ratio of the low energy levels in ^{94}Y for recorded ENSDF (normalised) data and the generated response from the different analyses, all normalised to 100% for shown levels. Where LX indicate level (L) scheme 1 and 2 level scheme 2 shown in Table 6.18 and analysis type (X) where A is the analysis without any level continuum, B is the standard analysis and C is the same as option B but without permitting feeding to the 1437 keV level.

The final comparison to the β-*gated* TAS response is shown in Figure 6.34a with each response giving a reasonable fit for the lower (<400 keV) energy region. The analysis without permitted feeding to the 1437 keV level show a better fit at 550 keV region, whereas the analysis (with and without continuum) permitting feeding to 1437 keV gives a small peak at 550 keV in comparison to the experimental data. These different analysis also differ at the 1100 - 1200 keV region going

above and below the collected experimental data. The comparison to the cleaned *β-gated* TAS data is shown in Figure 6.34b, showing clearer the fit to the lower energy part, with one experimental point at 820 keV not being replicated, but this could be an artefact from the subtraction. Each of the analysis fit to the trailing (higher energy) edge of the 1428-1437 keV peak are poor mirroring some of the problems fitting the tails of peaks in the calibration sources. This poor peak fit may be due to a problem in the MC model, but it is not seen as clearly in the other isotopes. The fit to the higher energy region (>1700 keV) is shown to be poor in the clean response possibly due to the large statistical uncertainty of the experimental data. This results in an unknown part for the analysis, but due to the low number of counts this should have small impact in the resultant mean β or γ energies.

Level scheme	1A	1B	1C	2A	2B	2C
χ^2	3934.63	3935.56	4236.74	3934.51	3935.44	4236.68

Table 6.22: Calculated χ^2 for the response fit to the experimental data. Where LX indicate level (L) scheme 1 and 2 level scheme 2 shown in Table 6.18 and analysis type (X) where A is the analysis without any level continuum, B is the standard analysis and C is the same as option B but without permitting feeding to the 1437 keV level.

The relative difference from the experimental data for each final analysis is shown in Figure 6.34c, with the computed χ^2 values collated in Table 6.22. Figure 6.34b shows small relative differences up to ≈2000 keV as expected from the fitting of the response, and the poor statistics of the subtracted. This higher energy effect is reflected in the large χ^2 values given for each analysis. The response of the analysis withholding feeding to the 1437 keV level showed a better fit to the lower energy region of the data but a poorer fit for the high energy region therefore there χ^2 are larger than the other analysis's values. The key differences in the β-feeding distribution have been shown in Table 6.20 and the full β-feeding distribution is shown in full in Figure 6.35 (a tabulated full version can be found in Appendix A). This feeding comparison shows as expected most feeing to the 1427 keV level.

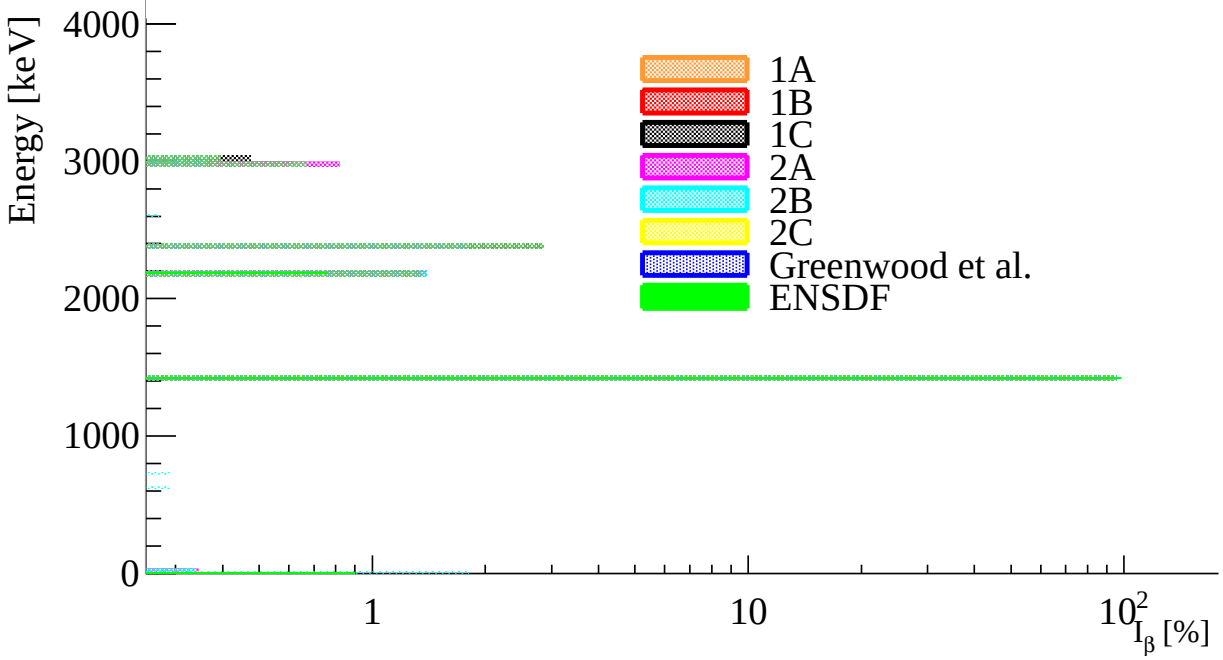

(a) Final generated β feeding distribution (rotated for clearer display which levels are feed).

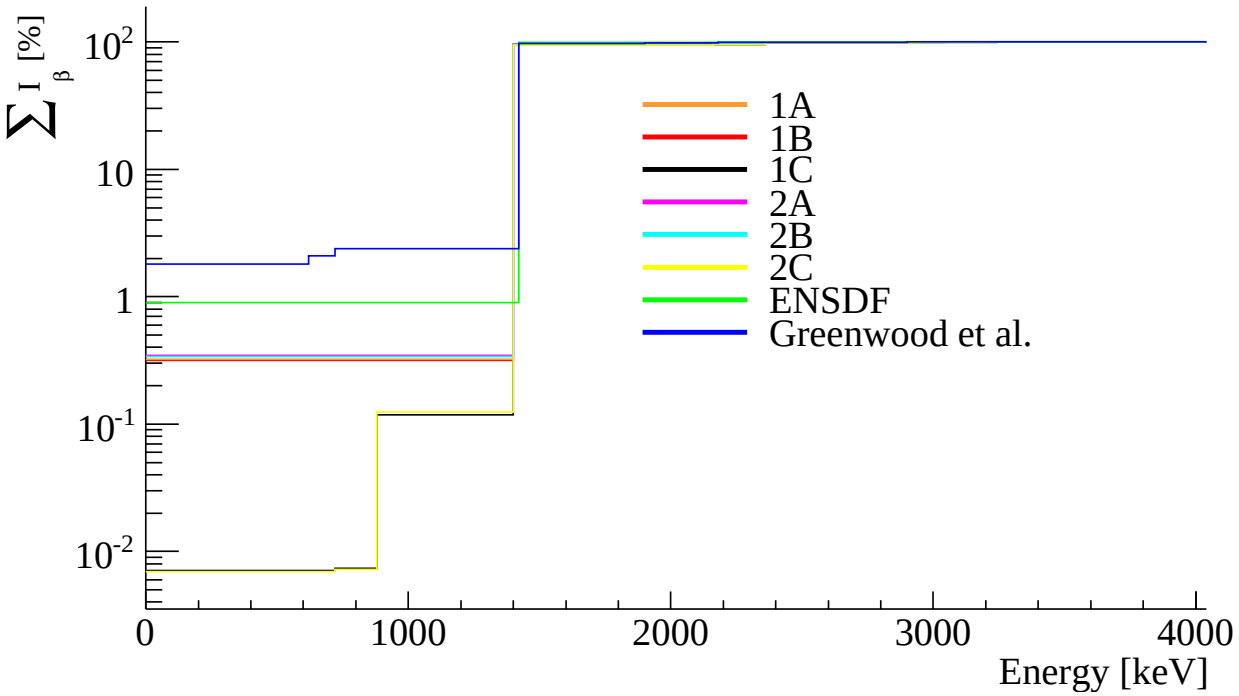

(b) Cumulative sum of the final generated β feeding distribution.

Figure 6.35: Final comparison of the generated β feeding distributions for the decay of ^{94}Sr. Where LX indicates level (L) scheme 1 and 2 level scheme 2 shown in Table 6.18 and analysis type (X) where A is the analysis without any level continuum, B is the standard analysis and C is the same as option B but without permitting feeding to the 1437 keV level.

6.6.4 Implications of the ^{94}Sr Analysis

The dominance of the 1427 keV level in the decay of ^{94}Sr results in difficulties to identify other fed levels using the TAS analysis. The analysis implies that the current recorded level scheme could be complete for the β decay transitions but the results are not conclusive either way.

The β Strength Function of ^{94}Sr

From the feeding distribution it is possible to calculate the β strength function for the ^{94}Sr decay for each of the final analyses, these results are shown in Figure 6.36 in combination to the recorded ENSDF data and the Greenwood at al. data set. The strength from the analyses matches the strength from the 1427 level but gives more strength to the high-energy levels, where in inclusion of this level continuum in unverified.

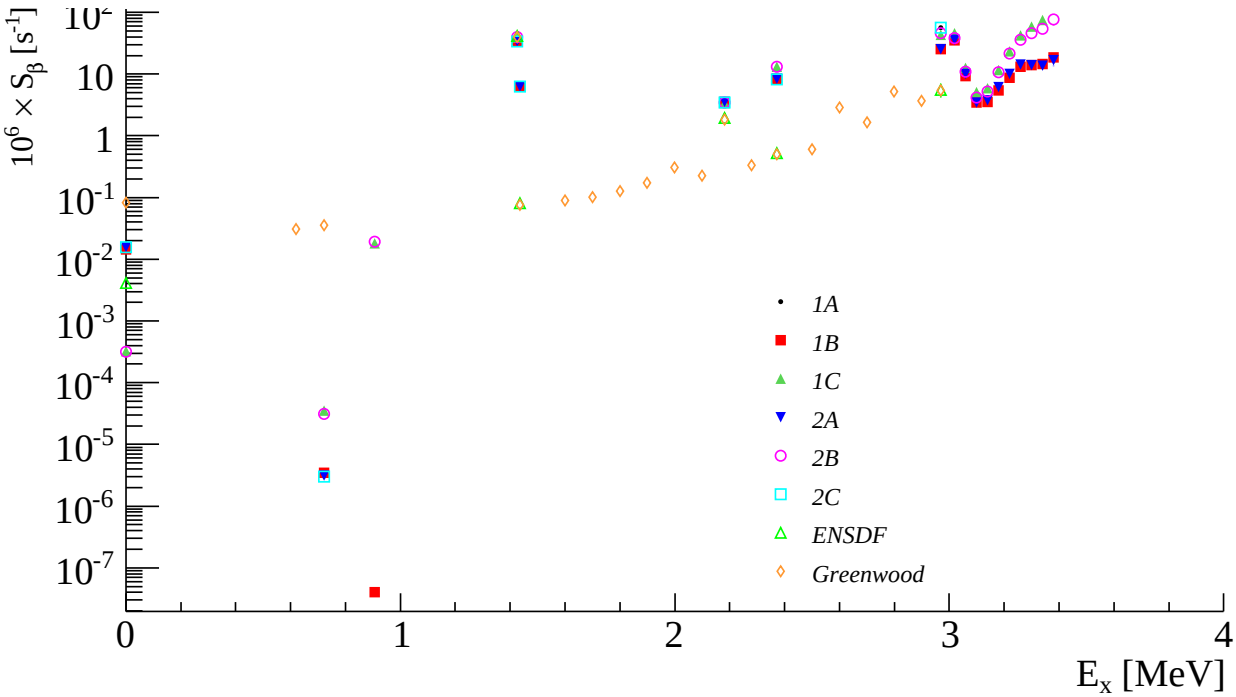

Figure 6.36: The calculated β strength function for the decay of ^{94}Sr for the final analyses and the previously recorded ENSDF data.

The Mean Decay Energy of ^{94}Sr

The mean average decay energy for the analyses is tabulated in Table 6.23 along side the results from nuclear databases.

The statistical uncertainty of these results were calculated from the uncertainty of the feeding distribution for each analysis. The combined statistical uncertainty for the final result was calculated

	$\overline{E_\gamma}$ [keV]	$\overline{E_\beta}$ [keV]
1A	1464.5(33)	828.8(20)
1B	1466.3(33)	828.1(20)
1C	1487.3(38)	819.0(22)
2A	1464.2(33)	829.0(20)
2B	1466.3(38)	828.1(22)
2C	1485.9(33)	819.6(20)
Final result	1472.4(85)[a](149)[b]	825.4(50)[a](64)[b]
Greenwood et al.	1419.2[c]	849.2[c]
ENDF/B-VI.8	1427(9)	840(3)
JEFF-3.1.1	1427(11)	833(6)
JENDL/FPD-2011	1573[c]	732[c]

Table 6.23: Mean average energy for β-particles and γ rays (all collected photons) from the decay of ^{94}Sr. *a*) Statistical uncertainty, *b*) uncertainty due to assumptions of the analysis and *c*) no uncertainty provided.

from summation in quadrature of each statistical uncertainty of the analyses (Table 6.20) combined for this final result. The good reproduction from each of the possible combinations of available spins, parities and level density models produced a range of mean decay values that were used to determine the variance from the final result and provided the uncertainty due to the analysis. The dominance of the 1428keV transition results in this uncertainty (due to the assumptions) being small, because the possible variance in the analysis can only affect a small amount of the feeding.

The comparison of these mean energy shows that the combined final analysis result for mean γ ray energy is increased by ≈50 keV from the JEFF and ENSDF databases, whereas the JENDL library shows a value 100 keV greater then the analysis value. The mean γ generated from the work by Greenwood et al. using the assumption of a 20 keV binning shows a value very close to the ENSDF and JEFF results. The mean average β-particle energy for the analysis is lower than the given values of ENSDF and JEFF and the value from the work by Greenwood et al. The data recorded in JENDL shows a value 100 keV below the analysis result.

7 Conclusion

7.1 Summary

The *pandemonium effect* recorded by high resolution measurements of fission fragment β-decays can be seen when comparing nuclear databases calculations to experimental calorimetry data for decay heat. It has been shown by previous work [76] that total absorption spectroscopy can be used to measure β-decays removing this *pandemonium effect*. The work presented in this thesis has shown that a segmented total absorption γ-ray spectrometer can also be used to unfold the beta feeding distribution without the inclusion of the *pandemonium effect*. This segmentation enabled a scintillation material (BaF_2) previously not used in the construction of a total absorption spectrometer and has showed potential for future measurements. The collection of events for by the whole detector rather then from each individual crystal has enabled an analysis procedure similar to previous TAS analyses.

Nuclear structure Implications

This work has shown that the TAS analysis is complimentary to high precision measurements such as high resolution γ-ray spectroscopy due to the need of an initial level scheme. The TAS analysis has shown that although the included levels are sensitive to if they are fed (from permitted transitions) they are less sensitive to the individual spin or parity within the possible allowed or first forbidden transition range. Outside of the range of permitted transitions the analysis is insensitive due to only assessing if these levels can be fed by gamma transitions. The inclusion of only the level density within the continuum, results in a probability of levels at set energies but this information alone is not enough to confirm new levels within a level scheme.

Mean Average Energy

It has been shown from the β feeding distribution, the mean average energy for β particles and γ rays can be calculated and the comparison of this data to database data gives a good indication of recorded *pandemonium effect*. The mean energy measurements from this work are summarised

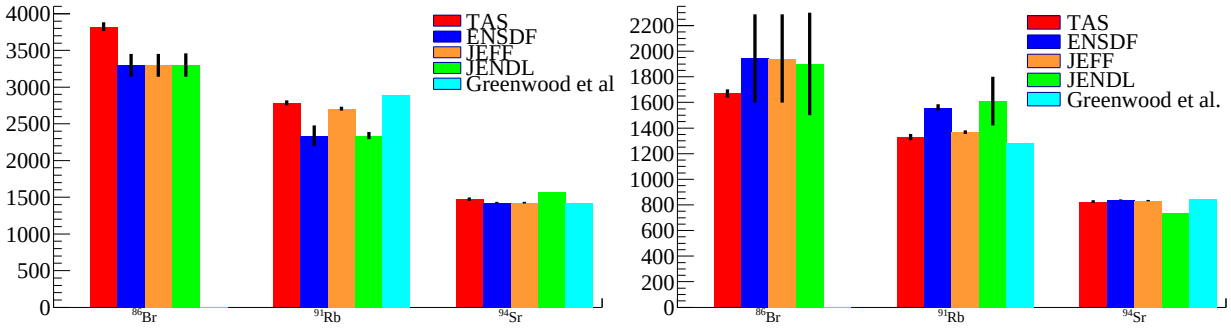

(a) mean average γ energy

(b) mean average β energy

Figure 7.1: Comparison of previously recorded and results from the TAS analysis for the average mean β ($\overline{E_\beta}$) and γ energy ($\overline{E_\gamma}$) for the β-decays of ^{86}Br ^{91}Rb and ^{94}Sr. With the (combined) uncertainties shown in black where available

		Final Results	Greenwood et al.	ENSDF /B-VII.1	JEFF 3.1.1	JENDL /FPD-2011
^{86}Br	$\overline{E_\gamma}$	3822(6)^a(54)^b	-	3297(156)	3297(156)	3300(160)
	$\overline{E_\beta}$	1670(4)^a(28)^b	-	1944(345)	1943(345)	1900(400)
^{91}Rb	$\overline{E_\gamma}$	2788(5)^a(29)^b	2885^c	2340(140)	2706(27)	2340(50)
	$\overline{E_\beta}$	1330(3)^a(22)^b	1282^c	1561(25)	1368(13)	1610(190)
^{94}Sr	$\overline{E_\gamma}$	1472(9)^a(15)^b	1419^c	1427(9)	1427(11)	1573^c
	$\overline{E_\beta}$	826(5)^a(6)^b	849^c	840(3)	833(6)	732^c

Table 7.1: Summary of the mean average energy for β-particles and γ rays (all collected photons) from the decay of ^{86}Br, ^{91}Rb and ^{94}Sr. *a*) Statistical uncertainty, *b*) uncertainty due to assumptions of the analysis and *c*) no uncertainty provided.

in Figure 7.1 and Table 7.1, where the TAS ^{86}Br measurement provides new values for the $\overline{E_\beta}$ and $\overline{E_\gamma}$. These new values for ^{86}Br highlight the *pandemonium effect* with the new $\overline{E_\gamma}$ increased in comparison to three of the different nuclear databases, and a decrease in the $\overline{E_\beta}$ value due to more feeding to higher lying levels in the daughter from this decay. The new results from the ^{91}Rb decay show a change from the ENSDF and JENDL values, but agree with the values included within JEFF, showing the inclusion of the Greenwood data to the JEFF database. The decay of ^{94}Sr is dominated by the β transition to the 1427 keV skewing the mean energy released for β particles and γ rays, resulting in the new measurement being very similar to the recorded database data.

Decay Heat

These new results for the mean decay energy provide new values to previously measured data for decay heat calculations enabling a more accurate theoretical model to be generated against the collected calorimetry data. Once combined with other to be calculated results from the other isotopes measured in the 2009 experiment the real physical and commercial impact will be seen. In combination to any improvements to the decay heat calculations, these new results can be combined

with neutrino data to improve information of the neutrino spectra from these isotopes and thus from nuclear reactors.

Validation of Greenwood et al.

The comparison to the generated feeding distribution for ^{91}Rb and ^{94}Sr with previous work by Greenwood et al. [125] have shown a similar structure. This result in combination with the agreement for the mean average energy for β and γ rays, ratify each TAS measurement technique against each other. The inability to fit the lower energy levels for the ^{91}Rb decay reduces the validity of its end result but the comparison with Greenwood et al. shows that the approximations performed are justifiable. The validation of measurements by Greenwood et al. with the ^{91}Rb and ^{94}Sr results, the methodology used by Greenwood et al. is then validated for a collection of TAS measurements. Increased evidence may be needed for the full inclusion of the previous measurements by Greenwood et al. within nuclear databases, but the improvements of decay heat measurements by TAS analysis has previously been shown.

Rudstam et al.

The difference in the mean γ ray energy for the decay of ^{91}Rb collected by this work and the value used by Rudstam et al. as a normalisation brings in to question the credibility of the results they collected for the γ spectra of many fission fragments. It has been shown that previous TAS analysis agrees with the new value from this work for the mean γ energy, supporting evidence that this previous value included the *pandemonium effect*. The large range of fission fragments measured by Rudstam et al. using ^{91}Rb for normalisation could result in a large impact on the total decay heat measurements by affecting a large number of mean decay energies of fission fragments rather than only ^{91}Rb.

7.2 Future Work

This research has shown the working concept of a multi-segmented total absorption spectrometer, with the use of multiple smaller components, a larger range of available detector materials are possible. Another possibility for a segmented design is a modular construction whereby different components can be added/ removed depending on the measurements requirements. Building on this project, a new segmented NaI(Tl) TAS detector designed by the group in Valencia consisting of 16 square crystal modules has been created, where NaI(Tl) was selected due to its reduced resolution, price and volumes available for manufacture.

The limited counting statistics meant that the full potential of this segmented design could not be fully investigated. The summation of the separate crystals events to form one detector event has been shown to be an effective way to collect the full γ ray cascade. The collection of energy in each crystal and the multiplicity of each event could be used to increase the accuracy of the response generated. The inclusion of this data to an already esoteric analysis may be found to be too complex for the end result required, but possibly a known test case could be used to identify the feasibility of this extra analysis. The use of the multiplicity and the sum of each individual crystal would be highly dependent on the correct scattering and absorption within the MC model.

The analysis of the decay heat of fission fragments using TAS analysis has increased the accuracy of nuclear database data by the elimination of the *pandemonium effect* in some measurements, but there are still many isotope measurements that require remeasurement. As well as isotopes important to decay heat, the improvement of mean decay energies and feeding distribution will reduce uncertainties in nuclear data and help shape the theoretical models.

Bibliography

[1] H. Becquerel. Sur les radiations émises par phosphorescence. *Comptes rendus*, 122:420–421, 1896.

[2] E. Rutherford. LXXIX. The scattering of α and β particles by matter and the structure of the atom. *Philosophical Magazine Series 6*, 21(125):669–688, 1911.

[3] N. Bohr. I. On the constitution of atoms and molecules. *Philosophical Magazine Series 6*, 26(151):1–25, 1913.

[4] D. Rudolph, U. Forsberg, P. Golubev, L. G. Sarmiento, A. Yakushev, L.-L. Andersson, A. Di Nitto, Ch. E. Düllmann, J. M. Gates, K. E. Gregorich, C. J. Gross, F. P. Heßberger, R.-D. Herzberg, J. Khuyagbaatar, J. V. Kratz, K. Rykaczewski, M. Schädel, S. Åberg, D. Ackermann, M. Block, H. Brand, B. G. Carlsson, D. Cox, X. Derkx, K. Eberhardt, J. Even, C. Fahlander, J. Gerl, E. Jäger, B. Kindler, J. Krier, I. Kojouharov, N. Kurz, B. Lommel, A. Mistry, C. Mokry, H. Nitsche, J. P. Omtvedt, P. Papadakis, I. Ragnarsson, J. Runke, H. Schaffner, B. Schausten, P. Thörle-Pospiech, T. Torres, T. Traut, N. Trautmann, A. Türler, A. Ward, D. E. Ward, and N. Wiehl. Spectroscopy of Element 115 Decay Chains. *Phys. Rev. Lett.*, 111:112502, Sep 2013.

[5] M. W. Reed, P. M. Walker, I. J. Cullen, Yu. A. Litvinov, D. Shubina, G. D. Dracoulis, K. Blaum, F. Bosch, C. Brandau, J. J. Carroll, D. M. Cullen, A. Y. Deo, B. Detwiler, C. Dimopoulou, G. X. Dong, F. Farinon, H. Geissel, E. Haettner, M. Heil, R. S. Kempley, R. Knöbel, C. Kozhuharov, J. Kurcewicz, N. Kuzminchuk, S. Litvinov, Z. Liu, R. Mao, C. Nociforo, F. Nolden, W. R. Plaß, Zs. Podolyak, A. Prochazka, C. Scheidenberger, M. Steck, Th. Stöhlker, B. Sun, T. P. D. Swan, G. Trees, H. Weick, N. Winckler, M. Winkler, P. J. Woods, F. R. Xu, and T. Yamaguchi. Long-lived isomers in neutron-rich Z=72-76 nuclides. *Phys. Rev. C*, 86:054321, Nov 2012.

[6] D. Steppenbeck, S. Takeuchi, N. Aoi, P. Doornenbal, M. Matsushita, H. Wang, H. Baba, N. Fukuda, S. Go, M. Honma, et al. Evidence for a new nuclear *magic number* from the level structure of 54Ca. *Nature*, 502(7470):207–210, 2013.

[7] IAEA. IAEA International Fact Finding Expert Mission Of The Fukushima Dai-Ichi NPP Accident Following The Great East Japan Earthquake And Tsunami, June 2011.

[8] L. E. Glendenin, J. E. Gindler, D. J. Henderson, and J. W. Meadows. Mass distributions for monoenergetic-neutron-induced fission of ^{235}U. *Phys. Rev. C*, 24:2600–2605, Dec 1981.

[9] M. A. Kellett, O. Bersillon, and R. W. Mills. The JEFF -3.1/-3.1.1 radioactive decay data and fission yields sub-libraies. Technical Report JEFF Report 20, Nuclear Energy Agency, 2009.

[10] B. Rubio and W. Gelletly. Beta Decay of Exotic Nuclei. In *The Euroschool Lectures on Physics with Exotic Beams Vol. III*, Lecture Notes in Physics 764, 2009.

[11] M. A. Kellett, A. L. Nichols, O. Bersillon, H. Henriksson, R. Jacqmin, B. Roque, J. Katakura, K. Oyamatsu, T. Tachibana, T. Yoshida, A. Algora, B. Rubio, J. L. Taín, C. J. Dean, W. Gelletly, R. W. Mills, I. C. Gauld, P. Möller, and A. Sonzogni. Assessment of Fission Product Decay Data for Decay Heat Calculations. volume Vol. 25 of *A Report by the Working Party on International Evaluation Co-operation of the NEA Nuclear Science Committee*, 2007.

[12] D. I. Poston and H. R. Trellue. Development of a fully-automated Monte Carlo burnup code MONTEBURNS. Technical report, Los Alamos National Laboratory (LANL), Los Alamos, NM, 1999.

[13] A. Tobias, Central Electricity Generating Board. Bekerley Nuclear Laboratories, and Great Britain. Central Electricity Generating Board. *Derivation of decay heat benchmarks for U235 and PU239 by a least squares fit to measured data.* Central Electricity Generating Board, 1989.

[14] R. W. Mills. Private Communication.

[15] A. Algora, D. Jordan, J. L. Taín, B. Rubio, J. Agramunt, A. B. Perez-Cerdan, F. Molina, L. Caballero, E. Nácher, A. Krasznahorkay, M. D. Hunyadi, J. Gulyás, A. Vitéz, M. Csatlós, L. Csige, J. Äysto, H. Penttilä, I. D. Moore, T. Eronen, A. Jokinen, A. Nieminen, J. Hakala, P. Karvonen, A. Kankainen, A. Saastamoinen, J. Rissanen, T. Kessler, C. Weber, J. Ronkainen, S. Rahaman, V. Elomaa, S. Rinta-Antila, U. Hager, T. Sonoda, K. Burkard, W. Hüller, L. Batist, W. Gelletly, A. L. Nichols, T. Yoshida, A. A. Sonzogni, and K. Peräjärvi. Reactor Decay Heat in ^{239}Pu: Solving the γ Discrepancy in the 4-3000-s Cooling Period. *Phys. Rev. Lett.*, 105:202501, Nov 2010.

[16] K. L. Kratz, H. Ohm, A. Schröder, H. Gabelmann, W. Ziegert, B. Pfeiffer, G. Jung, E. Monnand, J. A. Pinston, F. Schussler, G. I. Crawford, S. G. Prussin, and Z. M. de Oliveira. The beta-decay of ^{95}Rb and ^{97}Rb. *Zeitschrift für Physik A Hadrons and Nuclei*, 312:43–57, 1983. 10.1007/BF01411659.

[17] J. P. Dufour, R. Del Moral, A. Fleury, F. Hubert, D. Jean, M. S. Pravikoff, H. Delagrange, H. Geissel, and K. H. Schmidt. Beta decay of ^{17}C, ^{19}N, ^{22}O,^{24}F, ^{26}Ne, ^{32}Al, ^{34}Al,$^{35-36}$Si, $^{36-37-38}$P, ^{40}S. *Zeitschrift für Physik A Hadrons and Nuclei*, 324:487–488, 1986. 10.1007/BF01290934.

[18] J. C. Hardy, L. C. Carraz, B. Jonson, and P. G. Hansen. The essential decay of pandemonium: gamma-ray spectroscopy. *Phys. Lett. B*, 71:307–10 p, 1977.

[19] T. Yoshida, T. Tachibana, F. Storrer, K. Oyamatsu, and J. Katakura. Possible Origin of the Gamma-ray Discrepancy in the Summation Calculations of Fission Product Decay Heat. *J. of Nucl. Sci. Technol.*, 36(2):135–142, 1999.

[20] M. Fallot, S. Cormon, M. Estienne, A. Algora, V. M. Bui, A. Cucoanes, M. Elnimr, L. Giot, D. Jordan, J. Martino, A. Onillon, A. Porta, G. Pronost, A. Remoto, J. L. Taín, F. Yermia, and A.-A. Zakari-Issoufou. New Antineutrino Energy Spectra Predictions from the Summation of Beta Decay Branches of the Fission Products. *Phys. Rev. Lett.*, 109:202504, Nov 2012.

[21] C. Y. Wu, H. Hua, D. Cline, A. B. Hayes, R. Teng, R. M. Clark, P. Fallon, A. Görgen, A. O. Macchiavelli, and K. Vetter. Structure Of Neutron-Rich Nuclei In A 100 Region Observed In Fusion-Fission Reactions. *AIP Conference Proceedings*, 656(1):408–415, 2003.

[22] D. Mücher, J. Iwanicki, J. Jolie, I. Stefanescu, J. Van de Walle, F. Becker, U. Bergmann, A. Blazhev, E. Bouchez, P. Butler, J. Cederkäll, T. Czosnyka, T. Davinson, J. Eberth, T. Faestermann, S. Franchoo, C. Fransen, J. Gerl, R. Gernhäuser, D. Habs, R.-D. Herzberg, M. Huyse, D. Jenkins, G. Jones, O. Kester, W. Korten, J. Kownacki, T. Kröll, R. Krücken, Z. Liu, S. Mandal, P. Napiorkowski, T. Nilsson, N. Pietralla, G. Rainovski, H. Scheit, A. Scherillo, D. Schwalm, T. Sieber, Ch. Theisen, P. Van Duppen, N. Warr, D. Weisshaar, F. Wenander, B. Wolf, P. Woods, and M. Zielinska. Shell Structure and Shape Changes in Neutron Rich Krypton Isotopes. *AIP Conference Proceedings*, 1090(1):587–588, 2009.

[23] A. F. Stehney and E. P. Steinberg. A New Nuclide ^{86}Br. *Phys. Rev.*, 127:563–569, Jul 1962.

[24] E. T. Williams and C. D. Coryell. Decay of 54-sec $Br86$ and 55-sec $Br87$. *Phys. Rev.*, 144(3):945–951, Apr 1966.

[25] M.B. Chadwick, M. Herman, P. Obložinský, M.E. Dunn, Y. Danon, A.C. Kahler, D.L. Smith, B. Pritychenko, G. Arbanas, R. Arcilla, R. Brewer, D.A. Brown, R. Capote, A.D. Carlson, Y.S. Cho, H. Derrien, K. Guber, G.M. Hale, S. Hoblit, S. Holloway, T.D. Johnson, T. Kawano, B.C. Kiedrowski, H. Kim, S. Kunieda, N.M. Larson, L. Leal, J.P. Lestone, R.C. Little, E.A. McCutchan, R.E. MacFarlane, M. MacInnes, C.M. Mattoon, R.D. McKnight, S.F. Mughabghab, G.P.A. Nobre, G. Palmiotti, A. Palumbo, M.T. Pigni, V.G. Pronyaev, R.O. Sayer, A.A. Sonzogni, N.C. Summers, P. Talou, I.J. Thompson, A. Trkov, R.L. Vogt, S.C. van der Marck, A. Wallner, M.C. White, D. Wiarda, and P.G. Young. ENDF/B-VII.1 Nuclear Data for Science and Technology: Cross Sections, Covariances, Fission Product Yields and Decay Data. *Nuclear Data Sheets*, 112(12):2887–2996, 2011. Special Issue on ENDF/B-VII.1 Library.

[26] E. Achterberg, F. C. Iglesias, A. E. Jech, J. A. Moragues, M. L. Pérez, J. J. Rossi, W. Scheuer, and J. F. Suárez. Levels of ^{86}Kr Fed in the Decay of ^{86}Br. *Phys. Rev. C*, 5:1587–1592, May 1972.

[27] M.H. Hurdus and L. Tomlinson. Gamma-ray emission from 84–87Se and 85–88Br isotopes. *Journal of Inorganic and Nuclear Chemistry*, 37(1):1–9, 1975.

[28] D.R. Slaughter, F.M. Nuh, and S.G. Prussin. γ-Rays from decay of ^{88}Br. *Journal of Inorganic and Nuclear Chemistry*, 38(10):1753–1755, 1976.

[29] B. Singh. Nuclear Data Sheets for A = 86. *Nuclear Data Sheets*, 94(1):1–130, 2001.

[30] S. Rahaman, U. Hager, V.-V. Elomaa, T. Eronen, J. Hakala, A. Jokinen, A. Kankainen, P. Karvonen, I.D. Moore, H. Penttilä, S. Rinta-Antila, J. Rissanen, A. Saastamoinen, T. Sonoda, and J. Äystö. Precise atomic masses of neutron-rich Br and Rb nuclei close to the r-process path. *The European Physical Journal A*, 32(1):87–96, 2007.

[31] M.-G. Porquet, A. Astier, Ts. Venkova, I. Deloncle, F. Azaiez, A. Buta, D. Curien, O. Dorvaux, G. Duchêne, B.J.P. Gall, F. Khalfallah, I. Piqueras, M. Rousseau, M. Meyer, N. Redon, O. Stézowski, R. Lucas, and A. Bogachev. High-spin excitations of the odd-odd $^{88}_{37}$Rb$_{51}$ and $^{86}_{35}$Br$_{51}$ nuclei: πp3/2 νd5/2 and πf5/2 νd5/2 residual interactions. *The European Physical Journal A*, 40(2):131–141, 2009.

[32] N. Fotiades, M. Devlin, R. O. Nelson, and T. Granier. Low-spin states in ^{86}Kr from the $(n,n^{'})$ reaction. *Phys. Rev. C*, 87:044336, Apr 2013.

[33] O. Kofoed-Hansen and K. O. Nielsen. Short-Lived Krypton Isotopes and Their Daughter Substances. *Phys. Rev.*, 82:96–97, Apr 1951.

[34] M. D. Glascock, W. L. Talbert, and C. L. Duke. Level schemes of $Rb91$ and $Sr91$ populated in beta decay. *Phys. Rev. C*, 13(4):1630–1643, Apr 1976.

[35] E. Achterberg, F. C. Iglesias, A. E. Jech, J. A. Moragues, D. Otero, M. L. Pérez, A. N. Proto, J. J. Rossi, and W. Scheuer. Levels of ^{91}Rb and ^{91}Sr fed in the decays of ^{91}Kr and ^{91}Rb. *Phys. Rev. C*, 9:299–309, Jan 1974.

[36] G.C. Carlson, W.C. Schick Jr., W.L. Talbert Jr., and F.K. Wohn. Half-lives of some short-lived mass-separated gaseous fission products and their daughters. *Nuclear Physics A*, 125(2):267–275, 1969.

[37] I. Amarel, R. Bernas, R. Foucher, J. Jastrzebski, A. Johnson, J. Teillac, and H. Gauvin. Half life determination of some short-lived isotopes of Rb, Sr, Cs, Ba, La and identification of 93,

94, 95, 96Rb as delayed neutron precursors by on-line mass-spectrometry. *Physics Letters B*, 24(8):402–404, 1967.

[38] J. F. Mason and M. W. Johns. Level structures of ^{91}Rb and ^{91}Sr as populated in beta decay. *Canadian Journal of Physics*, 48(24):2895–2905, 1970.

[39] C. M. Baglin. Nuclear Data Sheets for A = 91. *Nuclear Data Sheets*, 86(1):1–150, 1999.

[40] G. Rudstam, P.I. Johansson, O. Tengblad, P. Aagaard, and J. Eriksen. Beta and gamma spectra of short-lived fission products. *Atomic Data and Nuclear Data Tables*, 45(2):239–320, 1990.

[41] J.D. Knight, D.C. Hoffman, B.J. Dropesky, and D.L. Frasco. Radiations of ^{93}Y and ^{94}Y and half-lives of ^{93}Sr and ^{94}Sr. *Journal of Inorganic and Nuclear Chemistry*, 10(3–4):183–197, 1959.

[42] Y. Funakoshi, K. Okano, and Y. Kawase. Studies of the β-decay of ^{94}Sr and the level scheme of ^{94}Y. *Nuclear Physics A*, 431(3):461–472, 1984.

[43] D. Abriola and A.A. Sonzogni. Nuclear Data Sheets for A = 94. *Nuclear Data Sheets*, 107(9):2423–2578, 2006.

[44] R.C. Greenwood, R.G. Helmer, M.H. Putnam, and K.D. Watts. Measurement of β–decay intensity distributions of several fission-product isotopes using a total absorption γ-ray spectrometer. *Nuclear Instruments and Methods in Physics Research Section A: Accelerators, Spectrometers, Detectors and Associated Equipment*, 390(1-2):95–154, 1997.

[45] O. Hahn and F. Strassmann. Über den Nachweis und das Verhalten der bei der Bestrahlung des Urans mittels Neutronen entstehenden Erdalkalimetalle. *Naturwissenschaften*, 27(1):11–15, 1939.

[46] L. Meitner and O. R Frisch. Disintegration of Uranium by Neutrons: a New Type of Nuclear Reaction (Reprinted from Nature, February 11, 1939) . *Nature*, 224(5218):466–467, November 1969.

[47] T. Radon, Th. Kerscher, B. Schlitt, K. Beckert, T. Beha, F. Bosch, H. Eickhoff, B. Franzke, Y. Fujita, H. Geissel, M. Hausmann, H. Irnich, H. C. Jung, O. Klepper, H.-J. Kluge, C. Kozhuharov, G. Kraus, K. E. G. Löbner, G. Münzenberg, Yu. Novikov, F. Nickel, F. Nolden, Z. Patyk, H. Reich, C. Scheidenberger, W. Schwab, M. Steck, K. Sümmerer, and H. Wollnik. Schottky Mass Measurements of Cooled Proton-Rich Nuclei at the GSI Experimental Storage Ring. *Phys. Rev. Lett.*, 78:4701–4704, Jun 1997.

[48] S. Rahaman, U. Hager, V.-V. Elomaa, T. Eronen, J. Hakala, A. Jokinen, A. Kankainen, P. Karvonen, I.D. Moore, H. Penttilä, S. Rinta-Antila, J. Rissanen, A. Saastamoinen, T. Sonoda, and J. Äystö. Precise atomic masses of neutron-rich Br and Rb nuclei close to the r-process path. *The European Physical Journal A*, 32(1):87–96, 2007.

[49] K. S. Krane. *Introductory Nuclear Physics*. John Wiley & Son, second edition, 1987.

[50] F. Dyson. A meeting with Enrico Fermi. *Nature*, 427(6972):297, 01 2004.

[51] A.M. Petros'yants. A pioneer of nuclear power. *IAEA Bulletin*, 26(4), 1984.

[52] International Atomic Energy Agency. *Energy, Electricity and Nuclear Power Estimates for the Period up to 2050*. IAEA, 2012.

[53] P. E. Hodgson. *Introductory nuclear physics*. Clarendon Press Oxford University Press, Oxford New York, 1997.

[54] NDA. Spent Fuels. https://www.nda.gov.uk/strategy/spentfuelsmgmt/.

[55] K. Shibata, O. Iwamoto, T. Nakagawa, N. Iwamoto, A. Ichihara, S. Kunieda, S. Chiba, K. Furutaka, N. Otuka, T. Ohsawa, T. Murata, H. Matsunobu, A. Zukeran, S. Kamada, and J. Katakura. Japanese Evaluated Nuclear Data Library.

[56] E. Rutherford. VIII. Uranium radiation and the electrical conduction produced by it. *Philosophical Magazine Series 5*, 47(284):109–163, 1899.

[57] W. Pauli. Pauli letter collection: letter to Lise Meitner. Typed copy, 1930.

[58] F. Reines and C. L. Cowan. The neutrino. *Nature*, 178(4531):446–449, 1956.

[59] J. S. Lilley. *Nuclear physics : principles and applications*. J. Wiley, Chichester New York, 2001.

[60] G. Longworth. *The Radiochemical manual*. AEA Technology, Harwell, Oxfordshire, 1998.

[61] H. Bateman. The solution of a system of differential equations occurring in the theory of radioactive transformations. In *Proc. Cambridge Philos. Soc*, volume 15, 1910.

[62] Pauli Exclusion Principle.

[63] E. Fermi. Versuch einer Theorie der -Strahlen. I. *Zeitschrift für Physik*, 88(3-4):161–177, 1934.

[64] F. L. Wilson. Fermi's Theory of Beta Decay. *American Journal of Physics*, 36(12):1150–1160, 1968.

[65] P. A. M. Dirac. The Quantum Theory of the Emission and Absorption of Radiation. *Proceedings of the Royal Society of London. Series A, Containing Papers of a Mathematical and Physical Character*, 114(767):pp. 243–265, 1927.

[66] C. Wu and S.A. Moszkowski. *Beta decay*. Interscience monographs and texts in physics and astronomy. Interscience Publishers, 1966.

[67] J. M. Blatt. *Theoretical nuclear physics / by John M. Blatt & Victor F. Weisskopf*. New York : Wiley, 1952. 864 p.

[68] N.B. Gove and M.J. Martin. Log-f tables for beta decay. *Atomic Data and Nuclear Data Tables*, 10(3):205–219, 1971.

[69] M.J. Martin. Nuclear Data Sheets for A = 208. *Nuclear Data Sheets*, 108(8):1583–1806, 2007.

[70] D. Cano-Ott, J.L. Taín, A. Gadea, B. Rubio, L. Batist, M. Karny, and E. Roeckl. Monte Carlo simulation of the response of a large NaI(Tl)total absorption spectrometer for -decay studies. *Nuclear Instruments and Methods in Physics Research Section A: Accelerators, Spectrometers, Detectors and Associated Equipment*, 430(2–3):333–347, 1999.

[71] E.J. Konopinski, M.E. Rose, and K. Siegbahn (Ed.). *Alpha-, beta- and gamma-ray spectroscopy*, volume 2 of *Alpha-, Beta- and Gamma-ray Spectroscopy*. North-Holland Pub. Co., 1965.

[72] K. Takahashi, M. Yamada, and T. Kondoh. Beta-decay half-lives calculated on the gross theory. *Atomic Data and Nuclear Data Tables*, 12(1):101–142, 1973.

[73] R. Capote, M. Herman, P. Obložinský, P.G. Young, S. Goriely, T. Belgya, A.V. Ignatyuk, A.J. Koning, S. Hilaire, V.A. Plujko, M. Avrigeanu, O. Bersillon, M.B. Chadwick, T. Fukahori, Zhigang Ge, Yinlu Han, S. Kailas, J. Kopecky, V.M. Maslov, G. Reffo, M. Sin, E.Sh. Soukhovitskii, and P. Talou. RIPL - Reference Input Parameter Library for Calculation of Nuclear Reactions and Nuclear Data Evaluations. *Nuclear Data Sheets*, 110(12):3107–3214, 2009.

[74] S. Goriely, F. Tondeur, and J.M. Pearson. A Hartree–Fock Nuclear Mass Table. *Atomic Data and Nuclear Data Tables*, 77(2):311–381, 2001.

[75] P. Demetriou and S. Goriely. Microscopic nuclear level densities for practical applications. *Nuclear Physics A*, 695(1–4):95–108, 2001.

[76] D. Jordan, A. Algora, J. L. Taín, B. Rubio, J. Agramunt, A. B. Perez-Cerdan, F. Molina, L. Caballero, E. Nácher, A. Krasznahorkay, M. D. Hunyadi, J. Gulyás, A. Vitéz, M. Csatlós, L. Csige, J. Äysto, H. Penttilä, I. D. Moore, T. Eronen, A. Jokinen, A. Nieminen, J. Hakala, P. Karvonen, A. Kankainen, A. Saastamoinen, J. Rissanen, T. Kessler, C. Weber, J. Ronkainen, S. Rahaman, V. Elomaa, U. Hager, S. Rinta-Antila, T. Sonoda, K. Burkard, W. Hüller, L. Batist, W. Gelletly, A. L. Nichols, T. Yoshida, A. A. Sonzogni, K. Peräjärvi, A. Petrovici, K. W. Schmid, and A. Faessler. Total absorption study of the β decay of ^{102,104,105}Tc. *Phys. Rev. C*, 87:044318, Apr 2013.

[77] W. Dilg, W. Schantl, H. Vonach, and M. Uhl. Level density parameters for the back-shifted fermi gas model in the mass range $40 < A < 250$. *Nuclear Physics A*, 217(2):269–298, 1973.

[78] T. Von Egidy, H.H. Schmidt, and A.N. Behkami. Nuclear level densities and level spacing distributions: Part {II}. *Nuclear Physics A*, 481(2):189–206, 1988.

[79] A. Gilbert and A. G. W. Cameron. A Composite Nuclear-Level Density Formula With Shell Corrections. *Canadian Journal of Physics*, 43(8):1446–1496, 1965.

[80] Glenn F Knoll. *Radiation Detection and Measurement*. John Wiley & Son, third edition, 1999.

[81] K. Debertin and W. Pe ara. Calibration of high-purity germanium detectors in the energy range from 25 to 122 keV. *The International Journal of Applied Radiation and Isotopes*, 34(2):515–517, 1983.

[82] A. Algora, B. Rubio, D. Cano-Ott, J. L. Taín, A. Gadea, J. Agramunt, M. Gierlik, M. Karny, Z. Janas, A. Płochocki, K. Rykaczewski, J. Szerypo, R. Collatz, J. Gerl, M. Górska, H. Grawe, M. Hellström, Z. Hu, R. Kirchner, M. Rejmund, E. Roeckl, M. Shibata, L. Batist, and J. Blomqvist. Fine structure of the Gamow-Teller resonance revealed in the decay of ^{150}Ho 2^- isomer. *Phys. Rev. C*, 68:034301, Sep 2003.

[83] C.L. Duke, P.G. Hansen, O.B. Nielsen, and G. Rudstam. Strength-function phenomena in electron-capture beta decay. *Nuclear Physics A*, 151(3):609–633, 1970.

[84] P. Hornshøj, B.R. Erdal, P.G. Hansen, B. Jonson, K. Aleklett, and G. Nyman. Beta-strength functions of neutron-deficient isotopes in the xenon and mercury regions. *Nuclear Physics A*, 239(1):15–28, 1975.

[85] K. H. Johansen, K. B. Nielsen, and G. Rudstam. Strength functions in the β-decay of short-lived fission products. *Nuclear Physics A*, 203:481–495, March 1973.

[86] AA Bykov, VD Vitman, FV Moroz, and Yu V Naumov. Spectrometer of Total γ-Rays Absorption for Measurement of β-Decay Strength Function. *Izv. AN SSSR, Ser. Fiz*, 44:918–926, 1980.

[87] R.C. Greenwood, M.H. Putnam, and K.D. Watts. Ground-state β-branching intensities of several fission-product isotopes measured using a total absorption γ-ray spectrometer. *Nuclear Instruments and Methods in Physics Research Section A: Accelerators, Spectrometers, Detectors and Associated Equipment*, 378(1â€“2):312–320, 1996.

[88] M. Karny, J.M. Nitschke, L.F. Archambault, K. Burkard, D. Cano-Ott, M. Hellström, W. Hüller, R. Kirchner, S. Lewandowski, E. Roeckl, and A. Sulik. Coupling a total absorption spectrometer to the {GSI} on-line mass separator. *Nuclear Instruments and Methods in Physics Research Section B: Beam Interactions with Materials and Atoms*, 126(1 – 4):411–415, 1997.

[89] B Rubio, W Gelletly, E Nácher, A Algora, J L Taín, A Pérez, and L Caballero. Beta decay studies with the total absorption technique: past, present and future. *Journal of Physics G: Nuclear and Particle Physics*, 31(10):S1477, 2005.

[90] E. Nácher, A. Algora, B. Rubio, J. L. Taín, M. J. G. Borge, D. Cano-Ott, S. Courtin, Ph. Dessagne, D. Escrig, L. M. Fraile, W. Gelletly, A. Jungclaus, G. Le Scornet, F. Maréchal, Ch. Miehé, E. Poirier, and O. Tengblad. Beta decay of ^{76}Sr using the Total Absorption Spectrometer "Lucrecia" at ISOLDE-CERN. *AIP Conference Proceedings*, 701(1):252–256, 2004.

[91] N. Metropolis and S. Ulam. The Monte Carlo Method. *Journal of the American Statistical Association*, 44(247):pp. 335–341, 1949.

[92] B.R. Erdal and G. Rudstam. Response function of a good-geometry detector for a γ-ray cascade. *Nuclear Instruments and Methods*, 104(2):263–283, 1972.

[93] J.T. Goorley et al. Initial MCNP6 Release Overview - MCNP6 version 1.0.

[94] A. Ferrari, P.R. Sala, A. Fasso, and J. Ranft. "FLUKA: a multi-particle transport code", 2005.

[95] J. Apostolakis, A. Bagulya, S. Elles, V. N. Ivanchenko, J. Jacquemier, M. Maire, T. Toshito, and L. Urban. Validation and verification of Geant4 standard electromagnetic physics. *Journal of Physics: Conference Series*, 219(3):032044, 2010.

[96] S. Agostinelli, J. Allison, K. Amako, J. Apostolakis, H. Araujo, P. Arce, M. Asai, D. Axen, S. Banerjee, G. Barrand, F. Behner, L. Bellagamba, J. Boudreau, L. Broglia, A. Brunengo, H. Burkhardt, S. Chauvie, J. Chuma, R. Chytracek, G. Cooperman, G. Cosmo, P. Degtyarenko, A. Dell'acqua, G. Depaola, D. Dietrich, R. Enami, A. Feliciello, C. Ferguson, H. Fesefeldt, G. Folger, F. Foppiano, A. Forti, S. Garelli, S. Giani, R. Giannitrapani, D. Gibin, Gomez, I. Gonzalez, Gracia, G. Greeniaus, W. Greiner, V. Grichine, A. Grossheim, S. Guatelli, P. Gumplinger, R. Hamatsu, K. Hashimoto, H. Hasui, A. Heikkinen, A. Howard, V. Ivanchenko, A. Johnson, F. W. Jones, J. Kallenbach, N. Kanaya, M. Kawabata, Y. Kawabata, M. Kawaguti, S. Kelner, P. Kent, A. Kimura, T. Kodama, R. Kokoulin, M. Kossov, H. Kurashige, E. Lamanna, T. Lampen, V. Lara, V. Lefebure, F. Lei, M. Liendl, W. Lockman, F. Longo, S. Magni, M. Maire, E. Medernach, K. Minamimoto, Mora, Y. Morita, K. Murakami, M. Nagamatu, R. Nartallo, P. Nieminen, T. Nishimura, K. Ohtsubo, M. Okamura, S. O'Neale, Y. Oohata, K. Paech, J. Perl, A. Pfeiffer, M. G. Pia, F. Ranjard, A. Rybin, S. Sadilov, E. Di Salvo, G. Santin, T. Sasaki, N. Savvas, Y. Sawada, S. Scherer, S. Sei, V. Sirotenko, D. Smith, N. Starkov, H. Stoecker, J. Sulkimo, M. Takahata, S. Tanaka, E. Tcherniaev, Safai, M. Tropeano, P. Truscott, H. Uno, L. Urban, P. Urban, M. Verderi, A. Walkden, W. Wander, H. Weber, J. P. Wellisch, T. Wenaus, D. C. Williams, D. Wright, T. Yamada, H. Yoshida, and D. Zschiesche. GEANT4 – a simulation toolkit. *Nuclear Instruments and Methods in Physics Research Section A: Accelerators, Spectrometers, Detectors and Associated Equipment*, 506(3):250–303, July 2003.

[97] J. L. Taín, A. Algora, E. Estevez, B. Rubio, E. Valencia, D. Jordan, J. Aysto, T. Eronen, A. Jokinen, I. Moore, H. Pentilla, J. Riisanen, L. Batist, M. Bowry, M. Bunce, W. Gelletly, R. Caballero, G. Cortes, B. Gomez-Hornillos, V. Gorlychev, D. Cano-Ott, A. Garcia, T. Martinez, C. Domingo-Pardo, M. Fallot, L. Giot, A. Porta, and B. Van Vinh. Beta Decay Studies of Neutron Rich Nuclei Using Total Absorption Gamma-ray Spectroscopy and Delayed Neutron Measurements. *Journal of the Korean Physical Society*, 59(2):1499–1502, 2011.

[98] V. F. Sears. Neutron scattering lengths and cross sections. *Neutron News*, 3(3):26–37, 1992.

[99] C. Guerrero, D. Cano-Ott, E. Mendoza, J.L. Taín, A. Algora, E. Berthoumieux, N. Colonna, C. Domingo-Pardo, E. González-Romero, M. Heil, D. Jordán, F. Käppeler, C. Lampoudis, T. Martínez, C. Massimi, and R. Plag. Monte Carlo simulation of the n_TOF Total Absorption Calorimeter. *Nuclear Instruments and Methods in Physics Research Section A: Accelerators, Spectrometers, Detectors and Associated Equipment*, 671(0):108–117, 2012.

[100] University of Jyväskylä. https://www.jyu.fi/fysiikka/en/research/accelerator/igisol/ionguide.html.

[101] J. Ärje, J. Äystö, H. Hyvönen, P. Taskinen, V. Koponen, J. Honkanen, K. Valli, A. Hautojärvi, and K. Vierinen. The ion guide isotope separator on-line, IGISOL. *Nuclear Instruments and Methods in Physics Research Section A: Accelerators, Spectrometers, Detectors and Associated Equipment*, 247(3):431–437, 1986.

[102] V.S. Kolhinen, S. Kopecky, T. Eronen, U. Hager, J. Hakala, J. Huikari, A. Jokinen, A. Nieminen, S. Rinta-Antila, J. Szerypo, and J. Äystö. JYFLTRAP: a cylindrical Penning trap for isobaric beam purification at {IGISOL}. *Nuclear Instruments and Methods in Physics Research Section A: Accelerators, Spectrometers, Detectors and Associated Equipment*, 528(3):776–787, 2004.

[103] U. Hager, T. Eronen, J. Hakala, A. Jokinen, V. S. Kolhinen, S. Kopecky, I. Moore, A. Nieminen, M. Oinonen, S. Rinta-Antila, J. Szerypo, and J. Äystö. First Precision Mass Measurements of Refractory Fission Fragments. *Phys. Rev. Lett.*, 96:042504, Feb 2006.

[104] E. Valencia Martin. Charaterization of a Segmented BaF_2 Total Absorption Gamma-Ray Spectrometer. Master's thesis, University of Valencia, University of Valencia, December 2010.

[105] R. Brun and F. Rademakers. ROOT - An Object Oriented Data Analysis Framework,. Proceedings AIHENP'96 Workshop, Lausanne, Sep. 1996, Nucl. Inst. & Meth. in Phys. Res. A 389 (1997) 81-86. See also http://root.cern.ch/.

[106] L.E Dinca, P Dorenbos, J.T.M de Haas, V.R Bom, and C.W.E Van Eijk. Alpha–gamma pulse shape discrimination in CsI: Tl, CsI: Na and BaF_2 scintillators. *Proceedings of the 6th International Conference on Inorganic Scintillators and their Use in Scientific and Industrial Applications*.

[107] D. Cano-Ott, J.L. Taín, A. Gadea, B. Rubio, L. Batist, M. Karny, and E. Roeckl. Pulse pileup correction of large NaI(Tl) total absorption spectra using the true pulse shape. *Nuclear Instruments and Methods in Physics Research Section A: Accelerators, Spectrometers, Detectors and Associated Equipment*, 430(2–3):488–497, 1999.

[108] C. M. Baglin. Nuclear Data Sheets for A = 92. *Nuclear Data Sheets*, 113(10):2187–2389, 2012.

[109] P. Dorenbos, J. T M de Haas, R. Visser, C. W E Van Eijk, and R.W. Hollander. Absolute light yield measurements on BaF2 crystals and the quantum efficiency of several photomultiplier tubes. *Nuclear Science, IEEE Transactions on*, 40(4):424–430, 1993.

[110] J. F. Ziegler, J. P. Biersack, and Matthias D. Ziegler. *SRIM, the stopping and range of ions in matter*. SRIM Co., 2008.

[111] J.L. Taín and D. Cano-Ott. Algorithms for the analysis of -decay total absorption spectra. *Nuclear Instruments and Methods in Physics Research Section A: Accelerators, Spectrometers, Detectors and Associated Equipment*, 571(3):728–738, 2007.

[112] Till von Egidy and Dorel Bucurescu. Systematics of nuclear level density parameters. *Phys. Rev. C*, 72:044311, Oct 2005.

[113] J. Kopecky and M. Uhl. Test of gamma-ray strength functions in nuclear reaction model calculations. *Phys. Rev. C*, 41:1941–1955, May 1990.

[114] M. E. Estevez Aguado, A. Algora, B. Rubio, J. Bernabeu, E. Nácher, J. L. Taín, A. Gadea, J. Agramunt, K. Burkard, W. Hüller, J. Döring, R. Kirchner, I. Mukha, C. Plettner, E. Roeckl, H. Grawe, R. Collatz, M. Hellström, D. Cano-Ott, M. Karny, Z. Janas, M. Gierlik, A. Płochocki, K. Rykaczewski, L. Batist, F. Moroz, V. Wittman, A. Blazhev, J. J. Valiente, and C. Espinoza. β-decay study of ^{150}Er, ^{152}Yb, and ^{156}Yb: Candidates for a monoenergetic neutrino beam facility. *Phys. Rev. C*, 84:034304, Sep 2011.

[115] P. Moller, J.R. Nix, W.D. Myers, and W.J. Swiatecki. Nuclear Ground-State Masses and Deformations. *Atomic Data and Nuclear Data Tables*, 59(2):185–381, 1995.

[116] P. Moller, J.R. Nix, and K.-L. Kratz. Nuclear Properties For Astrophysical And Radioactive-Ion-Beam Applications. *Atomic Data and Nuclear Data Tables*, 66(2):131–343, 1997.

[117] J.C. Hardy. Towards a reliable method for calculating average radiation widths in exotic nuclei. *Physics Letters B*, 109(4):242–244, 1982.

[118] J. Speth and A. van der Woude. Giant resonances in nuclei. *Reports on Progress in Physics*, 44(7):719, 1981.

[119] W.V. Prestwich, M.A. Islam, and T.J. Kennett. PrimaryE2 transitions observed following neutron capture for the mass region 144 A 180. *Zeitschrift für Physik A Atoms and Nuclei*, 315(1):103–111, 1984.

[120] A. P. Dempster, N. M. Laird, and D. B. Rubin. Maximum likelihood from incomplete data via the EM algorithm. *Journal of the Royal Statistical Society. Series B (Methodological)*, pages 1–38, 1977.

[121] D. Jordan. *β-decay Total Absorption Spectroscopy measurements for reactor decay heat calculations*. PhD thesis, Universidad de Valencia - CSIC, 2010.

[122] T. Von Egidy, H.H. Schmidt, and A.N. Behkami. Nuclear level densities and level spacing distributions: Part {II}. *Nuclear Physics A*, 481(2):189–206, 1988.

[123] J. Sinatkas, L. D. Skouras, D. Strottman, and J. D. Vergados. Shell-model calculations in the A=80-100 mass region: I. A study of the N=50 nuclei. *Journal of Physics G: Nuclear and Particle Physics*, 18(8):1377, 1992.

[124] Xiangdong Ji and B. H. Wildenthal. Shell-model calculations for the energy levels of the *N=50* isotones with *A=80 87*. *Phys. Rev. C*, 40:389–398, Jul 1989.

[125] R.C. Greenwood, R.G. Helmer, M.A. Lee, M.H. Putnam, M.A. Oates, D.A. Struttmann, and K.D. Watts. Total absorption gamma-ray spectrometer for measurement of beta-decay intensity distributions for fission product radionuclides. *Nuclear Instruments and Methods in Physics Research Section A: Accelerators, Spectrometers, Detectors and Associated Equipment*, 314(3):514–540, 1992.

[126] S. Y .F. Chu, L.P. Ekström, and R. B. Firestone. www Table of Radioactive Isotopes, Feb 1999.

A Analysis Inputs & Results Tabularized

A.1 Density Functions

Isotope	Level density Parameters				
	a	Δ	T	E0	Ex
^{86}Kr	8.434	1.599	0.833	1.518	4.342
^{91}Sr	9.754	0.264	0.662	0.425	1.946
^{94}Y	10.724	-0.156	0.546	0.124	1.960

Table A.1: Level Density parameters for daughter isotopes.

A.2 Gamma Strength Parameters

Isotope	Strength Function Parameters								
	E1			M1			E2		
	Energy [MeV]	Width [MeV]	σ [mb]	Energy [MeV]	Width [MeV]	σ [mb]	Energy [MeV]	Width [MeV]	σ [mb]
^{86}Kr	16.29 17.17	5.37 5.94	178.7 161.63	9.30	4.00	19.67	14.29	5.08	1.78
^{91}Sb	16.08 16.95	5.24 5.79	193.81 175.32	9.13	4.00	2.66	14.03	5.02	1.89
^{94}Y	14.59 17.69	4.35 6.28	240.44 166.60	9.03	4.00	2.25	13.88	4.98	1.94

Table A.2: Gamma strength parameters for daughter isotopes.

A.3 Level Schemes and Possible γ-ray Transitions From the Decay of ^{86}Br

Levels [keV]	J^{π}	γ-ray Emission [keV]	γ-ray Intensity	α	Permitted Feeding
1564.75	2^+	1564.75	100.00	0.00	Yes
2250.05	4^+	685.30	100.00	0.00	Yes
2349.95	2^+	785.20 2349.95	46.00 100.00	0.00 0.00	Yes
2726.75	0^+	376.80 1162.00	70.00 100.00	0.00 0.00	Yes
2850.35	2^+	500.40 1285.60	16.00 100.00	0.00 0.00	Yes
2917.05	3^+	666.70 1352.30	100.00 25.00	0.00 0.00	Yes
2926.32	2^+	1361.57 2926.32	100.00 19.00	0.00 0.00	Yes
3010.25	1^+	660.30 3010.25	75.00 100.00	0.00 0.00	Yes
3099.45	3^-	1534.7	100.00	0.00	Yes
3328.25	2^+	1763.50	100.00	0.00	Yes
3541.65	0^+	1191.70 1976.90	100.00 50.00	0.00 0.00	Yes

Table A.3: Low energy excitation levels of ^{86}Kr.

A.4 Level Schemes and Possible γ-ray Transitions From he Decay of ^{91}Rb

Levels [keV]	J^π	γ-ray Emission [keV]	γ-ray Intensity	α	Permitted Feeding
93.63	$3/2^+$	93.63	100.00	1.26	Yes
439.16	$3/2^+$	345.52 439.15	100.00 25.20	1.01 0.00	Yes
993.50	$9/2^+$	993.50	100.00	0.00	No
1042.03	$3/2^+$	602.85 948.49 1041.99	100.00 41.30 77.00	0.00 0.00 0.00	Yes
1230.84	$1/2^+$	1137.24 1230.64	100.00 7.60	0.00 0.00	Yes
1367.76	$7/2^-$	1274.05 1367.76	33.00 100.00	0.00 0.00	No
1482.12	$5/2^+$	1388.13 1482.17	15.10 100.00	0.00 0.00	Yes
1740.27	$3/2^+$	509.60 1646.51 1740.25	12.10 18.30 100.00	0.00 0.00 0.00	Yes
1917.09	$1/2^+$	875.00 1823.30	14.20 47.00	0.00 0.00	Yes
1942.91	$3/2^+$	1849.27 1917.11	100.00 100.00	0.00 0.00	Yes
		1942.81	12.00	0.00	
2064.66	$5/2^+$	1023.20 1625.40 1970.99 2064.69	6.60 10.70 100.00 11.70	0.00 0.00 0.00 0.00	Yes
2077.50	$11/2^-$	1084.00	100.00	0.00	No
2159.08	$5/2^+$	1719.90	100.00	0.00	Yes
2236.95	$5/2^+$	1006.30 2143.22 2236.90	14.00 100.00 21.00	0.00 0.00 0.00	Yes
2657.89	$3/2^-$	593.23 917.59 1615.86 2218.20 2564.19	10.30 1.48 19.60 2.20 100.00	0.00 0.00 0.00 0.00 0.00	Yes

Table A.4: Low energy excitation levels of ^{91}Sr.

A.5 Level Schemes and Possible γ-ray Transitions From the Decay of ^{94}Sr

Levels [keV]	J^π	γ-ray Emission [keV]	γ-ray Intensity	α	Permitted Feeding
432.30	3^-	432.20	100.00	0.00	No
621.70	3^+	621.70	100.00	0.00	No
723.80	1^-	102.10 723.80	0.27 100.00	0.00 0.00	Yes
906.91	$2^-/3^-$	906.90	100.00	0.00	Yes/No
1202.30	5^+	769.90 1202.40	100.00 17.60	0.00 0.00	No
1427.71	1^+	520.80 703.90 806.00 1427.70	0.16 2.26 1.86 100.00	0.00 0.00 0.00 0.00	Yes
1437.01	0^-	530.10	100.00	0.00	Yes
2182.42	1^+	754.70 1560.70 2182.40	21.00 11.00 100.00	0.00 0.00 0.00	Yes
2373.02	0^-	1649.20 1751.30	100.00 79.00	0.00 0.00	Yes
2969.93	1^+	2063.00 2246.10	89.00 100.00	0.00 0.00	Yes

Table A.5: low energy excitation levels of ^{94}Y

A.6 Feeding Distribution and Strength Function from the Decay of ^{86}Br

Energy	β Feeding		Strength Function	
[keV]	%	σ_F	10^6 [$S^{-1}MeV^{-1}$]	σ_S
0.00	15.01	0.08	0.03	0.00
1564.75	3.75	0.02	0.02	0.00
2250.05	0.00	0.00	0.00	0.00
2349.95	0.00	0.00	0.00	0.00
2726.75	2.91	0.02	0.05	0.00
2850.35	2.34	0.01	0.04	0.00
2917.05	0.21	0.00	0.00	0.00
2926.32	1.32	0.01	0.03	0.00
3010.25	2.95	0.02	0.06	0.00
3099.45	0.00	0.00	0.00	0.00
3328.25	3.58	0.02	0.10	0.00
3541.65	0.18	0.00	0.01	0.00
3580.00	0.36	0.00	0.01	0.00
3620.00	0.27	0.00	0.01	0.00
3660.00	0.30	0.00	0.01	0.00
3700.00	0.36	0.00	0.02	0.00
3740.00	0.39	0.00	0.02	0.00
3780.00	0.36	0.00	0.02	0.00
3820.00	0.22	0.00	0.01	0.00
3860.00	0.10	0.00	0.01	0.00
3900.00	0.06	0.00	0.00	0.00
3940.00	0.02	0.00	0.00	0.00
3980.00	0.01	0.00	0.00	0.00
4020.00	0.01	0.00	0.00	0.00
4060.00	0.02	0.00	0.00	0.00
4100.00	0.04	0.00	0.00	0.00
4140.00	0.13	0.00	0.01	0.00
4180.00	0.60	0.00	0.04	0.00
4220.00	1.95	0.01	0.15	0.00
4260.00	4.87	0.02	0.40	0.01
4300.00	9.48	0.04	0.82	0.02
4340.00	9.02	0.04	0.82	0.02
4380.00	5.31	0.02	0.51	0.01
4420.00	1.23	0.01	0.13	0.00
4460.00	0.28	0.00	0.03	0.00
4500.00	0.07	0.00	0.01	0.00
4540.00	0.01	0.00	0.00	0.00
4580.00	0.00	0.00	0.00	0.00

(a) Original result

Energy	β Feeding		Strength Function	
[keV]	%	σ_F	10^6 [$S^{-1}MeV^{-1}$]	σ_S
0.00	12.40	0.07	0.03	0.00
1564.75	3.35	0.02	0.02	0.00
2250.05	0.00	0.00	0.00	0.00
2349.95	0.18	0.00	0.00	0.00
2726.75	4.22	0.02	0.07	0.00
2850.35	2.91	0.02	0.05	0.00
2917.05	0.51	0.00	0.01	0.00
2926.32	1.41	0.01	0.03	0.00
3010.25	4.00	0.02	0.08	0.00
3099.45	0.00	0.00	0.00	0.00
3328.25	5.26	0.03	0.15	0.00
3541.65	0.44	0.00	0.02	0.00
3580.00	0.59	0.00	0.02	0.00
3620.00	0.42	0.00	0.02	0.00
3660.00	0.40	0.00	0.02	0.00
3700.00	0.44	0.00	0.02	0.00
3740.00	0.49	0.00	0.02	0.00
3780.00	0.52	0.00	0.02	0.00
3820.00	0.46	0.00	0.02	0.00
3860.00	0.30	0.00	0.02	0.00
3900.00	0.21	0.00	0.01	0.00
3940.00	0.10	0.00	0.01	0.00
3980.00	0.06	0.00	0.00	0.00
4020.00	0.05	0.00	0.00	0.00
4060.00	0.06	0.00	0.00	0.00
4100.00	0.11	0.00	0.01	0.00
4140.00	0.29	0.00	0.02	0.00
4180.00	0.90	0.00	0.07	0.00
4220.00	2.27	0.01	0.18	0.00
4260.00	4.72	0.02	0.39	0.01
4300.00	8.20	0.04	0.71	0.01
4340.00	7.88	0.04	0.72	0.02
4380.00	4.96	0.02	0.48	0.01
4420.00	1.32	0.01	0.13	0.00
4460.00	0.37	0.00	0.04	0.00
4500.00	0.11	0.00	0.01	0.00
4540.00	0.02	0.00	0.00	0.00
4580.00	0.01	0.00	0.00	0.00

(b) Optimized γ-ray branching ratio result

Table A.6: Generated Beta Feeding Distribution and strength function For ^{86}Kr.

Energy	β Feeding		Strength Function	
[keV]	%	σ_F	10^6 [$S^{-1}MeV^{-1}$]	σ_S
4620.00	0.00	0.00	0.00	0.00
4660.00	0.00	0.00	0.00	0.00
4700.00	0.00	0.00	0.00	0.00
4740.00	0.01	0.00	0.00	0.00
4780.00	0.04	0.00	0.01	0.00
4820.00	0.09	0.00	0.02	0.00
4860.00	0.15	0.00	0.03	0.00
4900.00	0.19	0.00	0.04	0.00
4940.00	0.16	0.00	0.03	0.00
4980.00	0.10	0.00	0.02	0.00
5020.00	0.06	0.00	0.01	0.00
5060.00	0.04	0.00	0.01	0.00
5100.00	0.03	0.00	0.01	0.00
5140.00	0.05	0.00	0.01	0.00
5180.00	0.08	0.00	0.03	0.00
5220.00	0.21	0.00	0.07	0.00
5260.00	0.63	0.00	0.24	0.01
5300.00	1.33	0.01	0.53	0.01
5340.00	2.33	0.01	1.00	0.03
5380.00	3.40	0.02	1.56	0.04
5420.00	3.47	0.02	1.72	0.04
5460.00	2.84	0.01	1.53	0.04
5500.00	2.06	0.01	1.20	0.03
5540.00	1.36	0.01	0.86	0.02
5580.00	0.98	0.01	0.67	0.02
5620.00	0.78	0.00	0.57	0.01
5660.00	0.64	0.00	0.51	0.02
5700.00	0.57	0.00	0.50	0.01
5740.00	0.48	0.00	0.46	0.01
5780.00	0.38	0.00	0.39	0.01
5820.00	0.29	0.00	0.32	0.01
5860.00	0.21	0.00	0.26	0.01
5900.00	0.17	0.00	0.23	0.01
5940.00	0.15	0.00	0.23	0.01
5980.00	0.16	0.00	0.27	0.01
6020.00	0.21	0.00	0.38	0.01
6060.00	0.31	0.00	0.64	0.02
6100.00	0.51	0.00	1.14	0.04
6140.00	0.77	0.01	1.92	0.07
6180.00	1.02	0.01	2.85	0.10
6220.00	1.05	0.01	3.26	0.11

(a) Original result

Energy	β Feeding		Strength Function	
[keV]	%	σ_F	10^6 [$S^{-1}MeV^{-1}$]	σ_S
4620.00	0.00	0.00	0.00	0.00
4660.00	0.01	0.00	0.00	0.00
4700.00	0.02	0.00	0.00	0.00
4740.00	0.03	0.00	0.00	0.00
4780.00	0.11	0.00	0.02	0.00
4820.00	0.21	0.00	0.04	0.00
4860.00	0.32	0.00	0.06	0.00
4900.00	0.32	0.00	0.07	0.00
4940.00	0.23	0.00	0.05	0.00
4980.00	0.13	0.00	0.03	0.00
5020.00	0.07	0.00	0.02	0.00
5060.00	0.04	0.00	0.01	0.00
5100.00	0.04	0.00	0.01	0.00
5140.00	0.05	0.00	0.02	0.00
5180.00	0.09	0.00	0.03	0.00
5220.00	0.24	0.00	0.08	0.00
5260.00	0.70	0.00	0.26	0.01
5300.00	1.38	0.01	0.55	0.01
5340.00	2.27	0.01	0.97	0.02
5380.00	3.09	0.02	1.42	0.04
5420.00	2.98	0.02	1.48	0.04
5460.00	2.37	0.01	1.28	0.04
5500.00	1.70	0.01	0.99	0.03
5540.00	1.16	0.01	0.74	0.02
5580.00	0.89	0.01	0.61	0.02
5620.00	0.72	0.00	0.53	0.01
5660.00	0.62	0.00	0.49	0.01
5700.00	0.55	0.00	0.49	0.01
5740.00	0.46	0.00	0.44	0.01
5780.00	0.35	0.00	0.36	0.01
5820.00	0.26	0.00	0.30	0.01
5860.00	0.19	0.00	0.24	0.01
5900.00	0.15	0.00	0.21	0.01
5940.00	0.14	0.00	0.21	0.01
5980.00	0.15	0.00	0.25	0.01
6020.00	0.19	0.00	0.35	0.01
6060.00	0.29	0.00	0.59	0.02
6100.00	0.48	0.00	1.08	0.04
6140.00	0.73	0.01	1.83	0.06
6180.00	0.96	0.01	2.66	0.09
6220.00	0.96	0.01	2.98	0.10

(b) Optimized γ-ray branching ratio result

Table A.7: Cont. Generated Beta Feeding Distribution and strength function For ^{86}Kr.

Energy	β Feeding		Strength Function	
[keV]	%	σ_F	10^6 [$S^{-1}MeV^{-1}$]	σ_S
6260.00	0.85	0.01	2.93	0.10
6300.00	0.57	0.00	2.20	0.08
6340.00	0.35	0.00	1.52	0.06
6380.00	0.25	0.00	1.24	0.05
6420.00	0.22	0.00	1.22	0.05
6460.00	0.23	0.00	1.50	0.06
6500.00	0.29	0.00	2.11	0.08
6540.00	0.37	0.00	3.05	0.14
6580.00	0.42	0.00	4.08	0.18
6620.00	0.40	0.00	4.54	0.20
6660.00	0.32	0.00	4.15	0.22
6700.00	0.21	0.00	3.18	0.17
6740.00	0.11	0.00	2.04	0.11
6780.00	0.06	0.00	1.25	0.07
6820.00	0.03	0.00	0.76	0.04
6860.00	0.02	0.00	0.52	0.03
6900.00	0.01	0.00	0.45	0.03
6940.00	0.01	0.00	0.55	0.04
6980.00	0.02	0.00	0.94	0.06
7020.00	0.03	0.00	2.09	0.14
7060.00	0.05	0.00	4.53	0.26
7100.00	0.07	0.00	8.16	0.66
7140.00	0.06	0.00	10.04	0.81
7180.00	0.04	0.00	7.44	0.78
7220.00	0.01	0.00	3.57	0.37
7260.00	0.00	0.00	1.37	0.14
7300.00	0.00	0.00	0.52	0.05
7340.00	0.00	0.00	0.21	0.03
7380.00	0.00	0.00	0.15	0.02
7420.00	0.00	0.00	0.16	0.03
7460.00	0.00	0.00	0.28	0.06
7500.00	0.00	0.00	0.84	0.23
7540.00	0.00	0.00	0.00	0.00
7580.00	0.00	0.00	0.00	0.00
7620.00	0.00	0.00	0.00	0.00

(a) Original result

Energy	β Feeding		Strength Function	
[keV]	%	σ_F	10^6 [$S^{-1}MeV^{-1}$]	σ_S
6260.00	0.74	0.01	2.58	0.09
6300.00	0.48	0.00	1.87	0.07
6340.00	0.29	0.00	1.26	0.05
6380.00	0.20	0.00	1.02	0.04
6420.00	0.18	0.00	1.04	0.04
6460.00	0.21	0.00	1.33	0.05
6500.00	0.26	0.00	1.93	0.08
6540.00	0.34	0.00	2.81	0.13
6580.00	0.40	0.00	3.83	0.17
6620.00	0.37	0.00	4.19	0.19
6660.00	0.28	0.00	3.70	0.20
6700.00	0.18	0.00	2.73	0.15
6740.00	0.09	0.00	1.69	0.09
6780.00	0.05	0.00	0.99	0.05
6820.00	0.02	0.00	0.59	0.03
6860.00	0.01	0.00	0.40	0.02
6900.00	0.01	0.00	0.36	0.02
6940.00	0.01	0.00	0.48	0.03
6980.00	0.02	0.00	0.87	0.06
7020.00	0.03	0.00	2.06	0.14
7060.00	0.05	0.00	4.61	0.27
7100.00	0.07	0.00	8.22	0.67
7140.00	0.06	0.00	9.11	0.74
7180.00	0.03	0.00	5.89	0.62
7220.00	0.01	0.00	2.39	0.25
7260.00	0.00	0.00	0.76	0.08
7300.00	0.00	0.00	0.26	0.03
7340.00	0.00	0.00	0.10	0.01
7380.00	0.00	0.00	0.07	0.01
7420.00	0.00	0.00	0.08	0.01
7460.00	0.00	0.00	0.15	0.03
7500.00	0.00	0.00	0.46	0.13
7540.00	0.00	0.00	0.00	0.00
7580.00	0.00	0.00	0.00	0.00
7620.00	0.00	0.00	0.00	0.00

(b) Optimized γ-ray branching ratio result

Table A.8: Cont. Generated Beta Feeding Distribution and strength function For ^{86}Kr.

A.7 Feeding Distribution and Strength Function from the Decay of ^{91}Rb.

Energy	β Feeding		Strength Function	
[keV]	%	σ_F	10^6 [$S^{-1}MeV^{-1}$]	σ_S
0.00	6.61	0.03	0.04	0.00
93.63	10.90	0.06	0.07	0.00
439.16	2.19	0.02	0.02	0.00
993.50	0.00	0.00	0.00	0.00
1042.03	0.66	0.01	0.01	0.00
1230.84	0.62	0.01	0.01	0.00
1367.76	0.00	0.00	0.00	0.00
1482.12	0.00	0.00	0.00	0.00
1740.27	0.00	0.00	0.00	0.00
1917.09	0.91	0.01	0.03	0.00
1942.91	1.46	0.01	0.05	0.00
2064.66	5.41	0.03	0.22	0.00
2077.50	0.00	0.00	0.00	0.00
2159.08	0.04	0.00	0.00	0.00
2236.95	0.00	0.00	0.00	0.00
2657.89	15.58	0.08	1.33	0.02
2700.00	0.39	0.00	0.03	0.00
2740.00	0.09	0.00	0.01	0.00
2780.00	0.03	0.00	0.00	0.00
2820.00	0.01	0.00	0.00	0.00
2860.00	0.01	0.00	0.00	0.00
2900.00	0.01	0.00	0.00	0.00
2940.00	0.02	0.00	0.00	0.00
2980.00	0.02	0.00	0.00	0.00
3020.00	0.01	0.00	0.00	0.00
3060.00	0.01	0.00	0.00	0.00
3100.00	0.00	0.00	0.00	0.00
3140.00	0.00	0.00	0.00	0.00
3180.00	0.00	0.00	0.00	0.00
3220.00	0.00	0.00	0.00	0.00
3260.00	0.01	0.00	0.00	0.00
3300.00	0.04	0.00	0.01	0.00
3340.00	0.12	0.00	0.03	0.00
3380.00	0.25	0.00	0.06	0.00

(a) Original

Energy	β Feeding		Strength Function	
[keV]	%	σ_F	10^6 [$S^{-1}MeV^{-1}$]	σ_S
0.00	6.61	0.03	0.04	0.00
93.63	10.90	0.06	0.07	0.00
439.16	2.19	0.02	0.02	0.00
993.50	0.00	0.00	0.00	0.00
1042.03	0.66	0.01	0.01	0.00
1230.84	0.62	0.01	0.01	0.00
1367.76	0.00	0.00	0.00	0.00
1482.12	0.00	0.00	0.00	0.00
1740.27	0.00	0.00	0.00	0.00
1917.09	0.91	0.01	0.03	0.00
1942.91	1.46	0.01	0.05	0.00
2064.66	5.41	0.03	0.22	0.00
2077.50	0.00	0.00	0.00	0.00
2159.08	0.04	0.00	0.00	0.00
2236.95	0.00	0.00	0.00	0.00
2657.89	15.58	0.08	1.33	0.02
2700.00	0.39	0.00	0.03	0.00
2740.00	0.09	0.00	0.01	0.00
2780.00	0.03	0.00	0.00	0.00
2820.00	0.01	0.00	0.00	0.00
2860.00	0.01	0.00	0.00	0.00
2900.00	0.01	0.00	0.00	0.00
2940.00	0.02	0.00	0.00	0.00
2980.00	0.02	0.00	0.00	0.00
3020.00	0.01	0.00	0.00	0.00
3060.00	0.01	0.00	0.00	0.00
3100.00	0.00	0.00	0.00	0.00
3140.00	0.00	0.00	0.00	0.00
3180.00	0.00	0.00	0.00	0.00
3220.00	0.00	0.00	0.00	0.00
3260.00	0.01	0.00	0.00	0.00
3300.00	0.04	0.00	0.01	0.00
3340.00	0.12	0.00	0.03	0.00
3380.00	0.25	0.00	0.06	0.00

(b) Modified Brm

Table A.9: Generated Beta Feeding Distribution and strength function For ^{91}Sr.

Energy	β Feeding		Strength Function	
[keV]	%	σ_F	10^6 [$S^{-1}MeV^{-1}$]	σ_S
3420.00	0.54	0.00	0.14	0.00
3460.00	0.79	0.00	0.22	0.00
3500.00	1.04	0.01	0.32	0.01
3540.00	1.38	0.01	0.45	0.01
3580.00	1.99	0.01	0.69	0.01
3620.00	2.96	0.01	1.11	0.02
3660.00	3.90	0.02	1.58	0.03
3700.00	3.98	0.02	1.74	0.03
3740.00	3.54	0.02	1.67	0.03
3780.00	2.21	0.01	1.13	0.02
3820.00	1.26	0.01	0.70	0.01
3860.00	0.86	0.00	0.52	0.01
3900.00	0.71	0.00	0.46	0.01
3940.00	0.79	0.00	0.55	0.01
3980.00	1.24	0.01	0.94	0.02
4020.00	1.81	0.01	1.50	0.03
4060.00	3.20	0.01	2.91	0.06
4100.00	4.29	0.02	4.27	0.09
4140.00	4.16	0.02	4.54	0.10
4180.00	3.38	0.02	4.05	0.09
4220.00	2.31	0.01	3.04	0.07
4260.00	1.49	0.01	2.14	0.05
4300.00	1.04	0.01	1.64	0.04
4340.00	0.89	0.01	1.56	0.04
4380.00	0.84	0.01	1.65	0.04
4420.00	0.79	0.01	1.74	0.04
4460.00	0.71	0.01	1.71	0.04
4500.00	0.57	0.00	1.52	0.04
4540.00	0.35	0.00	1.05	0.03
4580.00	0.23	0.00	0.78	0.02
4620.00	0.17	0.00	0.64	0.02
4660.00	0.14	0.00	0.58	0.02
4700.00	0.13	0.00	0.64	0.02
4740.00	0.13	0.00	0.75	0.03
4780.00	0.14	0.00	0.91	0.03

(a) Original

Energy	β Feeding		Strength Function	
[keV]	%	σ_F	10^6 [$S^{-1}MeV^{-1}$]	σ_S
3420.00	0.54	0.00	0.14	0.00
3460.00	0.79	0.00	0.22	0.00
3500.00	1.04	0.01	0.32	0.01
3540.00	1.38	0.01	0.45	0.01
3580.00	1.99	0.01	0.69	0.01
3620.00	2.96	0.01	1.11	0.02
3660.00	3.90	0.02	1.58	0.03
3700.00	3.98	0.02	1.74	0.03
3740.00	3.54	0.02	1.67	0.03
3780.00	2.21	0.01	1.13	0.02
3820.00	1.26	0.01	0.70	0.01
3860.00	0.86	0.00	0.52	0.01
3900.00	0.71	0.00	0.46	0.01
3940.00	0.79	0.00	0.55	0.01
3980.00	1.24	0.01	0.94	0.02
4020.00	1.81	0.01	1.50	0.03
4060.00	3.20	0.01	2.91	0.06
4100.00	4.29	0.02	4.27	0.09
4140.00	4.16	0.02	4.54	0.10
4180.00	3.38	0.02	4.05	0.09
4220.00	2.31	0.01	3.04	0.07
4260.00	1.49	0.01	2.14	0.05
4300.00	1.04	0.01	1.64	0.04
4340.00	0.89	0.01	1.56	0.04
4380.00	0.84	0.01	1.65	0.04
4420.00	0.79	0.01	1.74	0.04
4460.00	0.71	0.01	1.71	0.04
4500.00	0.57	0.00	1.52	0.04
4540.00	0.35	0.00	1.05	0.03
4580.00	0.23	0.00	0.78	0.02
4620.00	0.17	0.00	0.64	0.02
4660.00	0.14	0.00	0.58	0.02
4700.00	0.13	0.00	0.64	0.02
4740.00	0.13	0.00	0.75	0.03
4780.00	0.14	0.00	0.91	0.03

(b) Modified Brm

Table A.10: Cont. Generated Beta Feeding Distribution and strength function For ^{91}Sr.

Energy	β Feeding		Strength Function	
[keV]	%	σ_F	10^6 [$S^{-1}MeV^{-1}$]	σ_S
4820.00	0.15	0.00	1.07	0.04
4860.00	0.13	0.00	1.11	0.04
4900.00	0.11	0.00	1.07	0.04
4940.00	0.08	0.00	0.95	0.03
4980.00	0.06	0.00	0.74	0.03
5020.00	0.03	0.00	0.51	0.02
5060.00	0.02	0.00	0.33	0.02
5100.00	0.01	0.00	0.20	0.01
5140.00	0.00	0.00	0.12	0.01
5180.00	0.00	0.00	0.08	0.00
5220.00	0.00	0.00	0.05	0.00
5260.00	0.00	0.00	0.03	0.00
5300.00	0.00	0.00	0.03	0.00
5340.00	0.00	0.00	0.02	0.00
5380.00	0.00	0.00	0.02	0.00
5420.00	0.00	0.00	0.02	0.00
5460.00	0.00	0.00	0.02	0.00
5500.00	0.00	0.00	0.02	0.00
5540.00	0.00	0.00	0.01	0.00
5580.00	0.00	0.00	0.00	0.00
5620.00	0.00	0.00	0.00	0.00
5660.00	0.00	0.00	0.00	0.00
5700.00	0.00	0.00	0.00	0.00
5740.00	0.00	0.00	0.00	0.00
5780.00	0.00	0.00	0.00	0.00
5820.00	0.00	0.00	0.00	0.00
5860.00	0.00	0.00	0.00	0.00
5900.00	0.00	0.00	0.00	0.00

(a) Original

Energy	β Feeding		Strength Function	
[keV]	%	σ_F	10^6 [$S^{-1}MeV^{-1}$]	σ_S
4820.00	0.15	0.00	1.07	0.04
4860.00	0.13	0.00	1.11	0.04
4900.00	0.11	0.00	1.07	0.04
4940.00	0.08	0.00	0.95	0.03
4980.00	0.06	0.00	0.74	0.03
5020.00	0.03	0.00	0.51	0.02
5060.00	0.02	0.00	0.33	0.02
5100.00	0.01	0.00	0.20	0.01
5140.00	0.00	0.00	0.12	0.01
5180.00	0.00	0.00	0.08	0.00
5220.00	0.00	0.00	0.05	0.00
5260.00	0.00	0.00	0.03	0.00
5300.00	0.00	0.00	0.03	0.00
5340.00	0.00	0.00	0.02	0.00
5380.00	0.00	0.00	0.02	0.00
5420.00	0.00	0.00	0.02	0.00
5460.00	0.00	0.00	0.02	0.00
5500.00	0.00	0.00	0.02	0.00
5540.00	0.00	0.00	0.01	0.00
5580.00	0.00	0.00	0.00	0.00
5620.00	0.00	0.00	0.00	0.00
5660.00	0.00	0.00	0.00	0.00
5700.00	0.00	0.00	0.00	0.00
5740.00	0.00	0.00	0.00	0.00
5780.00	0.00	0.00	0.00	0.00
5820.00	0.00	0.00	0.00	0.00
5860.00	0.00	0.00	0.00	0.00
5900.00	0.00	0.00	0.00	0.00

(b) Modified Brm

Table A.11: cont. Generated Beta Feeding Distribution and strength function For ^{91}Sr.

A.8 Feeding Distribution and Strength Function from the Decay of ^{94}Sr

Energy	β Feeding		Strength Function	
[keV]	%	σ_F	10^6 [$S^{-1}MeV^{-1}$]	σ_S
0.00	0.32	0.00	0.01	0.00
432.30	0.00	0.00	0.00	0.00
621.70	0.00	0.00	0.00	0.00
723.80	0.00	0.00	0.00	0.00
906.91	0.00	0.00	0.00	0.00
1202.30	0.00	0.00	0.00	0.00
1427.71	80.87	0.23	33.78	0.58
1437.01	14.82	0.04	6.31	0.11
2182.42	1.38	0.01	3.49	0.08
2373.02	1.79	0.01	8.27	0.22
2969.93	0.82	0.00	56.50	3.14

(a) Level scheme 1

Energy	β Feeding		Strength Function	
[keV]	%	σ_F	10^6 [$S^{-1}MeV^{-1}$]	σ_S
0.00	0.35	0.00	0.02	0.00
432.30	0.00	0.00	0.00	0.00
621.70	0.00	0.00	0.00	0.00
723.80	0.00	0.00	0.00	0.00
906.91	0.00	0.00	0.00	0.00
1202.30	0.00	0.00	0.00	0.00
1427.71	80.84	0.23	33.77	0.57
1437.01	14.82	0.04	6.31	0.11
2182.42	1.38	0.01	3.49	0.08
2373.02	1.79	0.01	8.25	0.22
2969.93	0.82	0.00	56.73	3.15

(b) Level scheme 2

Table A.12: Generated Beta Feeding Distribution and strength function For ^{94}Sr (no continuum used).

Energy	β Feeding		Strength Function	
[keV]	%	σ_F	10^6 [$S^{-1}MeV^{-1}$]	σ_S
0.00	0.32	0.00	0.01	0.00
432.30	0.00	0.00	0.00	0.00
621.70	0.00	0.00	0.00	0.00
723.80	0.00	0.00	0.00	0.00
906.91	0.00	0.00	0.00	0.00
1202.30	0.00	0.00	0.00	0.00
1427.71	80.78	0.23	33.75	0.57
1437.01	14.82	0.04	6.31	0.11
2182.42	1.40	0.01	3.53	0.08
2373.02	1.80	0.01	8.32	0.22
2969.93	0.37	0.00	25.48	1.41
3020.00	0.36	0.00	34.82	1.93
3060.00	0.07	0.00	9.35	0.52
3100.00	0.02	0.00	3.46	0.26
3140.00	0.01	0.00	3.51	0.26
3180.00	0.01	0.00	5.49	0.41
3220.00	0.02	0.00	8.80	0.81
3260.00	0.01	0.00	13.06	1.45
3300.00	0.01	0.00	14.04	1.55
3340.00	0.00	0.00	14.45	2.13
3380.00	0.00	0.00	18.53	3.76
3420.00	0.00	0.00	0.00	0.00
3460.00	0.00	0.00	0.00	0.00
3500.00	0.00	0.00	0.00	0.00

(a) Level scheme 1

Energy	β Feeding		Strength Function	
[keV]	%	σ_F	10^6 [$S^{-1}MeV^{-1}$]	σ_S
0.00	0.34	0.00	0.02	0.00
432.30	0.00	0.00	0.00	0.00
621.70	0.00	0.00	0.00	0.00
723.80	0.00	0.00	0.00	0.00
906.91	0.00	0.00	0.00	0.00
1202.30	0.00	0.00	0.00	0.00
1427.71	80.73	0.23	33.73	0.57
1437.01	14.82	0.04	6.31	0.11
2182.42	1.40	0.01	3.54	0.08
2373.02	1.80	0.01	8.31	0.22
2969.93	0.37	0.00	25.27	1.40
3020.00	0.37	0.00	35.78	1.99
3060.00	0.08	0.00	9.98	0.55
3100.00	0.02	0.00	3.43	0.25
3140.00	0.01	0.00	3.73	0.28
3180.00	0.02	0.00	6.17	0.46
3220.00	0.02	0.00	10.04	0.93
3260.00	0.02	0.00	14.14	1.56
3300.00	0.01	0.00	14.08	1.56
3340.00	0.00	0.00	13.68	2.02
3380.00	0.00	0.00	16.73	3.39
3420.00	0.00	0.00	0.00	0.00
3460.00	0.00	0.00	0.00	0.00
3500.00	0.00	0.00	0.00	0.00

(b) Level scheme 2

Table A.13: Generated Beta Feeding Distribution and strength function For ^{94}Sr, standard result.

Energy	β Feeding		Strength Function	
[keV]	%	σ_F	10^6 [$S^{-1}MeV^{-1}$]	σ_S
0.00	0.01	0.00	0.00	0.00
432.30	0.00	0.00	0.00	0.00
621.70	0.00	0.00	0.00	0.00
723.80	0.00	0.00	0.00	0.00
906.91	0.11	0.00	0.02	0.00
1202.30	0.00	0.00	0.00	0.00
1427.71	94.24	0.26	39.37	0.67
1437.01	0.00	0.00	0.00	0.00
2182.42	1.35	0.01	3.42	0.08
2373.02	2.85	0.01	13.18	0.35
2969.93	0.62	0.00	42.76	2.37
3020.00	0.47	0.00	46.31	2.57
3060.00	0.09	0.00	12.48	0.69
3100.00	0.03	0.00	5.07	0.37
3140.00	0.02	0.00	5.95	0.44
3180.00	0.03	0.00	11.59	0.86
3220.00	0.04	0.00	23.49	2.17
3260.00	0.05	0.00	42.19	4.67
3300.00	0.04	0.00	59.17	6.55
3340.00	0.02	0.00	75.38	11.12
3380.00	0.02	0.00	116.05	23.52
3420.00	0.00	0.00	0.00	0.00
3460.00	0.00	0.00	0.00	0.00
3500.00	0.00	0.00	0.00	0.00

(a) Level scheme 1

Energy	β Feeding		Strength Function	
[keV]	%	σ_F	10^6 [$S^{-1}MeV^{-1}$]	σ_S
0.00	0.34	0.00	0.02	0.00
432.30	0.00	0.00	0.00	0.00
621.70	0.00	0.00	0.00	0.00
723.80	0.00	0.00	0.00	0.00
906.91	0.00	0.00	0.00	0.00
1202.30	0.00	0.00	0.00	0.00
1427.71	80.73	0.23	33.73	0.57
1437.01	14.82	0.04	6.31	0.11
2182.42	1.40	0.01	3.54	0.08
2373.02	1.80	0.01	8.31	0.22
2969.93	0.37	0.00	25.27	1.40
3020.00	0.37	0.00	35.78	1.99
3060.00	0.08	0.00	9.98	0.55
3100.00	0.02	0.00	3.43	0.25
3140.00	0.01	0.00	3.73	0.28
3180.00	0.02	0.00	6.17	0.46
3220.00	0.02	0.00	10.04	0.93
3260.00	0.02	0.00	14.14	1.56
3300.00	0.01	0.00	14.08	1.56
3340.00	0.00	0.00	13.68	2.02
3380.00	0.00	0.00	16.73	3.39
3420.00	0.00	0.00	0.00	0.00
3460.00	0.00	0.00	0.00	0.00
3500.00	0.00	0.00	0.00	0.00

(b) Level scheme 2

Table A.14: Generated Beta Feeding Distribution and strength function For ^{94}Sr (Restricted feeding to 1427 keV level).

B Subtractions from Calibrant Data

B.1 Subtractions of "*WithTube*" Data

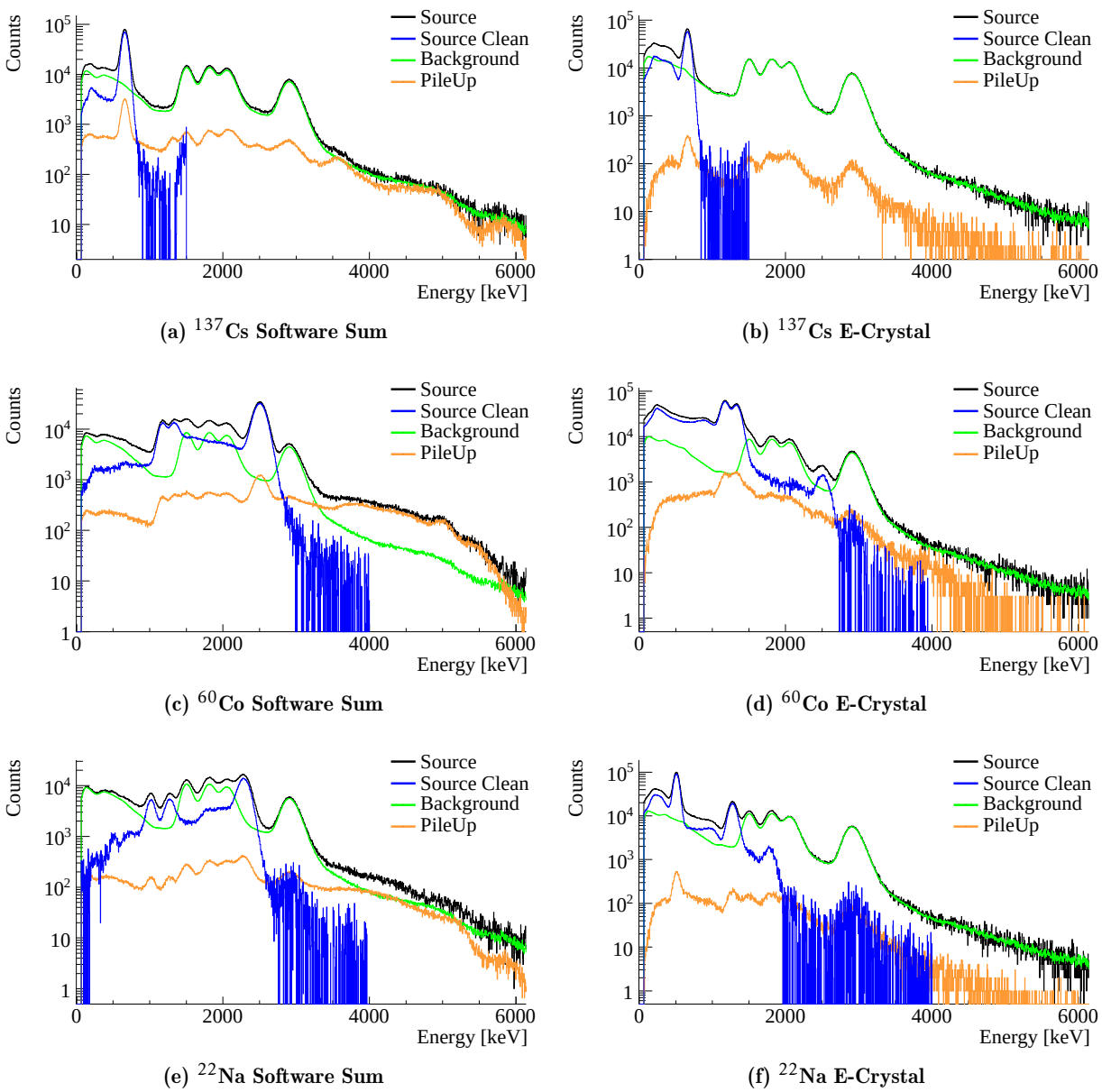

(a) ^{137}Cs Software Sum

(b) ^{137}Cs E-Crystal

(c) ^{60}Co Software Sum

(d) ^{60}Co E-Crystal

(e) ^{22}Na Software Sum

(f) ^{22}Na E-Crystal

Figure B.1: Full experiment set-up "*WithTube*" ^{137}Cs, ^{60}Co and ^{22}Na calibrant data (black) subtractions of background (green) and pile-up (orange) to produce cleaned calibrant data (blue).

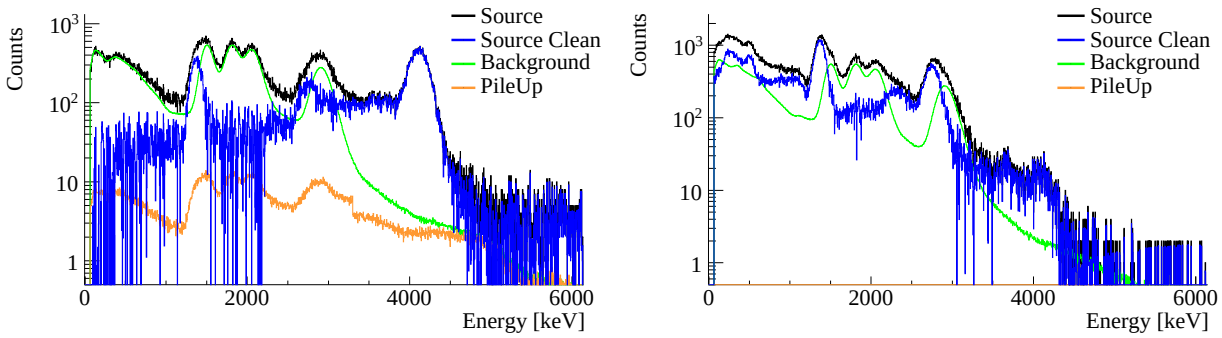

(a) ^{24}**Na Software Sum** **(b)** ^{24}**Na E-Crystal**

Figure B.2: Full experiment set-up "*WithTube*" ^{24}Na calibrant data (black) subtractions of background (green) and pile-up (orange) to produce cleaned calibrant data (blue).

B.2 Subtractions of "*NoTube*" Data

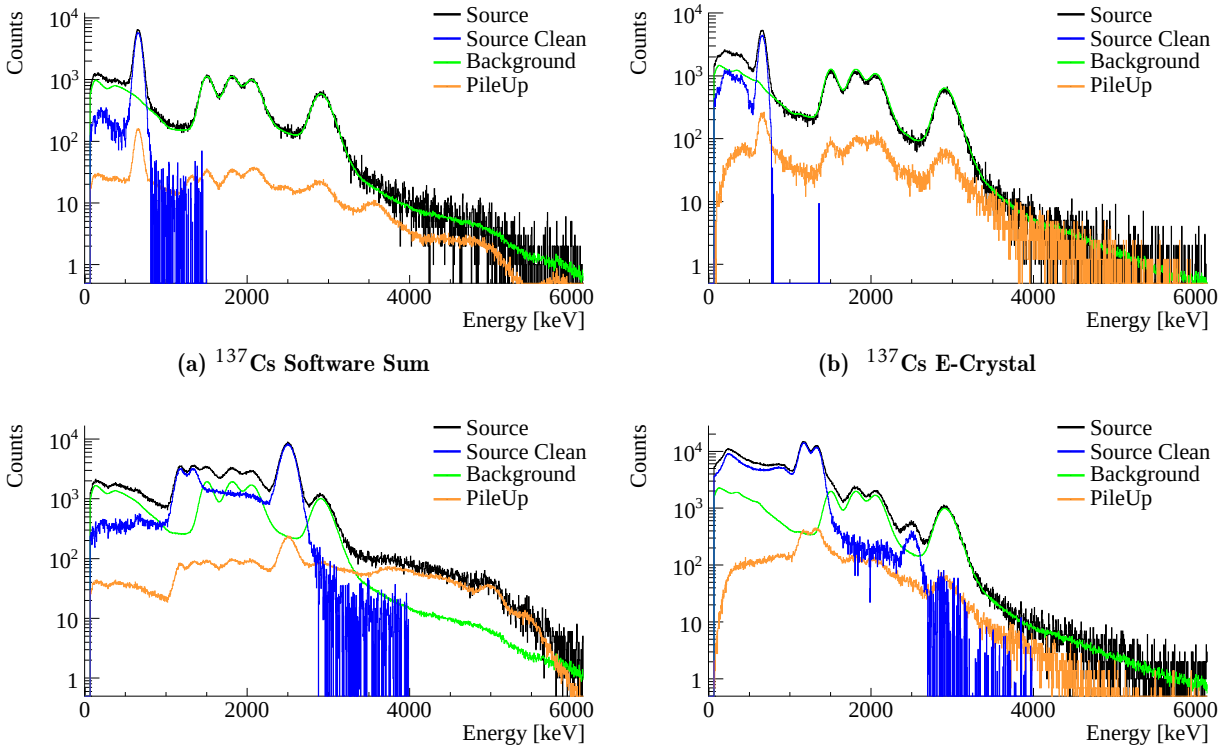

(a) ^{137}**Cs Software Sum** **(b)** ^{137}**Cs E-Crystal**

(c) ^{60}**Co Software Sum** **(d)** ^{60}**Co E-Crystal**

Figure B.3: Preliminary calibration set-up "*NoTube*" ^{137}Cs and ^{60}Co calibrant data (black) subtractions of background (green) and pile-up (orange) to produce cleaned calibrant data (blue).

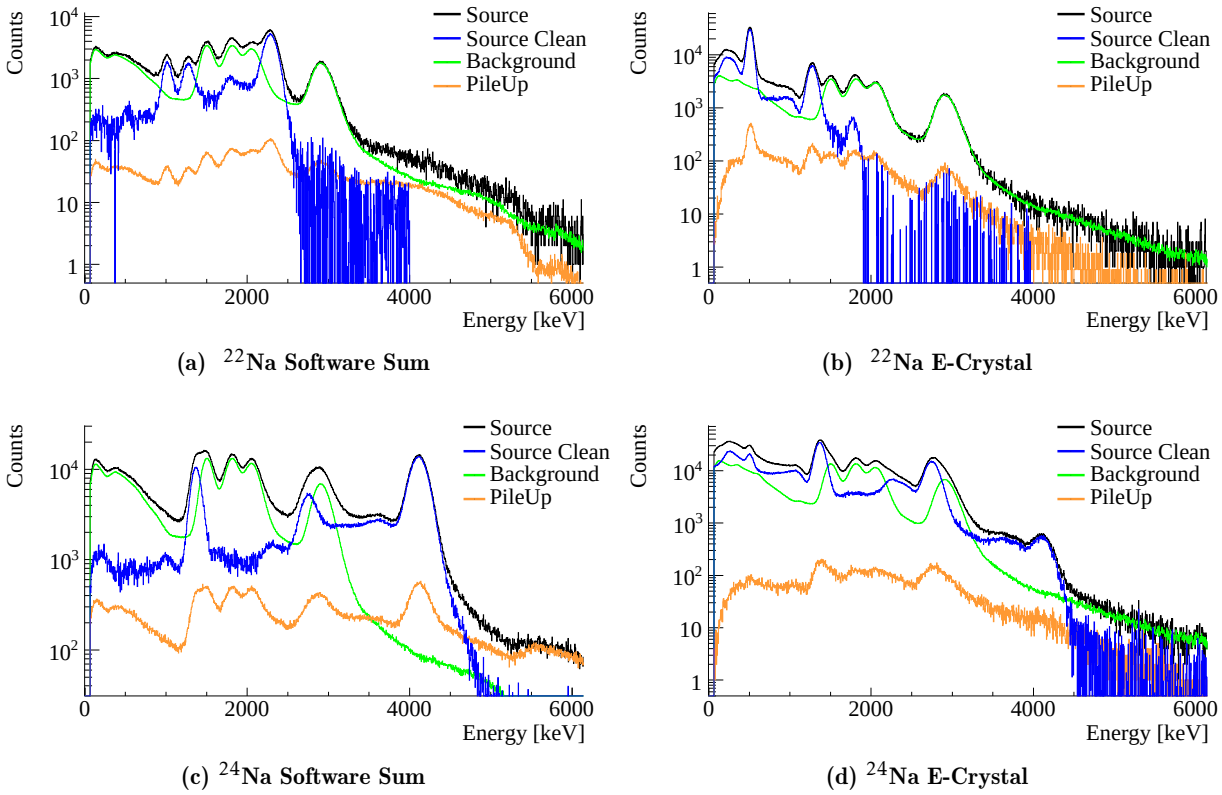

(a) ^{22}**Na Software Sum** **(b)** ^{22}**Na E-Crystal**

(c) ^{24}**Na Software Sum** **(d)** ^{24}**Na E-Crystal**

Figure B.4: Preliminary calibration set-up "*NoTube*" ^{22}Na and ^{24}Na calibrant data (black) subtractions of background (green) and pile-up (orange) to produce cleaned calibrant data (blue).

C Monte Carlo and Calibrant Data

C.1 Monte Carlo Comparison of "*WithTube*" Data

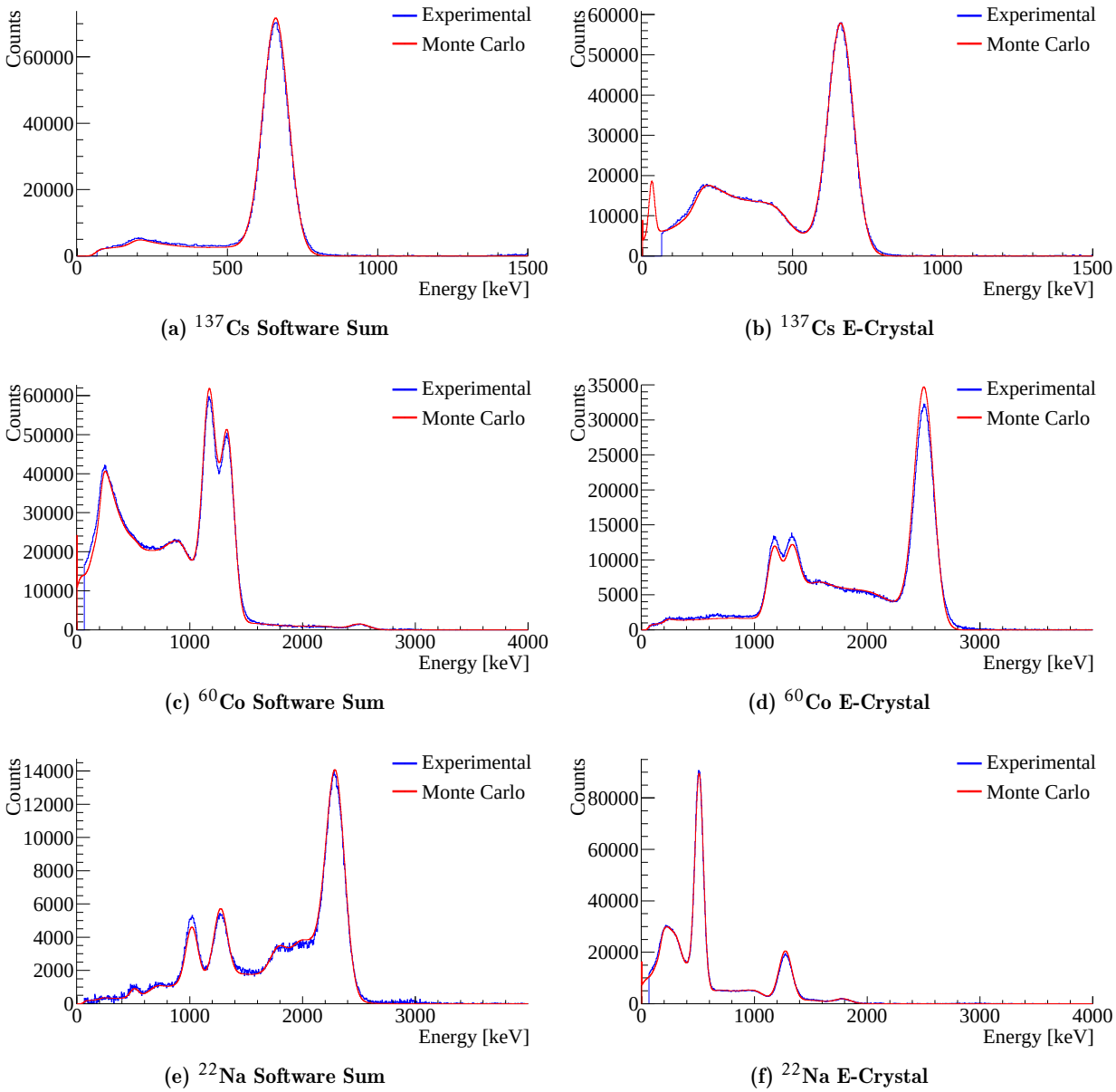

(a) ^{137}Cs Software Sum

(b) ^{137}Cs E-Crystal

(c) ^{60}Co Software Sum

(d) ^{60}Co E-Crystal

(e) ^{22}Na Software Sum

(f) ^{22}Na E-Crystal

Figure C.1: Full experiment set-up "*WithTube*" ^{137}Cs ^{60}Co and ^{22}Na calibrant data comparison of Monte Carlo results (Red) and Experiment Data (Blue) after subtraction of Background and Pile-up.

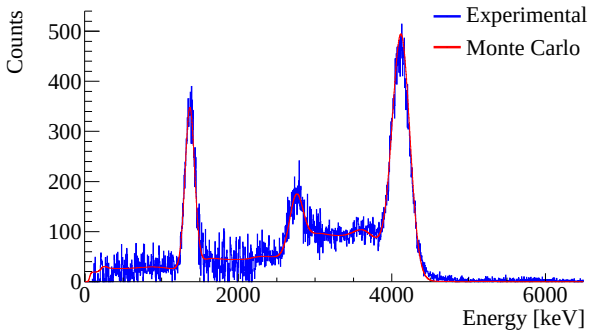

(a) ^{24}**Na Software Sum**

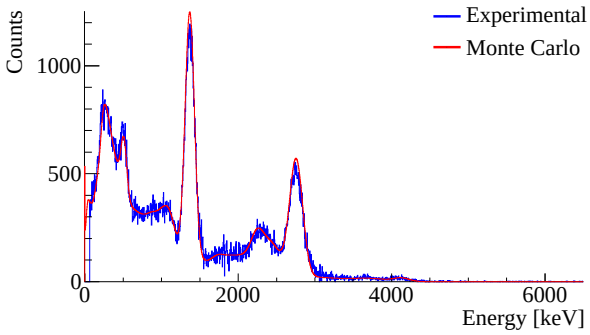

(b) ^{24}**Na E-Crystal**

Figure C.2: Full experiment set-up "*WithTube*" ^{24}Na calibrant data comparison of Monte Carlo results (Red) and Experiment Data (Blue) after subtraction of Background and Pile-up.

C.2 Monte Carlo Comparison of "*NoTube*" Data

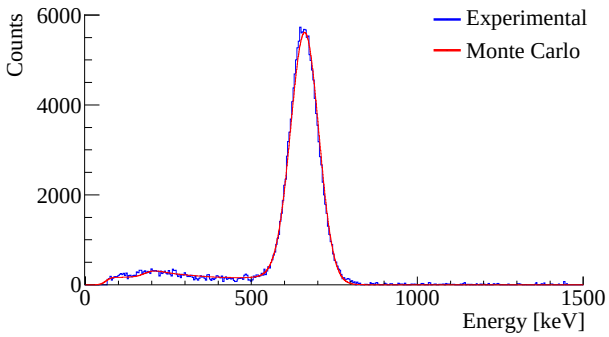

(a) ^{137}Cs **Software Sum**

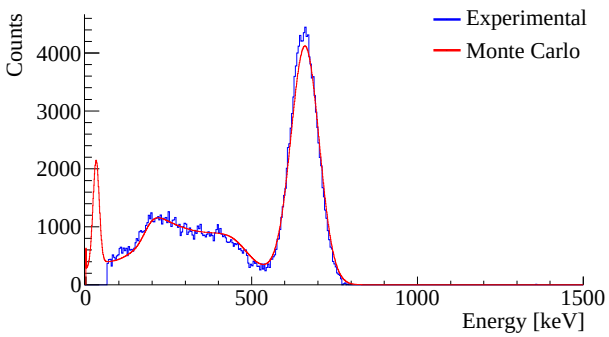

(b) ^{137}Cs **E-Crystal**

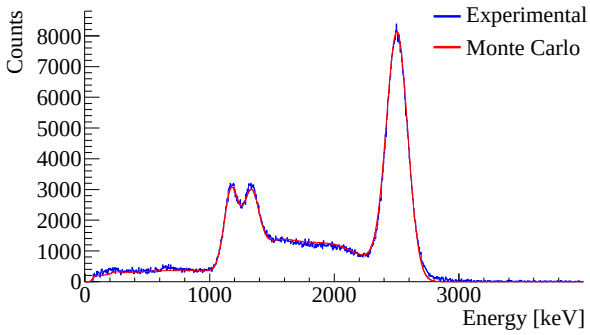

(c) ^{60}**Co Software Sum**

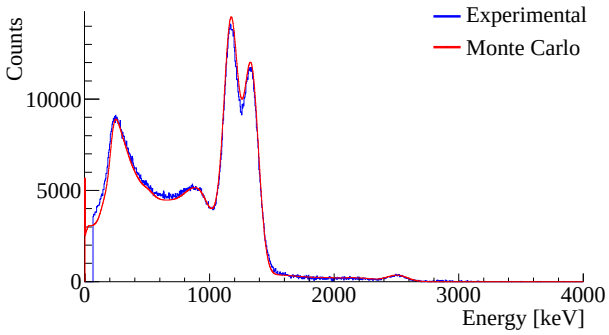

(d) ^{60}**Co E-Crystal**

Figure C.3: Preliminary calibration set-up"*NoTube*" ^{137}Cs and ^{60}Co calibrant data comparison of Monte Carlo results (Red) and Experiment Data (Blue) after subtraction of Background and Pile-up.

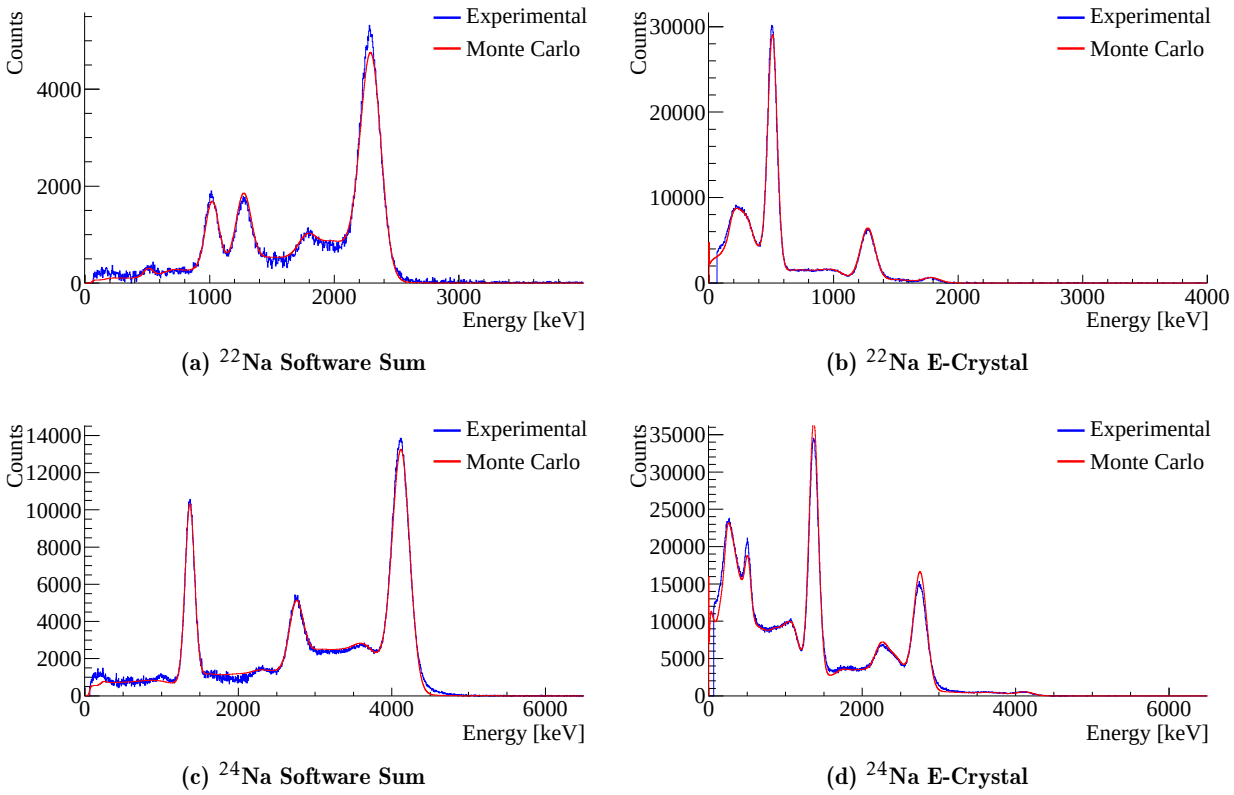

(a) ^{22}**Na Software Sum**

(b) ^{22}**Na E-Crystal**

(c) ^{24}**Na Software Sum**

(d) ^{24}**Na E-Crystal**

Figure C.4: Preliminary calibration set-up"*NoTube*"^{22,24}Na calibrant data comparison of Monte Carlo results (Red) and Experiment Data (Blue) after subtraction of Background and Pile-up.

D Previous Reported Level Schemes Data

D.1 Calibrant

Source	Gamma Energy (keV)	
	Software Sum	E-Crystal
^{137}Cs	661.7	661.7
^{60}Co	1173.2	1173.2
^{60}Co	1332.5	1332.5
^{60}Co	2505.7	2505.7
^{22}Na	1022.0	511.0
^{22}Na	1274.5	1274.5
^{22}Na	2296.5	-
^{24}Na	1368.6	511.0
^{24}Na	2754.0	1368.6
^{24}Na	4122.6	2754.0

Table D.1: Reference γ rays for the calibration sources taken from [126].

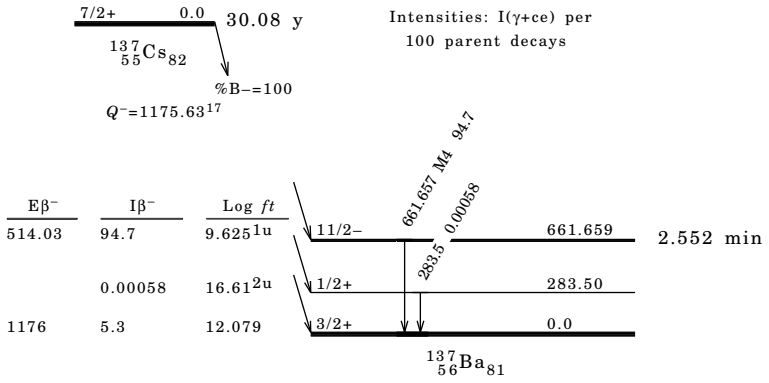

(a) ^{137}Cs

Figure D.1: Previously reported decay data for the ^{137}Cs calibrant, taken from [25].

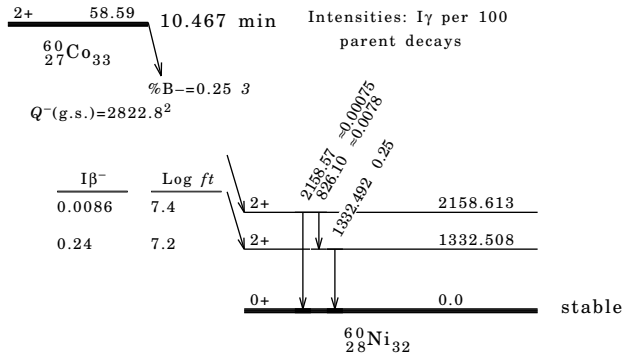

(a) ^{60}Co

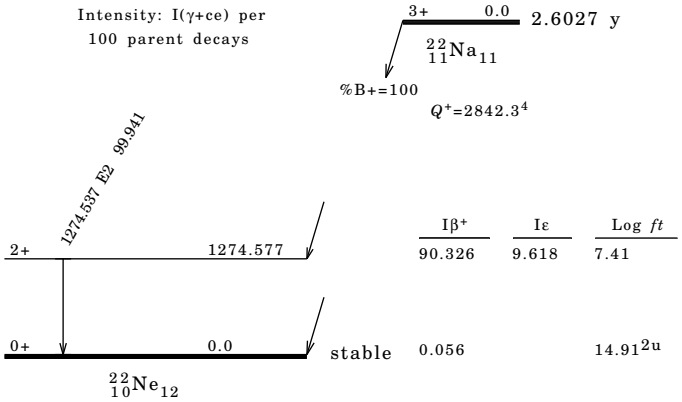

(b) ^{22}Na

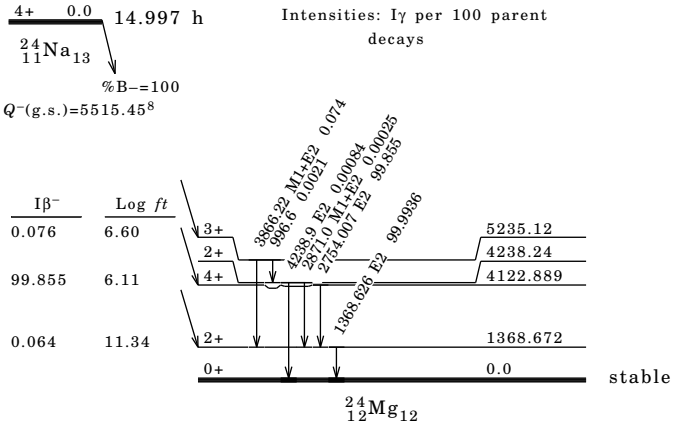

(c) ^{24}Na

Figure D.2: Previously reported decay data for the ^{60}Co, ^{22}Na and ^{24}Na calibrants, taken from [25].

D.2 Isotopes Under Investigation

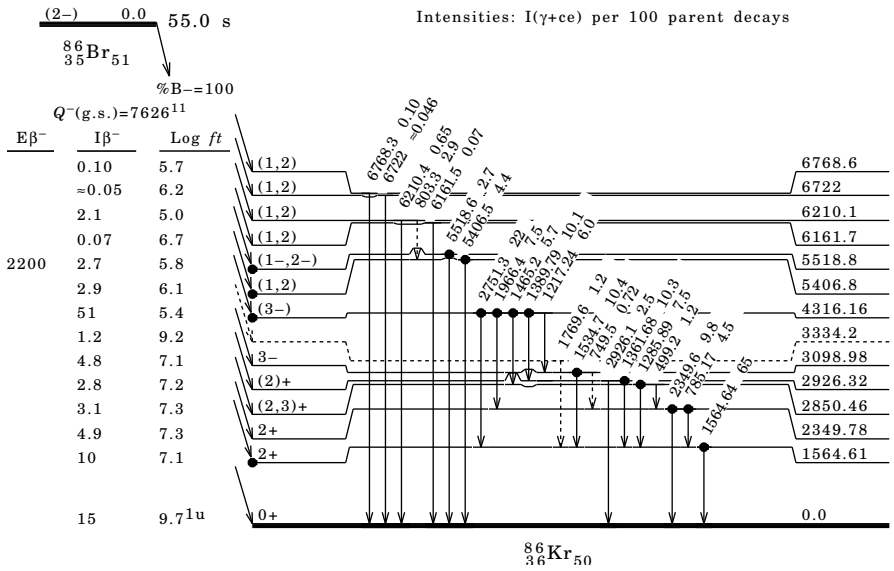

Figure D.3: Previously reported β decay data for ^{86}Br, taken from [29].

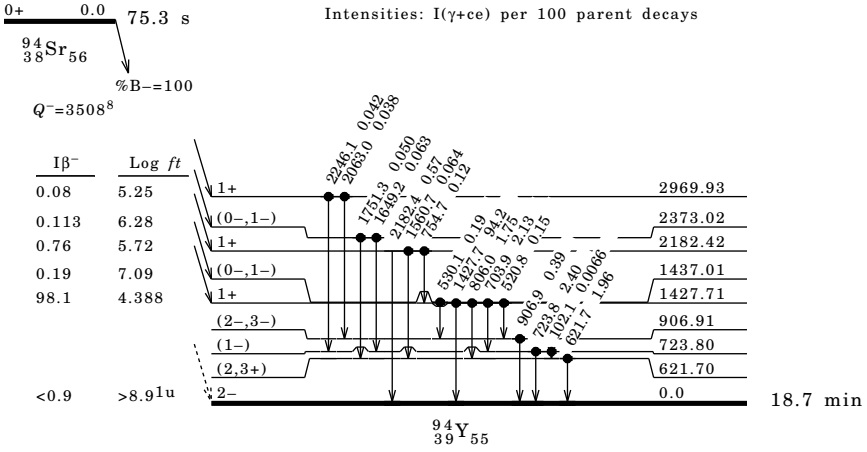

Figure D.4: Previously reported β decay data for ^{94}Sr, taken from [43].

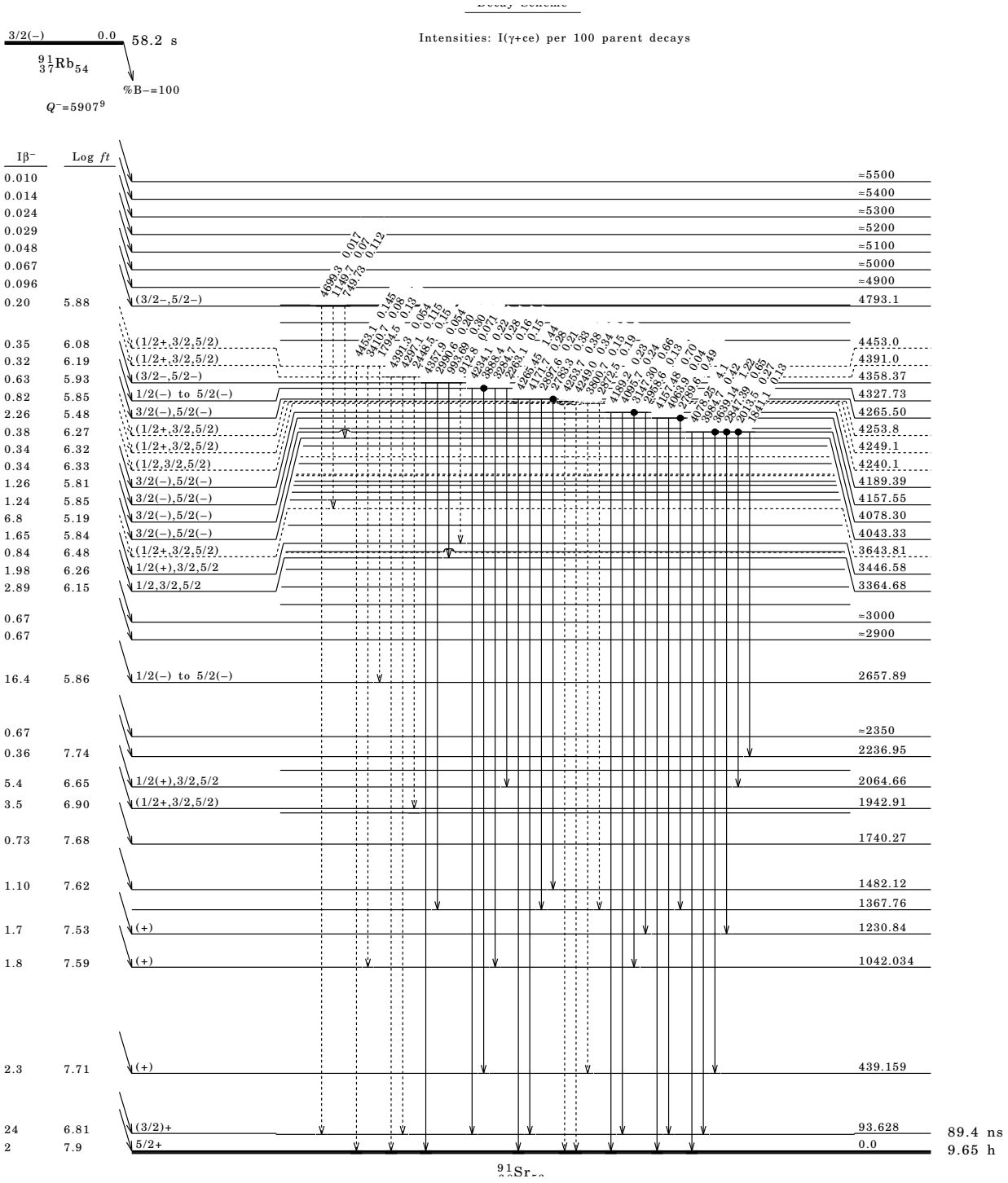

Figure D.5: Previously reported β decay data for ^{91}Rb (Part I), taken from [39].

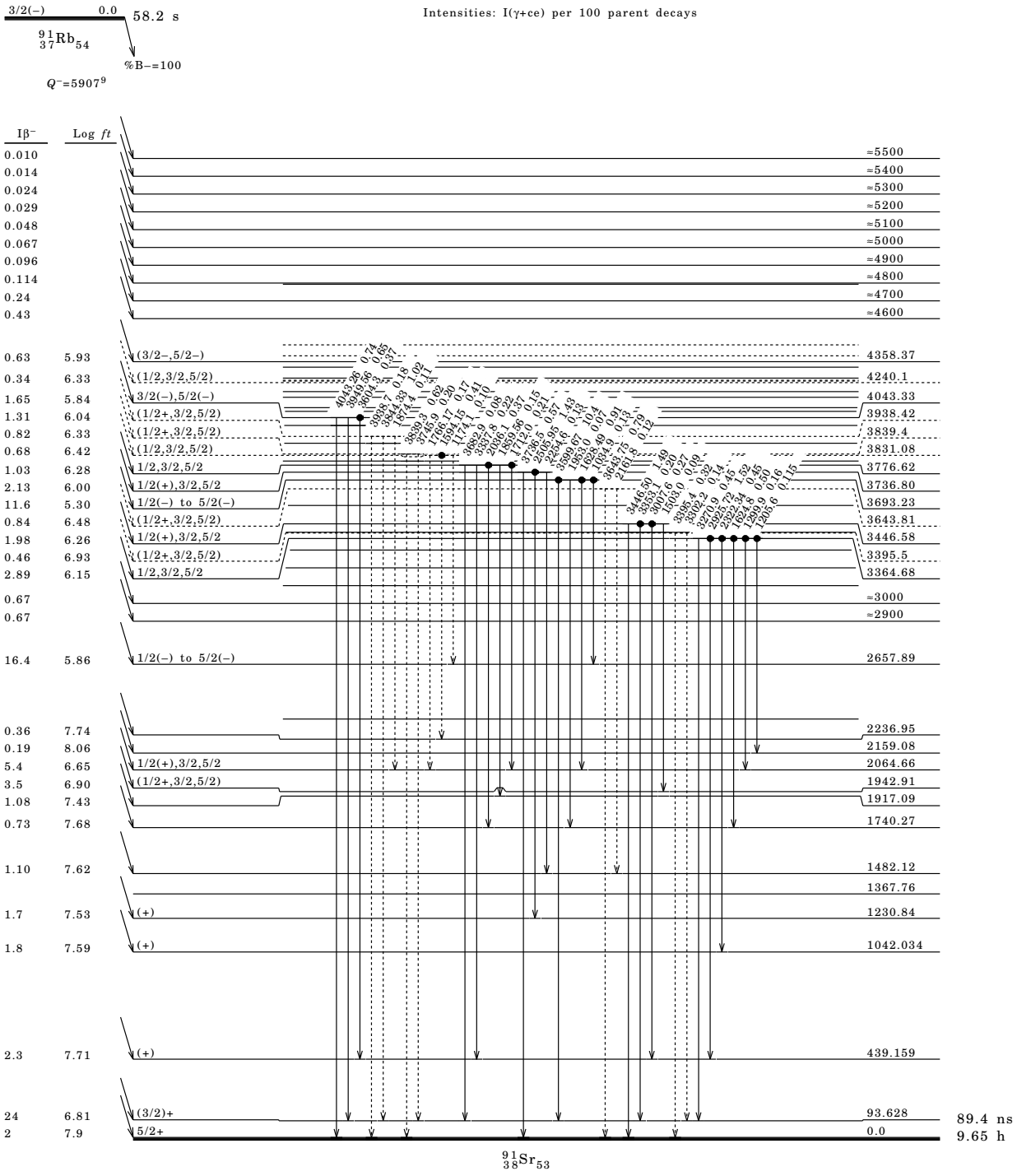

Figure D.6: Previously reported β decay data for ^{91}Rb (Part II), taken from [39].

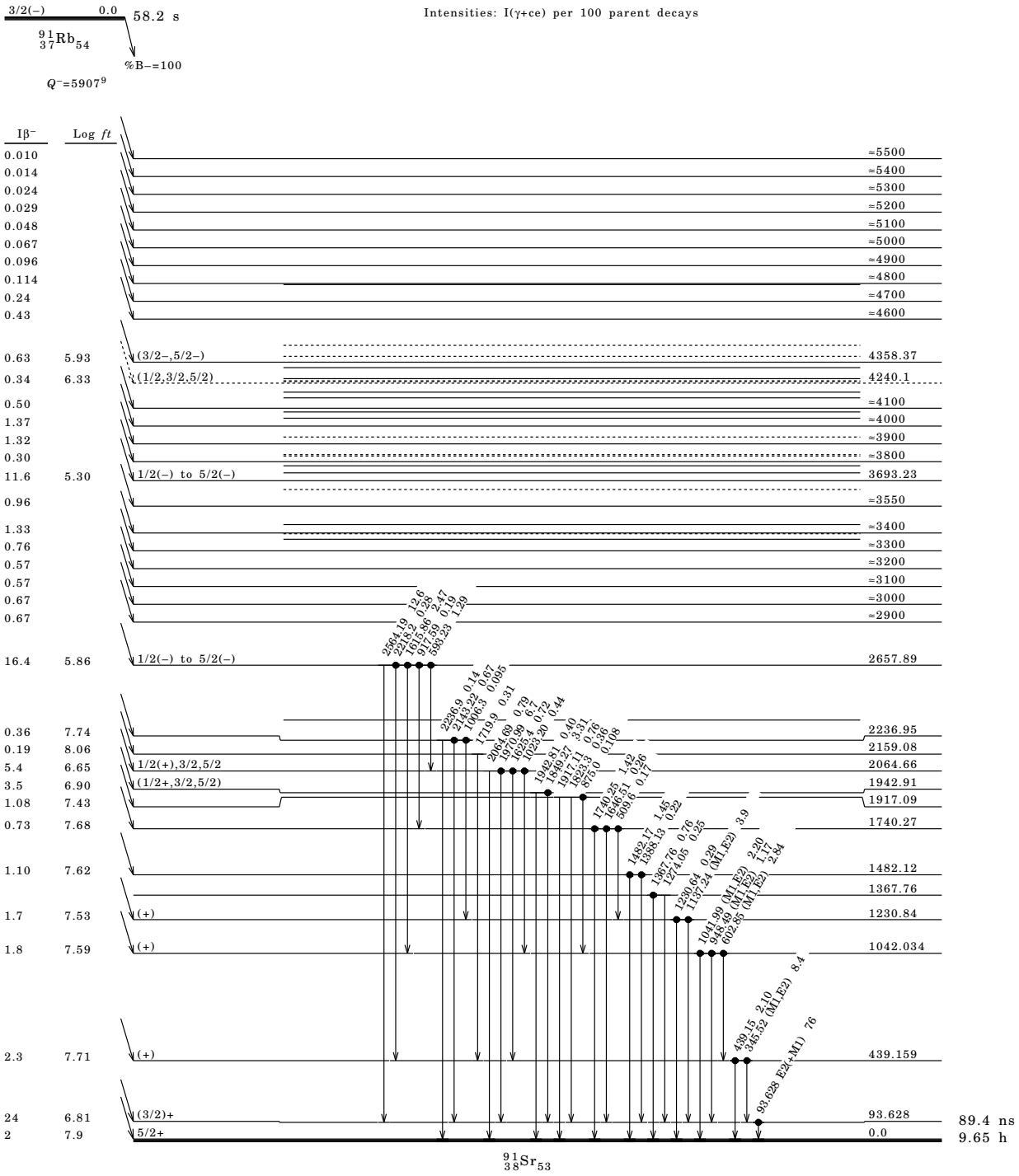

Figure D.7: Previously reported β decay data for ^{91}Rb (Part III), taken from [39].

E List of Publications & Oral Presentations

E.1 Conferences

(2011) Attended Institute of Physics (UK), Nuclear Physics Conference, Glasgow, UK.

(2011) Talk at the Rutherford Centennial Conference on Nuclear Physics, Manchester, UK.

(2012) Attended Institute of Physics (UK), Nuclear Physics Conference, Brighton, UK.

(2012) Poster at Joliot Curie School, Frejus, France.

(2013) Attended International Conference on Nuclear Data for Science and Technology, New York, USA.

E.2 Workshops

(2011) PreSPEC decay physics workshop, Brighton, UK.

(2011) CARIBU, decay workshop (decay heat), Argon Lab, Chicago, USA.

(2011) Autumn workshop on GEANT4, Častá-Papiernička Centre, Slovakia.

(2012) mini total absorption workshop on reactor neutrino physics, IFIC, Valencia, Spain.

E.3 Summer Schools

(2011) UK Nuclear Physics summer school, St Andrews, UK.

(2012) Joliot Curie school, Frejus, France. "Nuclei through the looking glass: High intensity stable and ISOL beam frontier"

(2012) European school on Experiments, Theory and Evaluation of Nuclear Data (EXTEND) school, Budapest, Hungary.

E.4 Experiments

- Lifetime measurement using fast timing set-up at Bucharest, Romania.
- Uranium and Krypton EURICA campaigns at RIKEN, Japan (β decay and isomer studies).
- Beta delayed neutron study at GSI, Germany.
- TAS and isomer studies at ISOLDE CERN.
- Lifetime measurements using a plunger experiment at Jyväskylä, Finland.

E.5 Publications

- Lifetime measurements in the transitional nucleus ^{138}Gd, M.G.Procter, et al. *Phys.Rev. C 84, 024314*. [2011]
- Decay Heat Measurements Using Total Absorption Gamma-ray Spectroscopy, S.Rice, et al. *J. Phys.: Conf. Ser. 381 012056*. [2012] (Attached in section E.6)
- X(5) critical-point symmetries in ^{138}Gd, M.G.Procter, et al. *J. Phys.: Conf. Ser. 381 012062* [2012]
- ^{7}Li -induced reactions for fast-timing with $LaBr_3$:Ce detectors, P.J.R.Mason et al. *AIP Conf. Proc. 1491, 93* [2012]
- Electromagnetic Transition Rate Measurements in the N=80 Isotone, ^{138}Ce, T Alharbi et al. *J. Phys.: Conf. Ser. 381 012057* [2012]
- Electromagnetic transition rates in the $N = 80$ nucleus $^{138}_{58}$Ce, T.Alharbi, et al. *Phys.Rev. C 87, 014323*. [2013]
- Half-life of the yrast 2^+ state in ^{188}W: Evolution of deformation and collectivity in neutron-rich tungsten isotopes, P.J.R.Mason et al. *Phys. Rev. C 88, 044301* [2013]
- Precision Lifetime Measurements Using $LaBr_3$ Detectors With Stable and Radioactive Beams, P.H.Regan et al.*EPJ Web of Conferences 63, 01008* [2013]
- Total absorption γ-ray spectroscopy of beta delayed neutron emitters, E. Valencia et al. *AIP Conf. Proc. 1541, 161* [2013]
- Characterization of a new modular decay total absorption gamma-ray spectrometer (DTAS) for FAIR, A.Montaner Pizá et al. *AIP Conf. Proc. 1541, 179* [2013]
- Measurement of fission products β decay properties using a total absorption spectrometer, A.-A. Zakari-Issoufou et al. *EPJ Web of Conferences 62, 01007* [2013]
- β-delayed neutron emission measurements around the third r-process abundance peak, R. Caballero-Folch et al. *AIP Conf. Proc. 1541, 137* [2013]
- Approaching the precursor nuclei of the third r-process peak with RIBs, C. Domingo-Pardo et al. *nuclear Physics in Astrophysics VI, Lisbon 2013, Conference Proceedings* [2013]
- Status of the EURICA Project After One Year at RIKEN, P. A. Söderström et al. *Proceedings of the 12th Asia Pacific Physics Conference (APPC12), Conference Proceedings* [2014]

Rutherford Centennial Conference on Nuclear Physics IOP Publishing
Journal of Physics: Conference Series **381** (2012) 012056 doi:10.1088/1742-6596/381/1/012056

Decay Heat Measurements Using Total Absorption Gamma-ray Spectroscopy

S Rice[1], E Valencia[2], A Algora[2], JL Taín[2], PH Regan[1], Z Podolyák[1] J Agramunt[2], W Gelletly[1] and AL Nichols[1]

[1] Department of Physics,The University of Surrey, Guildford, Surrey, GU2 7XH, UK
[2] Instituto de Fisica Corpusclar, Valencia, Spain

E-mail: s.rice@surrey.ac.uk

Abstract.
A knowledge of the decay heat emitted by thermal neutron-irradiated nuclear fuel is an important factor in ensuring safe reactor design and operation, spent fuel removal from the core, and subsequent storage prior to and after reprocessing, and waste disposal. Decay heat can be readily calculated from the nuclear decay properties of the fission products, actinides and their decay products as generated within the irradiated fuel. Much of the information comes from experiments performed with HPGe detectors, which often underestimate the beta feeding to states at high excitation energies. This inability to detect high-energy gamma emissions effectively results in the derivation of decay schemes that suffer from the *pandemonium effect*, although such a serious problem can be avoided through application of total absorption γ-ray spectroscopy (TAS). The beta decay of key radionuclei produced as a consequence of the neutron-induced fission of ^{235}U and ^{239}Pu are being re-assessed by means of this spectroscopic technique. A brief synopsis is given of the Valencia-Surrey (BaF_2) TAS detector, and their method of operation, calibration and spectral analysis.

1. Motivation

Commercial nuclear reactors produce roughly 1040 different nuclides, a large fraction of which are unstable. The energy released in their decays in the fuel produces heat known as decay heat. During operations in thermal fission nuclear reactors, approximately 8% of the total heat produced in the reactor is due to decay heat and this contribution must be factored into the energy production [1]. Decay heat is the sole source of heat from the fuel in the absence of fission and therefore is extremely important in reactor design, irradiated fuel operations and storage.

Decay heat has three components: heavy particles(H_{HP}), light particles(H_{LP}) and photons(H_{EM}). Heavy particles are defined as neutrons, protons, alpha particles and spontaneous fission fragments, whereas light particles are defined as electrons, positrons, Auger electrons and conversion electrons, but are sometimes referred to collectively as "betas" photons are defined as γ-rays, X-rays, bremsstrahlung and annihilation radiation [2]. Data from nuclear databases such as JEFF 3.1 [3] can be used to calculate the actinide and fission-product inventories for a specified condition of reactor operation as a function of the cooling period. The

Rutherford Centennial Conference on Nuclear Physics IOP Publishing
Journal of Physics: Conference Series **381** (2012) 012056 doi:10.1088/1742-6596/381/1/012056

decay heat can then be derived by summing the decay energies from the emitted heavy particles, light particles and photons weighted with the activities of the produced fission products:

$$H_{HP}(t) = \sum_{i=1}^{M} \lambda_i^T N_i(t) \bar{E}_{HP}^i \tag{1}$$

$$H_{LP}(t) = \sum_{i=1}^{M} \lambda_i^T N_i(t) \bar{E}_{LP}^i \tag{2}$$

$$H_{EM}(t) = \sum_{i=1}^{M} \lambda_i^T N_i(t) \bar{E}_{EM}^i \tag{3}$$

$\bar{E}$, λ^T and N represent the mean energy released per disintegration, the total decay constant for the nuclide and the number of the nuclides present respectively. The decay heat has also been experimentally measured by calorimetry thus providing an opportunity to test the accuracy of the nuclear datasets.

1.1. Pandemonium effect

The discrepancy between the calorimetry data and the modelled nuclear dataset is thought to be due to incorrect beta decay data (β^- and β^+) and more specifically missing beta feeding to higher-lying levels in some key nuclei (see for example Ref.[4]). The decay spectroscopy of many fission fragments was carried out using high-resolution γ-ray spectroscopy due to the simplicity of this technique. The application of high resolution γ-ray measurements to quantify the individual beta decays in some nuclei might suffer from the *pandemonium effect* resulting in the incorrect assignment of beta feeding to low-lying levels in the daughter nucleus [5]. This results in a systematic error in the deduced mean beta and gamma energies, thus affecting the decay heat calculations. Ref.[6] outlines a list of nuclear measurements that might be affected by the *pandemonium effect* and prioritises them according to their involvement in decay heat calculations for the most common nuclear fuels used in power generation.

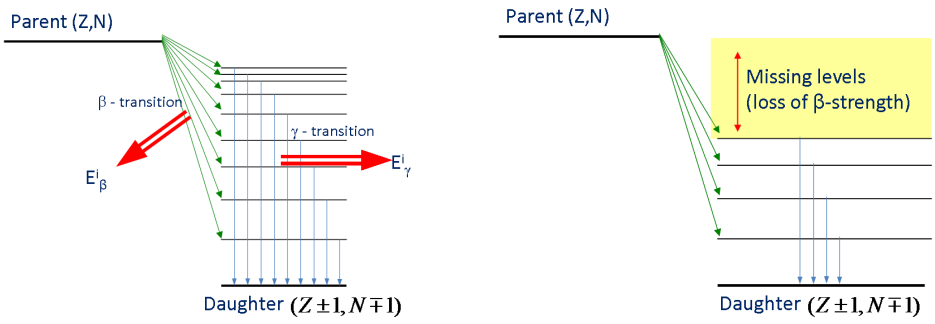

(a) Real feeding levels (b) Detected feeding levels

Figure 1: Schematic representation of the *pandemonium effect* in beta decay.

The beta-decaying parent nucleus populates many levels in the daughter nucleus, and each decay to a different level has a precise beta-decay end point. High resolution γ-ray spectroscopy is used to measure the γ-ray intensities that both depopulate and populate these daughter

Rutherford Centennial Conference on Nuclear Physics IOP Publishing
Journal of Physics: Conference Series **381** (2012) 012056 doi:10.1088/1742-6596/381/1/012056

nuclear levels, and by this means individual beta feeding can be deduced from the balance of γ-ray intensities populating and depopulating each level. Decays with large Q_β values may lead to the population of a large number of levels in the daughter nucleus including some at high excitation energies (Fig.1a). The *pandemonium effect* occurs when these β-feeding distributions to the higher excitation states are erroneously derived from the γ-ray spectra (Fig.1b).

The detection of β-feeding distributions to high excitation states is impeded. At high excitation energies, a higher density of nuclear levels exist in the daughter nucleus, and the detection of β-feeding distributions is impeded. Due to the proximity of these energy levels, the β-branching to each individual level will be weaker than at lower energies. The high-excitation energy levels are open to multiple γ-decay paths to the ground state, and therefore their β-population produces many weak γ-rays that are statistically difficult to detect. These processes alone restrict the measurement of the β-feeding distributions to the high excitation states, but when combined with the low efficiency of HPGe detectors and the significant reduction of this efficiency at higher energy (> 2 MeV) the probability of detection reduces even further.

A large number of beta decay measurements have been undertaken by means of HPGe detectors before this effect was fully understood. As a result some decay schemes were thought to be complete and the β-feeding was assumed to be correct. But in reality the incorrect assignment of β-feeding as a consequence of the pandemonium effect can produce significant errors in the nuclear data sets. Fig.2 compares the measured beta strength function of ^{150}Ho obtained from the Cluster Cube (HPGe array) with that from the GSI-TAS (NaI(Tl) TAS detector)). The resulting spectra show clear evidence of the *pandemonium effect* in the HPGe data above 5 MeV, whereas the TAS measurements do not suffer from this problem. These data and spectra are taken from Ref.[7].

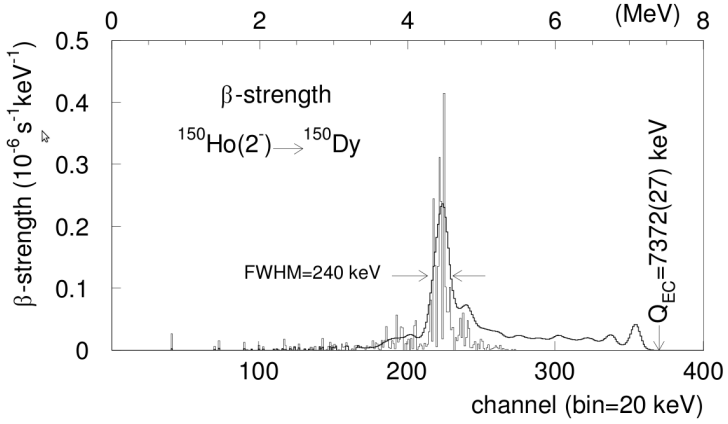

Figure 2: Beta-strength as a function of excitation energy in the daughter nucleus following the decay of the 2^- ground state in ^{150}Ho measured with the CLUSTER CUBE (depicted as a histogram) and the GSI-TAS spectrometer (continuous spectral data) [7].

2. Total Absorption Gamma-ray Spectroscopy

An ideal total absorption gamma-ray spectrometer would be 100% efficient in the detection of γ-ray radiation, cover a full 4π solid angle with good energy-resolution characteristics. TAS detectors can be made from scintillator materials (such as NaI(Tl) or BaF_2) with near 4π geometry. These relatively high-Z detection materials and the large volume of these detectors can

Rutherford Centennial Conference on Nuclear Physics IOP Publishing
Journal of Physics: Conference Series **381** (2012) 012056 doi:10.1088/1742-6596/381/1/012056

provide high overall detection efficiency, but with a significant deterioration in energy resolution compared with HPGe detectors. The collection of γ-rays in the TAS differs from conventional high-resolution gamma spectroscopy such as HPGe arrays, in that the TAS detector collects the full γ-ray energy cascade from a source, rather than measuring the individual γ-ray energies which make up the mutually coincident cascade.

The use of scintillators with an increased efficiency and the capability to collect full γ cascades reduces the *pandemonium effect*. Analysis of the TAS spectra is non-trivial and requires solution of equation (4):

$$d_i = \sum_j R_{ij} f_j \tag{4}$$

where d,R and f are the detector data, the response matrix and the feeding distribution respectively.

3. Experiments

The accelerator facility at the University of Jyvaskyla, Finland (JYFL), was used in November 2009 to generate eight separate radionuclides for TAS studies. Each of these nuclei had been defined as of high priority in decay heat studies [2, 6] and JYFL was selected due to the ability to produce high-purity sources. Analysis of the resulting spectral data has been divided between groups in Valencia, Nantes and Surrey.

3.1. Valencia-Surrey TAS detector

The Valencia-Surrey TAS spectrometer is a segmented barium fluoride (BaF_2) detector. The geometry of the 12 segments of BaF_2 is shown in Fig.(3) with detector dimensions of 25 cm length, 25 cm diameter with a 5 cm diameter, and 5 cm diameter longitudinal hole in the centre. Each BaF_2 crystal segment is optically insulated. Generally, BaF_2 crystals include contamination from radium due to radium and barium being chemical homologues. This contamination also gives rise to background radiation from the radioactive daughters produced within the natural decay chain of the radium isotopes. Detection of this internal radiation allows a constant gain matching between each of the PMT outputs. A planar silicon detector was placed at the centre of the TAS detector so that beta tagging could be used as a hardware trigger to reduce the random background counts in the final data.

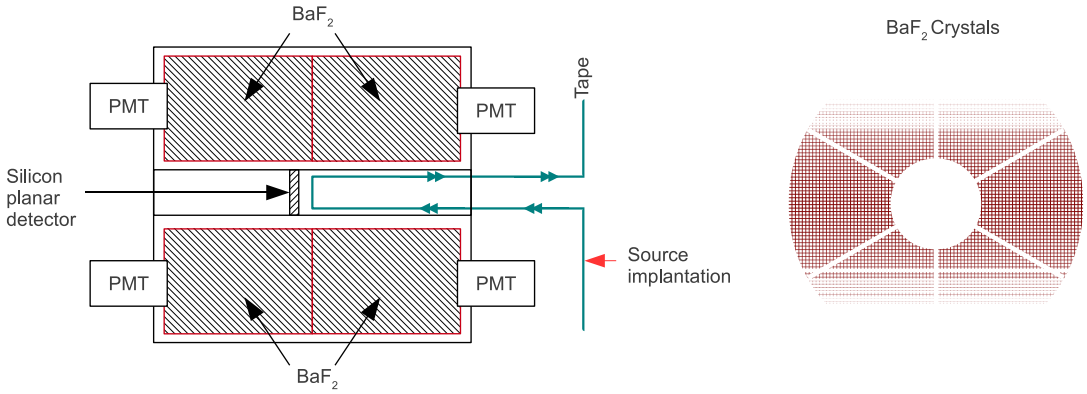

Figure 3: Valencia-Surrey TAS detector, ($left$) longitudinal cross section showing the locations of the tape and planar silicon detector; ($right$) cross section of the crystal arrangement.

Rutherford Centennial Conference on Nuclear Physics IOP Publishing
Journal of Physics: Conference Series **381** (2012) 012056 doi:10.1088/1742-6596/381/1/012056

The separated source from JYFL was deposited onto a tape delivery system which moved regularly to place the source at the centre of the TAS detector, simultaneously removing decayed sources and thus reducing the background produced by any daughter products. Each measuring cycle of the tape was optimised to the half-life of the decay being measured. Background measurements were taken at regular intervals between source measurement. Each segment of the TAS detector was readout separately producing many different output options. For the initial stage of the analysis two outputs were created: sum of each segment (E-crystal); and an online summation of the signals (Software Sum), which collects the signal as if the detector system was a single crystal (see Fig.4).

Standard sources of ^{22}Na, ^{137}Cs and ^{60}Co were used to calibrate and characterise the detector (however, these sources were sealed as a safety requirement, and therefore the silicon detector could not be applied for beta tagging in the initial set-up). ^{24}Na created by the JYFL was also used as a calibrant. The TAS data were cleaned-up and improved by undertaking both background and pile-up subtraction, prior to implementing energy and resolution calibrations. The detector manufacturer's specifications and the resulting energy and resolution calibrations were adopted as input to the GEANT4 code in order to create an appropriate Monte-Carlo (MC) model. This model is presently being used to characterise the detector on the basis of the calibrant sources.

4. Current State of Data Analysis

The spectra produced by the MC model for the calibration sources are currently being compared with the equivalent TAS data for each source (Fig.4). MC spectral data are not in satisfactory agreement with the TAS calibration data. Therefore, the existing MC code is being adjusted with respect to detector geometry, based on known differences between the original specified geometry and that subsequently quoted by the manufacturer. Physics processes within the *GEANT4* MC code will also be assessed for validity at a later stage. When the MC model is able to replicate a good agreement to the calibration data, attention will be turned with confidence towards analyses of the spectral data of interest.

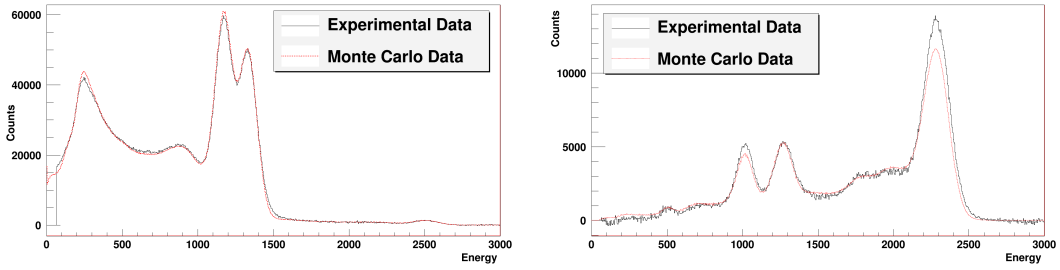

(a) E-crystal of ^{60}Co data (b) Software sum of ^{22}Na data

Figure 4: Comparison of the MC and the experimental data: (a) γ-rays from ^{60}Co calibration source collected in each crystal and then summed. (b) γ-rays collected from ^{22}Na source calibration source as if the complete detector array was a single crystal.

MC models are required for the measured nuclei of interest. These model are created as before, with adjustments to the decay read-in files as created for each source from the available decay schemes (taken from nuclear data sets). A statistical model will be used to extend the calculations to high energies. Since the experimental sources are unsealed, gating on the silicon detector should be possible in order to eliminate most of the spectral background. The effects

Rutherford Centennial Conference on Nuclear Physics IOP Publishing
Journal of Physics: Conference Series **381** (2012) 012056 doi:10.1088/1742-6596/381/1/012056

of pile-up and any contamination from daughter decay will also be removed. These cleaned-up spectra can then be compared with the MC spectra to show whether the *pandemonium effect* affects the nuclear data set.

Assuming that the original measurements are affected by the *pandemonium effect* as postulated in Ref.[6], a new decay scheme will be created for the MC model. This new decay scheme will be created from the recorded nuclear data up to an energy threshold set to exclude regions of excitation energy in the daughter that might have been affected by the *pandemonium effect*. Above this new threshold the decay scheme will consist of "pseudo levels" added with their corresponding γ-branching ratios on the basis of the adopted a statistical model. Once this is completed an iterative process of adjusting the feeding to all the levels will be carried out so that the MC spectra gives good agreement with the experimental data.

5. Conclusions

Total absorption γ-ray spectroscopy can be used to avoid the *pandemonium effect* found in some HPGe gamma measurements of beta feeding distributions. The analysis of the TAS data is non-trivial and accurate MC models of the system are needed to extract the beta feeding distributions. Hopefully, with the measurement of selected nuclei by means of TAS, more accurate decay heat calculations can be achieved, and so assist in providing even greater confidence in operational procedures involving irradiated fuel.

6. Acknowledgements

SR, PHR, ZP, ALN and WG acknowledge support by the Engineering and Physical Research Council, Spanish project number FPA 2008-06419-C02-01.

7. References

[1] Rubio B and Gelletly W 2009 Beta decay of exotic nuclei *The Euroschool Lectures on Physics with Exotic Beams Vol. III* Lecture Notes in Physics 764

[2] Kellett M A, Nichols A L, Bersillon O, Henriksson H, Jacqmin R, Roque B, Katakura J, Oyamatsu K, Tachibana T, Yoshida T, Algora A, Rubio B, Taín J L, Dean C J, Gelletly W, Mills R W, Gauld I C, Möller P and Sonzogni A 2007 Assessment of fission product decay data for decay heat calculations (*A Report by the Working Party on International Evaluation Co-operation of the NEA Nuclear Science Committee* vol Vol. 25) ed Yoshida T and Nichols A L ISBN 978-92-64-99034-0

[3] Kellett M A, Bersillon O and Mills R W 2009 The JEFF -3.1/-3.1.1 radioactive decay data and fission yields sub-libraies Tech. Rep. JEFF Report 20 Nuclear Energy Agency

[4] Algora A, Jordan D, Taín J L, Rubio B, Agramunt J, Perez-Cerdan A B, Molina F, Caballero L, Nácher E, Krasznahorkay A, Hunyadi M D, Gulyás J, Vitéz A, Csatlós M, Csige L, Äysto J, Penttilä H, Moore I D, Eronen T, Jokinen A, Nieminen A, Hakala J, Karvonen P, Kankainen A, Saastamoinen A, Rissanen J, Kessler T, Weber C, Ronkainen J, Rahaman S, Elomaa V, Rinta-Antila S, Hager U, Sonoda T, Burkard K, Hüller W, Batist L, Gelletly W, Nichols A L, Yoshida T, Sonzogni A A and Peräjärvi K 2010 *Phys. Rev. Lett.* **105**(20) 202501 URL `http://link.aps.org/doi/10.1103/PhysRevLett.105.202501`

[5] Hardy J C, Carraz L C, Jonson B and Hansen P G 1977 *Phys. Lett. B* **71** 307–10 p

[6] Yoshida T, Tachibana T, Storrer F, Oyamatsu K and Katakura J 1999 *J. of Nucl. Sci. Technol.* **36** 135–142

[7] Algora A, Rubio B, Cano-Ott D, Taín J L, Gadea A, Agramunt J, Gierlik M, Karny M, Janas Z, Płochocki A, Rykaczewski K, Szerypo J, Collatz R, Gerl J, Górska M, Grawe H, Hellström M, Hu Z, Kirchner R, Rejmund M, Roeckl E, Shibata M, Batist L and Blomqvist J (GSI Euroball Collaboration) 2003 *Phys. Rev. C* **68**(3) 034301 URL `http://link.aps.org/doi/10.1103/PhysRevC.68.034301`